Efficient Hysteresis Loop Analysis Based Structural Health Monitoring of Civil Structures

Cong Zhou

A thesis presented in partial fulfilment of the requirements for the Degree

of

Doctor of Philosophy

in

Mechanical Engineering
at the
University of Canterbury
Christchurch, New Zealand

University of Canterbury
2016

Abstract

Real time or rapid structural health monitoring (SHM) enables immediate post-event assessment of the damage state and health condition of civil structures, particularly for critical infrastructure, such as a hospital, fire station, power plant and bridge, which are needed most after an earthquake. They thus offer reliable information for deciding if the structure can continue to be used, and enable more optimum recovery planning and costs. Hence, such methods provide benefits in terms of assessment and recovery from major earthquake events.

This thesis examines structural health monitoring from a unique perspective. A model-free hysteresis loop analysis (HLA) is developed for damage identification and structural health monitoring of civil structures subjected to earthquake excitations. The HLA method developed within this research is based on the hypothesis testing and statistical analysis of the reconstructed hysteresis loops to identify the physical parameters that are directly related to structural damage and condition. This approach avoids constraints to a single or fixed model, and is implicitly based on fundamental underlying structural mechanics. It thus provides a novel and computationally efficient means to accurately detect, localize and quantify structural damage for different types of hysteretic structures during or immediately after an earthquake. Importantly, this thesis provides significant experimental validations on the performance of the method to different types of dynamic response, particularly for highly nonlinear hysteretic behaviours. In addition, the effectiveness of the HLA method is also compared to any of the vibration-based and model-based methods using calibrated numerical models. Finally, real data form a base-isolated building is also used to validate the method and its utility.

The SHM results on both reinforced concrete (RC) frame experimental structures indicate the HLA method is capable of detecting and assessing the damage location and severity accurately for realistic highly nonlinear RC structures by tracking the evolution of the elastic stiffness of significant half cycles with full dynamic response. More importantly, the method also offers the ability to identify stiffness degradation and damage that may not be evident by external visual appearance. In addition, the extraction of the effective linear stiffness using a multiresolution wavelet analysis (MRA) provides a further useful tool to characterize structural deterioration for more common small events.

Comparison of the SHM results between the model-free HLA method and the model-based adaptive LMS filters show that the HLA algorithm is more effective that the model-based method in identifying RC structures with highly nonlinear and variable pinching and/or rocking behaviours. The results also highlight the need for model-based methods to have an appropriate model that can capture the observed response, in order to yield accurate results, even in small events where the structure remain linear.

Overall, this thesis develops an efficient HLA-based SHM method to ensure a rapid assessment of the structural damage and safety during or immediately after an earthquake. Significant validation is implemented against both experimental and simulation data of realistic RC structures, as well as real data from a base-isolated building, which thus clearly demonstrate the advantages of this approach over other traditional SHM methods.

Publications

A number of published articles that are based on the work presented in this thesis, have been made during the course of this research. They are listed here for reference:

Journal Papers:

- **Zhou, C**, Chase, JG, Rodgers, GW, Tomlinson, H and Xu, C (2015). "Physical Parameter Identification of Structural Systems with Hysteretic Pinching", *Computer-Aided Civil and Infrastructure Engineering*, 30(4):247-262.

- **Zhou, C**, Chase, JG, Rodgers, GW, Xu, C and Tomlinson, H (2015). "Overall Damage Identification of Flag-shaped Hysteresis Systems under Seismic Excitation", *Smart Structures and Systems*, 16(3): 163-181.

- **Zhou, C**, Chase, JG, Rodgers, GW, Adam, K, Gutschmidt, S and Xu, C (2015). "Performance Evaluation of CWH Base Isolated Building during Two Major Earthquakes in Christchurch", *Bulletin of New Zealand Society for Earthquake Engineering,* 48(4): 264-273.

Conference Papers:

- **Zhou, C**, Chase, JG, Rodgers, GW, Huang BF and Xu, C (2016). "Structural health monitoring for reinforced concrete structures with damage occurred prior to a sequence of earthquake events", New Zealand Society for Earthquake Engineering (NZSEE) 2016 Annual Technical Conference, Christchurch, New Zealand, April 1-3, Paper ID: 104 (Accepted).

- **Zhou, C**, Chase, JG, Rodgers, GW, Kuang A, Gutschmidt S, and Xu, C (2015). "Response Prediction and Parameter Identification for Base-isolated Buildings with Limited Sensors", New Zealand Society for Earthquake Engineering (NZSEE) 2015 Annual Technical Conference, Rotorua, New Zealand, April 10-12, Paper ID: O11.

- **Zhou, C**, Chase, JG, Rodgers, GW and Xu, C (2015). "Real-time Structural Health Monitoring of Reinforced Concrete Frame Structure Using a Hysteresis Loop Method", New Zealand Society for Earthquake Engineering (NZSEE) 2015 Annual Technical Conference, Rotorua, New Zealand, April 10-12, Paper ID: O42.

- **Zhou, C**, Chase, JG, Rodgers, GW and Xu, C (2014). "Damage Identification of a Flag-shaped Hysteresis Structure Subject to Seismic Excitation", New Zealand Society for Earthquake Engineering (NZSEE) 2014 Annual Technical Conference, Auckland, New Zealand, March 21-23, Paper ID: P38.

Acknowledgements

I would like to first give many thanks to my supervisor, Distinguished Professor J. Geoffrey Chase, for his guidance and continuous support throughout my PhD study. I can never forget our first meeting in his office where he told me to trust him, which gave me strong faith on the success of this work through those difficult times. I could not have asked a better mentor, and I owe him much for all of his help that has been critical to my career and life.

I would also like to express my sincere appreciation to my co-supervisor, Dr. Geoffrey W. Rodgers, who helped me achieve the goal by providing insightful advice and technique comments along this journey. Thank you for arranging my travel to the NZSEE conference every year. Many thanks go to Professor Chao Xu at Northwestern Polytechnical University for sharing his experience and knowledge that I needed to succeed in this research. I would like to thank Dr. Baofeng Huang and Dr. Peizhen Li at Tongji for generously providing the experimental data presented in Chapters 4-6 of this thesis. I would also like to thank Adam Kuang and Dr. Stefanie Gutschmidt in our department for helping me access the real seismic data of the CWH building used in this research. Without them, this thesis would not have been possible.

I would like to specially thank Professor Shiming Chen and Associate Professor Ping Gu at Tongji University, whose inspiration and encouragement made me purse this PhD degree. My thanks also go to my friends, students, officemates and team members I have met during my time at UC. Their valuable help and support in my research and life are very much appreciated.

I would also like to acknowledge the financial support of China Scholarship Council (grant number: 201306260119) and Department of Mechanical Engineering at University of Canterbury.

Finally, I want to thank my wife Wenwen Li and my family for their love, patience and endless support that made me finish this research. My wife has been through a tough time during these years when we were apart. Without her understanding and encouragement, I would not be where I am today. Thank you.

Table of Contents

List of Figures

List of Tables

Chapter 1: Introduction

1.1 Background

Thousands of earthquakes occur across the world each year (USGS, 2012). Many are quite small, but some few can be destructive and cause grave loss of lives. The majority of the deaths and injury that result are due to building collapse (Coburm et al., 1992). For instance, the 1995 Kobe earthquake (Magnitude 6.9), which was the worst earthquake in Japan since the 1923 Great Kanto earthquake, killed 6,279 people, and nearly 90% of the deaths occurred as a direct result of building collapse (Tierney and Goltz, 1997). These collapsed buildings can be obviously discovered by visual inspection and subsequently demolished after the earthquake.

However, most buildings and infrastructures are designed to withstand strong ground shaking and remain standing after the main shock. Only local damage may have exist and is not always visible after a major event. Importantly, such local damage may have a great impact on the overall health or state of the structure, which can increase the potential risk of building collapse and loss of lives in an aftershock or new event in the future. In addition, structures may also be weakened by a foreshock earthquake event, and could thus have insufficient capacity for seismic resistance as designed in the following main shock. In both cases, it would be useful to understand the current state of a structure to a level of detail that allows effective decision making around building use and/or retrofit.

In the 2010-2011 Christchurch earthquake series, Christchurch was struck by a 7.1 magnitude earthquake on 4 September 2010. Fortunately, there were no deaths directly attributed to this

event, although this main shock caused widespread damage to the structures in the city. However, after several smaller aftershocks, a strong new major event with a magnitude of 6.3 occurred on 22 February 2011, which resulted in more severe damage and even collapse to the structures already weakened by the previous event, and killed 185 people (Davey, 2011). Therefore, it is important to determine the damage state of the structure immediately after any earthquake to decide if the structure has a sufficient resistance capacity for any subsequent event, and thus enable more optimal safety assessment and recovery planning. This need is particularly important for critical infrastructure, such as hospitals, fire stations, power plants and bridges, which are needed most after an earthquake.

Structural health monitoring (SHM) refers to the *in situ*, non-destructive sensing and analysis of structural response for the purpose of detecting the existence, location and degree of damage that may exist, particularly after a damaging input, such as an earthquake or other large environmental load (Housner et al., 1997). Given reliable condition assessment, two important benefits can be expected: (1) to avoid catastrophic accidents by detecting structural deterioration before major earthquake events; and (2) to ensure more rapid and safe return to normal use for critical infrastructure and business after an earthquake event. Current SHM methods, to date, cannot provide the resolution or accuracy necessary to achieve these outcomes for a wide range of, in particular, nonlinear structures.

Thus, the main aim of this research is to develop a novel and highly simplified method for damage detection, localization and severity assessment by identifying the physical parameters of structure during the earthquake.

1.2 Current SHM State of the Art

The literature for damage detection and structural health monitoring in civil engineering is quite broad and wide ranging. Non-destructive evaluation (NDE) methods, including acoustic or ultrasonic signals, electromagnetic, radiography and radar testing, is one of the important components of structural health monitoring for civil engineering structures (Chang and Liu, 2003). NDE methods can be applied without inducing any excitation to the structure. However, these methods require direct human access to the structure, which is not always safe during or after an earthquake. In addition, the application of these techniques is time-consuming and impractical for a quick assessment of large, complex structures, particularly after an earthquake. Finally, NDE methods can only detect damage on or near the surface of the structure, rather than the global damage due to yielding or loss of stiffness, which are desired.

SHM methods using sensor technology and computational data processing algorithms can provide more intelligent and detailed information for damage assessment in earthquakes. They are also better at turning this data into estimations of current structural properties, whose evolution can reflect damage. Therefore, the literature reviewed in this section focuses on the development of methods that can detect, locate and quantify damage from measured dynamic responses.

Many current SHM methods using sensor measurements are based on the identification of the changes in modal properties, including natural frequency, mode shapes and modal damping (Doebling et al., 1996; Yan et al., 2007; Zou et al., 2000). The existence of structural damage produces a decrease in stiffness and/or increase in damping, which thus leads to a decrease in natural frequency and modification of the vibration mode shapes of the structure. Due to its

relatively easy measurement, natural frequency has been used to detect damage in many research studies (Brincker et al., 2000; Cawley and Adams, 1979; Doebling et al., 1996; Fan and Qiao, 2011; Qiao et al., 2012; Salawu, 1997). However, natural frequency is not often sensitive to moderate, but significant amounts of damage, and perhaps more importantly, significant damage may also cause very small changes in natural frequency, particularly for large structures (Creed, 1987; Kim et al., 2003). In addition, it is difficult to determine the location of damage using these approaches because damage at different locations may produce the same net change in natural frequency or/and mode shapes, as they are global measures of structural status (Pandey and Biswas, 1994; Vafaei et al., 2013).

Other research indicates that changes in mode shape or mode shape curvature are more sensitive to local damage than natural frequency, and can be used to better localize damage region if damage is located near the points where the change of a mode shape function is significant (Khoo et al., 2004; Maia et al., 2003; Pandey et al., 1991; Stubbs and Kim, 1996), which is a significant limitation. However, damage is a local phenomenon and may not significantly influence mode shapes of the lower modes that are usually measured from dynamic vibration of civil structures (Kim et al., 2003). In addition, the measurement accuracy of mode shapes is much lower than that of natural frequency because the high density sensor placement is required for measuring a complete vibration mode, which is difficult and costly to achieve, particularly for complex structures. As a result, mode expansion is needed, which may further affect the accuracy of damage detection.

Finally, all these vibration-based methods are theoretically applicable only to structures where the dynamic response is primarily linear (Chase et al., 2005a). Thus, nonlinear response due to damage may be missed, unless they create significant changes in identified

linear behaviour. As a result, these approaches are not necessarily useful for in-event monitoring.

Another method, the Eigensystem Realization Algorithm (ERA) is also a common SHM approach for damage identification of civil structures (Bernal and Gunes, 2000; Juang and Pappa, 1985; Juang and Suzuki, 1988; Lus et al., 2003). The ERA method is based on the knowledge of time-domain free response data, which is not always easily segregated from the forced response due to ground acceleration after an earthquake event. In the ERA, a discrete Hankel matrix is formed, and the state and output matrices for the resulting discrete matrix are determined. The resulting vibration-based modal parameters are found by determining the eigenvalues of this continuous time system. A least squares approach can then be applied to determine the physical parameters of the structure. However, the accuracy of this approach depends on the amount of noise present in the measurements, the linearity and resolution of the sensors, and the error between the assumed form of the model identified and the actual system (Caicedo et al., 2003).

The flexibility-based method is based on the identification of the changes in flexibility matrix in which the inverse of the stiffness matrix is used to localize damage in a structure (Bernal, 2002; Bernal and Levy, 2001; Catbas et al., 2006; Pandey and Biswas, 1994). The damage locating vectors in the null space of the flexibility change are estimated from output signals without reference to a model of the structure, and then can be used to localize damage by inspecting zeros stress fields over damaged region. Hence, it does not rely upon a model or assumed behaviour, which can be advantageous. Unlike the stiffness, the flexibility of a structure converges rapidly with increasing frequency and a good estimate of the flexibility matrix can be obtained from only a few of the lower frequency modes (Pandey and Biswas,

1994). However, these approaches require the entire measured (free) response to process and identify damage, and thus the results might not be immediately available after an event, particularly if human input is required to manage the data and/or process. Hence, they are better suited for ambient vibration monitoring.

The classical frequency-domain methods employ fast Fourier transform (FFT) or discrete Fourier transform (DFT) to decompose time history of structural response into a set of frequency components for damage detection. However, the FFT and DFT cannot capture the time-varying features and indicate the time of damage occurrence in a signal because the transform is the result of an integration over the entire signal length.

The wavelet transform has proven its ability to overcome the limitations of FFT and DFT, and thus been applied extensively for SHM (Balafas and Kiremidjian, 2015; Hera and Hou, 2004; Hou et al., 2000; Kijewski and Kareem, 2003; Melhem and Kim, 2003; Taha et al., 2006). The wavelet transform is a linear transform with an adjustable window location and size, and can thus provide fine time resolution for long duration signals and fine resolution for high frequency signals. Because it does not simultaneously consider the whole record it offers the ability to effectively search for specific features associated with damage. Therefore, it can determine not only the extent of the damage, but also the time of its occurrence within the record. In addition, the wavelet transform isolates the transient high frequency components in the top frequency band and the low frequency components are presented as a continuous magnitude. Thus, it is very suitable to analyse non-stationary events, such as nonlinear, yielding structural response, and construct the needed feature extraction of structural damage (Taha et al., 2006). However, the identified wavelet coefficients for damage detection are not unique and depend on the wavelet selection for the analysis, and no

one class of wavelet can be used for all applications with accurate results (Chang and Shi, 2010; Ovanesova and Suarez, 2004). Hence, it requires *a-prior* trial and error to chosen the optimal wavelet for the analysis, making this approach not suited for real-time and automatically monitoring.

Finite element model (FEM) updating using experimental test analysis has also been used for SHM in civil structures (Brownjohn et al., 2001; Brownjohn et al., 2003; Cunha and Caetano, 2006; Jaishi and Ren, 2005; Kroggel, 1993). The structure is artificially excited using an impulse hammer or eccentric dynamic shaker to measure how much displacement, velocity or/and acceleration response the structure has at an output DOF, per unit of excitation force at an input DOF. (Schwarz and Richardson, 1999). It thus enables a direct identification of modal frequency or mode shapes. The mass, stiffness and damping parameters of the FEM can then be modified using a number of model updating methods, such as the direct method (Berman and Nagy, 1983), iteratively sensitivity based method (Fritzen et al., 1998) and response surface method (Ren and Chen, 2010), to obtain better agreement of the dynamic characteristics between the FEM and experimental test extraction. However, this approach can be difficult to apply for civil engineering structures due to the difficulty in exciting large civil structures in a controlled manner. In addition, the dynamic testing is prone to uncertainties and significant frequency changes may be identified in these ultra-low magnitude input tests due to changes in ambient conditions, rather than the desired identification of the existence of damage (Aktan et al., 1994; Brownjohn et al., 2001).

SHM methods based on a physical baseline structural model have also been developed for damage identification. Lin et al. (1990) investigated a simulated linear multi degree-of-freedom degrading system and a least squares method was used to evaluate the stiffness and

damping in real time based on measured response with and without noise. Adaptive H∞ filter techniques (Sato and Qi, 1998) can also achieve real-time or rapid results. However, they require a full response measurements of the system, and perform best for linear systems.

The extended Kalman filter (EKF) algorithm is one of the widely used algorithms for nonlinear structures, and it only requires the recorded acceleration response (Hoshiya and Saito, 1984; Jeen-Shang and Yigong, 1994; Yang et al., 2006; Zhang et al., 2002). The EKF is based on the linearization of the state transition matrix and the observation matrix with Taylor series expansions. Thus, for highly nonlinear structures, the accuracy and convergence of the estimation depend on the initial guesses of unknown parameters during the linearization process (Maruyama et al., 1990; Zhang et al., 2002), which can be significantly in error, especially if prior damage exists.

Adaptive least mean square (LMS) filters have used on benchmark problem data (Chase et al., 2005a) and also for a nonlinear pre-cast rocking structure (Chase et al., 2005b) to directly identify changes in structural stiffness over time by comparing the evolution of the identified stiffness matrix of the structure with the undamaged model matrix. Nayyerloo et al. (2011) developed a modified LMS-based method to identify both changes in stiffness and plastic deflection, making this approach more suitable for highly nonlinear structural responses. However, these methods are not as effective for more complex hysteretic pinching behaviour. Thus, there are still significant limitations in all these methods that limit the realistic nonlinear monitoring.

In addition, many current physical model-based methods were applied to the Bouc-Wen model or other linear hysteresis models. There are a very little research on the damage

identification of hysteretic systems with pinching behaviour, a sudden loss of stiffness caused by the opening or closing cracks and yielding of compression reinforcement, which is practically and commonly observed in reinforced concrete structures (Foliente and Noori, 1996). Such systems are more general and nonlinear, but also more difficult to use with SHM as a result. Hence, this field still lacks solutions that are generalizable enough.

More specifically, Kunnath et al. (1997) used a modified Gauss-Newton approach to determine the hysteretic control parameters of an extended Bouc-Wen model with pinching behaviour. The identified parameters can reproduce the experimental results of beam components, column components and assemblages of beam-column joints with reasonable accuracy. Zhang et al. (2002) compared three identification algorithms based on the simplex, extended Kalman filter and generalized reduced gradient methods to determine the control parameters of a degradation and pinching model. Both the simplex and generalized reduced gradient were not stable in the presence of noise indicating practical unidentifiability (Docherty et al., 2011), while the extended Kalman filter algorithm was the most effective, but with high computational cost. Li et al. (2004) used bootstrap filter techniques to estimate the parameters of a slip-lock pinching model. The method requires a crucial initial inputs and is not robust in the presence of high noise. Wu and Smyth (2008) used an unscented Kalman (UKF) filter to identify the on-line hysteretic differential models with degradation and pinching. The proposed UKF procedure was capable of on-line parametric system identification. However, slow or incorrect convergence of identified parameters occurred with the addition of noise in measured acceleration records. Hence, there remains a need for a simpler effective and robust approach to these more general and nonlinear systems.

Finally, these model-based techniques can perform effectively when the numerical model is suitable to represent the real system. However, they can produce erroneous or misleading results when the model is not well defined (Chase et al., 2005b; Yao and Pakzad, 2014). Hence, if a good baseline model is unavailable, there is a significant, but unknown, risk of a poor identification result, since ground truth is not fully known, and this result would not necessarily be obvious or clearly untrue.

Another class of SHM methods are nonparametric or model-free approaches that map the inputs and outputs to the structure by a set of equations that may not have any explicit physical meaning (Lozano‐Galant et al., 2013). These methods mainly take modern signal-processing techniques and artificial intelligence as analysis tools (Yan et al., 2007). The system is trained to approximate an arbitrary continuous function that represents a physical structure and predict the structural response, which is particularly effective for large-scale structures due to their complicated nonlinear behaviour and the incomplete, incoherent, and noise-contaminated measurements of structural response under extreme loadings (Adeli and Jiang, 2006).

The most common and representative of nonparametric SHM methods is neural networks (NN) (Elkordy et al., 1993; Flood and Kartam, 1994; Graf et al., 2012; Rajasekaran et al., 1996; Smith and Chase, 1994; Story and Fry, 2014; Wu et al., 1992). The NN is composed of three layers, an input layer, a hidden layer and an output layer, with a number of parallel operating processors called neurons. The input-output relationship of each neuron is represented by connection weights and can be obtained using a training algorithms. The great majority of the civil engineering applications of NN training algorithms is based on the use of back propagation (BP) primarily due to its simplicity (Adeli, 2001). The BP algorithm uses a

gradient descent method to modify weight and threshold so that the error between the desired output and the output signal of the network is minimized (Funahashi, 1989). Hence, the connection weights can be captured and stored in the trained NN when the iterative process converged. The output of a well and broadly trained model can then yield the location and severity of the structural damage for any novel or new input. However, a poorly trained model may lead to inaccurate results when the training data is incomplete or corrupted, and converging towards a global optimum in training and convergence speed are not guaranteed with a limited set of training samples, as is often the case for civil structures (Cao et al., 1998; Sirca Jr and Adeli, 2012).

NN techniques combined with wavelet transforms (WNNs) have also been developed for more powerful and efficient SHM methods. Hung et al. (2003) used a WNN to model the dynamic behaviour of a five-story test frame subjected to earthquake excitations in a shaking table test. The nonlinear autoregressive moving average with exogenous (NARMAX) model based on a wavelet functions is used to represent the nonlinear discrete system, and the WNN model is trained using the quasi-Newton algorithm that is similar to the BP procedure. The health condition of the building is identified by comparing the measured response and the computed response from the well trained WNN model. Jiang and Adeli (2005) also developed a dynamic fuzzy wavelet neural networks (WNN) for nonlinear identification of two high rise moment resisting buildings. The discrete wavelet packet transform is first used for feature extraction and denoising before the state space vector is constructed for the dynamic system. The fuzzy WNN model is then created using the fuzzy wavelets and trained using an adaptive Levenberg-Marquardt least squares algorithm. Finally, a backtracking inexact linear search algorithm is used to update the steepest decent iteration step length for accelerating the training convergence rate and achieving high computational efficiency.

Genetic algorithms (GAs) are another powerful adaptive optimization method for damage identification. The application of GAs is computationally simple because it is not limited by restrictive assumptions about search space, such as continuity or existence of derivatives (Rajeev and Krishnamoorthy, 1992; Whitley et al., 1990). In addition, a GA searches from a population of points in the region of the whole solution space, rather than a single point, and can thus obtain the global optimum solution of non-convex problems, which is a major advantage (Hao and Xia, 2002). Chou and Ghaboussi (2001) presented a method to detect the location and severity of damage using a GA. The material properties is obtained in the GA strings using a limited number of measured displacements. The unmeasured displacements are also determined by the GA based method to avoid the need for complete finite element analyses. The optimal solutions for both the possible damage and unmeasured displacements are successfully identified using an implicit redundant representation (IRR) GA.

Perera and Torres (2006) studied an optimization approach to predicted the location and severity of damage represented by a decrease in stiffness at element level. A fitness evaluation function considering the estimated and the measured response is defined to obtain the optimal value. The GA successfully identified the damage of both simulated and experimental beams with different damage scenarios by minimizing the objection function using the modified total modal assurance criterion (MTMAC) with the frequency incorporated into the criterion. However, the algorithm is not robust in real applications when noise is present and modal data are incomplete.

The hysteresis loop identification algorithm at the center of this work has significant advantages compared to the traditional SHM model-based and non-parametric algorithms that are based on matching the time history of response, because no differential equations need to

be solved to evaluate the modelling errors (Cifuentes and Iwan, 1989; Xu et al., 2014; Zhou et al., 2014; Zhou et al., 2015; Zhou et al., 2015; Zhou et al., 2015). The reconstructed hysteresis loops were initially used as a rapid visual qualitative indicator of system performance. Secant stiffness was deduced from the reconstructed hysteresis loops to determine the occurring of degradation and damage (Stephens and Yao, 1987). Hence, they are based on fundamental mechanics, but not necessarily limited to a model structure.

Recently, real-time data acquisition from a instrumented structure has become a readily possible reality with the significant development of innovative sensors, including fibre optic sensors (Chan et al., 2004; Ko and Ni, 2005; Mufti et al., 1997), wireless sensors (Lynch et al., 2004; Spencer et al., 2004), piezoelectric sensors (Baptista et al., 2012) and force balanced accelerometers that are specially designed for installation in civil structures for commercial monitoring system (Hsieh et al., 2006; Lynch et al., 2003). Based on these new sensor technologies, a near real time SHM system using reconstructed hysteresis loops called R-SHAPE was first applied to the Millikan Library Building (Iwan, 2002; Iwan et al., 2013). The hysteresis loops for each floor were established in near real time from data obtained during the earthquake, and the general shape of the reconstructed hysteresis loop were examined quickly as an indicator of the type of structural behaviour. However, they did not directly identify linear and nonlinear behaviour, and thus did not quantify damage severity.

Xu et al. (2014) developed a regression analysis based algorithm for the damage identification of a based-isolated structure using reconstructed hysteresis loops. A direct multiple linear regression analysis is used for the identification of the linear superstructure and a two-step regression analysis is proposed for the nonlinear isolation layer. The SHM algorithm is applied to a numerical three-story isolated building and yields accurate

estimations of elastic, post-yielding stiffness, yielding displacements and damping coefficients of the nonlinear isolation system. However, this regression analysis cannot be implemented automatically and cannot be applied to highly nonlinear structures with pinching behaviour.

1.3 Objective and Scope

The overall objective of this study is to develop a novel, and computationally and conceptually simple SHM method, based on hysteresis loop analysis (HLA), to identify the physical parameters that are directly related to structural damage and condition. The proposed HLA method is capable of accurately localizing and quantifying damage for different types of civil engineering structures in both elastic and nonlinear response regimes. In addition, the method requires no user input and could thus be automated and performed immediately after an event effectively in real-time for end-users, as well as during an event. Finally, the HLA method is computationally efficient and robust in the presence of measurement noise. It will thus be accurate, simple and entirely general.

Numerical simulation is implemented to develop the algorithms and evaluate their performance to various hysteretic behaviours in the presence of different levels of added noise. Experimental validation is investigated using both a single-bay 12-storey and a two-bays reinforced concrete frame buildings subjected to a sequence of different levels of earthquake events that lead to both linear and more complex nonlinear behaviours. The performance of the model-free HLA method is then compared to a known model-based adaptive least mean squares (LMS) method to demonstrate the robustness and effectiveness of different algorithms in damage identification of MDOF structural systems with different

dynamic behaviours during earthquakes. Finally, the seismic performance of the base-isolated Christchurch Women's Hospital (CWH) building is investigated using the HLA method, and further validated using a modified Guass-Newton method against a 4-DOF linear shear force model. The study focuses on several main areas:

- Method development for physical parameter identification of simulated flag-shaped hysteretic system and highly nonlinear pinched hysteretic to achieve real time or rapid structural health monitoring during or after earthquakes.
- Experimental validations of the performance of the HLA algorithm for different types of hysteretic behaviours.
- Performance comparison between the HLA algorithm and other known SHM algorithms using experimental structure and numerical models.
- Performance evaluation of a based isolated hospital building in Christchurch during two major earthquakes in 2011.

1.4 Chapter Overview

Chapter 2 presents the development of a parameter identification method for a flag-shaped hysteretic system based on hysteresis loop analysis (HLA) using overall least square method and log likelihood ratio test. The robustness of the proposed method is also demonstrated using different levels of added measurement noise and a suite of twenty earthquake records.

Chapter 3 presents the development of a general HLA SHM method for the identification of highly nonlinear hysteretic system with pinching behaviour. The performance of the proposed HLA method is evaluated using a simulated pinched model with variable pinching behaviour,

noise level and damping ratio assumption.

Chapter 4 presents an experimental validation for the HLA-based SHM algorithm based on a shaking table test of a single-bay 12-story scaled reinforced concrete frame structure sequentially subjected to a small and large earthquake events. Severity and localization of damage are achieved by tracking changes in elastic story stiffness as a damage index over time.

Chapter 5 presents the comparison of the HLA algorithm and other known SHM algorithms, including adaptive LMS filters and natural frequency analysis. These algorithms are applied to an experimental structure and a calibrated numerical model yielding damage similar to the experimental structure, as well as another simulated model representative of a steel moment resistance frame (SMRF) structure.

Chapter 6 presents the further validation of the HLA method using a two-bay 12-storey reinforced concrete frame building with damage occurred prior to a sequence of four earthquake events that lead to more complex hysteretic behaviours. Structural degradation is evaluated by tracking the changes of the elastic stiffness of significant half cycles. A wavelet multiresolution analysis (MRA) is also proposed to extract an effective linear stiffness to assess the severity of the structural damage.

Chapter 7 presents the performance evaluation and SHM of the base-isolated CWH building using the proposed HLA method during two major Christchurch earthquakes occurred within a few hours in December 2011.

Chapter 8 presents the parameter identification of the CWH building based on a 4-DOF linear shear force model during the two earthquakes. The equivalent stiffness and damping coefficient of the CWH building are identified using a modified Gauss-Newton method to reproduce the structural response comparing with the recorded response during the earthquakes.

Chapter 9 and 10 present the overall conclusions to the research and discuss possible extensions and future work.

1.5 Summary

This chapter presented the motivations for this study and an introduction to the structural health monitoring methods in civil engineering. Overall, the development of real time or rapid structural health monitoring can enable immediate post-event assessment of the damage state of critical civil infrastructure, and thus is crucial in providing reliable information for deciding if the structure can continue to be used, and enable more optimum recovery planning and costs. Hence, they provide benefits in terms of response and recovery from major ground motions.

The key issue with the current SHM method is their significant computational complexity and lack of feasibility to highly nonlinear hysteretic behaviour. In addition, the robustness of the algorithms to measurement noise is a challenging task. The development of a highly simplified SHM algorithm would enable accurate localization and quantification of damage for different types of hysteretic structural systems in the presence of noise, as well as

immediate assessment after or during an earthquake event, if required. It will thus be accurate, simple and entirely general.

Chapter 2: HLA-based Method for Flag-shaped Hysteretic Systems

2.1 Introduction

Under conventional seismic design strategy, civil engineering structures are designed to undergo inelastic deformation to dissipate earthquake energy, which can lead to residual displacements. Residual deformation increases the repair cost and downtime, as well as the difficulty in recovering the structure to its initial position. To solve the deficiency, a large number of self-centring systems and devices exhibiting a flag-shaped hysteretic behaviour have been developed to provide recentring, avoid residual deformation and provide energy dissipation capacity.

A self-centring system refers to the use of post-tensioning with stiffness, usually done with tendons associated with energy dissipation elements, to aid the system to return to its original position without introducing external load. They typically also offer yielding elements to localize damage. Examples include post-tensioned beam-to-column connections for moment-resisting steel frame (Christopoulos et al., 2002; Garlock et al., 2005; Ricles et al., 2001; Rodgers et al., 2008), steel brace dissipating elements (Bartera and Giacchetti, 2004; Christopoulos et al., 2008; Tremblay et al., 2008), and shape memory alloy (SMA) seismic isolation devices (Alam et al., 2009; Attanasi et al., 2009; Casciati and Hamdaoui, 2008; Ozbulut and Hurlebaus, 2011).

The seismic application of these flag-shaped hysteretic structures has increased since the 1994 Northridge earthquake in the United States and 1995 Hyogoken-Nambu earthquake in Japan. However, these structures can still experience various degrees or types of damage

under more extreme excitations. Therefore, it would be necessary and useful to be able to directly assess the health conditions of these structures, just as with standard structures, enabling a more optimum recovery planning immediately after an earthquake. However, such nonlinear systems have proven difficult for most typical SHM methods.

Hysteresis loops play a crucial role in seismic performance-based analysis and design, and capture the linear and nonlinear characteristics associated with damage. They thus provide the basis for a range of possible applications to compute the underlying physical parameters, such as elastic and plastic stiffness, and yielding deformation, all of which can be used to determine the extent of degradation and potential damage for structural health monitoring. However, the current hysteresis loop based SHM approaches reviewed in Chapter 1 do not directly quantify damage severity and cannot be applied to highly nonlinear structures with pinching and flag-shaped behaviours.

The objective of this chapter is to develop a simplified HLA-based method to identify the physical parameters directly related to structural health monitoring for a flag-shaped hysteretic structure. The method is based on least squares linear regression and the log likelihood test. The performance of the proposed method is demonstrated and validated using a simulated single degree of freedom (SDOF) flag-shaped hysteretic system. The effect of measurement noise is investigated by adding 5%, 10%, 15% and 20% root mean square (RMS) noise to the measured response to assess robustness to noise. The robustness of the method to input and response variability is evaluated using a suite of 20 different earthquake records.

2.2 The Log Likelihood Test Ratio Method (LLTR)

2.2.1 Equation of Motion

The equation of motion of a SODF system subjected to earthquake excitation is defined:

$$m\ddot{x} + c\dot{x} + F(x) = -m\ddot{x}_g \tag{2.1}$$

where $x, \dot{x}$ and $\ddot{x}$ are the displacement, velocity and acceleration of the SDOF system, m is the mass, $\ddot{x}_g$ is the ground acceleration, $F(x)$ is the restoring force of the hysteretic system, and c is the viscous damping coefficient:

$$c = \frac{4m\pi\xi}{T} \tag{2.2}$$

ξ is the initial fraction of critical damping, T is the time period of the system. Using Equation (2), it can be obtained:

$$F(x) = -m(\ddot{x}_g + \ddot{x}) - \frac{4m\pi\xi}{T}\dot{x} \tag{2.3}$$

In this equation, noisy ground and structural accelerations $\ddot{x}_g$ and $\ddot{x}$ are commonly measured using accelerometers at high sampling rates. The direct integration and double integration of accelerations to obtain the velocity and displacement are not accurate due to drift and numerical error (Smyth and Wu, 2007). However, the velocity and displacement can be derived from measured acceleration by integration and correction, or by applying a set of sensors and several different methods (Fu and Moosa, 2002; Hann et al., 2009; Hwang et al., 2012; Park et al., 2007; Psimoulis and Stiros, 2008; Safak and Hudnut, 2006; Skolnik and Wallace, 2010; Smyth and Wu, 2007).

In this study, a low-frequency measured displacement method is used to correct the integration error assuming the availability of global positioning system (GPS) damage or

similar to aid correction (Hann et al., 2009). Currently, GPS displacement measurement achieves rates up to 20 Hz and the accuracy of dynamic displacement measurement using GPS is at a sub-centimetre to millimetre level at a maximum distance from the GPS receivers to the monitoring buildings of up to 30 km (Yi et al., 2013). Displacement can even be measured with 1-3 mm accuracy for up to 2-4 Hz in the modal frequency of rigid structure (Psimoulis and Stiros, 2008), and for equal or less than 1 Hz, the measurement errors are less than 5%, provided the motion amplitude is greater than 20 mm (Chan et al., 2006). Thus, integration errors can be readily corrected using GPS measurements. In particular, the integrated velocity and displacement are defined:

$$\dot{x}(t) = \int_0^t \ddot{x} dt \tag{2.4}$$

$$x(t) = \int_0^t \left[\int_0^t \ddot{x} dt \right] dt \tag{2.5}$$

The integration displacement error to be corrected by GPS measured displacement is then calculated:

$$e_i = x_m(hi) - x(hi) \qquad i = 1, \cdots N \tag{2.6}$$

where h is the time interval at which displacement measurement x_m is recorded, N is the number of displacement measurement data. The velocity error c_i can be calculated by numerical differentiation of e_i:

$$c_i = \frac{e_i - e_{i-1}}{h} \qquad i = 1, \cdots N \tag{2.7}$$

A cubic spline interpolation can then be used to construct a time varying piecewise C^1 continuous displacement corrector function $\bar{f}(t)$ that satisfies $\bar{f}(hi) = e_i$. Therefore, the corrected displacement $d(t)$ can be estimated by adding the integrated displacement and the continuous corrector function $\bar{f}(t)$:

$$d(t) = \int_0^t \left[\int_0^t \ddot{x} dt \right] dt + \bar{f}(t) \tag{2.8}$$

The corrected velocity and acceleration are calculated by numerical differentiation as follow:

$$v(t) = \frac{d(t_{i+1}) - d(t_{i-1})}{2\Delta t} \tag{2.9}$$

$$a(t) = \frac{v(t_{i+1}) - v(t_{i-1})}{2\Delta t} \tag{2.10}$$

Assuming m, ξ and T to be available from the basic knowledge of the system, the restoring force $F(x)$ is thus consequently obtained. Hence, a measured hysteresis loop of the system can be constructed for use in identifying structural property and response metrics.

2.2.2 Hysteresis Model

Figure 2.1(a) shows a flag-shaped force displacement relationship representative of a self-centring system. The parameters for this hysteretic model are k_e, α, β and d_y. The coefficient k_e is the pre-yielding stiffness and α is the ratio of post-yielding stiffness to pre-yielding stiffness. The energy dissipation coefficient β reflects the dissipation capacity, and d_y is the yielding displacement of the hysteretic system.

In general, if the hysteresis loop can be divided into each single segment by the breakpoints x_1-x_8, a linear regression analysis can be applied to each segment for the identification of physical parameters. As mentioned in (Powell and Allahabadi, 1988), the deformation history is unlikely to consist of regular, complete cycles, so it is more appropriate to divide the response history in half cycles rather than full cycles. The rain flow counting method is a widely used means to divide the time history of structural response into a number of half cycles for cumulative damage assessment. However, the half cycles separated by the rain flow counting method are not in chronological order but are grouped instead by deformation magnitude, which is not appropriate to track the evolution of damage parameters over time.

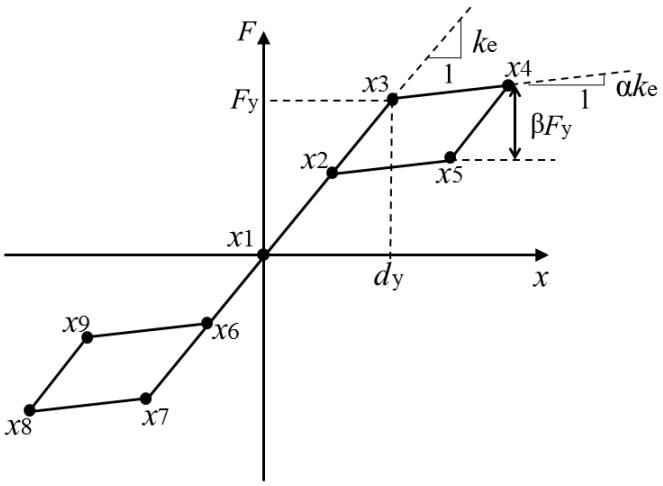

(a)

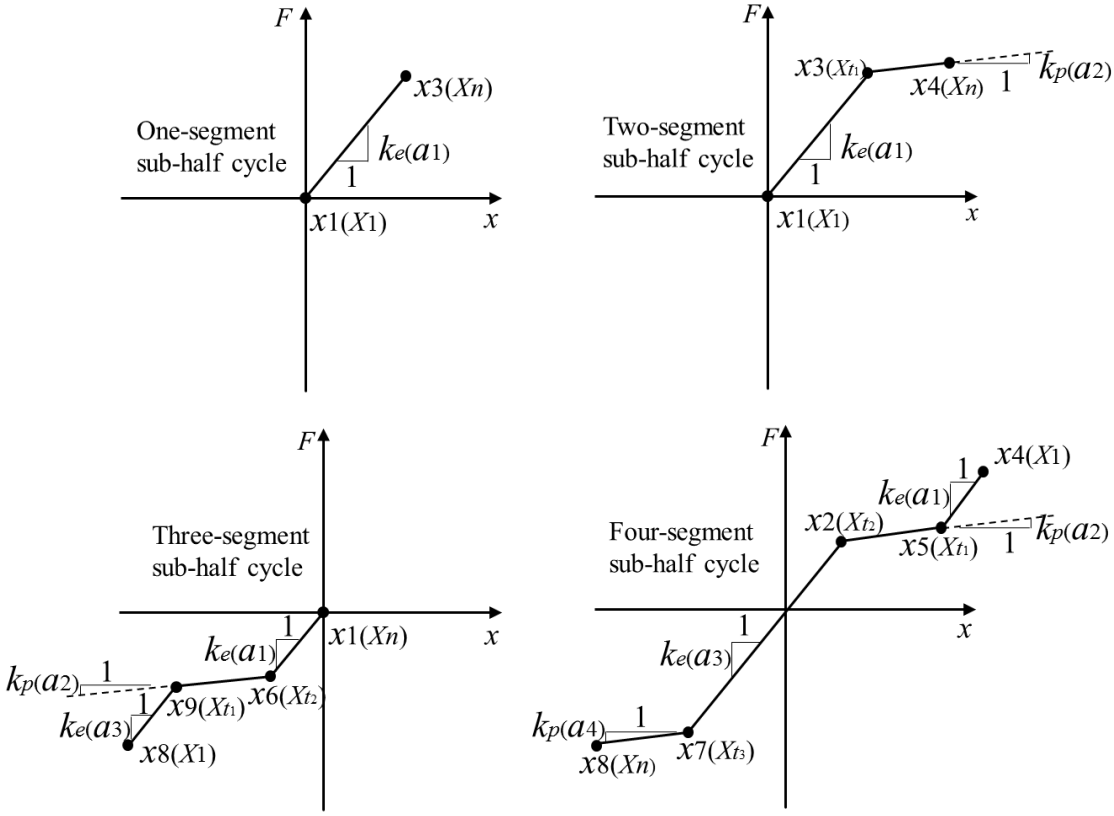

(b)

Figure 2.1: (a) Idealized flag-shaped hysteresis loop, with (b) four types of possible half cycles for r=1, 2, 3, 4

It can be seen form the hysteresis loop in Figure 2.1(a) that the total restoring force is path dependent. However, within a time segment, where the velocity holds the same sign, the restoring force is a single valued function of displacement. Hence, the whole hysteresis response in the proposed SHM method is divided into many half cycles in chronological order according to the turning points, such as x_4 and x_8, where the velocity is zero and the displacement is a local maximum or minimum.

All the half cycles are then divided into four types of piecewise linear model with one, two, three or four segments, as shown in Figure 2.1(b). If the numbers of segments of these piecewise linear models can be identified from the data, then the overall least squares solution (Hudson, 1966) can be implemented to identify the linear models for each segment and the estimated coefficients of the piecewise linear models will then be related to the system parameters to be found (k_e, α, β and d_y).

2.2.3 Parameter Identification Procedures

Assuming the number of segments for a half cycle is r, where r=1, 2, 3 ro 4, the r-phase linear model is then defined:

$$\begin{aligned} G(x) &= g_1(x) = a_1 x + b_1 \qquad && X_1 \le x \le X_{t_1} \\ &= g_2(x) = a_2 x + b_2 \qquad && X_{t_1} \le x \le X_{t_2} \\ &= \cdots \\ &= g_r(x) = a_r x + b_r \qquad && X_{t_{r-1}} \le x \le X_n \end{aligned} \tag{2.11}$$

where X_{t_1}, X_{t_2} and X_{t_3} are the breakpoints in the half cycles, as shown in Figure 2.1(b). (X_1, Y_1),…, (X_n, Y_n) are n pairs of displacement and restoring force data during one half cycle, and can be grouped to create:

$$Y_i = G(X_i) + e_i \qquad i = 1, \cdots, n \tag{2.12}$$

where e_i are added random errors caused by measurement noise or model uncertainty. Suppose e_i are normally and independently distributed with zero mean and standard deviation σ. Then the overall sum of squared residuals (SSR) for an r-phase linear model is determined:

$$R_r = \sum_{i=1}^{t_1} [Y_i - g_1(X_i)]^2 + \sum_{i=t_1+1}^{t_2} [Y_i - g_2(X_i)]^2 + \cdots + \sum_{i=t_{r-1}+1}^{n} [Y_i - g_r(X_i)]^2 \tag{2.13}$$

The optimum approximation for the r-phase linear model is to determine the minimum value of R_r in terms of (t_1, t_2,…, t_{r-1}) and (a_1, b_1,…, a_r, b_r).

The derivative equal to zero of Equation (2.13) cannot be used here due to the discontinuous nature of the observations (Quandt, 1958). Thus, the observations are divided into every feasible r groups, and the standard least squares linear regression is implemented to each segment to calculate the SSR and regression coefficients a_1,b_1,…, a_r,b_r (r=1, 2, 3 and 4). The estimation of breakpoints ($\hat{X}_{t_1}$,… $\hat{X}_{t_{r-1}}$) are then calculated at each join point between segments using linear constraint:

$$\widehat{X}_{t_j} = \frac{b_{j+1} - b_j}{a_j - a_{j+1}} \qquad j = 1, \cdots, r-1 \tag{2.14}$$

Therefore, a sequence of SSR functions $R_r(t_1, t_2 \cdots t_{r-1})$ with respect to (a_1, b_1,…, a_r, b_r) for $(3 \le t_1 < t_2 < \cdots < t_{r-1} \le n-2)$ can be obtained whenever $X_{t_j} \le \hat{X}_{t_j} \le X_{t_j+1}$ (Stoimenova et al., 2004; Xu et al., 2014). Finally, the overall solutions are the values of breakpoints ($\hat{X}_{t_1}$,… $\hat{X}_{t_{r-1}}$) and regression coefficients (a_1,b_1,…, a_r,b_r) that correspond to the smallest value of $R_r(t_1, t_2 \cdots t_{r-1})$.

To determine the optimum r value for the selected half cycle, a likelihood-ratio chi square hypothesis test is used. The likelihood ratio λ is defined:

$$\lambda = \left(\frac{R_{r+1}}{R_r} \right)^{\frac{n}{2}} \qquad r = 1,\ 2, 3 \tag{2.15}$$

The hypothesis test is performed between the null hypothesis H_0: there are r segments in this half cycle, and the alternative hypothesis H_1: there are r+1 segments in the half cycle. Then the large sample distribution of the log likelihood ratio defined as $-2\log\lambda$ is a chi-squared distribution with 2(r+1) degrees of freedom when the null hypothesis is true (Feder, 1975a; Feder, 1975b; Quandt, 1958). Therefore, the rejection of H_0 in favour of H_1 is true whenever:

$$-2\log\lambda \geq \chi^2_{\varepsilon}(k) \tag{2.16}$$

where ε is the user-defined significance level, and is usually set to a low value to reduce the probability of committing an error by rejecting H_0 when it is true (Walpole et al., 2011), and k is the number of degrees of freedom of the chi-squared distribution. The critical value of $\chi^2_{\varepsilon}(k)$ can be found in statistical tables (Walpole et al., 2011).

In this study, the significance level ε is set to 0.001 and k=2(r+1) for an r phase model identification. If the value of the log likelihood ratio $-2\log\lambda$ is less than $\chi^2_{\varepsilon}(k)$, then there is no evidence against H_0, and it is concluded that the half cycle is an r phase model.

Finally, the number of segments for all half cycles are identified, and the breakpoints ($X_{t_1}, \ldots X_{t_{r-1}}$) and regression coefficients (a_1,b_1,…, a_r,b_r) for each half cycle is obtained. The physical parameters (k_e, α, β and d_y) of the flag-shaped hysteretic system can then be defined. In particular:

As shown in Figure 2.1 (b), the pre-yielding stiffness k_e and post-yielding stiffness k_p are obtained:

$$\begin{aligned} k_e &= a_1 && for \;\; r = 1,2 \\ &= a_1 \; and \; a_3 && for \;\; r = 3,4 \end{aligned} \tag{2.17}$$

$$\begin{aligned} k_p &= a_2 && for \;\; r = 2,3 \\ &= a_2 \; and \; a_4 && for \;\; r = 4 \end{aligned} \tag{2.18}$$

For the yielding displacement d_y:

$$d_y = \left| X_{t_3} \right| \qquad for \;\; r = 4 \tag{2.19}$$

And the energy dissipation coefficient β is defined:

$$\beta = \left| \frac{Y_1 - Y_{t_1}}{Y_n} \right| = \left| \frac{(a_1 X_1 + b_1) - (a_2 X_{t_1} + b_2)}{a_4 X_{t_3} + b_4} \right| \qquad for \;\; r = 4 \tag{2.20}$$

The yielding dissipated hysteretic energy is calculated for each three-segment (r=3) and four-segment (r=4) half cycles (Chopra, 2001):

$$E_Y = \sqrt{\left(Y_1 - Y_{t_1}\right)^2 + \left(X_1 - X_{t_1}\right)^2} \sqrt{\left(Y_{t_1} - Y_{t_2}\right)^2 + \left(X_{t_1} - X_{t_2}\right)^2} \left| \frac{a_1 - a_2}{\sqrt{(a_1^2 + 1) + (a_2^2 + 1)}} \right| \tag{2.21}$$

Summary of the proposed identification method:

Step 1: Assume r=1 and r=2 for all the half cycles, respectively, and calculate R_1, a_1 and b_1 for r=1, and R_2, X_{t_1}, a_1, b_1, a_2 and b_2 for r=2 using Equations (2.11)-(2.14).

Step 2: Calculate the log likelihood ratio $-2\log\lambda$ for every half cycle using Equation (2.15), and identify the linear (r=1) half cycles using Equation (9), i.e. $-2\log\lambda < \chi^2_{0.001}(4) = 18.47$.

Step 3: Assume r=3 for all the remaining nonlinear half cycles, and calculate R_3, X_{t_1}, X_{t_1}, a_1, b_1, a_2, b_2, a_3 and b_3 for r=3. Then calculate $-2\log\lambda$ and obtain the two-segment (r=2) half cycles by $-2\log\lambda < \chi^2_{0.001}(6) = 22.46$.

Step 4: Assume r=4 for all the unidentified half cycles after Step 3, and calculate R_4, X_{t_1}, X_{t_2}, X_{t_3}, a_1, b_1, a_2, b_2, a_3, b_3, a_4 and b_4 for r=4. Calculate $-2\log\lambda$ and identify the three-segment (r=3) half cycles using $-2\log\lambda < \chi^2_{0.001}(8) = 26.12$. The remaining half cycles must then be four-segment (r=4) half cycles.

Step 5: Estimate the physical parameters k_e, α, β and d_y of the flag-shaped hysteretic system using Equations (17)-(20) for all the half cycles identified in steps 1-4.

Figure 2.2 shows the flowchart of the identification procedure. Once the hysteresis loop can be constructed using the measurement data, which has already been possible (Iwan, 2002; Iwan et al., 2013), the whole procedure to identify the segment number r for each sub-half cycle can be processed without user input, and thus be done in near real-time. Finally, the identified half cycles are fitted by the appropriate r phase linear model to obtain the physical parameters k_e, α, β and d_y.

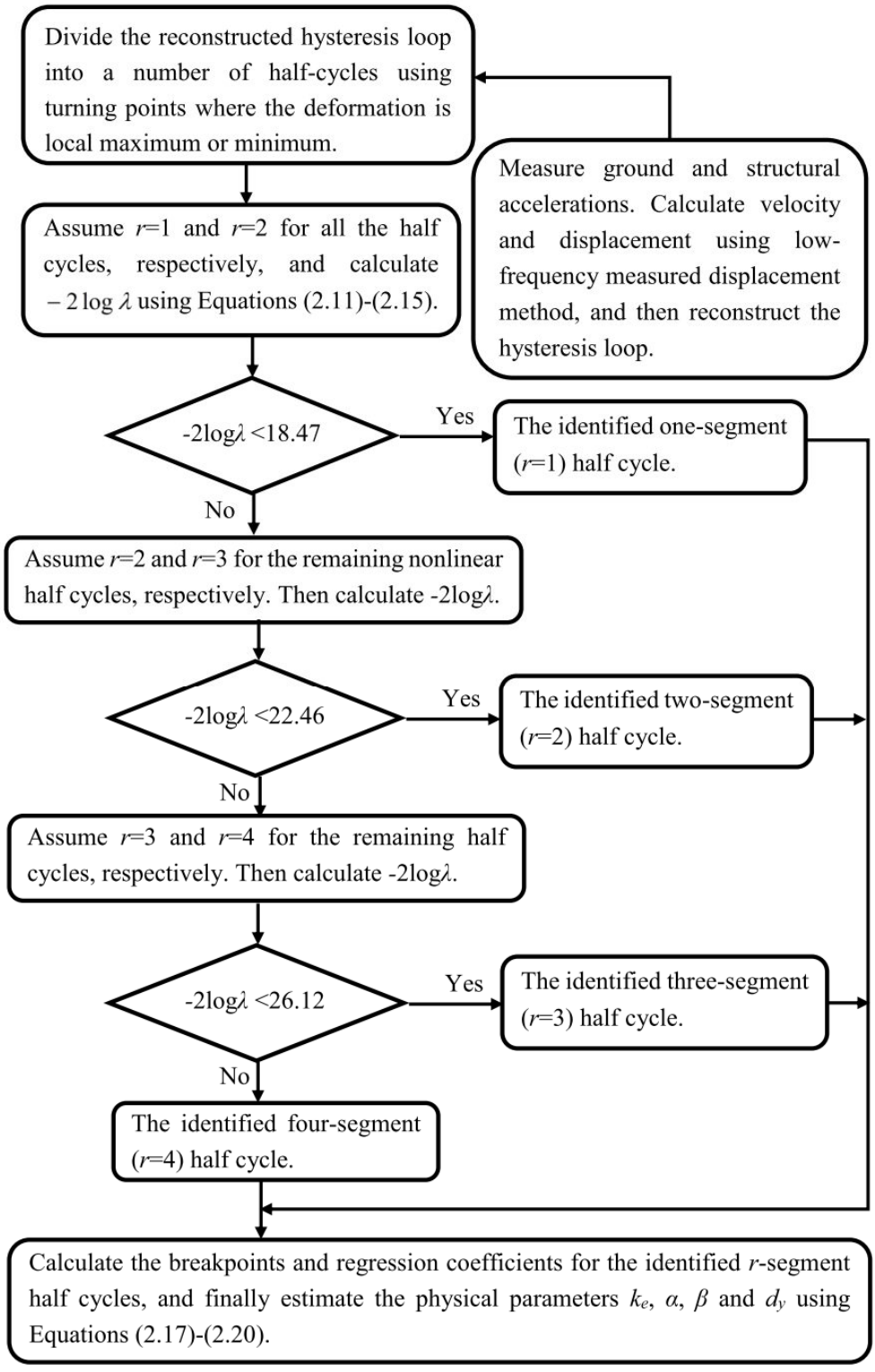

Figure 2.2: Flowchart of the identification procedure.

2.3 Simulated Proof of Concept Structure

The simulated proof-of-concept structure is a SDOF system representative of a seven storey steel moment resistance frame (SMRF) incorporating post-tensioned energy dissipating (PTED) connections at all beam-to-column connections and at the base of each column. The PTED connections incorporate high strength post-tensioned bars designed to remain elastic during seismic response, and confined energy-dissipation bars designed to yield in both tension and compression. Thus, the structural behaviour of this SMRF can be achieved without introducing residual drift during the seismic response, and the flag-shaped hysteretic model is considered to represent the hysteretic behaviour of this system (Christopoulos et al., 2002).

The story height of the fixed base SMRF system is 3.4m, and the seismic weight of the system is 4000kN that result in the first period of 1.0s and the pre-yielding stiffness k_e of 157.9kN/mm. The post-yielding stiffness k_p is 23.68kN/mm with the post-yielding stiffness coefficient α set to be 0.15. The energy dissipation coefficient β is set to be 0.5 and the yielding displacement d_y is 24.85mm for the SMRF with PTED connections. In addition, a 5% damping, which is commonly adopted by design codes and standards (Atkinson and Pierre, 2004; Pekcan et al., 1999), is considered in simulating the structural response.

The proposed identification procedure was implemented in Matlab. The simulated structure was subjected to 1989 Loma Prieta earthquake Hollister Differential Array record with peak ground acceleration (PGA) of 0.269g. The system acceleration response was simulated using a Newmark-β integration method with time step Δt=0.001s. The low-frequency measured displacement was taken at 1Hz and acceleration data was taken at 1000Hz in this case study. Different levels of random RMS noise were added to the simulated acceleration

measurements to provide a more realistic measurement situation.

The added RMS noise is a random normal distribution of the square root of the average of the clean simulated measurement, and is defined:

$$\mathbf{X}_{noise} = \mathbf{X} + \sqrt{\frac{\sum_{i=1}^{n} X_i^2}{n}} \times (noise\ level) \times randn(n,1)/3 \tag{2.22}$$

where $\mathbf{X}_{noise}$ is the simulated measurement with added RMS noise, $\mathbf{X}$ is the clean simulated measurement without noise, n is the number of measurement observations and $randn(n,1)$ is a normal (Gaussian) distribution with the mean value μ=0 and standard deviation σ=1. Based on three-sigma rule, 99.7% of the values of this normal distribution are within [μ-3σ, μ+3σ]=[-3, 3]. Therefore, a 10% RMS noise level corresponds to random observations within 10% from the clean simulated measurement with a probability of 99.7%.

To assess the robustness of the proposed method over different ground motions, a suite of 20 different earthquake events that are representative of ordinary earthquakes having a probability of exceedance of 10% in 50 years are used to generate the hysteresis loop of the simulated structure. The characteristics of these 20 earthquake records are listed in Table 1. More details about the selected records can be found in Christopoulos et al. (2002). These earthquake records can be downloaded from the strong motion data base in Pacific Earthquake Engineering Research Center (PEER, 2005). The same modal parameters were used for all the records and 5%, 10%, 15% and 20% RMS noise were added to the simulated acceleration and displacement response measurements.

Table 2.1 Characteristics of selected ground motions

Earthquake Record	Event	Year	Magnitude	Station	R-distance (m)	Soil type	Duration (s)	PGA (g)
EQ1	Superstition	1987	6.7	Brawley	18.2	D	22.0	0.156
EQ2				El Centro Imp. Co. Cent	13.9	D	40.0	0.358
EQ3				Plaster City	21.0	D	22.2	0.121
EQ4	Northridge	1994	6.7	Beverly Hills 14145 Muuhol	19.6	C	30.0	0.516
EQ5				Canoga Park-Topanga Can	15.8	D	25.0	0.356
EQ6				Glendale-Las Palmas	25.4	D	30.0	0.206
EQ7				LA-Holleywood Stor. FF	25.5	D	40.0	0.231
EQ8				N. Hollywood-Coldwater	14.6	C	21.9	0.273
EQ9				La-N Faring Rd	23.9	D	30.0	0.298
EQ10				Sunland-Mt Gleason Ave	17.7	C	30.0	0.127
EQ11	Loma Prieta	1989	6.9	Capitola	14.5	D	40.0	0.529
EQ12				Gilroy Array # 3	14.4	D	39.9	0.555
EQ13				Gilroy Array # 4	16.1	D	40.0	0.417
EQ14				Gilroy Array # 7	24.2	D	40.0	0.226
EQ15				Hollister Diff. Array	24.8	D	39.6	0.269
EQ16				Saratoga-W Valley Coll.	24.9	C	40.0	0.332
EQ17	Cape Mendocino	1992	7.1	Fortuna-Fortuna Blvd	13.7	C	44.0	0.116
EQ18				Rio Dell Overpass-FF	23.6	C	36.0	0.171
EQ19	Landers	1992	7.3	Desert Hot Springs	18.5	C	50.0	0.385
EQ20				Yermo Fire Station	23.3	D	44.0	0.245

Finally, the segment numbers (r=1, 2, 3, 4) of all the half cycles were identified and the physical parameters of the structure were obtained in each case using the LLTR method. During the earthquake excitation, some sub-half cycles exhibited narrow almost negligible plastic or nonlinear behaviour, as shown in Figure 2.3. The plastic segment in this half cycle is very small, so that is difficult to find the correct slope, which in this case significantly affects the accuracy of the estimate of the post-yielding stiffness (k_p).

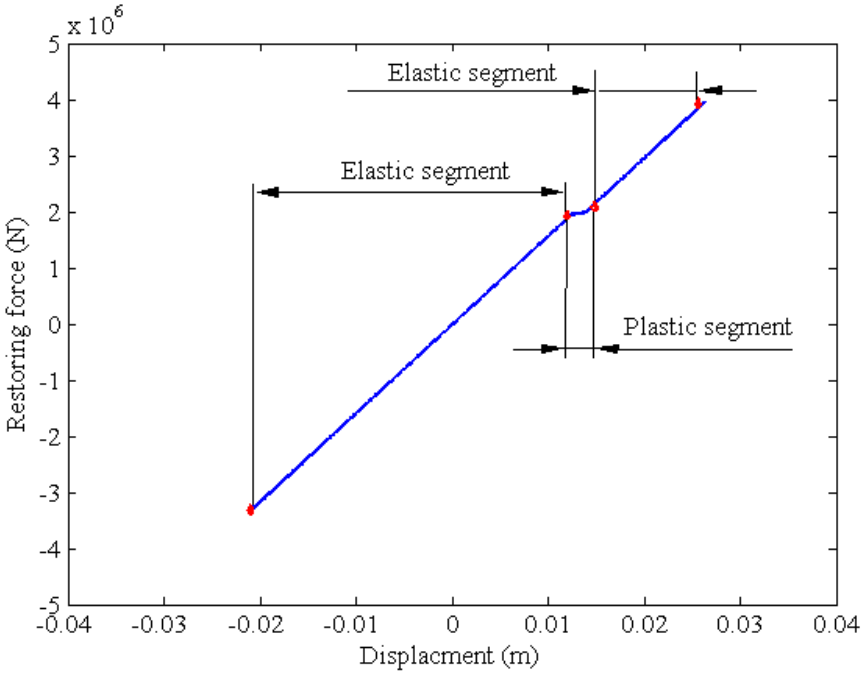

Figure 2.3: Narrow nonlinear half cycle (three-segment (r=3)).

Thus, Equation (2.18) is used to estimate the post-yielding stiffness k_p only when the plastic deformation Δd_p calculated form Equation (2.23) is more than an pre-defined threshold value, Δd.

$$\begin{aligned} \Delta d_p &= \left| X_{t_2} - X_{t_1} \right| && for\ r = 2,3 \\ &= \left| X_{t_2} - X_{t_1} \right| \ and\ \left| X_{t_4} - X_{t_3} \right| && for\ r = 4 \end{aligned} \tag{2.23}$$

However, some small amplitude plastic cycles can be missed when the threshold Δd is used. The hysteretic dissipation energy by a large number of such small amplitude can significantly

exceed the energy dissipated up to failure through the application of one or a few large amplitude cycles (Teran-Gilmore et al., 2003; Teran-Gilmore and Jirsa, 2005). Therefore, the effect of ignoring these half cycles on the results was investigated by varying the user defined threshold of Δd.

Performance is assessed by accuracy in recovering the true model values in the presence of noise over several events. The impact of thresholds used to ensure significant nonlinear motion (r=2, 3, 4) in identified half cycles is also assessed. The overall analyses thus assess both performance accuracy and robustness to noise providing a range of trade-offs.

2.4 Results and Discussion

2.4.1 Identification of the Number of Segments of Half Cycles

There were 28 half cycles in the response. Figure 2.4 shows the identification results for one segment (r=1) half cycles for the Loma Prieta earthquake event. The values of -2log λ for the half cycles (#11-14, 17, 19-28), with variable noise levels are less than χ^2 (4)=18.47 and rejection is not permitted according to the model hypothesis by Equation (2.16). Note that the cycle number is out of all identified half cycles (N=28) and then segregated for each case. They are thus not necessarily contiguously numbered. Finally, the half cycles below the rejection value, as shown in Figure 2.4(a), are identified as one-segment (r=1) linear models or simply linear structural response. The half cycles in Figure 2.4(b) that are not fitted well by one-segment (r=1) model are processed to the next identification step, as shown in Figure 2.5.

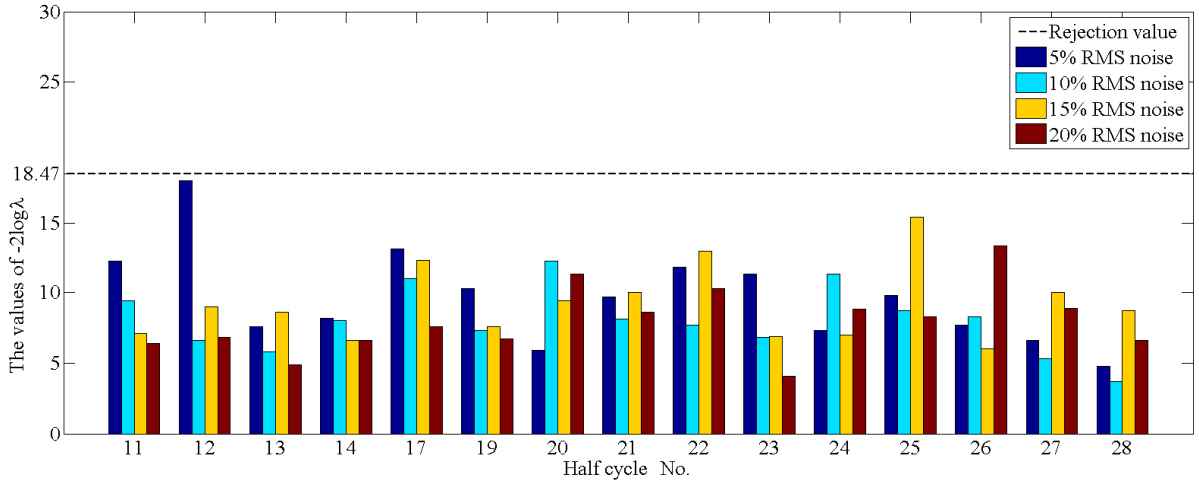

(a) One-segment (r=1) half cycles

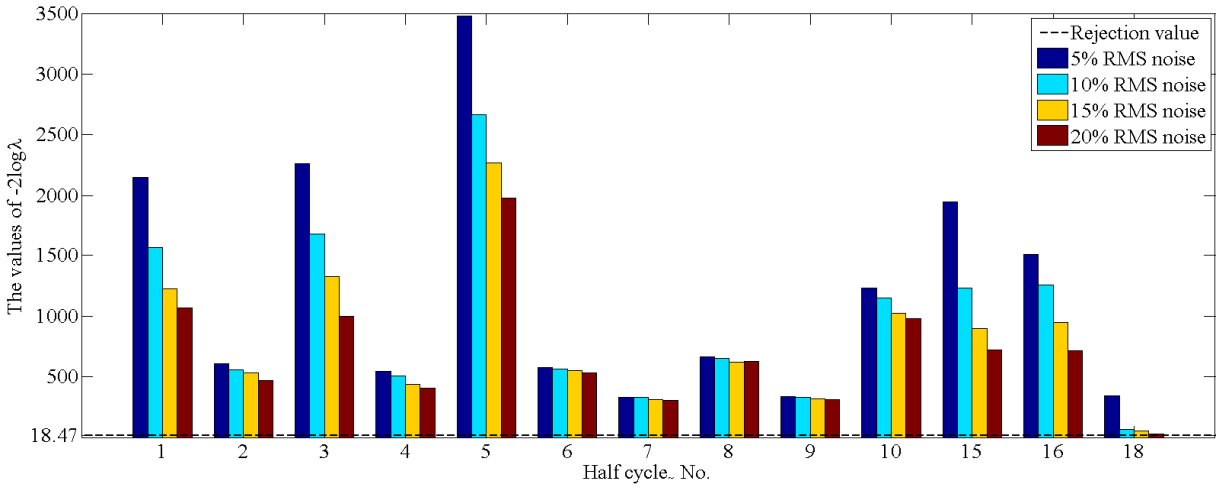

(b) More than one-segment half cycles (r=2, 3 and 4)

Figure 2.4: Identification of one-segment (r=1) half cycles with variable noise level: (a) one segment half cycles with $-2\log\lambda < 18.47$, (b) more than one-segment half cycles with $-2\log\lambda > 18.47$. Note that the cycle numbering is out of all identified half cycles (N=28) and then segregated for each case. They thus not necessarily contiguous.

Figure 2.5 shows the identification results for two-segment (r=2) half cycles, excluding the half cycles found to be one-segment (r=1) in Figure 2.4(a). The half cycles in Figure 2.5(a) are below the rejection value of χ^2 (6) =22.46, and thus are identified as two-segment (r=2) half cycles. The identification results for the remaining unidentified half cycles in Figure 2.5(b) are shown in Figure 2.6. It can be seen from Figure 2.6(a) that the three-segment (r=3) half cycles are identified using the values of $-2\log\lambda$ below the rejection value of χ^2 (8) =26.12. And the remained half cycles in Figure 2.6(b) are then identified, by default, as four-segment (r=4) with a full flag-shaped response.

In addition, it can be seen from Figures 2.4(a), 2.5(a) and 2.6(a) that the values of $-2\log\lambda$ for the half cycles that are fitted well by the r-segment model, vary essentially randomly with increasing noise level. However, the values of $-2\log\lambda$ for the half cycles that are not well fitted by that value of r, as shown in Figures 2.4(b), 2.5(b) and 2.6(b), decrease as the added noise level increases, because the value of $-2\log\lambda$ represents the degree of matching difference between the assumed r-segment and r+1-segment models. Thus, the values of $-2\log\lambda$ for the half cycles that cannot be well fitted by the assumed r-segment model, are very large and above the rejection value, which indicates a significant degree of matching difference. However, the matching difference between the r-segment and r+1 segment model is less distinguishable when the noise level is increasing and the true state of the half cycle is more discrete. Hence, the values of $-2\log\lambda$ representing the degree of matching difference are also decreasing when the added noise level is increasing.

However, the matching difference between the assumed r-segment and r+1-segment models is very small when the half cycle can be well fitted by the r-segment model. Even with increasing noise level, this matching difference is also very small. Therefore, the variation of

the values of $-2\log\lambda$ for these half cycles is mainly caused by the randomness of added noise.

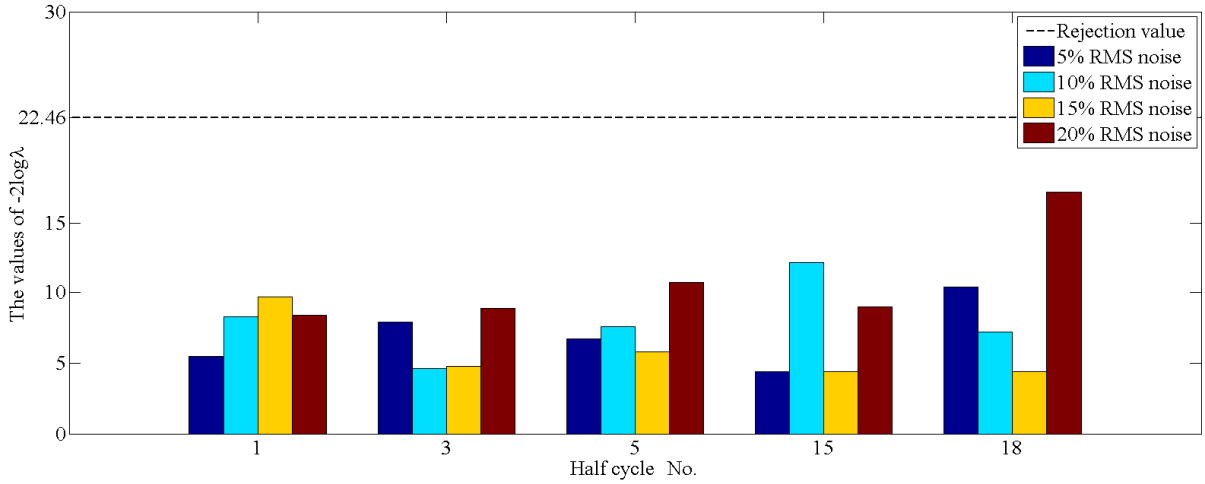

(a) Two-segment (r=2) half cycles

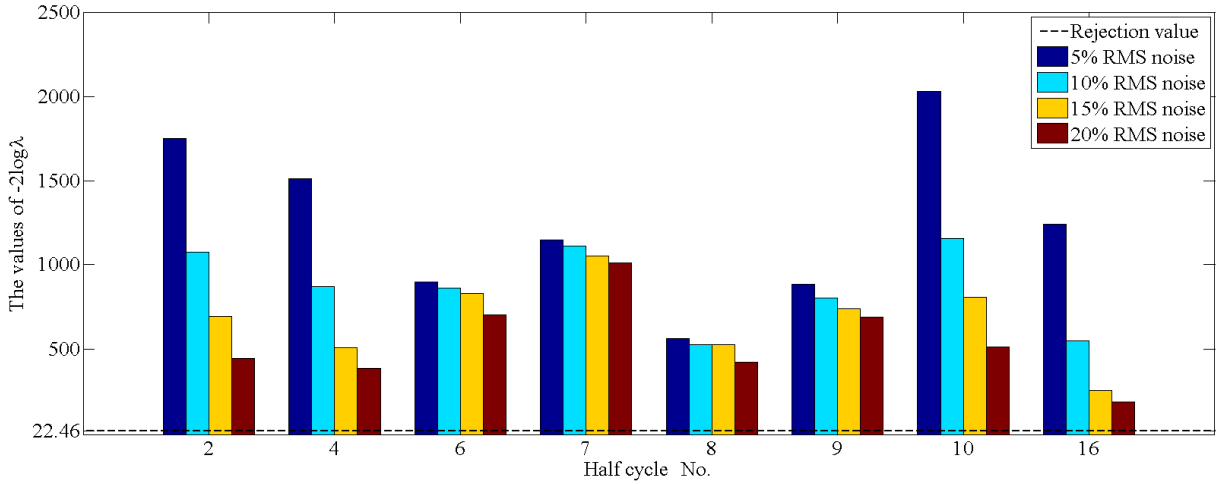

(b) More than two-segment half cycles (r=3 and 4)

Figure 2.5: Identification of two-segment (r=2) half cycles with variable noise level, excluding half cycles found to be one segment (r=1): (a) two-segment half cycles with $-2\log\lambda$ <22.46, (b) more than two-segment half cycles with $-2\log\lambda$ >22.46. Note that the cycle numbering is out of all identified half cycles (N=28) and then segregated for each case. They thus not necessarily contiguous.

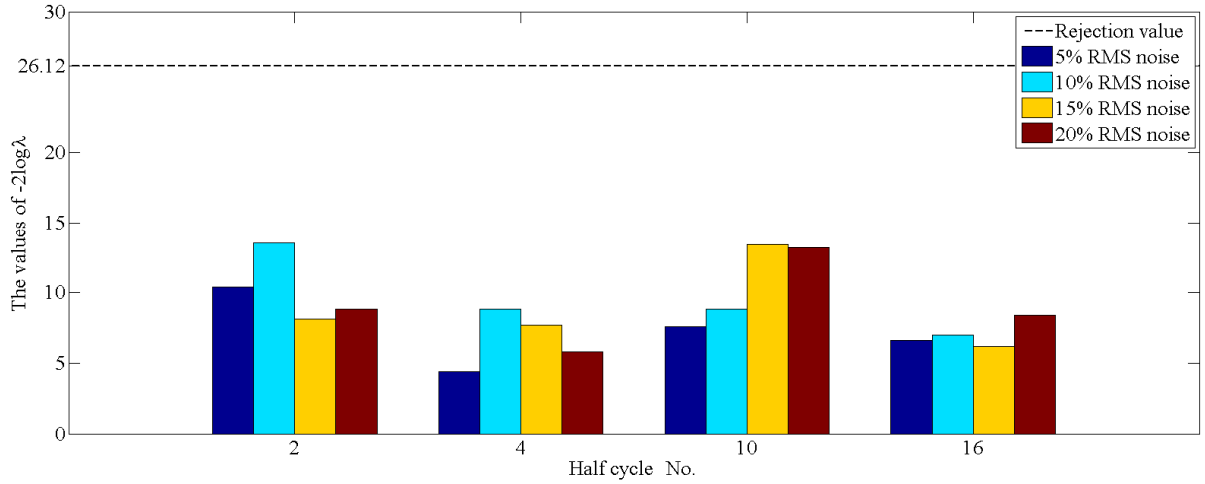

(a) Three-segment (r=3) half cycles

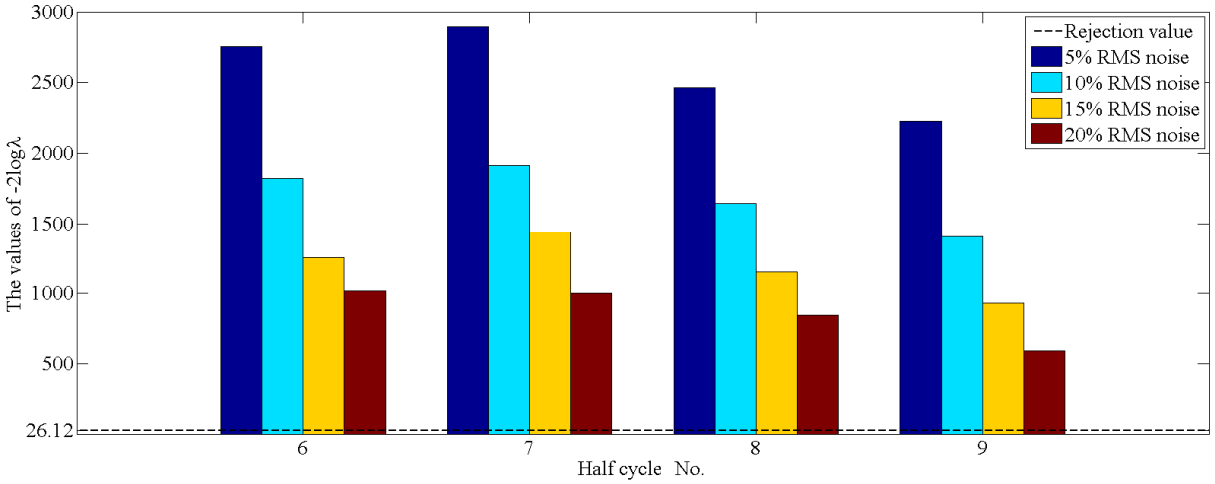

(b) Four-segment half cycles (r=4)

Figure 2.6: Identification of three-segment (r=3) and four-segment (r=4) half cycles with variable noise level, excluding one segment (r=1) and two-segment half cycles: (a) three-segment half cycles with $-2\log\lambda$ <26.12, (b) four-segment half cycles with $-2\log\lambda$ >26.12. Note that the cycle numbering is out of all identified half cycles (N=28) and then segregated for each case. They thus not necessarily contiguous.

2.4.2 Effect of Threshold

Figure 2.7 shows the estimates of the pre-yielding stiffness (k_e) and post-yielding stiffness (k_p) with different thresholds of Δd for 5%, 10%, 15% and 20% added noise. For different thresholds at the same noise level, the pre-yielding stiffness k_e is robust because the elastic segments of all the selected half cycles are big enough to obtain good estimates. However, the estimation of the post-yielding stiffness k_p is not robust and a high threshold Δd can lead to a much more accurate estimation of k_p with low standard deviations as relatively very small plastic segments are ignored. In addition, the estimates of k_e and k_p vary with noise level, and good estimates can be obtained using a high thresholder to ensure significant nonlinear motion is available for the least square problem even at 20% noise level.

Figures 2.8 and 2.9 show the estimated results for the yield displacement d_y and the energy dissipation coefficient β. It can be seen that the estimations of d_y and β are robust with varying threshold Δd at the same noise level because the breakpoints used to calculate d_y and β are not affected by the narrow half cycles. In addition, the results give a good approximation of the true input with the estimation errors less than 5% for different levels of noise and the standard deviations of estimations shows a smaller increase with noise level increasing, which indicate a low sensitivity to noise.

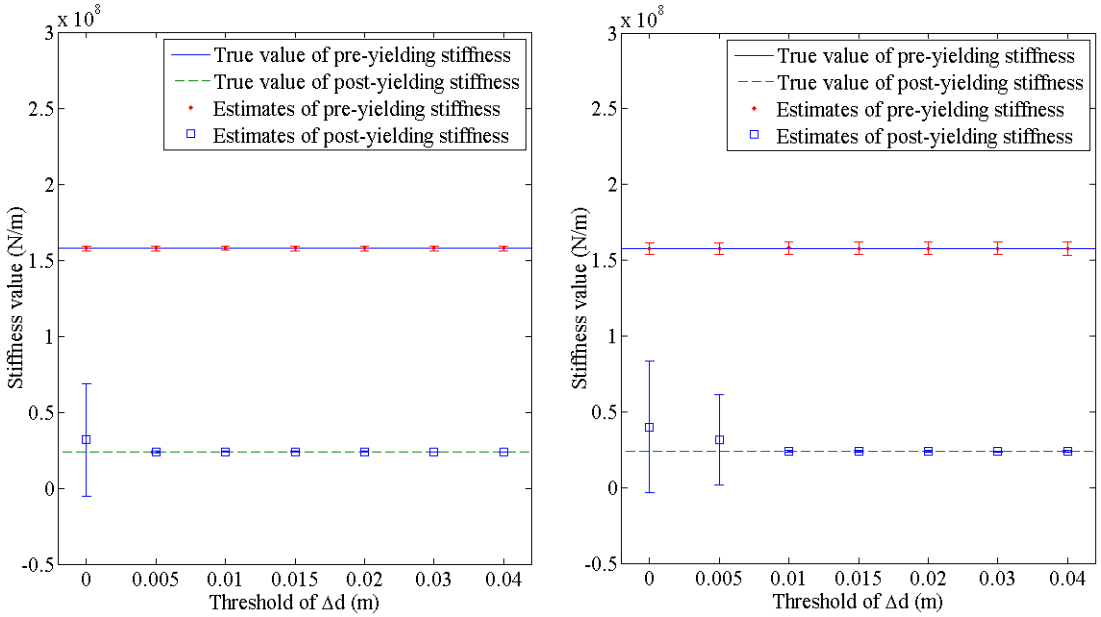

(a) 5% RMS noise

(b) 10% RMS noise

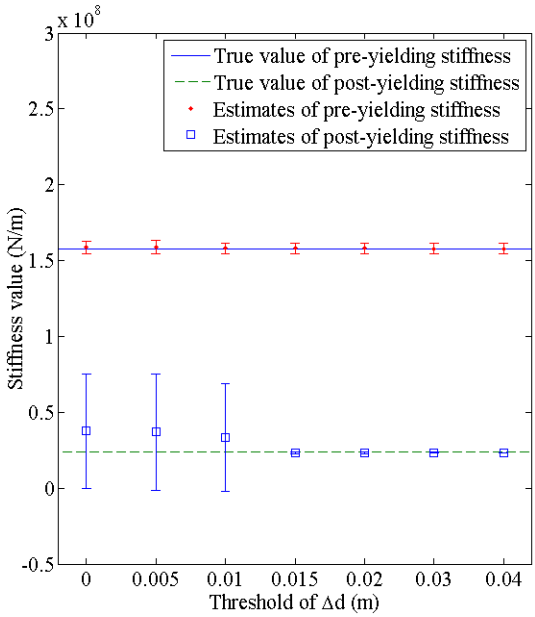

(c) 15% RMS noise

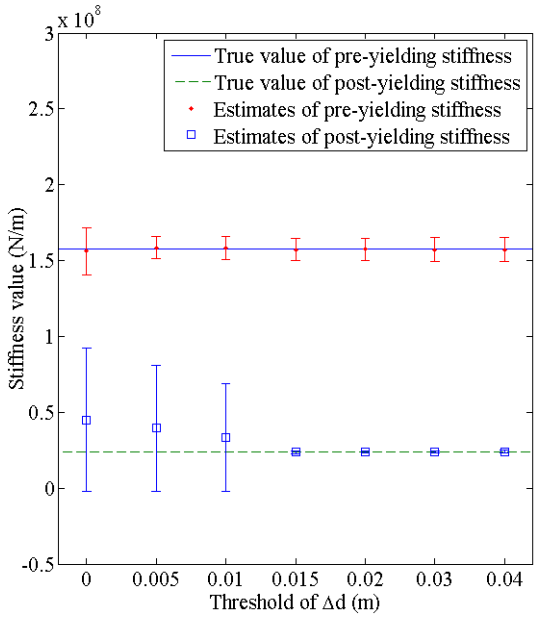

(d) 20% RMS noise

Figure 2.7: Estimated results of stiffness at, (a) 5% noise level, (b) 10% noise level, (c) 15% noise level, and (d) 20% noise level.

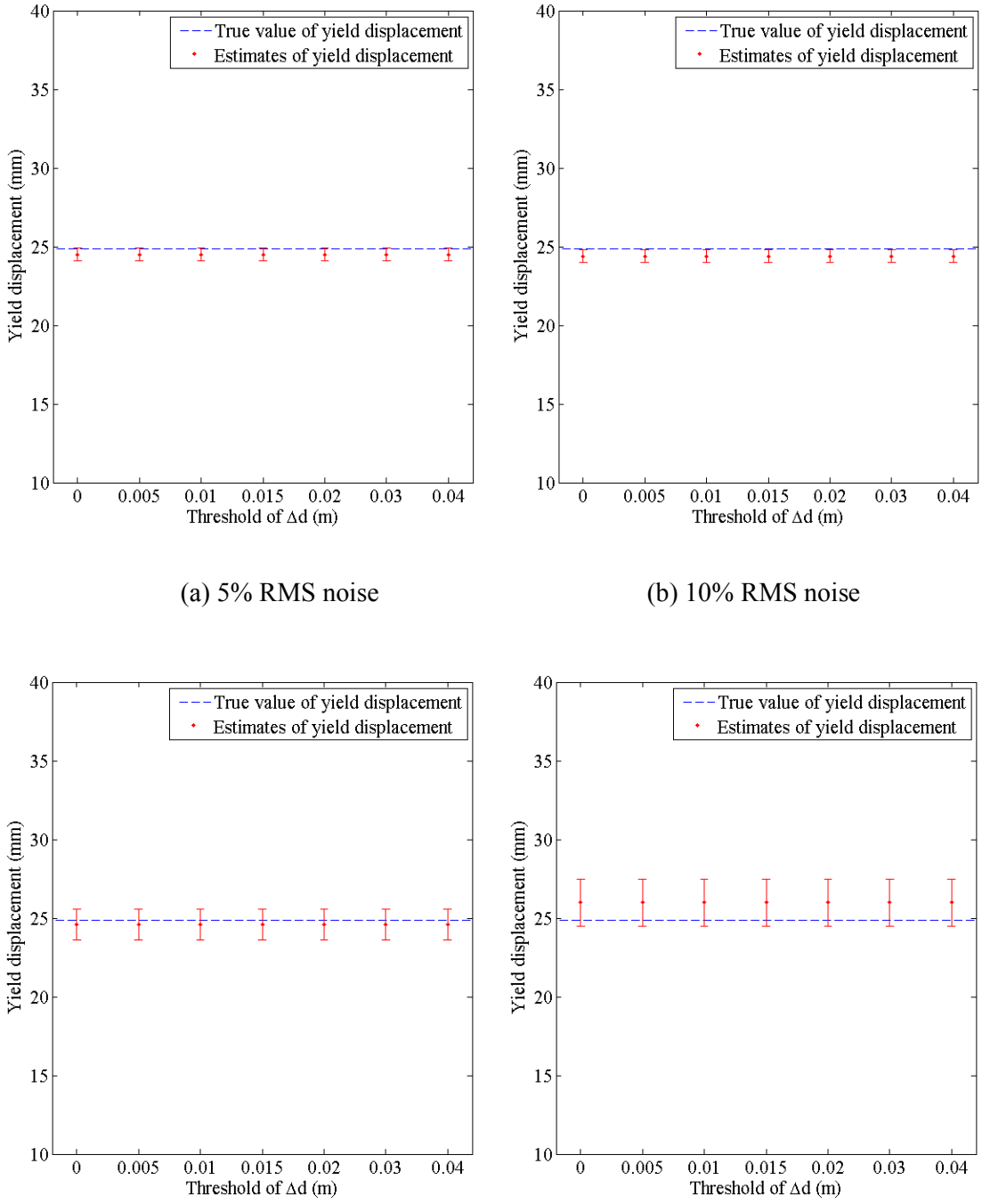

(a) 5% RMS noise

(b) 10% RMS noise

(c) 15% RMS noise

(d) 20% RMS noise

Figure 2.8: Estimated results of yield displacement d_y at, (a) 5% noise level, (b) 10% noise level, (c) 15% noise level, and (d) 20% noise level.

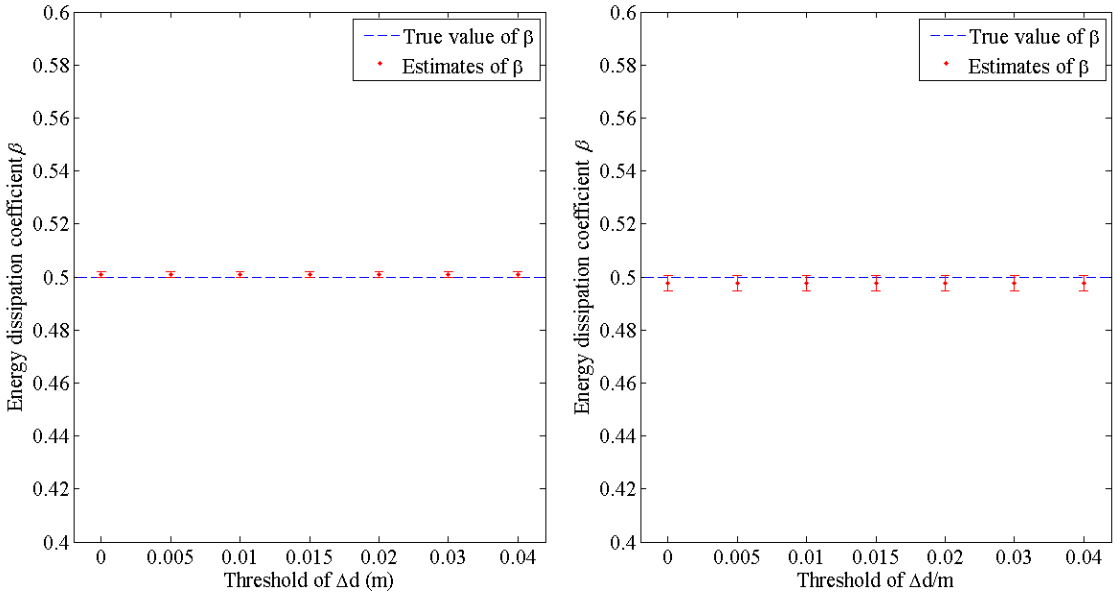

(a) 5% RMS noise

(b) 10% RMS noise

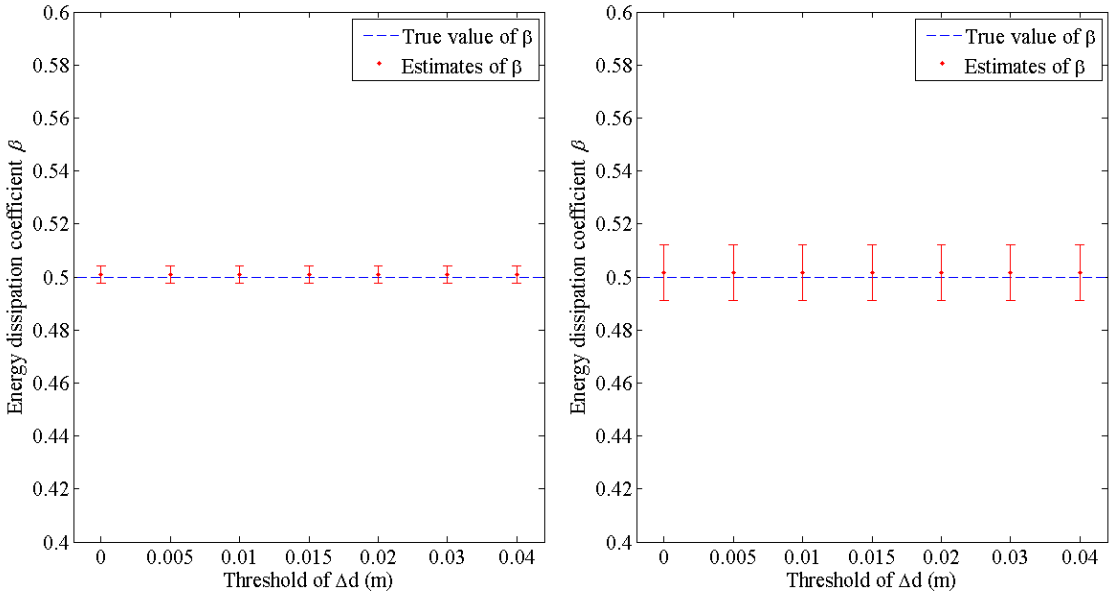

(c) 15% RMS noise

(d) 20% RMS noise

Figure 2.9: Estimated results of energy dissipation coefficient β at, (a) 5% noise level, (b) 10% noise level, (c) 15% noise level, and (d) 20% noise level.

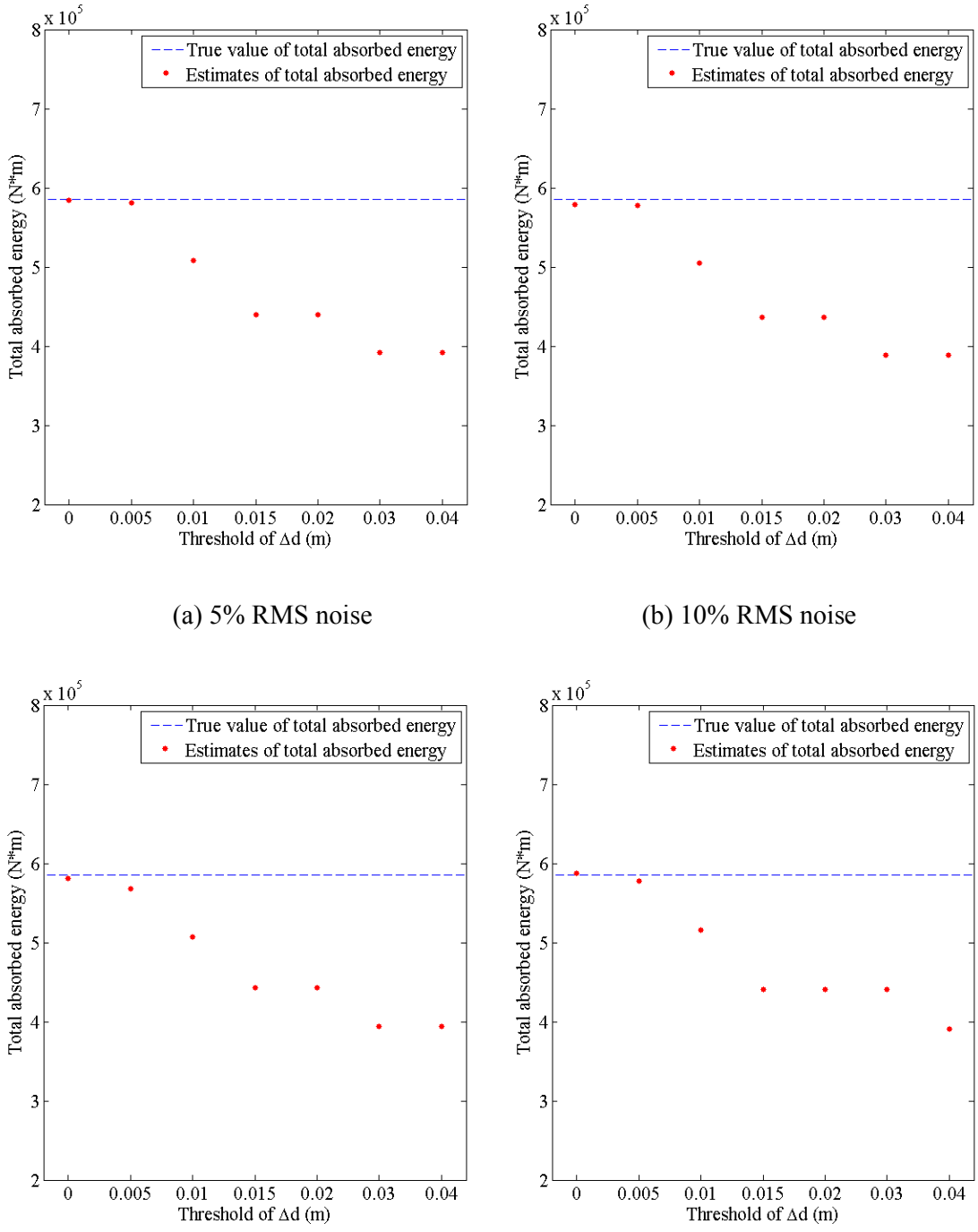

(a) 5% RMS noise

(b) 10% RMS noise

(c) 15% RMS noise

(d) 20% RMS noise

Figure 2.10: Estimated results of total dissipated energy at, (a) 5% noise level, (b) 10% noise level, (c) 15% noise level, and (d) 20% noise level.

Figure 2.10 shows the estimates of the total absorbed hysteretic energy due to plastic deformation seen in the hysteresis loop, which is not the total dissipated when one considers inherent or internal viscous damping in the linear case. It is thus a measure of damage due to nonlinear response and not a measure of the energy of the total system. It can be seen that the total energy dissipation shows a low sensitivity to different noise levels at the same threshold because all four panels are almost the same. In addition, the total energy dissipation dropped as more cycles are ignored when using a larger threshold at the same noise level. This result is expected and no threshold (Δd=0) should be used in calculating energy dissipation, or a very low threshold, so that damage or low cycle fatigue assessment is not affected. Importantly, using large thresholds to estimate k_e, k_p, d_y and β, and a Δd=0 threshold for determining dissipated energy, is computationally simple and efficient once all half cycles are identified. Hence, any compromises are minimized, allowing a best possible assessment of all these responses and structural properties.

2.4.3 Results for 20 Different Earthquake Records

As a result, a threshold Δd=0.04 is selected to evaluate the identification results of k_e, k_p, d_y and β for a suite of 20 earthquake records. Results with 5%, 10%, 15% and 20% added RMS noise are listed in Tables 2.2-2.5, respectively. A '-' represents elastic behaviour during the entire earthquake. Hence, both linear and nonlinear cases are tested for the same fixed method with no added tuning or user input required.

It can be seen from Tables 2.2-2.5 that the structural stiffness was identified as remaining linear during EQ1, 3, 6, 9, 10, 12, 14, 17 and 19 (9 of 20 events) when the structural response of the system is only linear during the whole earthquake event. This result indicates the

method is robust to a wide range of different ground motions and responses. The mean estimates of k_e, k_p, d_y and β across all the half cycles of events at different levels of noise matched well with the true input parameters (k_e=157.9, k_p=23.7, d_y=24.9, β=0.5). Although the errors of the mean estimates of k_e, k_p, d_y and β show a small increase with increasing noise level, the average errors of the estimates of k_e, k_p, d_y and β are within 3.6% even with 20% added RMS noise.

In addition, the coefficient of variation (COV) for k_e, k_p, d_y and β are less than 8.1% for all the earthquake events at a 5% RMS noise level, and the COV increases with noise level, as might be expected. However, the maximum COV is 18.7% of the mean value even at 20% RMS noise, and most are within 10%, which is, practically speaking, a good result given uncertainty in construction and degradation over time.

Finally, the results show that the stiffness values k_e and/or k_p for each half cycle in chronological order can be identified accurately. Thus, the evolution of stiffness can be tracked over time for structural health monitoring to determine if degradation occurs and assess its magnitude. In addition, the obtained half cycles can also be grouped in the order of different deformation amplitude using the rain flow counting method to assess the cumulative damage due to low cycle fatigue that may not lead to significant changes in the identified stiffness, but still reduce expected structural life (Mander et al., 1994). Therefore, if the values of stiffness degradation and/or cumulative nonlinear demands exceed pre-defined design or safety limits, an alarm or other notice can be immediately provided to emergency response and/or the owners and managers of the structure without detailed engineering analysis.

Table 2.2 Results for 20 different earthquake events with 5% noise

Earthquake Record	k_e=157.9 (kN/mm)		k_p=23.7 (kN/mm)		d_y=24.9 (mm)		β=0.500	
	Mean	COV	Mean	COV	Mean	COV	Mean	COV
EQ1	157.8	0.5%	-	-	-	-	-	-
EQ2	157.8	1.2%	23.8	2.3%	25.0	3.8%	0.486	8.4%
EQ3	157.9	0.4%	-	-	-	-	-	-
EQ4	158.2	1.8%	23.8	1.0%	24.4	3.9%	0.500	2.5%
EQ5	158.3	0.6%	24.0	1.1%	24.7	3.3%	0.501	2.1%
EQ6	157.6	0.8%	-	-	-	-	-	-
EQ7	157.7	0.6%	23.7	1.9%	24.7	2.2%	0.494	4.1%
EQ8	157.3	1.0%	23.9	1.8%	24.9	2.6%	0.501	1.5%
EQ9	157.8	0.3%	-	-	-	-	-	-
EQ10	157.8	0.5%	-	-	-	-	-	-
EQ11	157.6	1.1%	23.8	2.3%	24.7	3.4%	0.485	11.5%
EQ12	158.0	0.6%	-	-	-	-	-	-
EQ13	157.5	1.2%	23.7	0.6%	24.9	2.0%	0.499	0.8%
EQ14	157.9	0.3%	-	-	-	-	-	-
EQ15	157.9	0.8%	23.8	0.3%	24.5	1.3%	0.499	0.1%
EQ16	158.1	1.2%	23.8	0.8%	24.9	3.5%	0.499	1.7%
EQ17	157.9	0.4%	-	-	-	-	-	-
EQ18	157.9	1.4%	23.6	0.9%	24.6	4.1%	0.498	1.9%
EQ19	158.0	0.5%	-	-	-	-	-	-
EQ20	158.4	1.1%	23.8	0.7%	24.7	3.6%	0.499	1.3%

Table 2.3 Results for 20 different earthquake events with 10% noise

Earthquake Record	k_e=157.9 (kN/mm)		k_p=23.7 (kN/mm)		d_y=24.9 (mm)		β=0.500	
	Mean	COV	Mean	COV	Mean	COV	Mean	COV
EQ1	157.5	0.8%	-	-	-	-	-	-
EQ2	157.5	1.6%	24.4	7.7%	24.7	3.7%	0.500	1.4%
EQ3	157.9	0.6%	-	-	-	-	-	-
EQ4	157.7	4.1%	23.9	1.8%	24.6	11.8%	0.498	5.4%
EQ5	157.0	1.9%	22.9	6.7%	22.9	13.1%	0.504	2.9%
EQ6	157.2	1.8%	-	-	-	-	-	-
EQ7	158.7	1.9%	24.3	3.5%	24.6	3.0%	0.496	1.5%
EQ8	157.2	0.9%	24.2	6.4%	25.1	7.2%	0.503	2.3%
EQ9	158.2	0.7%	-	-	-	-	-	-
EQ10	157.9	0.9%	-	-	-	-	-	-
EQ11	158.5	4.1%	23.8	5.0%	24.7	4.5%	0.476	11.8%
EQ12	157.5	1.1%	-	-	-	-	-	-
EQ13	157.7	1.7%	23.6	1.4%	24.7	4.5%	0.495	3.2%
EQ14	158.0	0.6%	-	-	-	-	-	-
EQ15	158.8	2.4%	23.3	1.7%	25.0	3.4%	0.496	1.5%
EQ16	157.3	1.5%	23.7	2.3%	24.9	6.8%	0.492	4.0%
EQ17	157.9	0.8%	-	-	-	-	-	-
EQ18	157.2	1.6%	23.7	2.6%	24.8	4.4%	0.502	2.1%
EQ19	157.6	1.1%	-	-	-	-	-	-
EQ20	157.9	2.6%	23.5	3.3%	24.9	4.0%	0.479	19.5%

Table 2.4 Results for 20 different earthquake events with 15% noise

Earthquake Record	k_e=157.9 (kN/mm)		k_p=23.7 (kN/mm)		d_y=24.9 (mm)		β=0.500	
	Mean	COV	Mean	COV	Mean	COV	Mean	COV
EQ1	157.7	1.0%	-	-	-	-	-	-
EQ2	158.1	3.3%	23.6	4.5%	24.5	7.3%	0.488	4.3%
EQ3	158.0	1.7%	-	-	-	-	-	-
EQ4	156.4	5.5%	24.4	4.6%	24.8	10.1%	0.483	8.1%
EQ5	157.6	2.8%	22.5	6.3%	24.4	4.5%	0.484	4.8%
EQ6	158.2	2.1%	-	-	-	-	-	-
EQ7	158.3	2.5%	23.3	1.7%	25.0	5.2%	0.502	2.4%
EQ8	154.1	2.1%	23.4	3.1%	24.7	6.9%	0.502	5.4%
EQ9	157.7	0.8%	-	-	-	-	-	-
EQ10	157.5	1.8%	-	-	-	-	-	-
EQ11	156.9	5.8%	23.5	4.3%	25.7	10.1%	0.481	13.6%
EQ12	157.1	2.4%	-	-	-	-	-	-
EQ13	158.3	3.1%	23.9	2.0%	25.2	4.4%	0.489	3.1%
EQ14	157.4	1.2%	-	-	-	-	-	-
EQ15	157.2	2.8%	24.1	4.9%	24.8	5.6%	0.500	1.3%
EQ16	158.0	2.7%	24.0	6.3%	24.2	10.3%	0.508	4.5%
EQ17	157.9	1.4%	-	-	-	-	-	-
EQ18	157.1	3.1%	23.9	3.2%	25.1	7.2%	0.500	2.8%
EQ19	157.8	1.5%	-	-	-	-	-	-
EQ20	158.1	3.5%	23.4	3.2%	25.4	8.3%	0.485	5.6%

Table 2.5 Results for 20 different earthquake events with 20% noise

Earthquake Record	k_e=157.9 (kN/mm)		k_p=23.7 (kN/mm)		d_y=24.9 (mm)		β=0.500	
	Mean	COV	Mean	COV	Mean	COV	Mean	COV
EQ1	157.8	1.3%	-	-	-	-	-	-
EQ2	156.6	4.0%	24.5	14.8%	25.8	6.6%	0.506	2.5%
EQ3	158.0	1.0%	-	-	-	-	-	-
EQ4	157.3	7.5%	23.7	2.2%	26.1	9.6%	0.511	7.7%
EQ5	156.8	3.0%	26.1	11.3%	24.7	6.5%	0.506	6.2%
EQ6	158.2	2.7%	-	-	-	-	-	-
EQ7	157.8	2.5%	25.1	7.5%	23.9	5.9%	0.499	3.1%
EQ8	154.4	3.4%	23.7	9.0%	24.8	12.9%	0.491	10.4%
EQ9	157.3	1.3%	-	-	-	-	-	-
EQ10	157.6	2.2%	-	-	-	-	-	-
EQ11	154.9	5.3%	23.9	3.2%	23.8	11.3%	0.472	18.7%
EQ12	157.2	2.7%	-	-	-	-	-	-
EQ13	158.0	3.7%	24.1	3.1%	24.8	10.1%	0.474	10.7%
EQ14	158.2	1.0%	-	-	-	-	-	-
EQ15	157.6	3.0%	23.5	4.3%	23.3	10.7%	0.498	2.8%
EQ16	157.4	3.3%	23.6	7.5%	24.2	9.9%	0.507	4.6%
EQ17	157.8	1.6%	-	-	-	-	-	-
EQ18	155.2	7.1%	24.5	5.2%	25.6	7.4%	0.503	3.7%
EQ19	157.5	3.0%	-	-	-	-	-	-
EQ20	157.0	6.0%	23.9	6.1%	25.3	9.1%	0.498	4.8%

2.5 Summary

This chapter has presented a simple method for parameter identification of a highly nonlinear flag-shaped hysteretic structure. A simulated system with variable levels of added noise is used to demonstrate the robustness of the method. The results show that a high threshold can yield a good estimate of the post-yielding stiffness, and the estimations of the pre-yielding stiffness, yield displacement and energy dissipation coefficient are robust to different thresholds. Good estimates of total hysteretic energy dissipation can be obtained when the threshold is not used. Given the computational simplicity of the method, the result can be evaluated with and without thresholds to ensure the best quality metrics are obtained from the final step of the method.

The sensitivity analysis shows good robustness of the method with average coefficient of variation within 10% to different levels of noise and a range of 20 different earthquake events. The accuracy of the method is also validated by identifying the structure as linear when the structural response of the system is only linear during the whole ground motion. In addition, the method can be extended to the multi degree of freedoms system if the hysteresis loop are generated from measurement data obtained at each floor or selected groups of floors that make sense, by using greater numbers of sensors. Increased sensor density would capture in these inter-story hysteresis loops, any multi-mode effects that appear in the response.

Finally, the method is computationally simple and can be implemented automatically without requiring human input at any point. Thus, a rapid assessment can be made to offer significant information about structural damage and safety after an event.

Chapter 3: HLA-based Method for Structural Systems with Pinching

3.1 Introduction

Damage identification of highly nonlinear hysteretic systems is a challenging problem due to the complexity and continually altering structural characteristics over a response, particularly for hysteretic pinching structures. Hysteretic pinching is primarily caused by damage and interaction of structural components under large deformation (Foliente and Noori, 1996). It is commonly observed in reinforced concrete systems due to sliding of two cracked surfaces or yielding of compression reinforcement (Ozcebe and Saatcioglu, 1989), and in wood joint systems where a cavity around the fastener is formed by wood crushing (Foliente, 1995). In steel structures with bolted connections, pinching behaviour can also occur due to the development of connection gaps resulted from elongation and slipping of bolts (Astaneh et al., 1989; Iannone et al., 2011). Hence, it can be common, not occur over all response cycles, and is thus highly nonlinear. It also does not necessarily have a common or constant modelled effect.

A novel LLTR identification method based on hysteresis loop analysis and chi-squared hypothesis test was developed for SHM of high nonlinear flag-shaped hysteretic systems in Chapter 2. However, the application of chi-squared distribution for the likelihood ratio $-2\log\lambda$ in the LLTR method requires that the consistency of the observations can determine the *r*-set regression coefficients uniquely using *r* simultaneous equations (Feder, 1975a), which is not true when the transition part between each segment of the half cycle is ignored for hysteretic pinching systems (Zhou et al., 2015).

In addition, the LLTR method tests the difference of the overall sum of squared residuals between the assumed *r*-segment and *r*+1-segment. Thus, an exhaustive grid search with C_{n-2}^{r-1} possible data combinations for each *r*-segment half cycle assumption is needed to obtain the global minimum of the objective function. Particularly for the *r*=4 full nonlinear response (Zhou et al., 2015).

In this chapter, a modified HLA-based method is developed based on a sup *F* type hypothesis test for the identification of physical parameters of highly nonlinear hysteretic pinching systems. The modified HLA method does not impose the restriction that the regression function is continuous at the breakpoints to allow for pinching and other highly nonlinear behaviours. Thus, each segment can be treated as an independent statistic test (Bai and Perron, 1998). In addition, the *F* type test employs a different strategy to obtain the overall minimal value of the sum of squared residuals for the alternative hypothesis, which highly improves the computational efficiency.

The performance of the proposed method is illustrated using a simulated reinforced concrete structure modelled by the Baber-Noori model (Baber and Noori, 1985). The Baber-Noori model is specifically developed to describe the pinching behaviour that is associated with high shear loads and slippage of longitudinal reinforcement in reinforced concrete structures. In particular, the load-deformation relation for pinching exhibits a sudden loss of stiffness resulting from repeated opening and closing of cracks commonly observed in reinforced concrete structures (Kunnath et al, 1997; Zhang et al, 2002; Wu and Smyth, 2008), which is different with the stiffness softening mechanism that is used to define the reduction in component strength capacity under cyclic loading after reaching the ultimate strength limit for cracking reinforced concrete elements(Bazant et al., 1987; Ghobarah et al., 1999).

Robustness is investigated by adding different levels of RMS noise and varying the loop parameters of the hysteretic pinching differential model, as well as the assumed damping ratio. The method described for a SDOF system can be readily extended to a MDOF system with measurement data available or reliably estiamted at each floor.

3.2 Hysteretic Pinching Model

The modified HLA method utilizes a slip-lock (SL) pinching model proposed by (Baber and Noori, 1985). The pinching characteristic in the hysteresis loop was presented by adding a slip-lock spring, with the slip zone stiffness near zero and on infinite lock zone stiffness, in series with the smooth Bouc-Wen hysteresis spring (Bouc, 1967; Wen, 1976). The equation of motion for a SDOF SL pinching model is defined:

$$m\ddot{x} + c\dot{x} + \alpha k_e x + (1-\alpha)k_e z = -m\ddot{x}_g \tag{3.1}$$

where $x, \dot{x}$ and $\ddot{x}$ are the structural displacement, velocity and acceleration of the SDOF system, $\ddot{x}_g$ is the ground acceleration, m is the mass of the system and c is the viscous damping coefficient. The parameter α represents the ratio of the post-yielding stiffness k_p to the pre-yielding stiffness k_e, and z is the hysteretic displacement. The differential model to introduce the pinching behaviour is defined:

$$\dot{z} = A\dot{x}_1 - \beta\left|\dot{x}_1\right|\left|z\right|^{p-1} z - \gamma\dot{x}_1\left|z\right|^{p} \tag{3.2}$$

$$\dot{x}_2 = \sqrt{\frac{2}{\pi}}\frac{a}{\mu}\dot{z}e^{-z^2/2\mu^2} \tag{3.3}$$

$$x = x_1 + x_2 \tag{3.4}$$

where parameters A, β, γ and p control the shape of the hysteresis loop, and μ is the control parameter for pinching sharpness. The parameter a controls the amplitude of the pinching region and is determined:

$$a = \delta_a \varepsilon(t) \tag{3.5}$$

where δ_a is a constant specified for the desired rate of pinching, and $\varepsilon(t)$ is the total energy dissipated by hysteretic element:

$$\varepsilon(t) = (1-\alpha)\frac{k_e}{m}\int_0^t z(\tau)\dot{x}(\tau)d\tau \tag{3.6}$$

The desired hysteretic pinching behaviour observed in civil engineering structure is then obtained using the SL pinching model. The structural and ground accelerations can be measured during the earthquake. The structural velocity and displacement can then be obtained using the low-frequency GPS-measured displacement method presented in Chapter 2. Hence, the restoring force $F(x)$ can be obtained using Equation (2.3) and the hysteresis loop for the pinching system can be reconstructed subsequently.

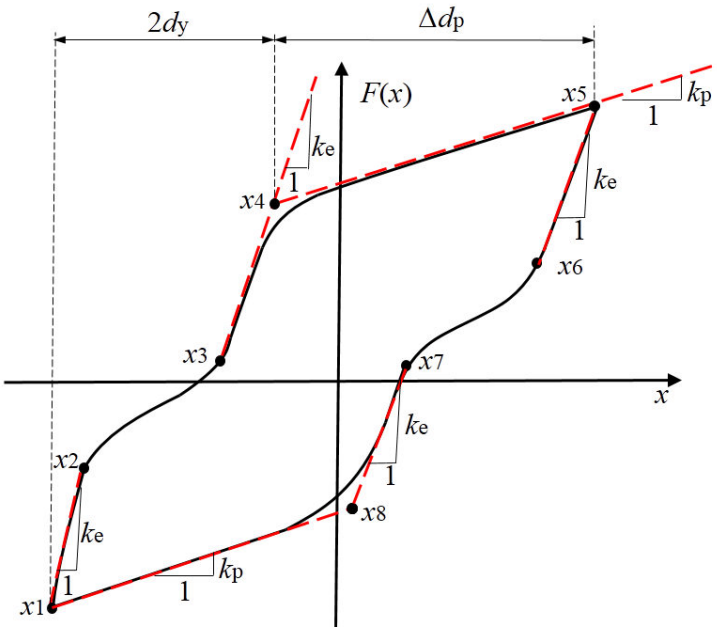

Figure 3.1: General pinching hysteresis loop of civil engineering structure

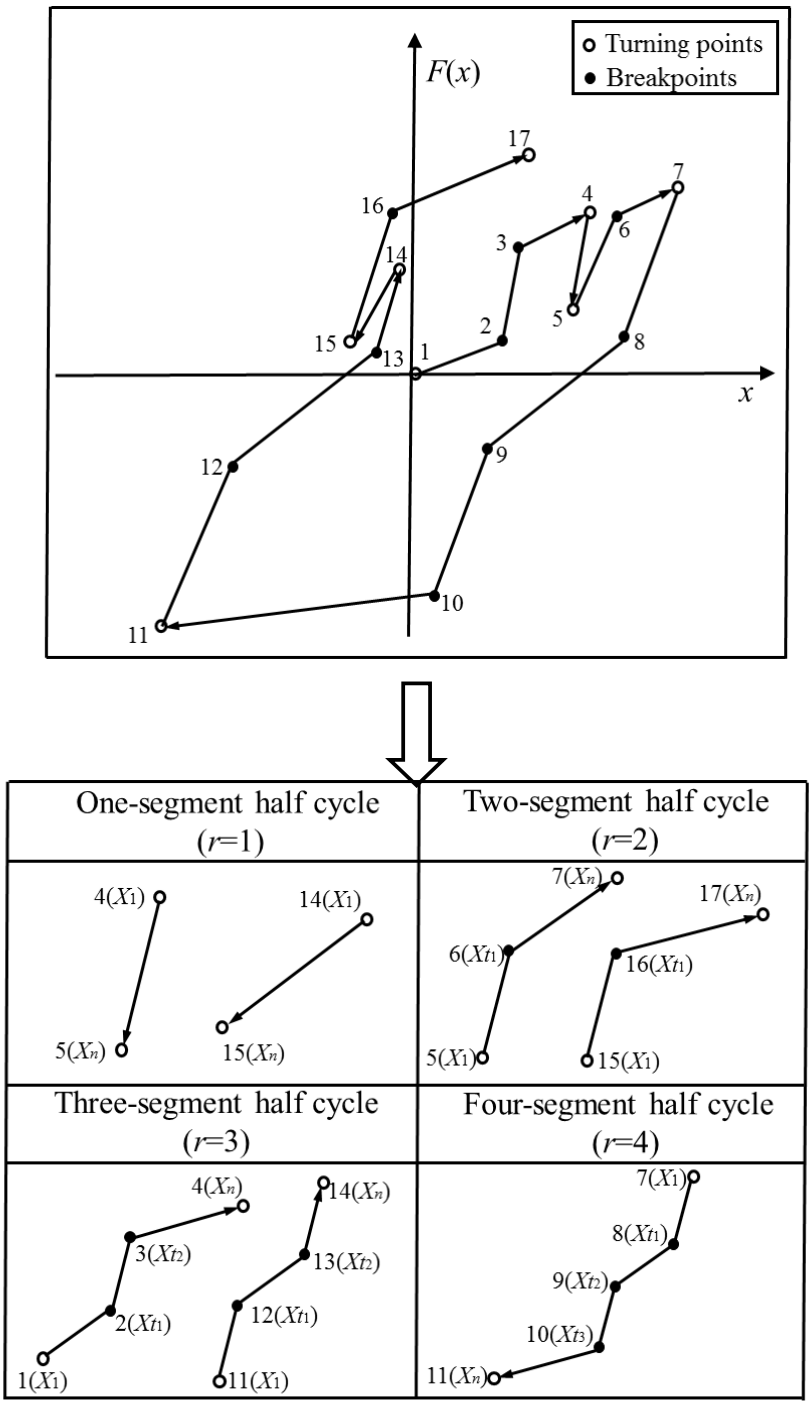

Figure 3.2: A typical hysteresis response with four types of half cycles with 1, 2, 3, and 4-segment. The bottom panel shows node number from the top panel.

Figure 3.1 shows a general pinching hysteresis loop for a civil structure subjected to a strong motion earthquake. The nonlinear response and potential damage of civil structures after a

seismic event can be assessed by identifying the underlying physical parameters (k_e, k_p, Δd_p) as damage indices. In particular, the stiffness k_e and k_p can be calculated to determine the extent degradation over time and thus reflect the severity of damage, because stiffness may be reduced in some floors if damage occurs in those layers (Yoshimoto et al., 2005). In addition, the plastic deformation Δd_p can also be computed to provide a key reference for assessing cumulative damage, low cycle fatigue, potential for future failure, and thus safety.

Figure 3.2 shows a typical piece of a hysteresis response for a pinching system. It can be seen that the whole hysteresis response can be sliced into a number of half cycles using the turning points labelled 4, 5, 7, 11, 14, 15 and 17, where the deformation is a local maximum or minimum. Thus, all the half cycles are divided into four types of piecewise linear model with one, two, three and four-segments, respectively, as shown in Figure 3.2(b) with the same labels. The statistical analysis can then be applied to each of the selected half cycles to obtain the breakpoints and regression coefficients that are related to the estimated physical parameters (k_e, k_p, Δd_p).

3.3 Identification Procedure

To identify the optimum number of segments for the selected half cycle of the pinching system, an r-segment (r=1, 2, 3 and 4) piecewise linear model is first assumed and defined using Equations (2.11) and (2.12). The half cycle is then divided into r segments T_i (i=1,…,r) using turning points (X_1, X_n) and breakpoints ($X_{t_1},\ldots, X_{t_{r-1}}$), again following the presentation in Chapter 2. The optimum solution for the breakpoints is to find the minimum value of the objective function of SSR R_r:

$$R_r(X_1, X_{t_1}, \cdots X_{t_{r-1}}, X_n) = \sum_{i=1}^{t_1}[Y_i - g_1(X_i)]^2 + \sum_{i=t_1+1}^{t_2}[Y_i - g_2(X_i)]^2 + \cdots + \sum_{i=t_{r-1}+1}^{n}[Y_i - g_r(X_i)]^2 \quad (3.7)$$

$$(\hat{X}_{t_1}, ..., \hat{X}_{t_{r-1}}) = \arg\min_{X_{t_1}, ..., X_{t_{r-1}}} R_r(X_1, X_{t_1}, ..., X_{t_{r-1}}, X_n) \quad (3.8)$$

where $X_{t_0} = X_1$ and $X_{t_r} = X_n$. The minimization is taken over all feasible partitions, and the regression coefficients (a_1, b_1,…, a_r, b_r) are associated with the estimated breakpoints $\hat{X}_{t_1}, \ldots \hat{X}_{t_{r-1}}$.

Next, an addition breakpoint X_τ is assumed for each of the obtained segments T_1, T_2,… or T_r. Thus, r+1 partitions are now presented in this half cycle with the fixed breakpoints X_{t_1} ,…, $X_{t_{r-1}}$ and the overall SSR R'_{r+1} for this r+1 segment model can be calculated:

$$R'_{r+1} = \min_{1 \le j \le r} \inf_{X_\tau \in \Lambda_{i,\eta}} R_{r+1}(X_1, \hat{X}_{t_1}, ..., \hat{X}_{t_{j-1}}, X_\tau, \hat{X}_{t_j}, ..., \hat{X}_{t_{r-1}}, X_n) \quad (3.9)$$

$$\Lambda i, \eta = \left\{ X_\tau ; \hat{X}_{t_{j-1}} + 0.05(\hat{X}_{t_j} - \hat{X}_{t_{j-1}}) \le X_\tau \le \hat{X}_{t_{j-1}} - 0.05(\hat{X}_{t_j} - \hat{X}_{t_{j-1}}) \right\} \quad (3.10)$$

The sup F type hypothesis test is then performed between the null hypothesis H_0 that the optimum number of segment for this half cycle is r, and the alternative hypothesis H_1 that the optimum number of segment for the half cycle is r+1, and is defined (Bai and Perron, 1998):

$$F(r+1 \mid r) = \frac{n(\sum_{i=1}^{r} R_1(T_i) - R'_{r+1})}{R_r} \ge S_\theta^r \qquad r = 1, 2, 3 \quad (3.11)$$

where $R_1(T_i)$ represents the sum of squared residuals for T_i partition.

Therefore, it permits the rejection of H_0 in favor of H_1 when the value of $F(r+1|r)$ is larger

than the critical value of S_θ^r, where θ is the user-defined significance level. The critical value of S_θ^r can be found in Bai and Perron (1998). In this research, the significance level is set to be 0.01, and $S_{0.01}^1$, $S_{0.01}^2$ and $S_{0.01}^3$ are found to be 16.64, 17.98 and 18.66, for r=1, 2, and 3, respectively.

In addition, the identification procedure starts with the value of r=3 that can ensure that any full nonlinear four-segment half cycle is identified first, which is more important in determining damage severity as soon as possible during or after the earthquake. However, if starting with r=1, the linear one-segment half cycle is identified first, which is not as important in damage assessment. Thus, with this approach assuming r=3 first, one could stop after identifying simply if damage occurred with this method, which is strictly pragmatic, and avoid identifying linear half cycles if desired. Importantly, in the end, all the half cycles can be identified with same results starting with different r value.

Finally, the number of segments for the selected half cycles are identified, and the breakpoints ($X_{t_1},\ldots,X_{t_{r-1}}$) and associated regression coefficients (a_1, b_1,…, a_r, b_r) can be obtained to estimate the physical parameters (k_e, k_p and Δd_p) for the pinching system. Figure 3.3 shows the flowchart of the identification procedure.

The step by step procedure is summarized:

Step 1: Assume r=3 for all the half cycles, and calculate R_3, $\hat{X}_{t_1}$ and $\hat{X}_{t_2}$ using Equations (3.7) and (3.8). The standard least linear regression is then implemented to T_1, T_2 and T_3 to obtain $R_1(T_1)$, $R_1(T_2)$ and $R_1(T_3)$.

Step 2: According to the fixed breakpoints ($\hat{X}_{t_1}$,…, $\hat{X}_{t_{r-1}}$)and turning points (X_1, X_n), calculate R_4' using Equations (3.9) and (3.10).

Step 3: Calculate $F(4|3)$ using Equation (3.11) and identify four-segment half cycles by $F(4|3) > S_{0.01}^3 = 18.66$. All the remaining half cycles will thus be best fit by one, two and three segment model.

Step 4: Assume $r=2$ for the remaining half cycles, and calculate R_2, $\hat{X}_{t_1}$, $R_1(T_1)$, $R_1(T_2)$, and R_3' using Equations (3.7)-(3.10). Thus, the three-segment half cycles are identified by $F(3|2) > S_{0.01}^2 = 17.98$.

Step 5: Assume linear response ($r=1$) for the unidentified half cycles, and repeat steps 1-3 to calculate R_1, $R_1(T_1)$, R_2' and $F(2|1)$. Obtain the two-segment half cycles by $F(2|1) > S_{0.01}^1 = 16.64$, and one-segment (linear response) half cycles by $F(2|1) < S_{0.01}^1 = 16.64$.

Step 6: Estimate the physical parameters k_e, k_p and Δd_p using the calculated regression coefficients and breakpoints of each half cycle with the optimum number of segment identified. Appropriate statistics and/or time trajectories are used to summarize the results if no degradation is assumed or to track evolution of stiffness overtime if degradation occurs.

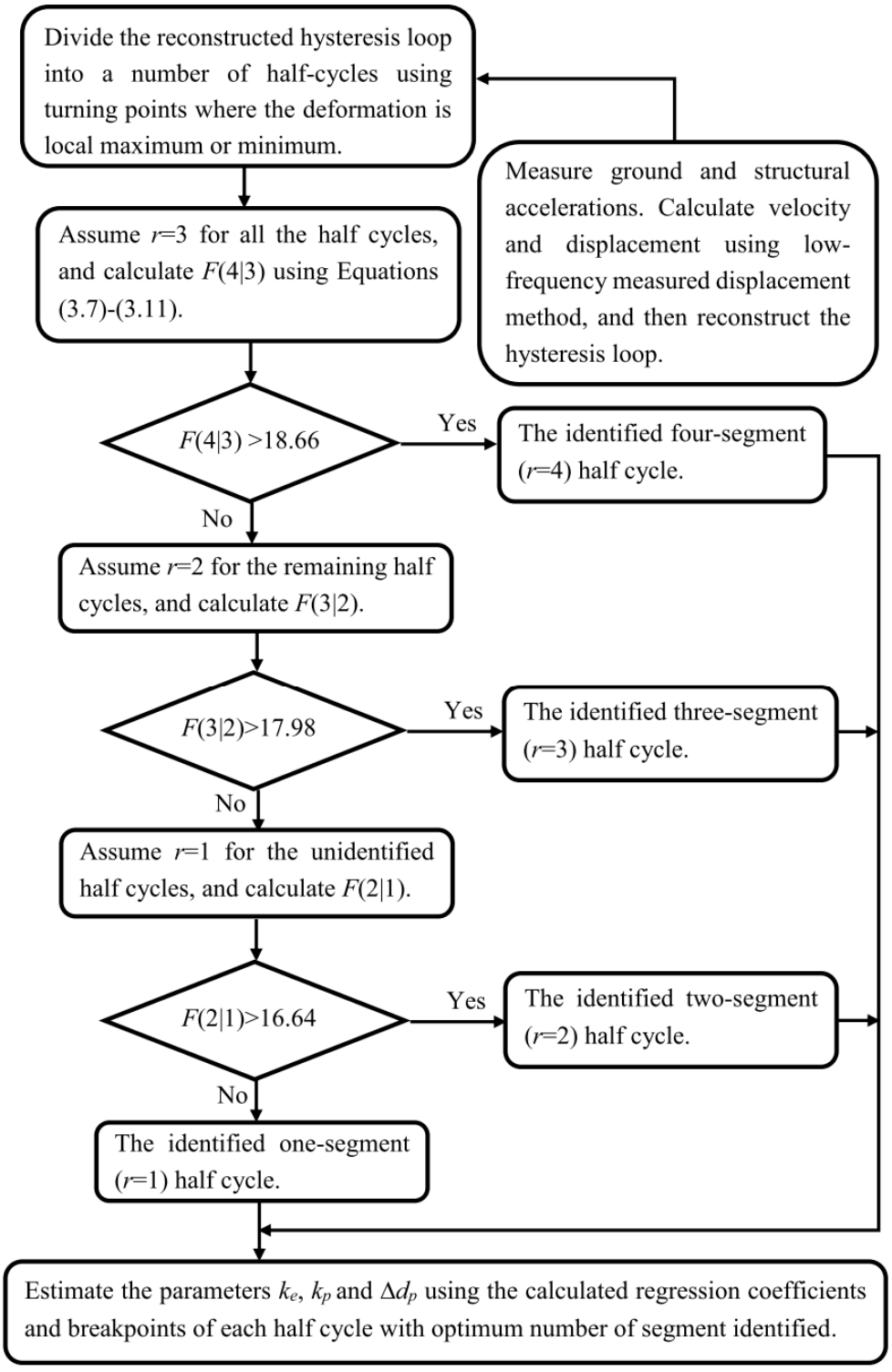

Figure 3.3: Flowchart of the identification procedure.

3.4 Case Study

3.4.1 Simulated proof-of-concept structure

The simulated proof-of-concept structure is a SODF moment resisting frame model of a five story reinforced concrete building (Nayyerloo et al., 2011). The seismic weight per floor is 1692kN for the roof level and 2067 for other levels. The first period of the structure is 1.2s and a 5% constant viscous damping, which is commonly adopted by design codes and standards (Atkinson and Pierre, 2004; Chopra, 2001; Pekcan et al., 1999), is considered in simulating the structural response. The system has a pre-yielding stiffness of k_e=27.3kN/mm, a post-yielding stiffness of k_p=1.78kN/mm, and yielding displacement of d_y=46.5mm. To simulate the structural response of the hysteretic pinching system, the shape parameters A=1.0, β=0.95, γ=0.05 and p=2 are used to provide realistic nonlinear structural behaviour of reinforced concrete system (Kunnath et al., 1997), and the pinching parameters δ_a=0.2, and μ=0.05 are adopted for pinching behaviour.

The proposed identification is implemented in Matlab. The simulated structure is subjected to the Superstition Hill Event El Centro Station record with PGA of 0.358g and a duration of 40s from the earthquake record used (PEER, 2005), as shown in Figure 3.4. The noise free ground acceleration is first used to generate the true structural response using a Runge-Kutta method with a time step of Δt=0.001s. Figure 3.5 shows the resulting simulated true hysteresis loops of the modelled structure.

A 10% RMS noise is then added to the ground acceleration, simulated structural acceleration and displacement to provide a realistic measurement situation. The low-frequency measured displacement is assumed measurable at 1Hz and acceleration is assumed to be measured at

1000Hz in this case study. Figure 3.6 shows the comparison between the true structural response and corrected response using the GPS-measured displacement method. Good agreement between the true response and corrected response was presented, despite a reasonable to high level of added noise, which indicates the accuracy of the GPS correction method.

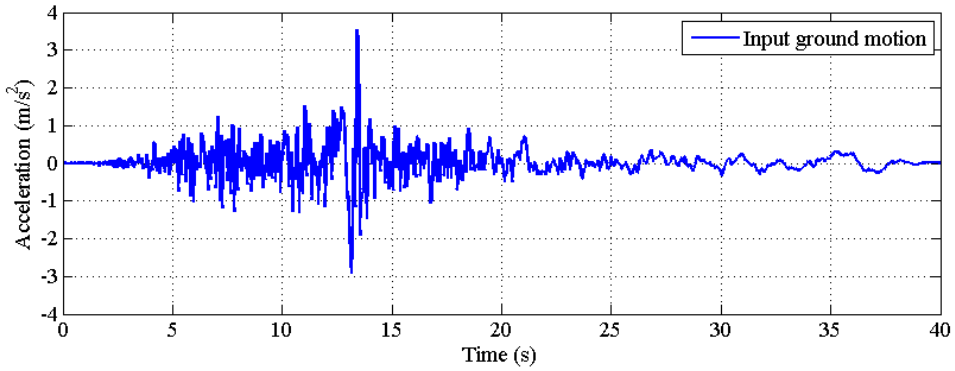

Figure 3.4: Ground acceleration of the Super Hill Event El Centro Station.

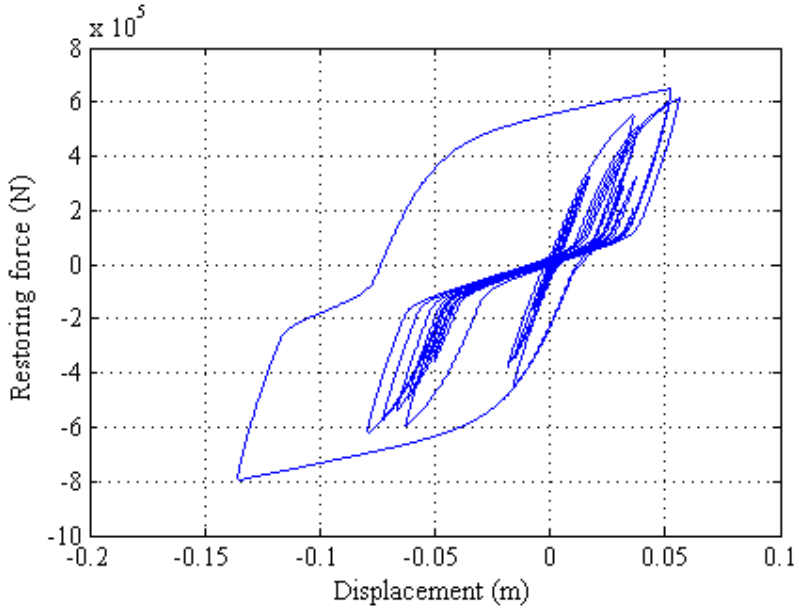

Figure 3.5: Simulated hysteresis loop for the modelled structure.

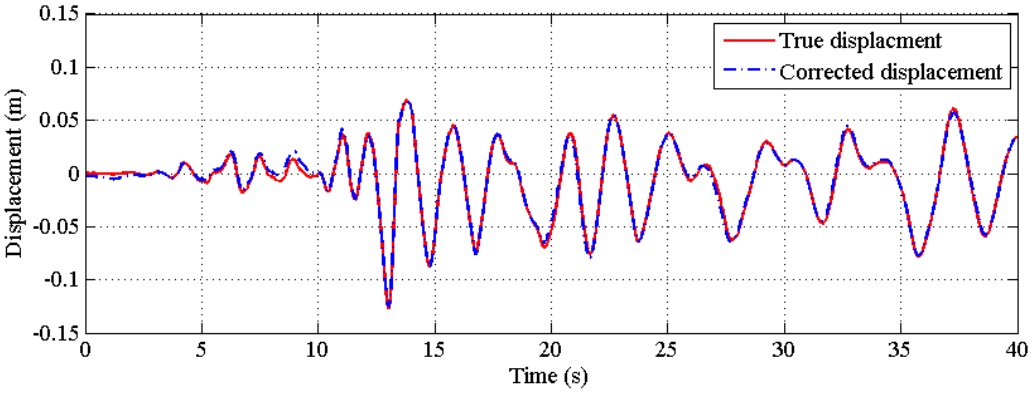

(a)

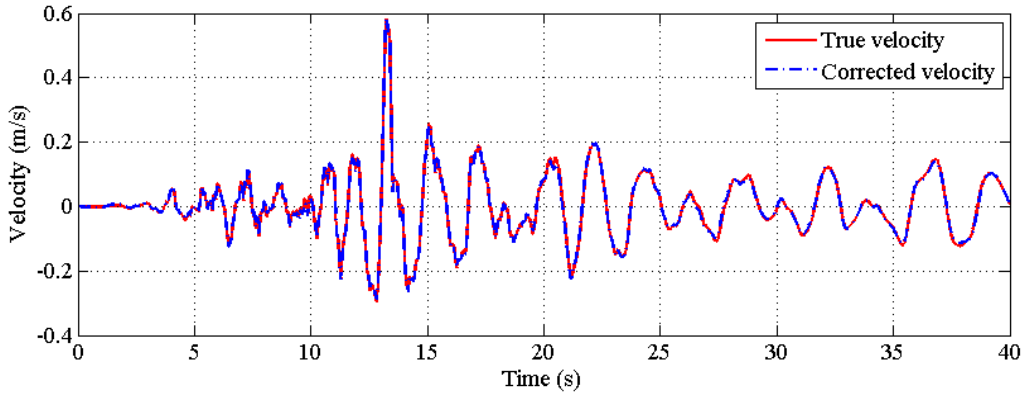

(b)

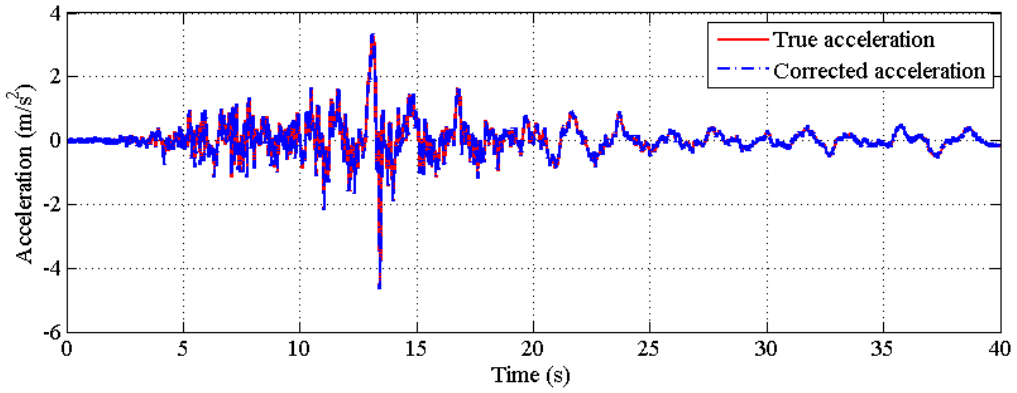

(c)

Figure 3.6: Comparison between true response and corrected response of (a) displacement, (b) velocity and (c) acceleration.

3.4.2 Analyses and Implementation

As discussed in the Chapter 2 for the flag-shaped system, narrow almost negligible plastic or nonlinear segments can significantly affect the accuracy of the estimated post yielding stiffness k_p. Thus, a threshold Δd is used to ignore those small half cycles to obtain the correct slope of the plastic segment. For the pinching system, a similar threshold Δd is also defined to ensure the estimation accuracy of k_p. As shown in Figure 3.7, segment 4 representing the plastic response, can be used to estimate the value of the plastic deformation Δd_p and post-yielding stiffness, k_p. In particular, the plastic deformation Δd_p in this half cycle is calculated:

$$\Delta d_p = \left| X_n - X_{t_3} \right| \tag{3.12}$$

And the post-yielding stiffness k_p can be estimated using the slope of segment 4:

$$k_p = a_4 \tag{3.13}$$

The plastic response of the half cycle in Figure 3.7 is significant and the segment 4 is large enough for the estimation of the post-yielding stiffness. However, the plastic segment 4 of the narrow nonlinear half cycle in Figure 3.8 is very small and it is thus difficult to find the correct slope. Hence, the slope of plastic segment 4 is used to estimate the post-yielding stiffness k_p only when the plastic deformation Δd_p is more than an optimal user-defined threshold, Δd. The selection of this optimal threshold Δd is investigated in the next section.

In addition, even for the half cycle with significant plastic response in Figure 3.7, the accuracy of the linear stiffness estimation is also affected by the transition between the elastic and plastic part, as shown in Figure 3.9. In the presence of this transition part, both segments 3 and 4 contain a linear part and a curved part. Due to this curved part, the slope of segment 4 is larger than the true slope of the post-yielding stiffness and the slope of segment 3 is smaller than the true value of the pre-yielding stiffness. Therefore, more accurate estimates can be

obtained if less data from this curved part is used for the regression analysis for segments 3 and 4. To reduce the data in the curved part used in the linear regression, another threshold $P(n)$ is introduced and defined:

$$P(n) = \frac{\Delta n}{n} \tag{3.13}$$

where n is the total number of data in this half cycle and Δn is the number of data eliminated in the regression analysis.

Thus, the linear regression can be implemented using data $[X_{t_2}, X_{t_3-\Delta n}]$ in segment 3 for estimation of k_e and data $[X_{t_3+\Delta n}, X_n]$ in segment 4 for estimation of k_p. It can be seen that if the selection of $P(n)$ is too small, the effect of the curved part would not be reduced effectively, and if too big, the data in the linear part could also be eliminated, which may affect the accuracy of the estimates due to the insufficient regression data. Therefore, the selection of the optimal threshold $P(n)$ is also investigated.

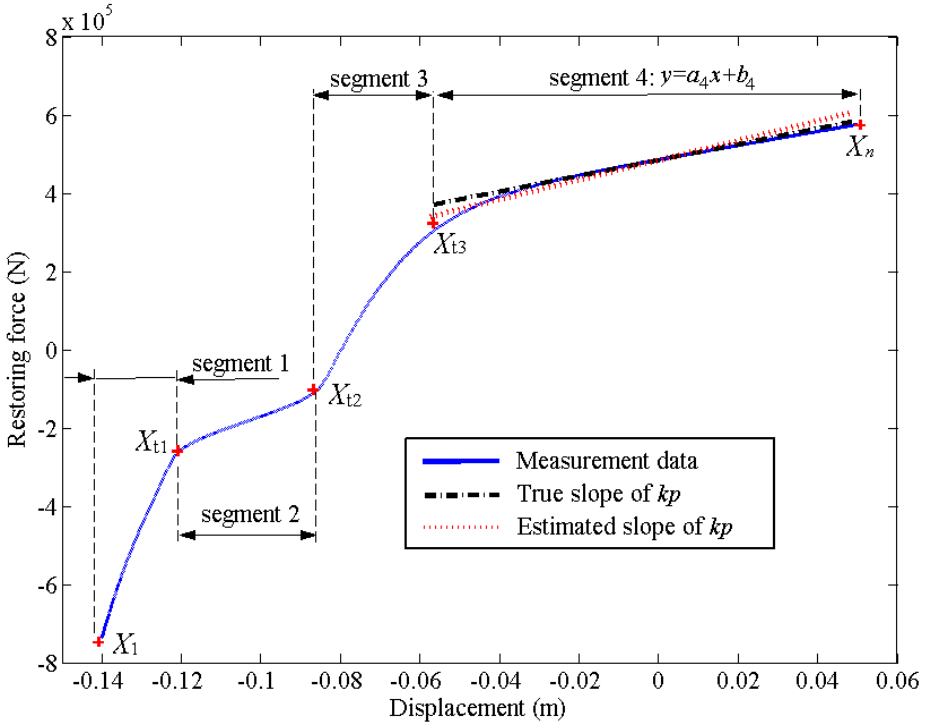

Figure 3.7: Nonlinear half cycle with significant plastic response.

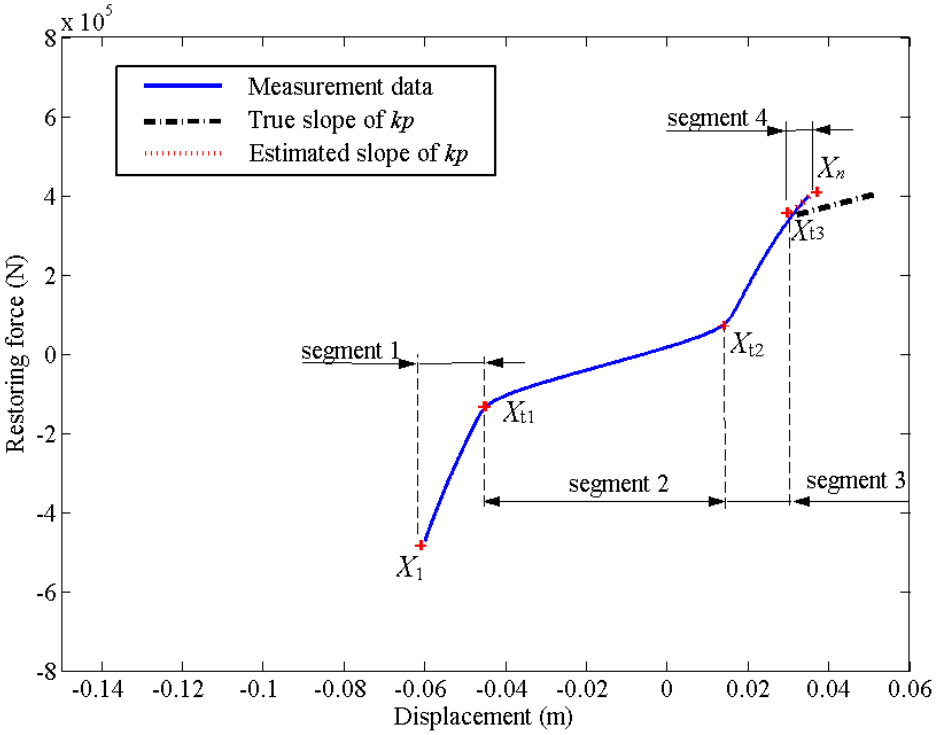

Figure 3.8: Nonlinear half cycle with narrow plastic response.

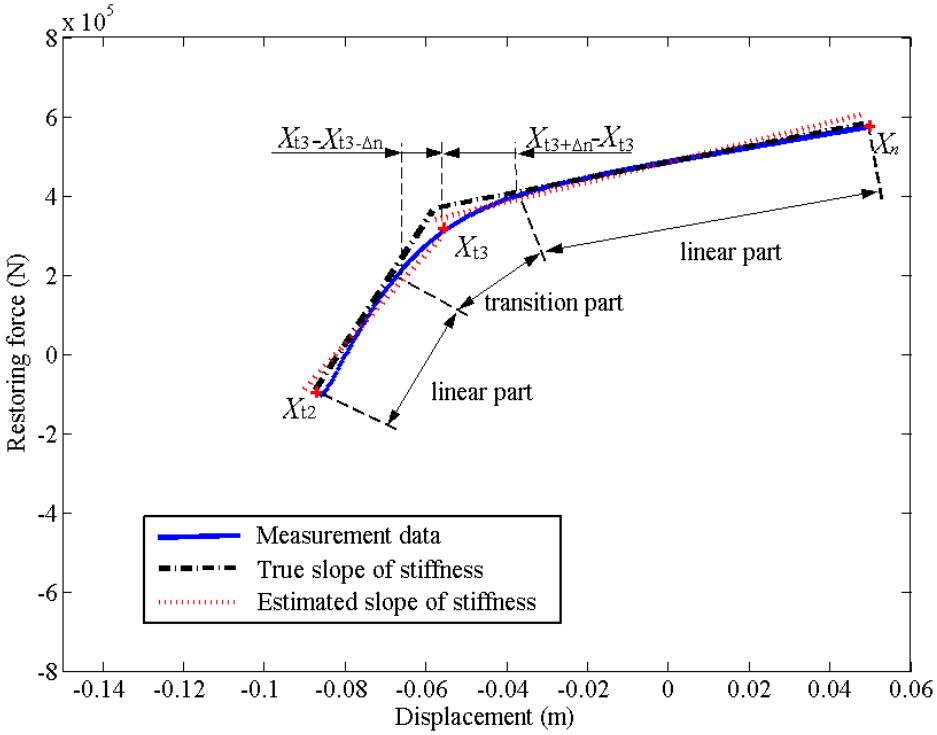

Figure 3.9: Effect of transition part on stiffness estimation.

3.5 Results and Discussion

3.5.1 Identification of the Number of Segment of Half Cycles

Figure 3.10 shows the identification for the four-segment (r=4) half cycle over all 26 half cycles in the response. The calculated values of $F(4|3)$ for four-segment half cycles are larger than $S^3_{0.01}$=18.66, which indicates the overall sum of squared residuals from the four-segment model is sufficiently smaller than the three-segment model. Thus, it permits the rejection of r=3 in favor of the four-segment (r=4) models for all half cycles above the rejection value $S^3_{0.01}$ =18.66. The half cycles below the rejection value are processed to the next identification step.

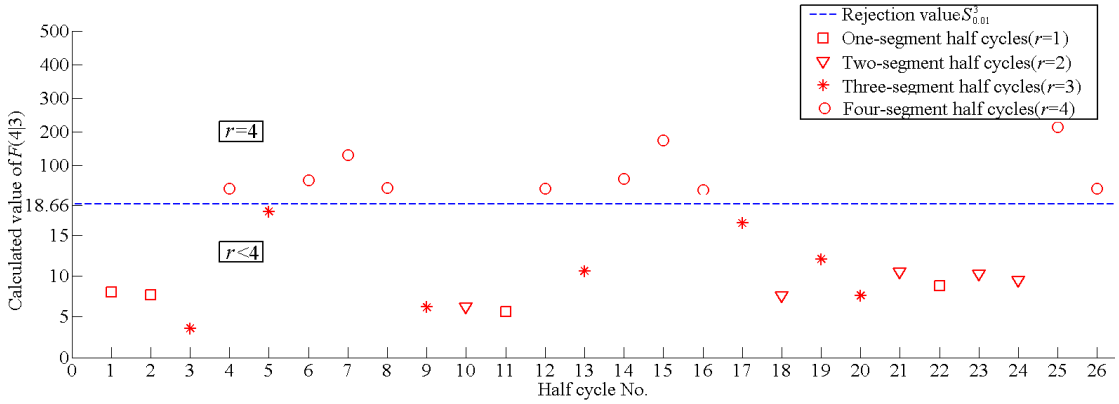

Figure 3.10: Identification of four-segment (r=4) half cycles.

Figure 3.11 shows the identification results for the three-segment (r=3) half cycles, excluding from the analysis the half cycles found to be four-segment in Figure 3.10. The half cycles with the value of $F(3|2)$ above the rejection value $S^2_{0.01}$=17.96 are identified as three-segment (r=3). And the remaining half cycles are identified in Figure 3.12. The half cycles with the value of $F(2|1)$ above the rejection value $S^1_{0.01}$=16.64 in Figure 3.12 are identified as two-segment (r=2), and the half cycles below $S^1_{0.01}$ are identified as one-segment (r=1) by default.

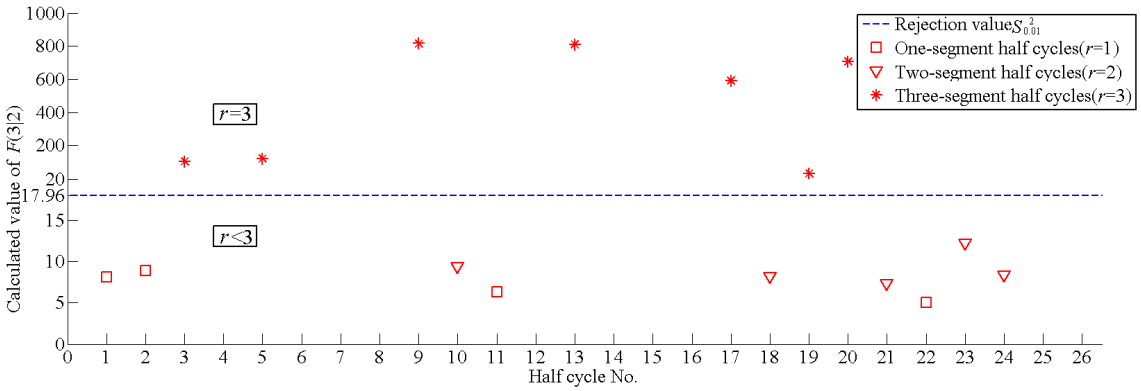

Figure 3.11: Identification of three-segment (r=3) half cycles, excluding the half cycles found to be four-segment (r=4).

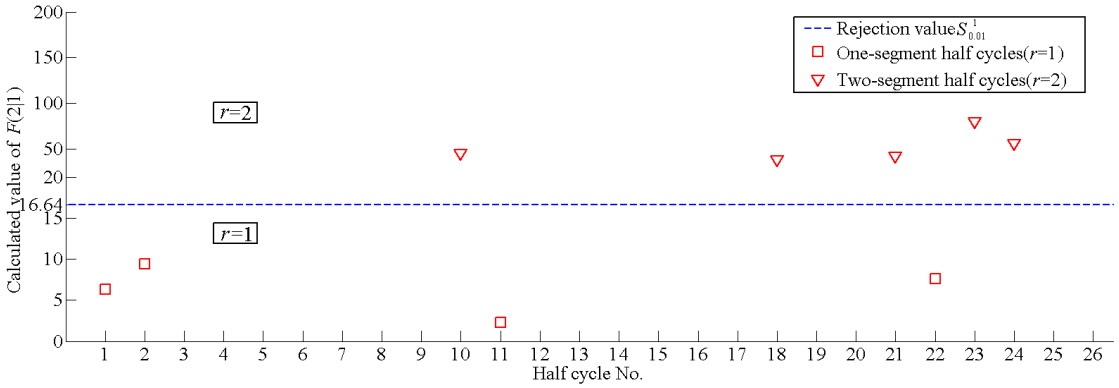

Figure 3.12: Identification of one and two-segment half cycles, excluding three and four segment half cycles.

3.5.2 Effect of Thresholds Δd and P(n)

Figures 3.13 and 3.14 show the effect of the magnitude of Δd on the estimate of the post-yielding stiffness and pre-yielding stiffness (k_p and k_e). The estimated value used in the error bars from Figures 3.13-3.20 are calculated by all the 26 investigated half cycles in Figure 3.10, and the error bars show the mean value with one standard deviation over these half cycles. For variable Δd, the pre-yielding stiffness k_e is robust because the elastic parts for all half cycles are large enough for assessment. However, the error of the estimated post-yielding stiffness k_p is very large when the threshold Δd is not used (Δd=0) and the threshold Δd is low

(Δd=0.01m and Δd=0.02m). The estimates of k_p are robust with error of 10.1% when the threshold Δd is chosen to be 0.04m.

Although the estimates are robust for both k_e and k_p when the threshold Δd is chosen to be 0.04m, the estimated value for pre-yielding stiffness k_e is smaller than the true value, and the post-yielding stiffness k_p is larger than the true value due to the effect of the transition part shown in Figure 3.9. Thus, the threshold $P(n)$ in Equation (3.13) is used to obtain an accurate result. Figures 3.15 and 3.16 show the effect of selection of this threshold $P(n)$ on the estimates of the post-yielding stiffness k_p and pre-yielding stiffness k_e with Δd=0.04m. With increasing $P(n)$, the estimated value is decreasing for post yielding stiffness and increasing for pre-yielding stiffness. The errors of estimates of k_e and k_p are within 5% when the thresholds $P(n)$=5% and Δd=0.04m are used. Thus, accurate estimation of the post-yielding stiffness and pre-yielding stiffness can be obtained using larger thresholds $P(n)$=5% and Δd=0.04m.

Figure 3.17 shows the resulting calculated cumulative plastic deformation. The cumulative plastic deformation drops as more half cycles are ignored with larger thresholds, as would be expected. However, the estimated result shows good agreement with the true value when the thresholds are not used ($P(n)$=0 and Δd=0) for assessment, matching similar result in Chapter 2. Thus, the threshold should not be used for the assessment of the cumulative plastic deformation, but should be used to obtain the post-yielding stiffness k_p and pre-yielding stiffness k_e. Such mixed use of thresholds is computationally simple and highly effective, as shown in Chapter 2.

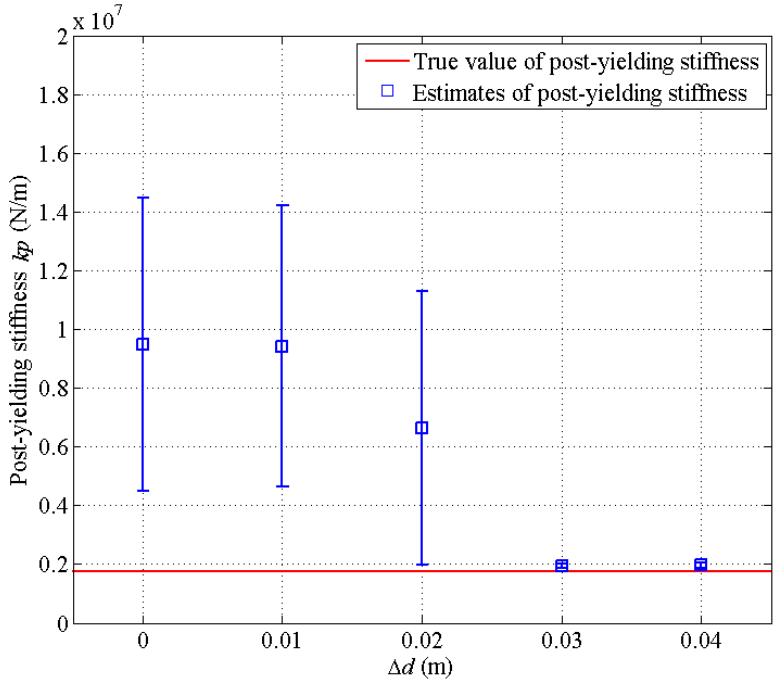

Figure 3.13: Effect of Δd on the estimates of post-yielding stiffness. The error bars show mean and one standard deviation over all half cycles.

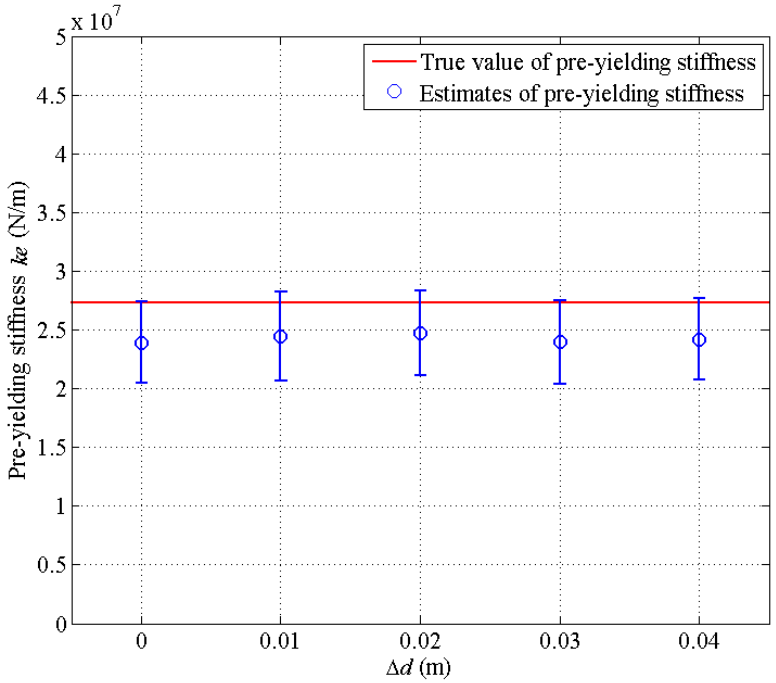

Figure 3.14: Effect of Δd on the estimates of pre-yielding stiffness. The error bars show mean and one standard deviation over all half cycles.

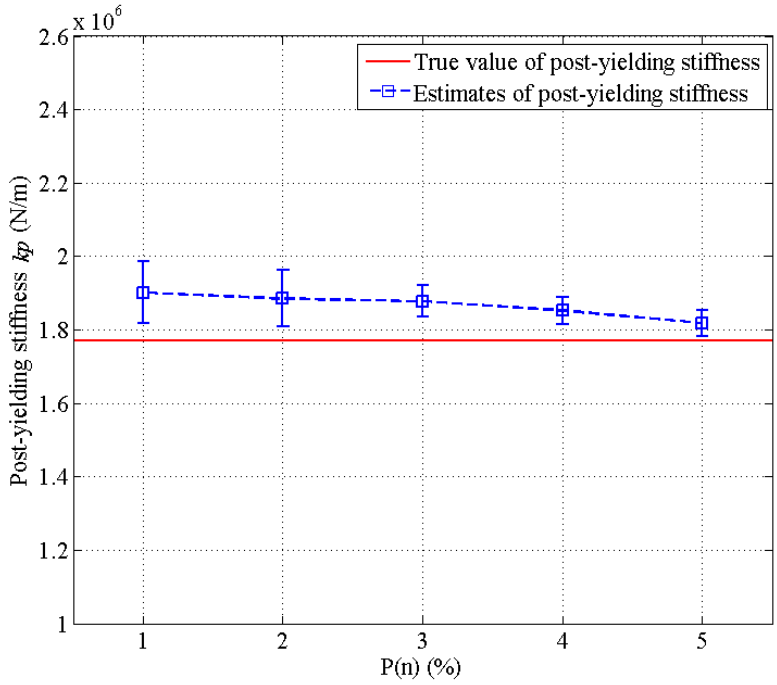

Figure 3.15: Effect of $P(n)$ on the estimates of post-yielding stiffness. The error bars show mean and one standard deviation over all half cycles.

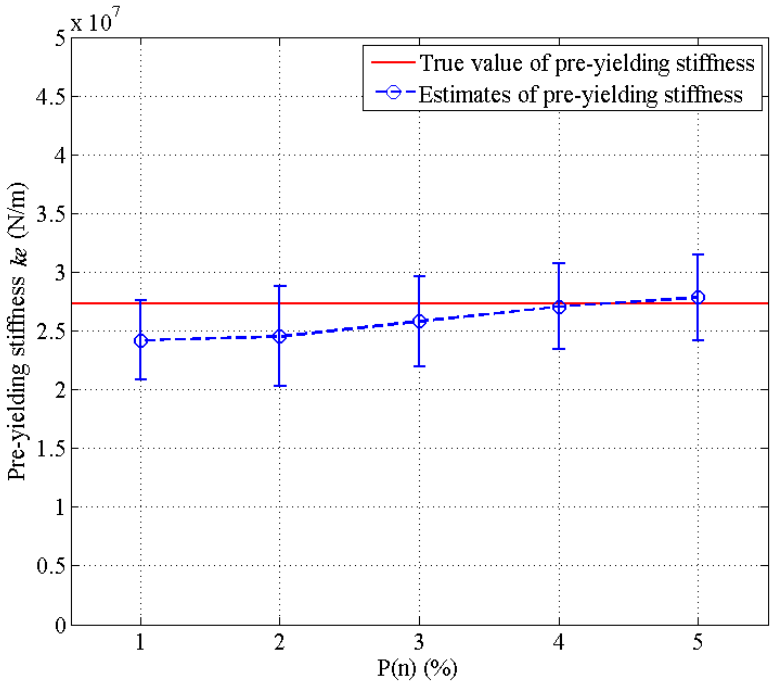

Figure 3.16: Effect of $P(n)$ on the estimates of pre-yielding stiffness. The error bars show mean and one standard deviation over all half cycles.

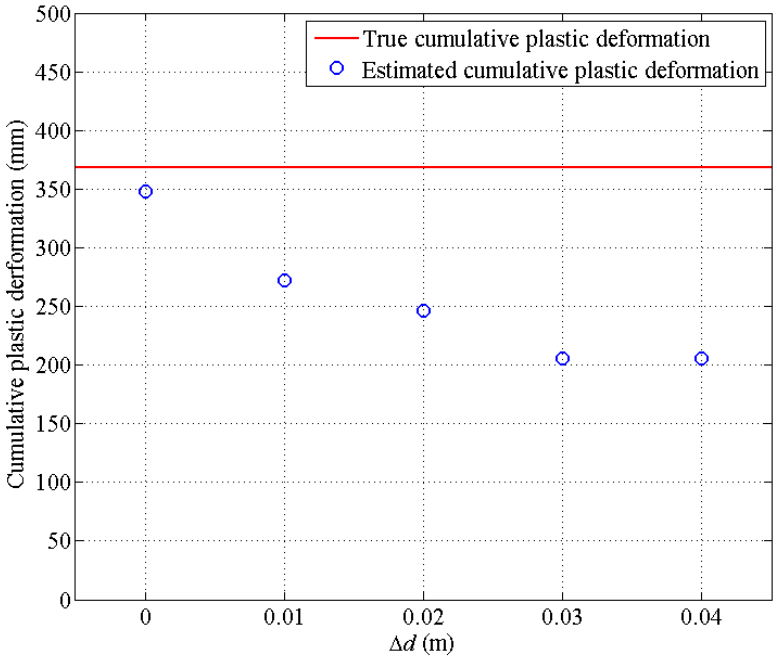

Figure 3.17: Estimates of cumulative plastic deformation.

3.5.3 Effect of Loop Parameters (p, δa and μ) and Variable Pinching

For different types of structural element, the pinching behaviour is obtained using variable loop parameters (p, δ_a and μ) of the SL model (Kunnath et al., 1997). As a result, the effect of variation in the loop parameters (p, δ_a and μ) on the estimated results is investigated. The thresholds $P(n)$=5% and Δd=0.04m are used to evaluate the results with 10% RMS added noise.

Figures 3.18 and 3.19 shows the effect of the transition parameter p when other parameters are constant. With the increase of p, both the post-yielding stiffness and pre-yielding stiffness show more accurate results compared to the true values, because the hysteresis loop with a larger value for p is closer to the underlying piecewise linear models assumed in this method. However, even for the extreme nonlinear hysteresis loop (p=1), the average errors for the estimates are less than 10%.

Figures 3.20-3.23 show the effect of the pinching sharpness parameter, μ, and pinching amplitude parameter, δ_a, when other parameters are constant, respectively. It can be seen that the estimates show a good agreement with the true value with variable of μ or δ_a for both post-yielding stiffness and pre-yielding stiffness.

In addition, the effect of the loop parameters (p, μ and δ_a) on the estimation of the cumulative plastic deformation, which is a critical indicator of structural damage (Park et al., 1985), is also presented in Table 3.1. It can be seen that the worst estimated error is 10.9% of the true value and most errors are less than 5%, which indicates the estimation of the cumulative plastic deformation is robust to variation in loop parameters. Therefore, the method can yield accurate estimation of post-yielding stiffness, pre-yielding stiffness and cumulative plastic deformation for different types of hysteretic pinching behaviours.

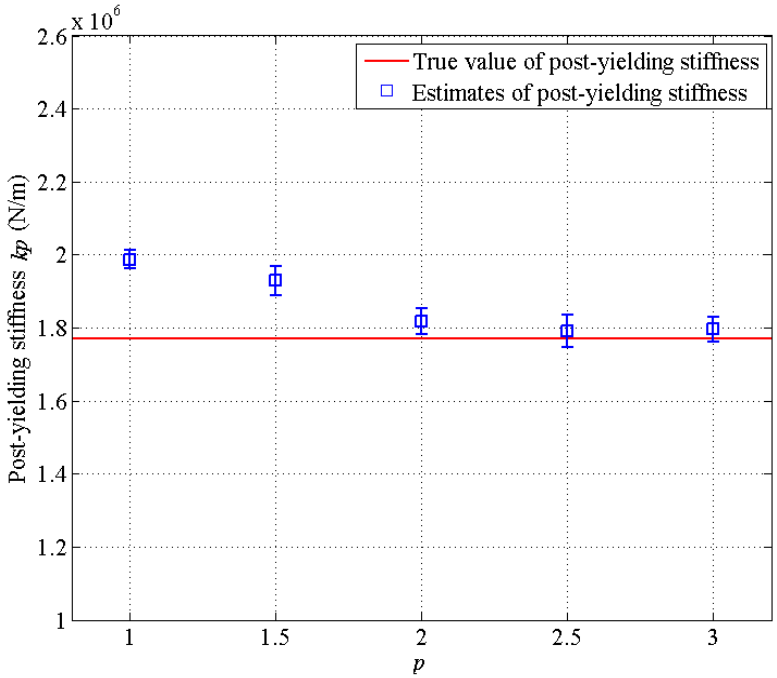

Figure 3.18: Effect of p on the identified post-yielding stiffness. The error bars show mean and one standard deviation over all half cycles.

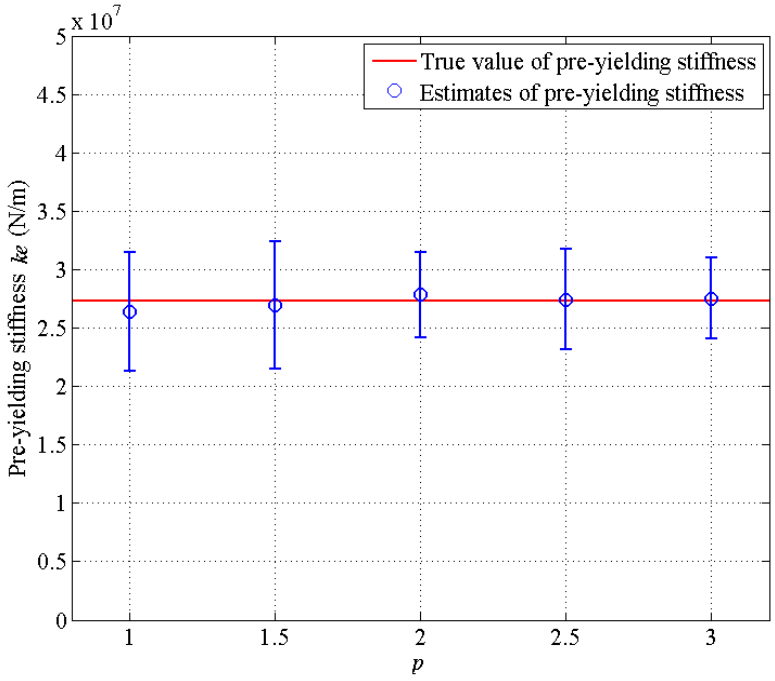

Figure 3.19: Effect of p on the identified pre-yielding stiffness. The error bars show mean and one standard deviation over all half cycles.

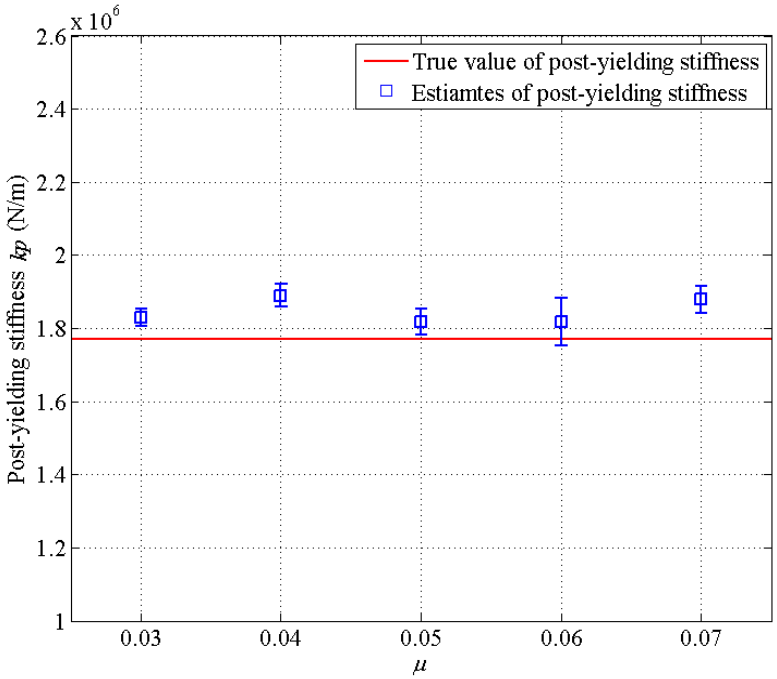

Figure 3.20: Effect of μ on the identified post-yielding stiffness. The error bars show mean and one standard deviation over all half cycles.

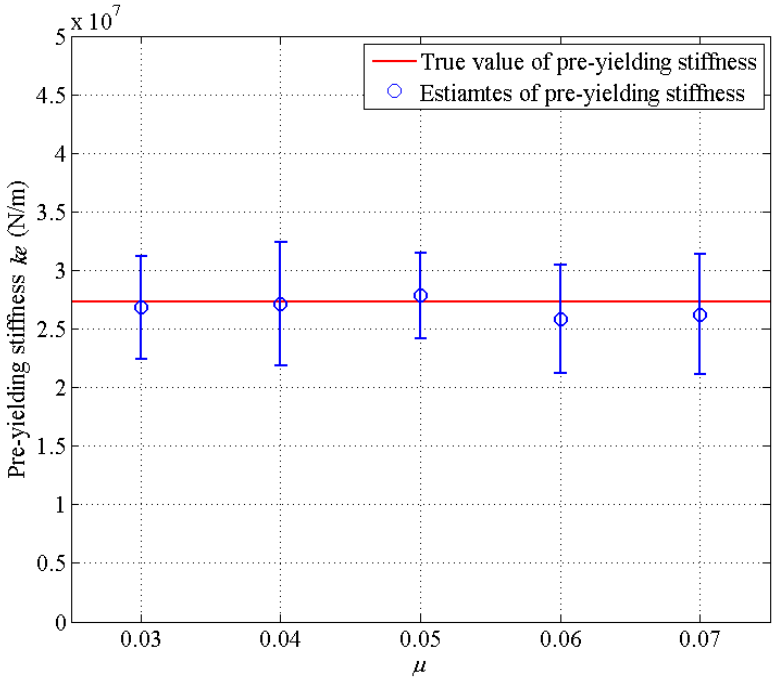

Figure 3.21: Effect of μ on the identified pre-yielding stiffness. The error bars show mean and one standard deviation over all half cycles.

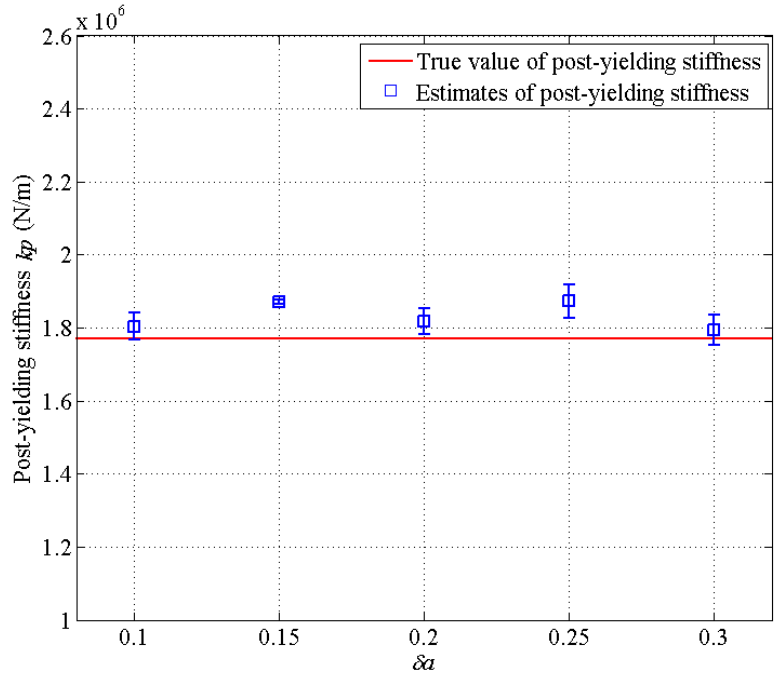

Figure 3.22: Effect of δ_a on the identified post-yielding stiffness. The error bars show mean and one standard deviation over all half cycles.

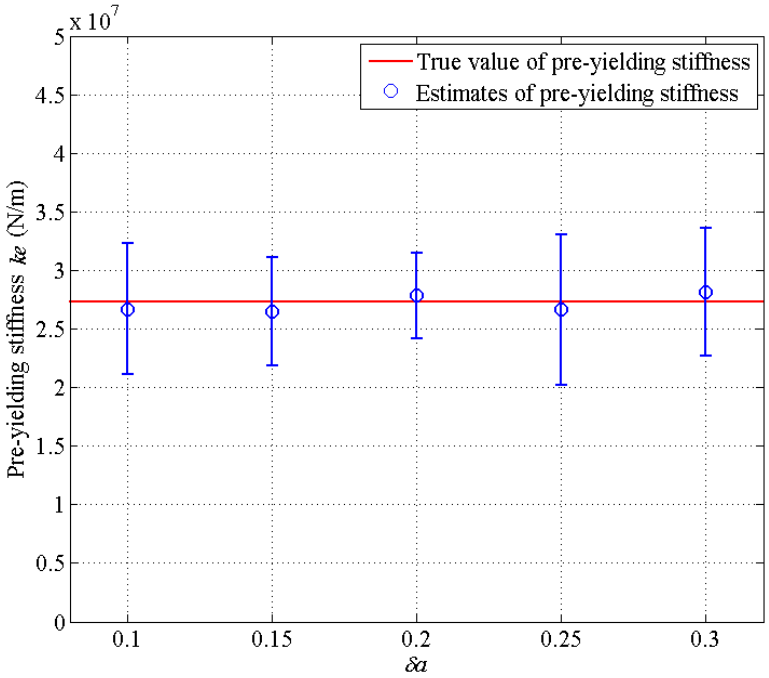

Figure 3.23: Effect of δ_a on the identified pre-yielding stiffness. The error bars show mean and one standard deviation over all half cycles.

Table 3.1 Effect of loop parameters on the identified cumulative plastic deformation.

Loop parameters		**Cumulative plastic deformation (mm)**	
		Estimates	**Error**
μ=0.05 δ_a=0.2	p=1.0	326	10.9%
	p=1.5	354	3.3%
	p=2.0	348	4.9%
	p=2.5	380	3.8%
	p=3.0	349	4.6%
p=2 δ_a=0.2	μ=0.03	378	3.2%
	μ=0.04	397	8.4%
	μ=0.05	348	4.9%
	μ=0.06	349	4.8%
	μ=0.07	337	8.0%
p=2 μ=0.05	δ_a=0.1	396	8.1%
	δ_a=0.15	352	3.8%
	δ_a=0.2	348	4.9%
	δ_a=0.25	330	9.8%
	δ_a=0.3	359	2.0%
True		366	

3.5.4 Effect of Measurement Noise Level

The 10% RMS noise was selected as a base noise level and added to measurements of ground acceleration, structural acceleration and displacement because it is considered to be a normal working range for civil engineering applications (Smyth and Wu, 2007), and big enough for good GPS sensor accuracy (Chan et al., 2006; Hann et al., 2009; Psimoulis and Stiros, 2008; Yi et al., 2013). However, the robustness of the proposed method to noise was also evaluated using high level noise compared with the base noise level with one set of loop parameters (p=2, δ_a=0.2, and μ=0.05), as shown in Table 3.2. It can be seen that the errors for k_e, k_p and Δd_p show a smaller increase with the increase of noise level, which indicate a low sensitivity to noise. Thus, the proposed identification method can yield robust estimates of pre-yielding stiffness k_e, post-yielding stiffness k_p and cumulative plastic deformation Δd_p even at 20% noise level.

Table 3.2 Effect of added RMS noise level on estimates.

Parameters	Noise level	Estimates	Error	True
k_e (kN/m)	10%	27.8	1.8%	27.3
	15%	28.5	4.4%	
	20%	29.7	8.7%	
k_p (kN/m)	10%	1.82	2.8%	1.77
	15%	1.91	7.9%	
	20%	1.89	6.8%	
Δd_p (mm)	10%	348	4.9%	366
	15%	334	8.7%	
	20%	327	10.7%	

3.5.5 Effect of Assumed Damping Ratio on the Estimates

The commonly adopted 5% damping ratio used by design codes and standards (Atkinson and Pierre, 2004; Chopra, 2001; Pekcan et al., 1999) was used to reconstruct the restoring force in the identification algorithm. However, the damping ratio is variable for different structures. Thus, the effect of structural damping ratio on the estimated parameters was investigated under 10% added RMS noise, as shown in Table 3.3. It can be seen that the estimates of the pre-yielding stiffness, k_e, are almost the same for different damping ratios, because the contribution of damping in the construction of restoring force is relatively very small during the elastic response. As the proportion of damping force in the total restoring force increases during the plastic response, the effect of different damping ratios on the estimates of k_p and Δd_p are relatively larger than for k_e. However, the estimation errors are no more than 10% as the damping force is still a relatively small part of the total restoring force.

Table 3.3 Effect of damping ratio on estimates.

Parameters	Damping ratio	Estimates	Error	True
k_e (kN/m)	3%	27.7	1.5%	27.3
	5%	27.8	1.8%	
	7%	27.9	2.2%	
k_p (kN/m)	3%	1.91	7.9%	1.77
	5%	1.82	2.8%	
	7%	1.65	6.7%	
Δd_p (mm)	3%	368	0.5%	366
	5%	348	4.9%	
	7%	331	9.6%	

Overall, the sensitivity analysis shows very good robustness of the method to a wide range of hysteresis loop shapes and noise. It thus also shows the ability to track the evolution of stiffness k_e and/or k_p as a simple indicator of potential damage if necessary to identify degradation or other changes over an event or long time periods. Thus, the method should be able robustly to track a wide range of nonlinear behaviours and to monitor their temporal changes as underlying behaviours change.

In addition, the method described for a SDOF system can be extended to a MODF system if the hysteresis loops are generated at each DOF. The overall method is also fully generable to different hysteretic structural models as the types of half cycles generated from different hysteresis loop are similar regardless of underlying mechanics. Hence, the method presented here is effectively general and significantly extends the results and method of Chapter 2.

3.6 Summary

This chapter develops a modified HLA method for the damage identification of a civil structure with nonlinear pinching behaviour from seismic response data. A general and nonlinear slip-lock pinching model was used to generate the pinching behaviour observed in civil structures, and a SDOF reinforced concrete structure was simulated for proof-of-concept with added RMS noise in measured acceleration and displacement records. The results show that the number of segments for the assumed piecewise linear model can be identified using an F type hypothesis test and the physical parameters of the structure were estimated by regression analysis for each identified half cycle. The pre-yielding stiffness and post-yielding stiffness were estimated accurately with the selection of two thresholds, and good estimates of cumulative plastic deformation can also be obtained without thresholds. In addition, the sensitivity analysis show that the identification method is robust to different pinching

behaviour and thus robust to evolution in response model parameters or degradation.

Finally, the method avoids constraint to a highly specific structural model, and are thus fully generalizable to more complex structures. It is also not a completely black box approach as it is implicitly based on fundamental underlying knowledge of structural mechanics and uses a far simpler computational method than GA's and many other nonparametric algorithms. Thus, it is computationally simple and can be implemented automatically without requiring human input, which ensure a rapid assessment to offer significant information about structural damage and safety after a seismic event.

Chapter 4: HLA-based Structural Health Monitoring of a 12-storey single-bay Reinforced Concrete Frame Building

4.1 Introduction

Seismic damage in a steel moment resistance frame (SMRF) structure is primarily due to excessive plastic or yielding deformations, as observed in field investigations of damaged steel buildings after the Northridge (Mahin, 1998; Malley, 1998) and Hyogo-ken Nanbu earthquakes (Tremblay et al., 1996), as well as many seismic laboratory tests of steel structures (Krawinkler and Zohrei, 1983; Nader and Astaneh, 1991; Sabelli et al., 2003; Stelmack et al., 1986; Yamanouchi et al., 1989). However, structural damage for reinforced concrete (RC) frame structures, which are also very common in seismic zones, is not always due to such easily observed yielding during an earthquake. In these RC cases, damage may be significantly caused by cracking of concrete and/or bonding slip of reinforcement that result in a pinching behaviour in the hysteresis loop and reduced energy dissipation. Thus, detecting plastic, nonlinear effects as quantitative damage indices, such as cumulative plastic deformation and cumulative dissipated hysteretic energy, is more useful for damage assessment of SMRF structures, but may be less useful for RC structures. A lack of indices that easily quantify these more variable or diffuse forms of damage make this task more difficult.

Storey stiffness is a good damage index in SHM, because stiffness in some floors will be reduced if damage occurs in those layers (Yoshimoto et al., 2005). In addition, stiffness degradation can reflect the severity of damage caused by both cumulative plastic deformation and cracking of concrete for RC structures (Maeck et al., 2000; Saatcioglu and Ozcebe, 1989;

Zhong et al., 2009). Further, no complex exponents are required to calculate the damage index of story stiffness. Therefore, many SHM methods, such as least squares estimation (Lin et al., 1990; Yang et al., 2007), extended Kalman filter (Jeen-Shang and Yigong, 1994; Yang et al., 2006; Zhang et al., 2002), and adaptive least mean squares (Chase et al., 2005a; Chase et al., 2005b; Nayyerloo et al., 2011), have been developed to track the variation of an elastic or secant stiffness of baseline model parameters to identify damage during earthquakes. However, these methods are sensitive to the addition of noise in the measured response and not as effective for highly nonlinear structures, especially with complex hysteretic behaviour. In addition, the accuracy and convergence of the estimation can typically depend on the quality of the initial guesses of unknown parameters. Thus, there are still significant limitations in all these methods that limit realistic nonlinear monitoring immediately after the earthquake. Finally, and most critically, none of them have been tested for RC structures with both low and high level events to see if they can detect and localize damage that may not be visible, or observable in overall structural response or modal properties.

The ability to detect damage that is not visible is critical as many structures may be subject to many "small" events before a major event. The resulting damage after a major event is thus likely to be great due to initial damage. Pragmatically, all the major Christchurch events had two or more events at one time (GeoNet). Hence, the ability to detect highly nonlinear and variable damage across events is critical, for RC structures in particular, and an aspect that has not yet been directly tested in SHM.

In Chapter 3, a HLA method was proposed for parameter identification of a SDOF pinching system using reconstructed hysteresis loop. The method showed the ability to track the variation of story stiffness automatically if degradation occurs during an earthquake and is

fully generalizable so it can be readily generalized to MDOF systems with different hysteretic behaviours. Thus, in this chapter, the identification algorithm is applied to an experimental, scaled 12-storey single-bay RC frame building subjected to low and high intensity shaking table tests to experimentally demonstrate the feasibility and robustness of this method for highly nonlinear response across multiple events. Severity assessment and localization of structural damage are achieved by tracking changes in elastic storey stiffness as a damage index over time for RC structures, and validated against experimental measurements and observations.

4.2 Test Structure and Tests

The shaking table test was conducted on a 1:10 scaled structural model of a 12-storey single-bay RC frame building, as shown in Figure 4.1 (Lu and Li, 2004). The plan dimension of the building is 600×600mm. Each storey consist of a 12 mm thick floor slab and the storey height is 300mm. Thus, the total height of the structure is 3600mm excluding a 200mm high rigid base. All the columns have a constant cross section of 50×60mm, and the beams have the same cross section of 30×60mm. Figure 4.1(b) shows the elevation and main dimensions of the test structure.

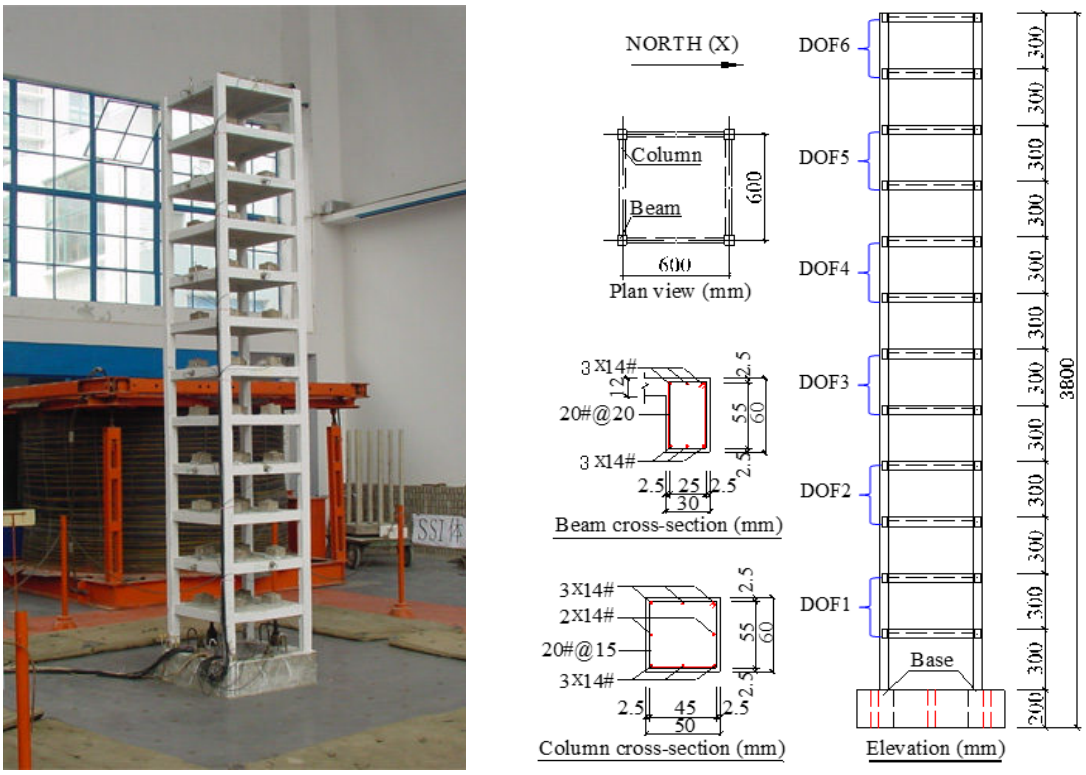

(a) (b)

Figure 4.1: (a) Photo of shaking table test of RC frame model, and (b) Elevation of the testing RC frame model.

The seismic weight of each floor for this test structure is 29.8kg, including artificial mass. The lateral stiffness *k* for each storey of the frame structure can be computed using the static condensation method. In particular, the stiffness matrix is formulated with 3-DOFs for the first storey and 5-DOFs for the other storeys of the structure, as shown in Figure 4.2.

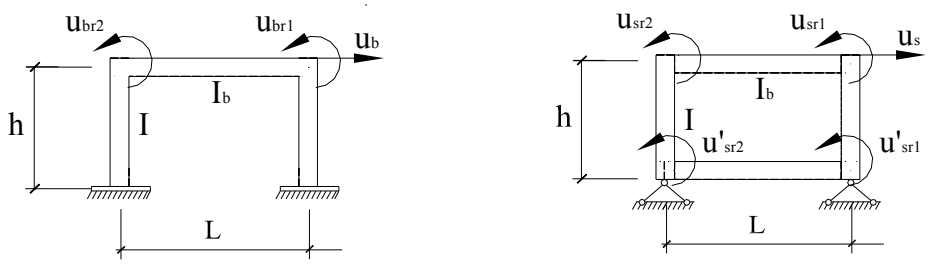

(a) (b)

Figure 4.2: Degree of freedom for (a) the first story and (b) the other stories.

Equilibrium equations can be written for the first and other storeys:

$$\begin{bmatrix} \frac{24EI}{h^3} & A_1 \\ A_1^T & A_2 \end{bmatrix} \begin{bmatrix} u_b \\ u_{br} \end{bmatrix} = \begin{bmatrix} f_b \\ \mathbf{0}_{2\times1} \end{bmatrix} \tag{4.1}$$

$$\begin{bmatrix} \frac{24EI}{h^3} & A_1 & A_1 \\ A_1^T & A_2 & A_3 \\ A_1^T & A_3 & A_2 \end{bmatrix} \begin{bmatrix} u_s \\ u_{sr} \\ u'_{sr} \end{bmatrix} = \begin{bmatrix} f_s \\ \mathbf{0}_{2\times1} \\ \mathbf{0}_{2\times1} \end{bmatrix} \tag{4.2}$$

$$A_1 = \frac{6EI}{h^2}\begin{bmatrix} 1 & 1 \end{bmatrix} \quad A_2 = \begin{bmatrix} \frac{4EI}{h} + \frac{4EI_b}{L} & \frac{2EI_b}{L} \\ \frac{2EI_b}{L} & \frac{4EI}{h} + \frac{4EI_b}{L} \end{bmatrix} \quad A_3 = \frac{2EI}{h}\begin{bmatrix} 1 & 0 \\ 0 & 1 \end{bmatrix} \tag{4.3}$$

Thus, the lateral stiffness k_b and k_s for the first and other storeys are determined by eliminating the rotational DOFs in Equations (4.1) and (4.2):

$$k_b = \frac{f_b}{u_b} = \frac{24EI}{h^3} - A_1 A_2^{-1} A_1^T \tag{4.4}$$

$$k_s = \frac{f_s}{u_s} = \frac{24EI}{h^3} - \begin{bmatrix} A_1 & A_1 \end{bmatrix} \begin{bmatrix} A_2 & A_3 \\ A_3 & A_2 \end{bmatrix}^{-1} \begin{bmatrix} A_1 & A_1 \end{bmatrix}^T \tag{4.5}$$

Two stages of input ground motions based on the Shanghai artificial wave (SHW) were applied in the uniaxial direction (*X* direction), denoted as SHW1 and SHW2. The peak ground accelerations (PGA) are scaled to 0.09g for SHW1 and 0.258g for SHW2. Figure 4.3 shows the time histories of the scaled input ground motions. The low and high intensity motions capture the possibility of unseen or unobserved, local damage becoming worse in a subsequent large event. The accelerations of the test building were recorded in the shaking *X* direction at the base and every two levels, at a sampling rate of 250Hz. Measured accelerations thus include the 2nd, 4th, 6th, 8th, 10th and 12th (top) floor.

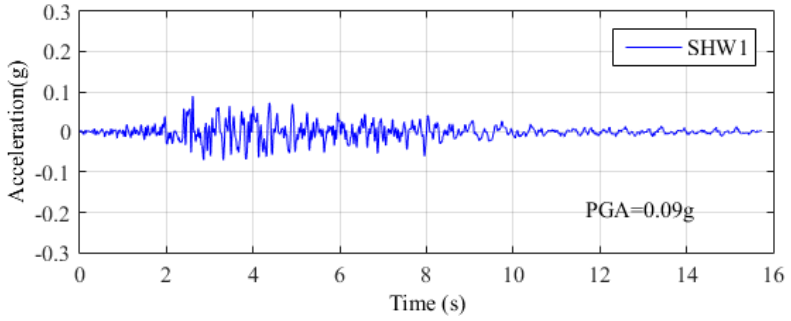

(a) SHW1

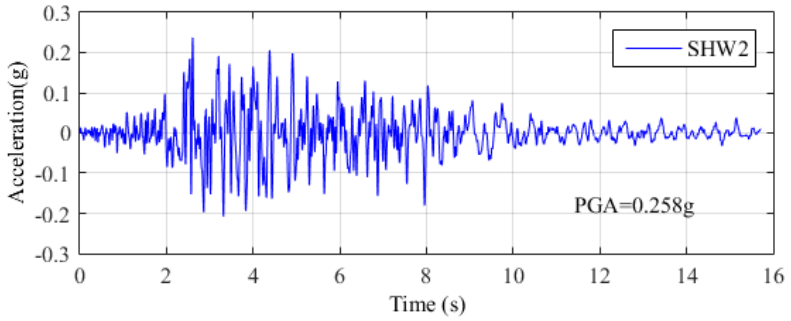

(b) SHW2

Figure 4.3: Time histories of scaled input ground motion (a) SHW1 and (b) SHW2.

4.3 Analysis

4.3.1 Reduction of Degrees of Freedom for the Test Structure

To reconstruct a hysteresis loop for a storey, the measured response at each DOF is required. Therefore, the test structure is reduced to a six degree of freedom system with the accelerations of each DOF recorded. The reduction of degree of freedom is justified based on the fact that the response of the test structure is dominated by the fundamental mode and because the deformations for all recorded levels are of same sign (Chopra, 2001), as shown in Figure 4.4.

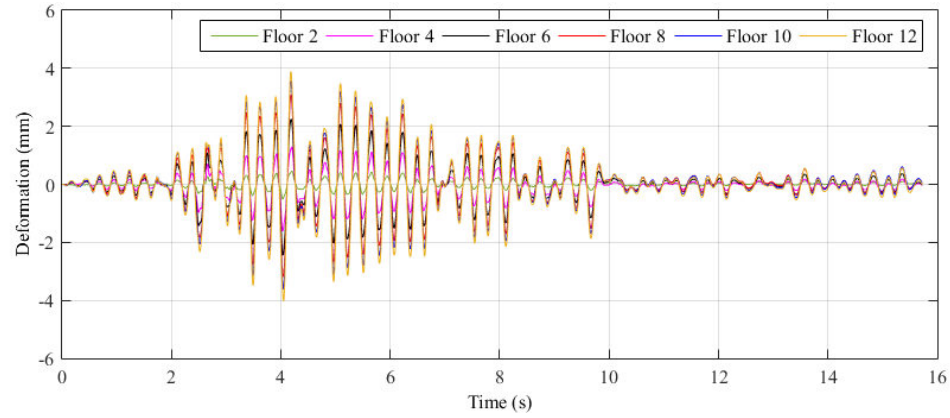

(a) SHW1

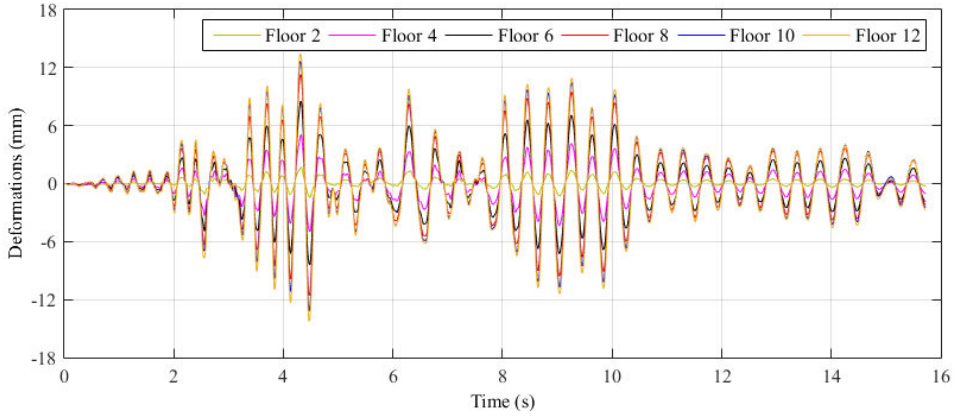

(b) SHW2

Figure 4.4: Time histories of deformations for all levels under (a) SHW1 and (b) SHW2.

In particular, each two levels can be approximately modelled as a two DOF system, and then an equivalent single DOF model with an equivalent mass and stiffness can be calculated to represent the two DOF system, as shown in Figure 4.5. These equivalent calculated stiffnesses can be used to compare the initial HLA identified values.

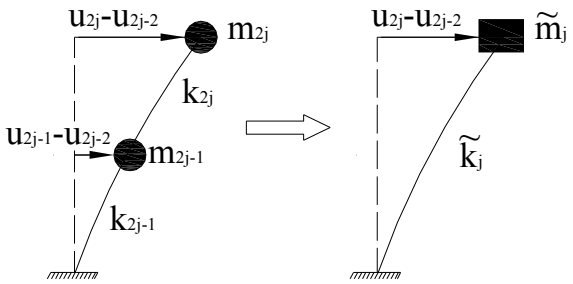

Figure 4.5: Equivalent single DOF model for each two levels.

Therefore, the equivalent stiffness for each reduced DOF can be calculated:

$$\widetilde{k}_j = \frac{k_{2j-1}k_{2j}}{k_{2j-1}+k_{2j}} \tag{4.6}$$

The equivalent mass can be calculated using the principle of virtual work. In particular, at each time interval $h=t_{i+1}-t_i$, the acceleration is defined:

$$\overline{\ddot{u}}_{2j}(i,i+1) = \frac{\ddot{u}_{2j}(i)+\ddot{u}_{2j}(i+1)}{2} \quad \overline{\ddot{u}}_{g}(i,i+1) = \frac{\ddot{u}_{g}(i)+\ddot{u}_{g}(i+1)}{2} \tag{4.7}$$

The displacement increment at each time step is obtained:

$$\Delta u_{2j}(i,i+1) = u_{2j}(i+1) - u_{2j}(i) \tag{4.8}$$

Thus, the virtual work done by the external forces for the 2-DOF system can be determined:

$$\Delta W_i = m(\overline{\ddot{u}}_{2j}(i,i+1)+\overline{\ddot{u}}_{g}(i,i+1))\Delta u_{2j}(i,i+1) + m(\overline{\ddot{u}}_{2j-1}(i,i+1)+\overline{\ddot{u}}_{g}(i,i+1))\Delta u_{2j-1}(i,i+1) \tag{4.9}$$

Similarly, the virtual work done by the external forces for the equivalent single DOF system is given:

$$\Delta \widetilde{W}_i = \widetilde{m}(\overline{\ddot{u}}_{2j}(i,i+1)+\overline{\ddot{u}}_{g}(i,i+1))\Delta u_{2j}(i,i+1) \tag{4.10}$$

The sum of virtual work done by external forces in the two systems during the given excitation should be equal, yielding:

$$\sum_{i=1}^{n-1}\Delta W_i = \sum_{i=1}^{n-1}\Delta \widetilde{W}_i \tag{4.11}$$

Because the structural behaviour is dominated by the first mode, the structural displacement, velocities and accelerations can be approximated:

$$U \approx \Phi_1 q \quad \dot{U} \approx \Phi_1 \dot{q} \quad \ddot{U} \approx \Phi_1 \ddot{q} \tag{4.12}$$

where q is the modal coordinate, and Φ_1 is the first mode shape vector:

$$\Phi_1 = \begin{bmatrix} \phi_1 & \phi_2 & \cdots & \phi_{2j-1} & \phi_{2j} & \cdots & \phi_{11} & \phi_{12} \end{bmatrix}^{\mathrm{T}} \tag{4.13}$$

Therefore, the response in the 2*j*-2, 2*j*-1 and 2*j* level can be expressed in terms of Φ_1 using:

$$\frac{\Delta u_{2j-1} - \Delta u_{2j-2}}{\Delta u_{2j} - \Delta u_{2j-2}} = \frac{\phi_{2j-1} - \phi_{2j-2}}{\phi_{2j} - \phi_{2j-2}} = \gamma_j \tag{4.14}$$

$$\frac{\ddot{u}_{2j-1} - \ddot{u}_{2j-2}}{\ddot{u}_{2j} - \ddot{u}_{2j-2}} = \frac{\phi_{2j-1} - \phi_{2j-2}}{\phi_{2j} - \phi_{2j-2}} = \gamma_j \tag{4.15}$$

Substituting Equations (4.9)-(4.10) and (4.14)-(4.15) into Equation (4.11), the equivalent mass of the single DOF system covering two physical levels can be obtained:

$$\tilde{m}_j = m\left(1 + \frac{\sum_{i=1}^{n-1} (\gamma_j \ddot{\bar{u}}_{2j} + (1-\gamma_j)\ddot{\bar{u}}_{2j-2} + \ddot{\bar{u}}_g)(\gamma_j \Delta u_{2j} + (1-\gamma_j)\Delta u_{2j-2})}{\sum_{i=1}^{n-1} (\ddot{\bar{u}}_{2j} + \ddot{\bar{u}}_g)\Delta u_{2j}}\right) \tag{4.16}$$

It is noted that it is not necessarily needed to simplify the monitored structure into a reduced degree of freedom system by calculating the equivalent mass, if the accelerations of each floor are measured. In that case, the hysteresis loops can simply be reconstructed at each floor for the implementation of the identification algorithm. However, to obtain an accurate input force for the HLA method requires an equivalent mass when not all storeys are measured.

4.3.2 Reconstruction of the Hysteresis loops

To reconstruct the hysteresis loop for each reduced DOF, the equation of motion for the inelastic system subjected to earthquake excitation can be expressed:

$$F = -\tilde{M} I \ddot{x}_g - \tilde{M}\ddot{X} - C\dot{X} \tag{4.17}$$

where $\tilde{M}$ is the equivalent mass matrix. A 5% damping ratio is typically used by design codes and standards for the calculation of classical damping matrix *C* if similar material and

damping mechanism are distributed over the height (Atkinson and Pierre, 2004; Chopra, 2001; Pekcan et al., 1999). In addition, the half-power bandwidth approach is also commonly used in practice to evaluate the viscous damping ratios both in the field and laboratory (Olmos and Roesset, 2010), by finding two frequencies f_a and f_b that are equal to square root of 2 of the frequency f_p at which the maximum amplitude of the response occurs. The formula for the calculation of damping ratio is then expressed:

$$\zeta^2 = \frac{1-\beta''}{2} \tag{4.18}$$

where:

$$\beta'' = \frac{1+1/\beta'}{2}; \quad \beta' = 1+16\beta^2; \quad \beta = \frac{f_b^2 - f_a^2}{4f_p^2} \tag{4.19}$$

The restoring force vector F in Equation (4.17) is defined for j=1, 2, 3, …, N=6:

$$F_j = \begin{cases} f_j - f_{j+1} & 1 \le j \le N-1 \\ f_j & j = N \end{cases} \tag{4.20}$$

where f_j is the restoring force between the j^{th} and $(j\text{-}1)^{th}$ DOF. Combining Equations (4.17) and (4.20), f_j can be written:

$$f_j = \sum_{i=j}^{N} F_i = \sum_{i=j}^{N} (-\tilde{m}_i \ddot{x}_g - \tilde{m}_i \ddot{x}_i - [C\dot{X}]_i), \qquad N = 6 \tag{4.21}$$

The accelerations for the ground motion $\ddot{x}_g$ and each reduced DOF $\ddot{x}_i$ were measured during the test. The displacements and velocities are obtained by direct integration of measured accelerations after a band pass filtering with a cut-off frequency of 0.5-20Hz to eliminate low and high frequency noise (Boroschek et al., 2003; Chaudhary et al., 2000; Ji et al., 2010; Masri et al., 2004; Sridhar et al., 2014).

Finally, the equivalent mass for each DOF is calculated using Equation (4.16) and listed in Table 4.1. It can be seen that the calculated equivalent mass matches very well between SHW1 and SHW2 with the largest difference only 0.39%. This small difference implies the motions of the test structure under these two events are both in the fundamental deflection mode as indicated in Figure 4.4.

In addition, the calculated equivalent mass for both levels of ground motion is increasing from the base to the top DOF, because the relative displacement between each storey increases with height in the fundamental mode of vibration for this particular structure. Although the equivalent mass was calculated in this case, the mass matrix M in Equation (4.17) for the reconstruction of hysteresis loops can be simply obtained using the mass of each storey without modal analysis if measurements are available at each storey.

Table 4.1 Calculated equivalent mass under SHW1 and SHW2

DOF	SHW1(kg)	SHW2(kg)	Difference (%)
1	30.95	30.95	0.00
2	50.09	49.97	0.24
3	54.86	54.88	0.04
4	57.48	57.57	0.16
5	58.89	59.12	0.39
6	59.21	59.31	0.17

Hence, the hysteresis loops representing the load-deformation relationship for the j^{th} DOF are finally reconstructed using the calculated restoring force f_j from Equation (4.21) and the relative deformation (x_j-x_{j-1}) obtained from the measured accelerations. Figure 4.6 shows the

reconstructed hysteresis loops for each of the 6 reduced DOF under SHW1 and SHW2. It is clear that as PGA increases significantly between the two events, the structural response goes from linear to highly nonlinear, particularly in the second, third and fourth reduced DOF. Significant pinching behaviour and stiffness degradation occurred in these DOFs for the SHW2 event, which indicates a significant cracking damage in the related floors.

Dividing the hysteresis loops into a number of half cycles in chronological order using the turning points where the deformation is local maximum or minimum, the changes of the stiffness and structural nonlinearity in response to strong ground motions can be extracted from the significant half cycles for damage detection and severity assessment. Figure 4.7 shows four of the degrading half cycles (cycles 1-4) of the second DOF. It is clearly shown that the slopes of the elastic segments ($k1$, $k2$, $k3$, $k4$) of cycles 1-4 are decreasing as structural damage accumulates, which also enlarges the pinching range in the dynamic response.

To quantify the degrees of damage, the number of segments of each of the half cycles is first identified using the proposed HLA method from Chapter 3. Regression analysis is then applied to the elastic segment of the identified half cycle, and the elastic stiffness is used as a damage index and tracked over time by calculating the slope value of this elastic segment. Note that any and all other measures noted in Chapters 2-3 might also be used.

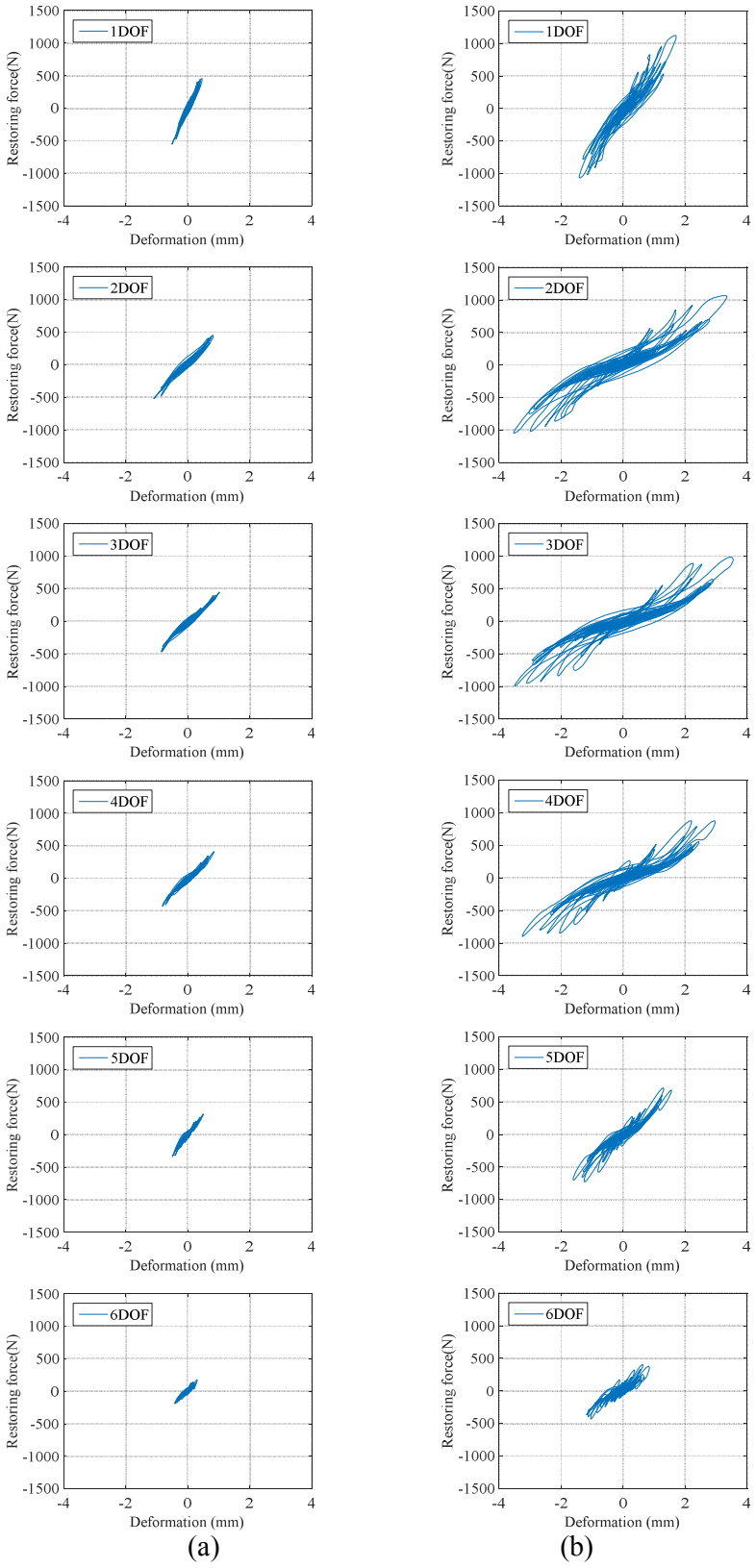

Figure 4.6: Reconstructed hysteresis loop for each DOF=1 (top) to 6 (bottom) under column (a) SHW1 and (b) SHW2.

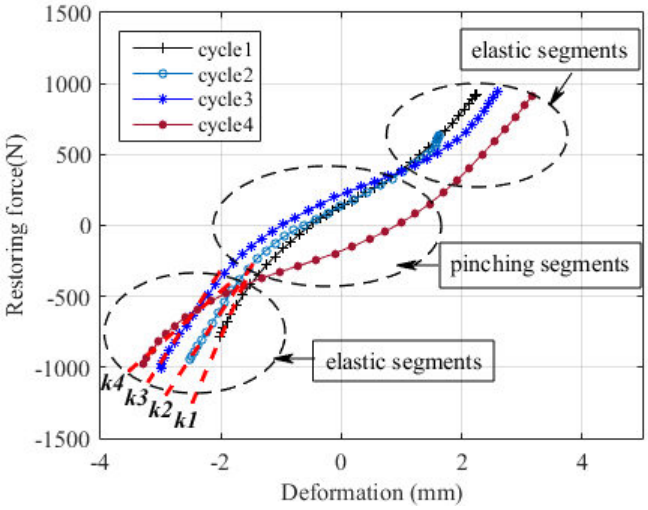

Figure 4.7: Degrading half cycles for the second DOF during SHW2.

4.4 SHM Results for the Experimental RC Structure

4.4.1 Results for SHW1

The identification algorithm was first applied to the six hysteresis loops under the SHW1 event as shown in the six Figures 4.6(a). The separated half cycles of each loop were approximated using piecewise regression models with the identified number of segments. The measured output restoring force obtained from the recorded data is plotted against the estimated model output in Figures 4.8(a) for comparison of the regression accuracy using the identified segment models. Figures 4.8 (b) show the estimation error between the measured and model output. It can be seen that the estimated model outputs of all six degrees of freedom fit very well with the measured data, which indicates the identified piecewise regression models accurately estimated the force-deflection relationships (hysteresis loops) of each degree of freedom of the building. Therefore, the slope of the elastic segment of the selected half cycles can be used to represent the elastic stiffness of the structure for damage identification during earthquake excitations.

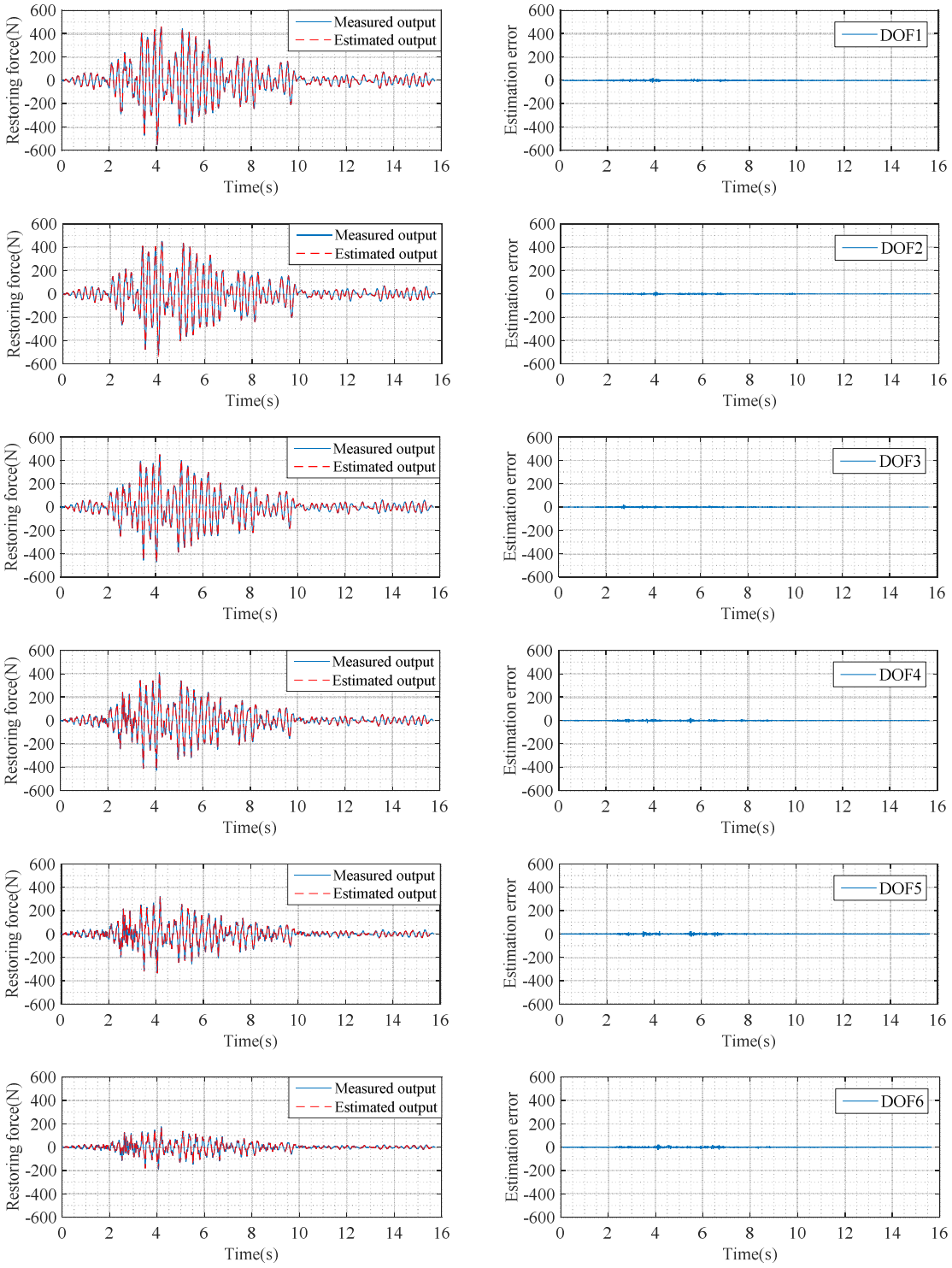

Figure 4.8: Force response under SHW1: (a) comparison of measured and estimated force output, (b) estimation error.

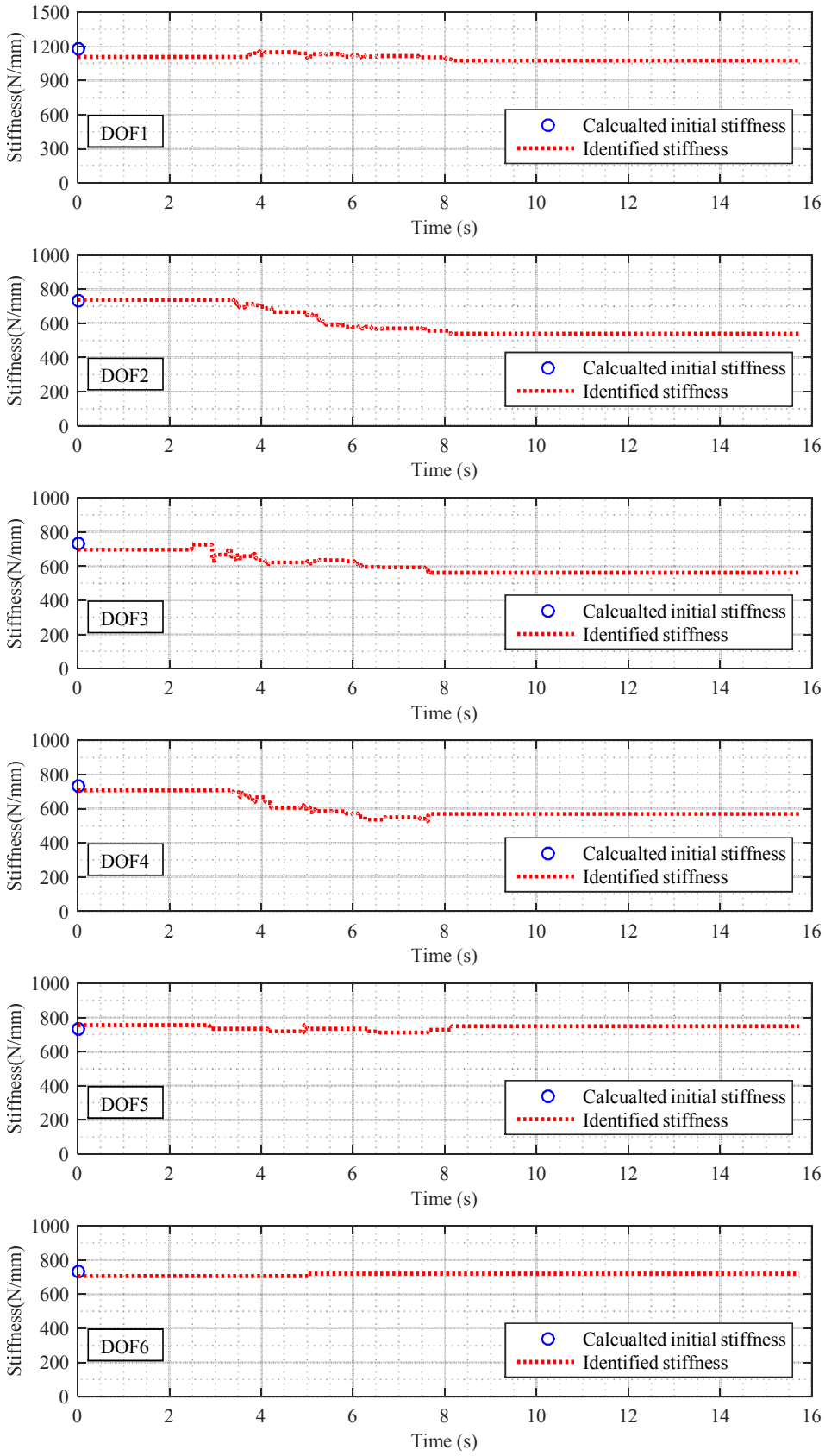

Figure 4.9: Identified evolution of elastic storey stiffness of each DOF under SHW1.

Figures 4.9 show the identified evolution of the elastic stiffness of each DOF under the SHW1 event. The calculated initial stiffness in Figure 4.9 is the initial stiffness of the equivalent DOF before the test and is obtained using Equations (4.1)-(4.6). Table 4.2 lists the comparison of the calculated and identified initial stiffness of each DOF under the SHW1 event. It can be seen that the identified initial stiffness matches well with the calculated stiffness before the test and the largest initial estimation error is 5.7%. This result indicates the test structure was accurately represented using the proposed equivalent six DOF system with the equivalent mass estimated using Equation (4.16). It also shows the accuracy of the algorithm on a completely linear response.

Table 4.2 Comparison of the identified and calculated initial stiffness of SHW1

DOF	Identified (N/mm)	Calculated (N/mm)	Difference
1	1108	1175	-5.7%
2	736	730	+0.8%
3	696		-4.7%
4	708		-3.0%
5	755		+3.4%
6	706		-3.3%

From the evolution of the stiffness in Figure 4.9, it can be seen that no significant stiffness degradation is identified for the first, fifth and sixth DOF (DOF1, DOF5 and DOF6). These results indicate that these floors were behaving within a totally elastic response without damage when subject to the SHW1 event. However, linear stiffness for the second, third and fourth DOF (DOF2, DOF3 and DOF4) dropped 24%, 23% and 21% compared to the initial stiffness after SHW1, respectively. These changes occur between 3~6 seconds in Figure 4.9, which corresponds to the stronger motion period of SHW1 in Figure 4.3, providing a further qualitative validation.

Visual detection was implemented to the test building, but no cracks were observed after SHW1 (Lu and Li, 2004). However, slight pinching behaviour, caused by opening or closing cracks of concrete (Foliente and Noori, 1996), were observed from the significant half cycles of these DOFs, such as cycle-1 and cycle-2 for DOF2 shown in Figure 4.10. It is clearly shown that the hysteretic pinching behaviour occurred during these two half cycles, and cause a decrease in stiffness in this pinching area, as well as the stiffness degradation in the elastic segment. Thus, the structural elements of these floors could have experienced micro cracking or reinforcement slip during the SHW1 event, though they were not significantly damaged by external visual appearance. Hence, the method has detected what is visually clear in Figures 4.6 (a) and 4.10, and has quantified and localized this damage that was not evident by visual detection.

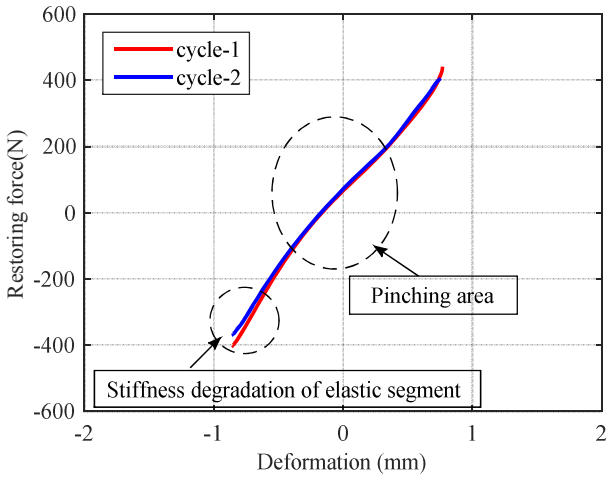

Figure 4.10: Pinching behaviour for the second DOF during SHW1.

4.4.2 Results for the SHW2 Event (Damage Cracking Observed)

SHW2 is much stronger than SHW1. Therefore, significant pinching behaviour was observed from the hysteresis loops of all the DOFs, as shown in Figures 4.6(b). Figure 4.11 compares

the force response output for the hysteresis loops under SHW2. Again, the model output shows very good agreement with the measured data of all six DOFs of the building subjected to the strong event SHW2.

Figure 4.12 shows the evolution of the identified elastic stiffness for each DOF during the SHW2 event. Note the final stiffness of SHW1 in Figure 4.12 refers to the identified final stiffness of each DOF in Figure 4.9. It can be seen that the identified initial stiffnesses of SHW2 match well with the identified final stiffnesses of SHW1 with the identification difference within 7.5%, as listed in Table 4.3. These results should be expected for a good SHM method, and thus help validate the method and its continuity over different events. In addition, both the identified initial stiffnesses of SHW2 and the identified final stiffnesses of SHW1 for the first, fifth and sixth DOF (DOF1, DOF5 and DOF6) match well with the calculated initial stiffnesses before the SHW1 event, which also validate the lack of stiffness degradation seen for these DOF during the SHW1 event.

Table 4.3 Comparison between the identified initial stiffness of SHW2 and the identified final stiffness of SHW1

DOF	Identified initial stiffness of SHW2 (N/mm)	Identified final stiffness of SHW1 (N/mm)	Difference
1	1106	1090	+1.5%
2	566	556	+1.8%
3	604	562	+7.5%
4	608	571	+6.5%
5	775	748	+3.6%
6	728	720	+1.1%

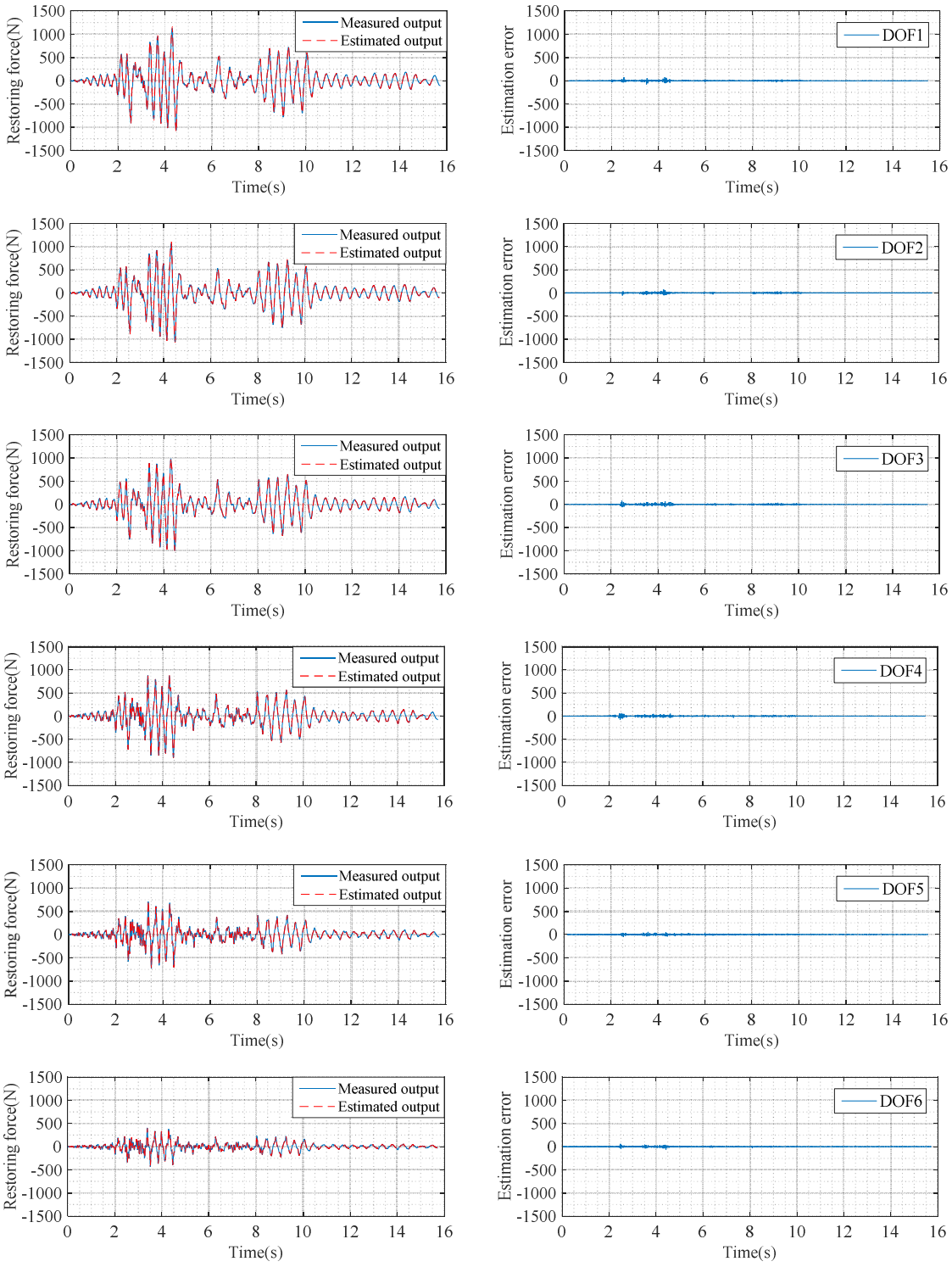

Figure 4.11: Force response under SHW2: (a) comparison of measured and estimated force output, (b) estimation error.

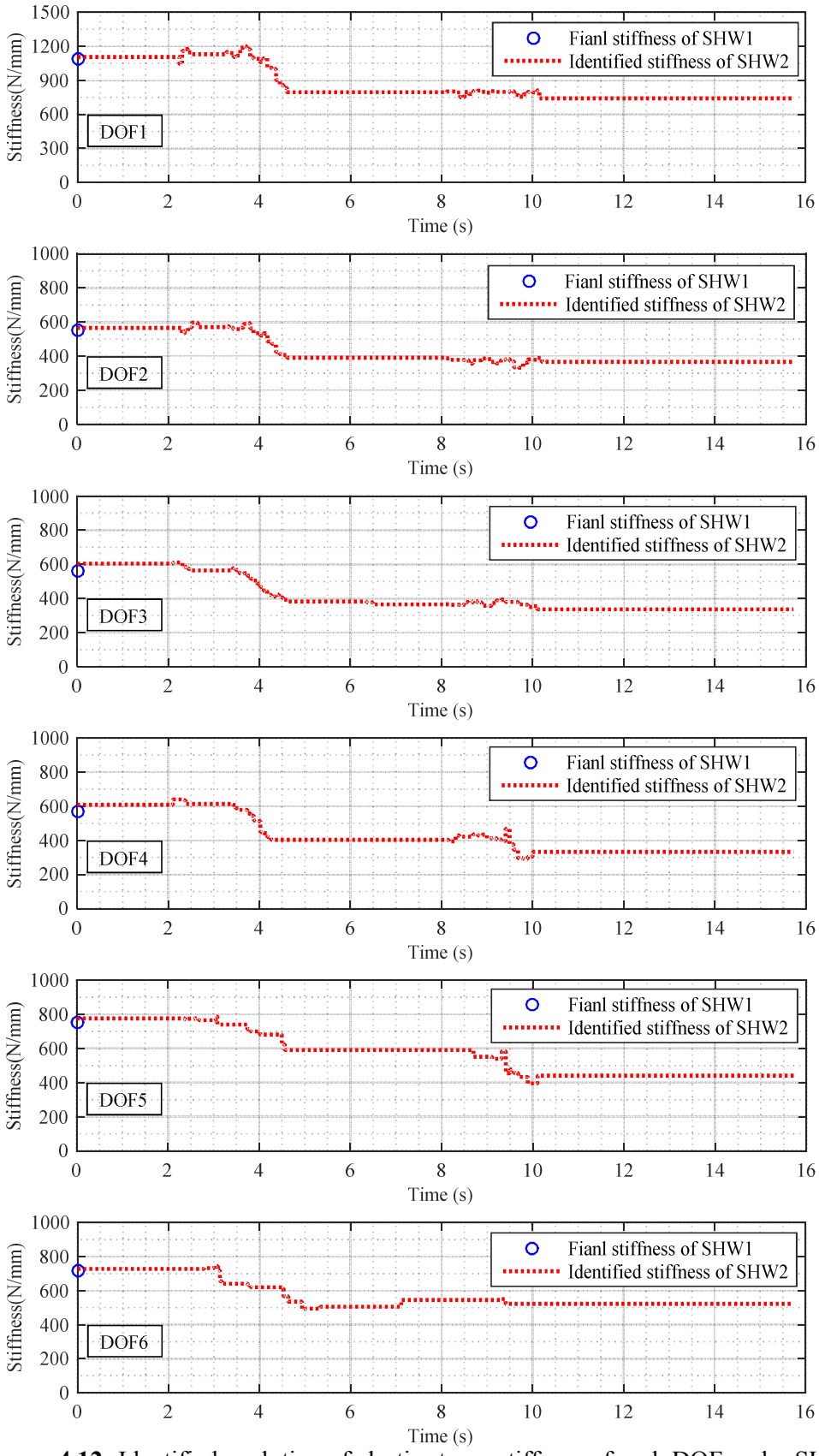

Figure 4.12: Identified evolution of elastic storey stiffness of each DOF under SHW2.

From Figure 4.12, it can be seen that significant stiffness degradation for the test building was identified for all the DOFs during the SHW2 event. In particular, the stiffness for the previously undamaged first, fifth and sixth DOF (DOF1, DOF5 and DOF6) dropped 35%, 37% and 27%, respectively, compared to initial value of calculated stiffness. In addition, the stiffness for the previously damaged second, third and fourth DOF (DOF2, DOF3 and DOF4) dropped 50%, 53%, and 54%, respectively, compared to the calculated initial stiffness before the test, and significantly further from the reduced value seen after SHW1. Again, this degradation occurred, as expected, in the stronger motion portion of the ground motion from 3~6 seconds.

Visual inspection after the SHW2 event showed vertical cracks were observed at the beam-column joint connection at floors 4, 5 and 6 (Lu and Li, 2004), which corresponds to the large drop of stiffness reported for the second, third and fourth reduced DOF (DOF2, DOF3 and DOF4), as shown in Figure 4.13. Therefore, the visual detected damage state of the test structure was successfully assessed by tracking the evolution of the structural elastic stiffness, and a large drop of the identified stiffness over 50% indicated a significant damage occurred to the structure.

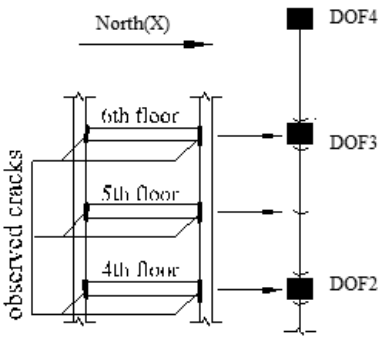

Figure 4.13: Observed vertical cracks at the beam-column connection at floors 4, 5 and 6 after the SHW2 event.

Stiffness degradation and damage of a RC structure are mainly caused by the inelastic yielding deformation and cracking of concrete resulting a pinching behaviour in the hysteresis loop. (Basu, 2005; Lee and Fenves, 1998; Powell and Allahabadi, 1988). Half cycles with both yielding and pinching behaviour were observed for the significantly damage second, third, and fourth reduced DOF (DOF2, DOF3 and DOF4) during the strong SHW2 event, as shown in Figure 4.14. However, the yielding deformation for these DOFs is relatively small, and not the main cause of the observed and identified stiffness degradation compared to the pinching behaviour due to concrete cracking during the SHW2 event.

In addition, structural degradation due to damage was also identified for DOF2, DOF3 and DOF4 during the small SHW1 event. However, yielding behaviour was not observed in the degrading half cycles of these DOFs, such as was shown in Figure 4.10. Thus, a simple method using a cumulative plastic deformation for damage estimation of RC structures ignores the fact that a significant portion or almost all of the damage can be caused by only the hysteretic pinching without yielding deformation occurring in the response. This result implies that changes in elastic structural stiffness could be a better damage index than the cumulative yielding deformation for reinforced concrete structures with hysteretic pinching for structural health monitoring.

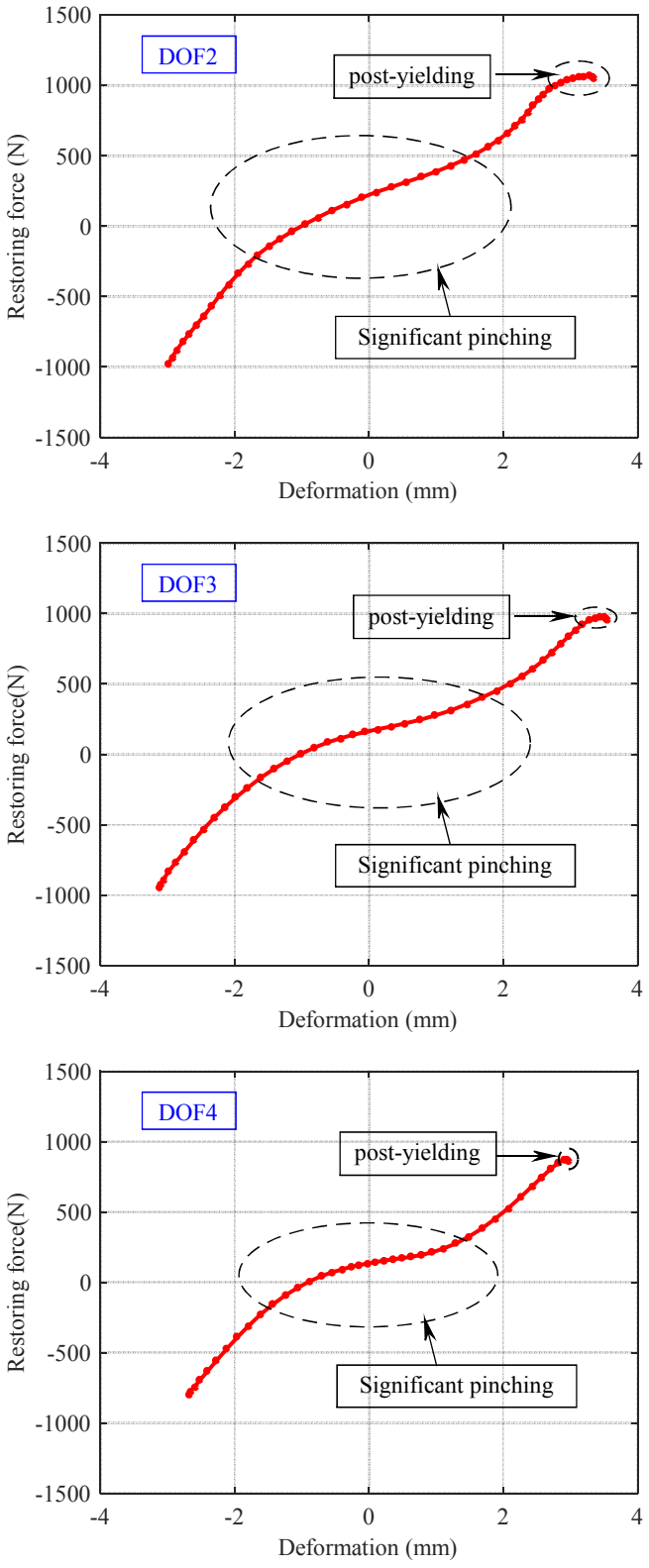

Figure 4.14: Identified half cycles with yielding and pinching deformation for the second, third and fourth DOF during the SHW2 event.

4.4.3 SHM results compared to the natural frequency analysis

Three identical low intensity white noise excitations WN1, WN2 and WN3 were applied to the test structure as input ground motions before the SHW1 event, after the SHW1 event (before SHW2) and after the SHW2 event, respectively. These tests provide an assessment based on examine the natural frequency of the test structure at each stage, and thus another measure against which to validate the results shown. The transfer functions amplitude of accelerations at each measured floor are plotted in Figure 4.15. Although the measures of natural frequencies for all the modes depend on the characteristics and locations of input and output, the variations of natural frequency before SHW1, after SHW1 and after SHW2 can be identified by the exhibited modes under the white noise excitation.

It is apparent that the fundamental natural frequency dominates the transfer functions for WN1, WN2 and WN3, as would be expected. Figures 4.15(a) and 4.15(b) show that the fundamental frequency after the SHW1 event (WN2) is reduced by 14% compared to WN1 before the SHW1 event. This reduction indicates the stiffness of the test structure has deteriorated during the SHW1 event. This result corresponds to the prior identification result that the test structure has experienced micro concrete cracking, but not significant damage during the SHW1 event with stiffness degradation over half the structure.

It can also be seen that the frequency after the SHW2 event (WN3) is 38% smaller than the frequency in WN2 before the SHW2 event. This result also coincides with the prior identification result that the test structure was much more significantly damaged during the SHW2 event. Hence, the qualitative assessment by modal analysis matches the results of the identification of elastic stiffness.

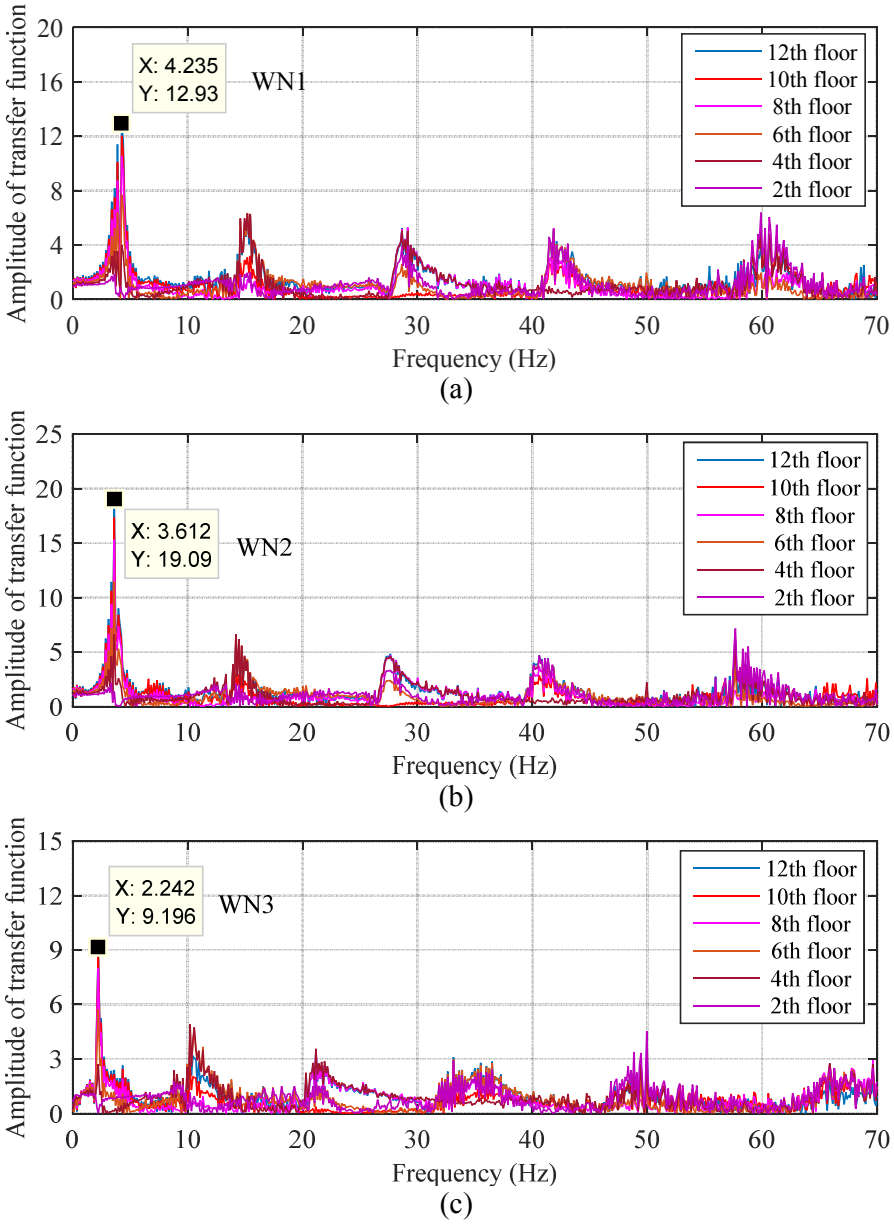

Figure 4.15: Amplitude of transfer functions of accelerations at each measured floor under (a) WN1 before the SHW1, (b).WN2 after the SHW1 and (c) WN3 after the SHW2

However, the changes of natural frequency between WN1 and WN2, as well as between WN2 and WN3 for all the measured floors are for the whole structure. Thus, the damage cannot be localized by detecting modal properties. In addition, the severity of damage is thus only generally identified to the whole test structure, but not specifically detected for each storey using this type of frequency-based analysis. Finally, the small changes before and after

the SHW1 event are close to some experimental errors and instantaneous variation of frequency in the field (Clinton et al., 2006), and do not necessarily capture the level of local damage found in this study. Therefore, the proposed identification method offers significant advantages and insight in detecting the location and severity of damage over any typical vibration-based methods, as discussed in Chapter 1.

4.5 Summary

In this chapter, the proposed HLA SHM algorithm was applied to a single-bay 12-storey scaled experimental reinforced concrete structure subjected to two sequentially small and large input ground motions, SHW1 and SHW2. The test structure was assessed to be within safe stage with slightly damage after the SHW1 event, because no stiffness degradation was identified for the first, fifth and sixth DOF, and less than 24% losses of stiffness were identified for the other DOFs without visual cracking damage observed. Significant damage was then identified during the SHW2 event for the second, third and fourth DOF with over 60% losses of stiffness, and visual vertical cracks were observed at the beam-column joint connections of the corresponding floors. The natural frequency in WN1 before the SHW1 event was also found to be 14% smaller than the frequency in WN2 after the SHW1 event, and much larger reduction of frequency by 38% was found between the WN2 before the SHW2 event and WN3 after the SHW2 event. The identification results between the proposed method and the natural frequency analysis show that the monitoring algorithm is capable of assessing the damage severity and location of the MDOF RC structure by tracking the evolution of the structural elastic stiffness of each DOF.

In addition, the differences between the identified initial stiffness and the calculated initial stiffness before the test are less than 5.7%. This outcome indicates the test structure can be

accurately represented using the equivalent six-DOF system dominated by the fundamental mode of vibration. For more complex structures, the method is fully generable to more DOF if the accelerations of each DOF are recorded. The identified initial stiffness before the SHW2 event also matches well with the identified final stiffness after the SHW1 event, which validates the continuity of the method over different event.

Finally, no yielding behaviour was observed for the slightly damaged floors during the SHW1 event. However, stiffness degradation was identified for these floors with pinching behaviour observed in the hysteresis loops. In addition, only small yielding deformations were found for these damage floors with significantly degradation of stiffness during the SHW2 event. These results imply that the damage and degradation to the test structure were mainly caused by the cracking of concrete rather than the structural yielding, and the storey stiffness could be a better damage index than the cumulative yielding deformation for the reinforced concrete structures with hysteretic pinching behaviour.

Chapter 5: Comparing the Model-free HLA method and Model-based Adaptive LMS Filters for Structural Health Monitoring

5.1 Introduction

Numerous structural health monitoring (SHM) techniques have been developed to detect seismic structural damage of civil infrastructure. As discussed in Chapter 1, many current SHM algorithms are based on a proposed baseline structural model and identify parameters, using least square estimation (Lin et al., 1990; Yang and Lin, 2004; Yang et al., 2007), H ∞ filters (Sato and Qi, 1998), extended Kalman filters (Jeen-Shang and Yigong, 1994; Yang et al., 2006; Zhang et al., 2002), unscented Kalman filters (Wu and Smyth, 2007; Wu and Smyth, 2008) and adaptive LMS filters (Chase et al., 2005a; Chase et al., 2005b). These model techniques can perform effectively when the numerical model is a suitable representation of the real system. However, they can produce erratic results when the model is not well defined, or for linear systems based methods, poorly linearized (Yao and Pakzad, 2014). Hence, if a good baseline model is unavailable, there is a significant, but unknown, risk of a poor identification result, since ground truth is not fully known, experimentally.

The HLA method presented in Chapters 2-3 and applied in Chapter 4 is implicitly based on fundamental underlying structural mechanics, and is not a black-box approach like neural networks or similar. It thus avoids the constraint of a single or fixed model as the model-based methods require, while identifying structurally relevant parameters. In this chapter, the performance of the proposed model-free HLA method is compared to a known model-based SHM algorithm to demonstrate the robustness and effectiveness of different algorithms in damage identification of MDOF structural systems with different hysteretic behaviours

during earthquakes.

The model-based SHM method for comparison is an adaptive LMS filter based algorithm directly identifying changes in structural stiffness due to damage or modelling error. The major advantages for the adaptive LMS-based filter are its noise resistance and computational efficiency (Ifeachor and Jervis, 2002), which is not necessarily the case for the Kalman filters and recursive least square methods. This model-based adaptive LMS algorithm has been used for a benchmark problem (Chase et al., 2005a) and also for a nonlinear experimental pre-cast rocking structure with response regimes changing rapidly during a large magnitude seismic event (Chase et al., 2005b). However, it has not been verified for more typical buildings, such as RC frame structures, which can experience highly nonlinear pinching behaviour during large earthquakes, as seen in Chapter 4.

In this chapter, the adaptive LMS filter algorithm is first applied to the 12-storey single-bay experimental structure presented in Chapter 4, and the SHM results between the adaptive LMS method and the HLA method are compared for linear and nonlinear response including hysteretic pinching. A calibrated numerical model yielding damage similar to the experimental structure is used to further validate the experimental SHM results against known true changes, and thus quantify the relative efficacy of the two different methods for RC structures. Finally, the algorithms are also tested using a simulated model representative of a steel moment resistance frame (SMRF) structure that has similar overall damage, but a simpler hysteretic behaviour typical of steel structures.

This last test assesses any error as a function of the mismatch between the model used for identification and the actual outcome and response. The method of Chase et al. (Chase et al.,

2005a; Chase et al., 2005b; Kuang et al., 2015) used a typical shear structure model frame work, which may not capture a RC structure perfectly, but better matches SMRF response. Hence, this analysis can quantify the impact of model mismatch on identification.

5.2 Adaptive LMS-based Filter Method

5.2.1 SHM Problem Definition

If major damage occurs in a structure from an earthquake, structural stiffness will change significantly over time. However, changes in mass are not likely to be significant. Changes in the damping matrix could occur slightly due to hysteresis, but can also be identified in hysteretic changes of stiffness. Thus, in this case, the simplest equation of motion for a damaged structure with *n* degrees-of-freedom can be defined:

$$\mathbf{M}\cdot\{\ddot{v}\}+\mathbf{C}\cdot\{\dot{v}\}+\left(\mathbf{K}+\Delta\mathbf{K}(t)\right)\cdot\{v\}=-\mathbf{M}\cdot\mathbf{I}\cdot\ddot{x}_g=\mathbf{F} \tag{5.1}$$

where **M**, **C** and **K** are the mass, damping and stiffness matrices, respectively. $\{v\}$, $\{\dot{v}\}$ and $\{\ddot{v}\}$ are the measured response of the damaged structure, and $\ddot{x}_g$ is the ground acceleration. The time-varying term $\Delta\mathbf{K}(t)$ represents the changes in stiffness and can be sub-divided into *n* matrices with time-varying scalar parameters α_i, to be identified using the adaptive LMS filter.

For the 6-DOF reduced system of the experimental structure of Chapter 4 in this case, $\Delta\mathbf{K}$ is divided into six matrices to allow independent identification of changes in effective stiffness of each DOF Δk_1, Δk_2, Δk_3, Δk_4, Δk_5, Δk_6:

$$\Delta\mathbf{K}=\alpha_1\Delta K_1+\alpha_2\Delta K_2+\alpha_3\Delta K_3+\alpha_4\Delta K_4+\alpha_5\Delta K_5+\alpha_6\Delta K_6 \tag{5.2}$$

where

$$\alpha_1 = \Delta k_1,\ \alpha_2 = \Delta k_2,\ \alpha_3 = \Delta k_3,\ \ \alpha_4 = \Delta k_4,\ \ \alpha_5 = \Delta k_5,\ \ \alpha_6 = \Delta k_6 \tag{5.3}$$

and the ΔK_i are defined for a typical shear structure:

$$\Delta K_1 = \begin{bmatrix} 1 & 0 & 0 & 0 & 0 & 0 \\ 0 & 0 & 0 & 0 & 0 & 0 \\ 0 & 0 & 0 & 0 & 0 & 0 \\ 0 & 0 & 0 & 0 & 0 & 0 \\ 0 & 0 & 0 & 0 & 0 & 0 \\ 0 & 0 & 0 & 0 & 0 & 0 \end{bmatrix} \quad \Delta K_2 = \begin{bmatrix} 1 & -1 & 0 & 0 & 0 & 0 \\ -1 & 1 & 0 & 0 & 0 & 0 \\ 0 & 0 & 0 & 0 & 0 & 0 \\ 0 & 0 & 0 & 0 & 0 & 0 \\ 0 & 0 & 0 & 0 & 0 & 0 \\ 0 & 0 & 0 & 0 & 0 & 0 \end{bmatrix} \quad \Delta K_3 = \begin{bmatrix} 0 & 0 & 0 & 0 & 0 & 0 \\ 0 & 1 & -1 & 0 & 0 & 0 \\ 0 & -1 & 1 & 0 & 0 & 0 \\ 0 & 0 & 0 & 0 & 0 & 0 \\ 0 & 0 & 0 & 0 & 0 & 0 \\ 0 & 0 & 0 & 0 & 0 & 0 \end{bmatrix}$$

$$\Delta K_4 = \begin{bmatrix} 0 & 0 & 0 & 0 & 0 & 0 \\ 0 & 0 & 0 & 0 & 0 & 0 \\ 0 & 0 & 1 & -1 & 0 & 0 \\ 0 & 0 & -1 & 1 & 0 & 0 \\ 0 & 0 & 0 & 0 & 0 & 0 \\ 0 & 0 & 0 & 0 & 0 & 0 \end{bmatrix} \quad \Delta K_5 = \begin{bmatrix} 0 & 0 & 0 & 0 & 0 & 0 \\ 0 & 0 & 0 & 0 & 0 & 0 \\ 0 & 0 & 0 & 0 & 0 & 0 \\ 0 & 0 & 0 & 1 & -1 & 0 \\ 0 & 0 & 0 & -1 & 1 & 0 \\ 0 & 0 & 0 & 0 & 0 & 0 \end{bmatrix} \quad \Delta K_6 = \begin{bmatrix} 0 & 0 & 0 & 0 & 0 & 0 \\ 0 & 0 & 0 & 0 & 0 & 0 \\ 0 & 0 & 0 & 0 & 0 & 0 \\ 0 & 0 & 0 & 0 & 0 & 0 \\ 0 & 0 & 0 & 0 & 1 & -1 \\ 0 & 0 & 0 & 0 & -1 & 1 \end{bmatrix}$$

(5.4)

Hence, Equation (5.1) can be rewritten:

$$\mathbf{M} \cdot \{\ddot{v}\} + \mathbf{C} \cdot \{\dot{v}\} + \mathbf{K} \cdot \{v\} + \sum_{i=1}^{6} \alpha_i \Delta K_i \{v\} = \mathbf{F} \tag{5.5}$$

Note Equation (5.5) is true only if the α_i have the correct values. Thus, the varying stiffness term at any discrete time k, is simply the error between the linear model and the actual measurements of the structure:

$$y_k = \sum_{i=1}^{6} \alpha_i \Delta K_i v_k = \mathbf{F}_k - \mathbf{M} \cdot \ddot{v}_k - \mathbf{C} \cdot \dot{v}_k - \mathbf{K} \cdot v_k \tag{5.6}$$

where $\mathbf{F}_k$ is the input load vector at time k, and v_k , $\dot{v}_k$ and $\ddot{v}_k$ are the measured displacement, velocity and acceleration at time k. Hence, the signal y_k represents the error of the linear model due to damage and/or nonlinear effects, and can be readily modelled using

an adaptive LMS filter so that the coefficients α_i can be readily determined form the reduced noise modelled signal at each time step.

5.2.2 Adaptive LMS-based Filter

An adaptive filter is a digital filter with coefficients that can change over time to improve its performance, allowing the filter to adapt to changes in the noisy input signal characteristics. Because of their self-adjusting performance and built-in flexibility, adaptive filters have found use of modelling signals in many applications, particularly if:

- It is necessary for the filter characteristics to be variable and algorithmically, adapted to changing conditions,
- There is spectral overlap between the signal and noise, or
- The band occupied by the noise is unknown or varies with time.

Adaptive filters can be used for adaptive noise cancelling, linear prediction and system modelling (Ifeachor and Jervis, 2002). In this case, the adaptive filter is used as a system modeller to identify the individual scalar elements α_i of the signal y_k in Equation (5.6). Figure 5.1 shows the process of this system modelling filter (Blome, 2004).

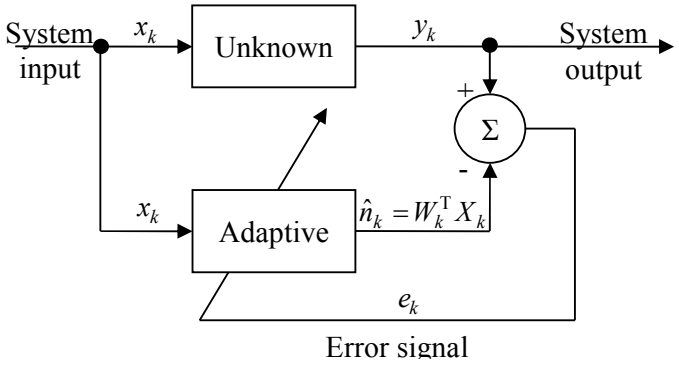

Figure 5.1: Adaptive filter for system modelling.

x_k is the input signal of the filter, y_k is the measured output signal, $\hat{n}_k$ is the modelled output signal and e_k is the error between the measured output and the filter estimation. W_k is the adjustable filter coefficient vector or weight vector. Thus, the goal is to adjust the coefficients of the filter to minimize the error signal using an adaptive algorithm.

One of the most widely used adaptive filtering algorithms is the least mean squares (LMS) algorithm using an estimator of the gradient instead of its actual value, considerably simplifying the calculations of the algorithm (Diniz, 2013). In particular, the coefficients of the filter are adjusted sample-to-sample to minimize the error signal e_k between the measured output signal and the modelled output signal:

$$e_k = y_k - \hat{n}_k = y_k - W_k^{\mathrm{T}} X_k = y_k - \sum_{j=1}^{m}\sum_{i=1}^{n} \alpha_{ij} \Delta K_i v_k \tag{5.7}$$

where X_k is the vector input to the filter model of current and previous filter output, n is the number of degrees-of-freedom and m is the number of prior time steps or taps considered. W_k is the adjustable filter coefficient and the Widrow-Hopf LMS algorithm is employed to update the filter weigh W_k (Ifeachor and Jervis, 2002):

$$W_{k+1} = W_k - \mu \nabla MSE \tag{5.8}$$

where μ is a positive scalar that controls the stability and rate of convergence. ∇MSE is the gradient of MSE and can be obtained：

$$\nabla MSE_{\alpha_{ij}} = 2\left(\hat{n}_k^{\mathrm{T}} - y_k^{\mathrm{T}}\right)\frac{\partial \hat{n}_k}{\partial \alpha_{ij}} = -2e_k^{\mathrm{T}} \Delta K_i v_k \tag{5.9}$$

Therefore, Equation (5.8) can be rewritten:

$$W_{k+1} = W_k + 2\mu\left[e_k^{\mathrm{T}} \Delta K_i v_k\right]_{n \times m} \tag{5.10}$$

where the $n \times m$ matrix $\left[e_k^{\mathrm{T}} \Delta K_i v_k\right]_{n \times m}$ is the same for all m elements in the i^{th} row. Hence, the changes of effective stiffness of i^{th} storey will be the sum over j of α_{ij} at time k.

5.3 Case Study 1: Experimental Evaluation for an Experimental RC Structure

This case study uses the same structure and data detailed in Chapter 4, sections 4.2-4.4.

5.3.1 SHM Results and Verification under SHW1

The effectiveness and robustness of the adaptive LMS and HLA methods were first compared using the data from the experimental structure used in Chapter 4. Figure 5.2(a), left column, shows the experimental SHM results of the SHW1 event for both methods and all six DOFs, where the initial value is the calculated linear stiffness before the test in Chapter 4, section 4.3. It can be seen that no stiffness degradation was identified for the first DOF (DOF1) using both adaptive LMS and HLA algorithms, which indicate the linear force-deformation relationship for this floor during the small event SHW1. Larger drops of stiffness were identified for the second, third, and fourth DOF (DOF2, DOF3 and DOF4) using the adaptive LMS algorithm than with the HLA algorithm when slight pinching behaviour was observed for these DOFs as shown in Figure 4.10. Because the baseline model used for the adaptive filter is a linear effective model (per Chase et al, 2005b), there exists a model error as highly nonlinear pinching behaviour occurs, resulting in an overestimation of the stiffness degradation.

In addition, no stiffness degradation was identified for the fifth and sixth DOF (DOF5 and DOF6) using the HLA algorithm. However, significant stiffness drops were identified for these DOFs by the adaptive LMS algorithm, as shown in Figure 5.2(a). These drops are due

to the baseline shear model creating a change in α that is not in data and then finding a best set of values of α_i in Equation (5.2) to fit the data. It thus arises from the model structure imposed, per Equation (5.4).

In addition, a rocking mechanism of RC structures can be activated by the vertical cracks at the beam-column interface during earthquakes, which have been observed in the Darfield (Canterbury) earthquake in 2010 (Kam et al., 2010). Thus, the pinching that occured for the second, third and fourth DOF, of which vertical cracks were observed consequently at the beam-column joint connection after the SHW2 event, suggest that these floors experienced micro concrete cracking or connection debonding at the beam-column interface during the SHW1 event and then induced a small amount of rocking to the dynamic response of higher floors. Hence, the response for the fifth and sixth DOF (DOF5 and DOF6) are not fully linear either, and the stiffnesses are underestimated using the shear model in the adaptive LMS algorithm.

5.3.2 Model-based Verification of SHW1 Experimental Results

Because the actual stiffness evolution is unknown *a priori* for the experimental structure, it is necessary to verify these SHM results using a near equivalent numerical model where everything is known. Therefore, a numerical model denoted Model I is simulated using the generalized Baber-Noori hysteretic differential model (Baber and Noori, 1985) to produce a similar damage state to the identified experimental building. Precise simulation for the damage scenario of the experimental RC structure with highly nonlinear hysteretic behaviour is very difficult. However, the magnitudes of stiffness degradation and hysteretic pinching in Model I were simulated to be similar to the identified experimental building for the second,

third and fourth DOFs using a set of time-varying model parameters. In addition, rocking behaviours for the fifth and sixth DOF were also considered in the simulation to represent a more accurate damage situation.

In particular, the 6-DOF system of Model I can be formulated:

$$\mathbf{M}\cdot\{\ddot{x}\}+\mathbf{C}\cdot\{\dot{x}\}+\mathbf{K_e}\cdot\{x\}+\mathbf{K_h}\cdot\{z\}=-\mathbf{M}\cdot\mathbf{I}\cdot\ddot{x}_g \tag{5.11}$$

where **M**, **C**, $\mathbf{K_e}$ and $\mathbf{K_h}$ are the mass, damping, initial elastic stiffness and hysteretic stiffness matrices, respectively. $\{x\}$, $\{\dot{x}\}$ and $\{\ddot{x}\}$ are the measured relative response to the ground, and $\ddot{x}_g$ is the ground motion acceleration. The relative hysteretic displacement $\{z\}_r$ and total displacement $\{x\}_r$ between each storey can be determined:

$$\{z\}_r=\mathbf{D}^{-1}\cdot\{z\} \qquad \{x\}_r=\mathbf{D}^{-1}\cdot\{x\} \tag{5.12}$$

where **D** is the transformation matrix and defined:

$$\mathbf{D}=\begin{bmatrix}1&0&0&0&0&0\\1&1&0&0&0&0\\1&1&1&0&0&0\\1&1&1&1&0&0\\1&1&1&1&1&0\\1&1&1&1&1&1\end{bmatrix} \tag{5.13}$$

The relationship between the hysteretic displacement z_i and total displacement x_i at the i-th storey can be obtained (Baber and Noori, 1985):

$$\dot{z}_i=h(z_i)[A\dot{x}_i-\nu(\beta|\dot{x}_i||z_i|^{n-1}z_i+\gamma\dot{x}_i|z_i|^n)]/\eta \tag{5.14}$$

where A, β, γ and n are the shape parameters. ν and η are the strength and stiffness degradation parameters, and defined:

$$\nu=1+\delta_\nu\varepsilon(t) \tag{5.15}$$

$$\eta = 1 + \delta_\eta \varepsilon(t) \tag{5.16}$$

$$\varepsilon(t) = (1-\alpha)\frac{k_e}{m}\int_0^t z_i(\tau)\dot{x}_i(\tau)d\tau \tag{5.17}$$

The pinching function $h(z_i)$ is determined (Baber and Noori, 1985):

$$h(z_i) = 1 - \zeta_1 \exp[-(z_i \operatorname{sgn}(\dot{x}_i) - qz_u)/\zeta_2^2] \tag{5.18}$$

$$z_u = \left[\frac{1}{\nu(\beta+\gamma)}\right]^{1/n} \tag{5.19}$$

$$\zeta_1 = \zeta_{10}(1 - \exp(-p\varepsilon)) \tag{5.20}$$

$$\zeta_2 = (\psi + \delta_\psi \varepsilon)(\lambda + \zeta_1) \tag{5.21}$$

where ζ_{10} is the measure of total slip; p is the constant that controls the rate of initial drop in slope; ψ is the parameter that contribute to the amount of pinching; δ_ψ is the constant specified for the desired rate of pinching spread; and λ is the small parameter that controls the rate of change of ζ_1 and ζ_2. The model parameters for Model I are listed in Table 5.1.

The simulated response of Model I was obtained using a Runge-Kutta integration method with a sample frequency of 250Hz, which is the same as the experimental sampling rate. Structural accelerations with 10% added RMS sensor noise were taken for each of the six DOFs, and then used for the application of these two SHM algorithms. The hysteresis loops based on the simulated response of Model I subjected to the SHW1 event are plotted in Figure 5.3(a).

Table 5.1 Baber-Noori model parameters for Model I

Parameters	DOF1	DOF2	DOF3	DOF4	DOF5	DOF6
A	1.0	1.0	1.0	1.0	1.0	1.0
β	0.5	0.5	0.5	0.5	0.5	0.5
γ	0.5	0.5	0.5	0.5	0.5	0.5
n	2	2	2	2	2	2
δ_v	0.01	0.01	0.01	0.01	0.01	0.01
δ_η	0~0.044	0.024~0.3	0.024~0.3	0.044~0.3	0~0.12	0~0.1
ζ_{10}	0.88	0.88	0.88	0.88	0.88	0.88
p	0.004~0.1	0.2~0.6	0.2~0.6	0.2~0.6	0.3~1.0	0.7~4.8
ψ	0.1	0.1	0.1	0.1	0.1	0.1
δ_ψ	0.005	0.005	0.005	0.005	0.005	0.005
λ	0.2	0.2	0.2	0.2	0.2	0.2
q	0.01	0.01	0.01	0.01	0.01	0.01

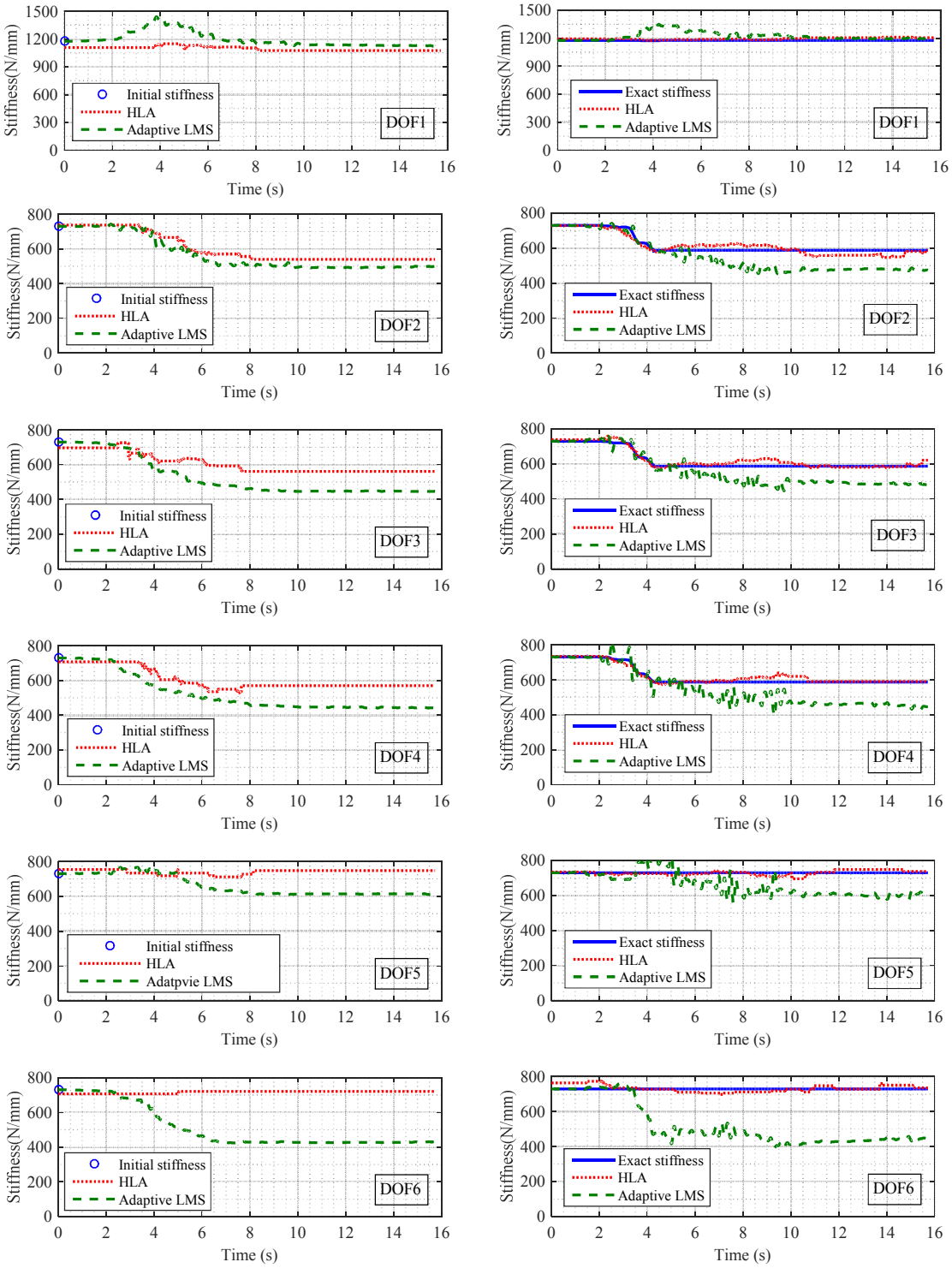

Figure 5.2: Comparison of SHM results under SHW1 for (a) the experimental structure data and (b) the numerical simulated structure (Model I).

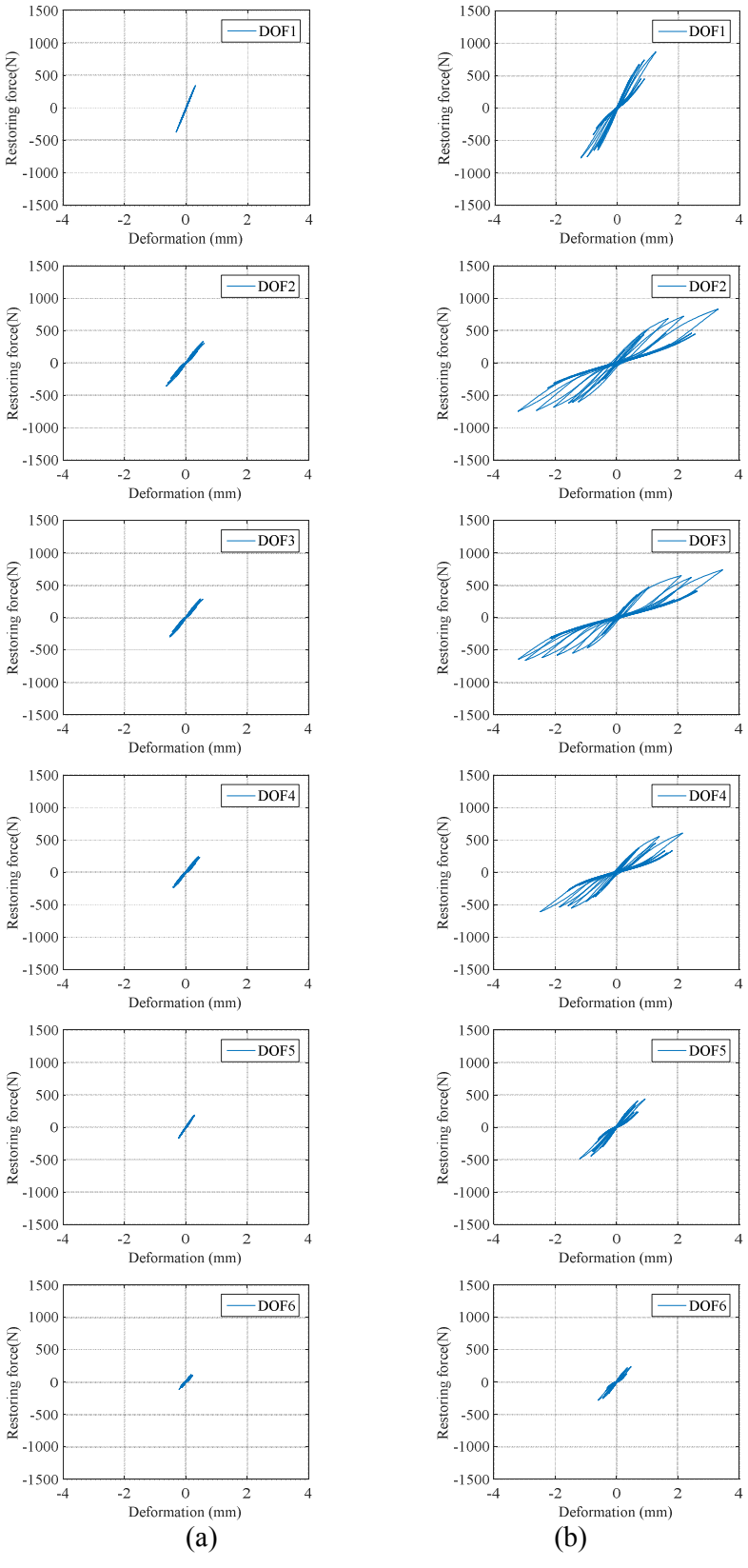

Figure 5.3: Hysteresis loop for each DOF of Model I subjected to (a) the SHW1 event and (b) the SHW2 event.

Figure 5.2(b), right column, compares the SHM results of Model I subjected to the SHW1 event using the adaptive LMS and HLA algorithms. It is thus a simulated numerical analogue of the experimental left column. Note that the exact stiffness in Figure 5.2(b) represents the true simulated evolution of Model I during SHW1.

Comparing the same DOF between Figures 5.2(a) and (b), the identified stiffness evolution for Model I is very similar to the experimental structure. In addition, the identified total drops of stiffness of the experimental structure using the HLA method are also very close to Model I with the largest difference of 4.6%, as listed in Table 5.2. It can also be seen from Table 5.2 that the identified stiffness degradation between the experimental structure and Model I using the adaptive LMS algorithm are also similar with the largest difference of 4.9%. These results imply that the damage scenarios of each DOF of the experimental structure subjected to the SHW1 event are well simulated using Model I, where the true evolution of stiffness is known for further more detailed and quantifiable examination of the two methods.

Table 5.2 Identified total stiffness degradation of the experimental structure and Model I under SHW1 using the HLA and adaptive LMS method

DOF	HLA			Adaptive LMS		
	Experimental	Model I	Difference	Experimental	Model I	Difference
1	7.2%	2.6%	4.6%	0.9%	1.6%	0.7%
2	23.8%	21.8%	2.0%	32.9%	34.9%	2.0%
3	23.0%	18.4%	4.6%	38.9%	34.0%	4.9%
4	21.8%	19.2%	2.6%	39.5%	40.1%	0.6%
5	2.5%	1.1%	1.4%	16.2%	17.3%	1.1%
6	1.4%	0.7%	0.7%	41.2%	38.5%	2.7%

Results from Figures 5.2(b) show that the HLA algorithm successfully captured the changes in stiffness of each DOF of Model I during the SHW1 event as it did experimentally, and also yielded accurate estimates of the final stiffness degradation with the largest error only 2.6%, as listed in Table 5.3. The adaptive LMS algorithm also yields an accurate estimation for the first DOF (DOF1), where only linear response occurred. However, stiffness degradation was again overestimated using the adaptive LMS method for the damaged second, third and fourth DOF (DOF2, DOF3 and DOF4) with nonlinear pinching behaviour occurred. In addition, stiffness estimations with errors of 17.3% and 38.5% were identified for the undamaged fifth and sixth DOF (DOF5 and DOF6), respectively, due to the nonlinear rocking behaviour in those floors, similar to the experimental results for DOF5 and DOF6 with 16.2% and 41.2% stiffness degradation identified, respectively, and further validating what was observed. Again, these differences and resulting errors arises from a mismatch between the model used by the adaptive LMS method, and the observed behaviour.

Table 5.3 Identification errors of stiffness degradation of Model I under SHW1 using the HLA and adaptive LMS method

DOF	Simulated true stiffness degradation	HLA		Adaptive LMS	
		Identified	Error	Identified	Error
1	0%	2.6%	2.6%	1.6%	1.6%
2	19.7%	21.8%	2.1%	34.9%	15.2%
3	19.7%	18.4%	1.3%	34.0%	14.3%
4	19.7%	19.2%	0.5%	40.1%	20.4%
5	0%	1.1%	1.1%	17.3%	17.3%
6	0%	0.7%	0.7%	38.5%	38.5%

5.3.3 Experimental and Model-based SHM Results and Verification under SHW2

Figure 5.4(a), left column, compares the experimental SHM results of SHW2 using these two algorithms. Note the initial stiffness in Figure 5.4(a) represents the identified final stiffness of SHW1 using the HLA method. Again, the damage scenario of the experimental structure subjected to the SHW2 event is simulated using the numerical model (Model I). The hysteresis loops of each DOF of Model I subjected to the SHW2 event are plotted in Figure 5.3(b). Table 5.4 compares the identified stiffness degradation between the experimental structure and Model I using the HLA and adaptive LMS method. It can be seen that the stiffness degradation of Model I is very close to the experimental structure with the largest differences only 3.0% and 6.2% for the HLA and adaptive LMS method, respectively, which indicate a similar damage scenario between the experimental structure and Model I.

Table 5.4 Identified total stiffness degradation of the experimental structure and Model I under SHW2 using the HLA and adaptive LMS method

DOF	HLA			Adaptive LMS		
	Experimental	Model I	Difference	Experimental	Model I	Difference
1	35.2%	37.4%	2.2%	53.2%	59.6%	6.2%
2	49.9%	52.9%	3.0%	75.6%	78.4%	2.8%
3	53.8%	54.0%	0.2%	80.8%	80.0%	0.8%
4	54.4%	53.6%	0.8%	78.4%	79.3%	0.9%
5	37.0%	37.8%	0.8%	61.9%	63.7%	1.8%
6	27.0%	23.4%	2.6%	61.8%	59.5%	2.3%

Figure 5.4(b), right column, compares the SHM results of Model I subjected to the SHW2 event using the two methods. It can be seen that the HLA algorithm still accurately captures the proper changes and trends in stiffness evolution under this large seismic event SHW2, and the largest identification error of the final stiffness is only 2.4% for all the DOFs, as listed in Table 5.5. However, the stiffness degradation is overestimated for all six DOFs using the adaptive LMS algorithm because of the nonlinear pinching behaviours that occur in all the floors during the larger SHW2 event do not match the underlying assumed model. These results also match the SHM results of the experimental structure in the fact that the identified stiffness degradation using the adaptive LMS algorithm is larger than the HLA algorithm to account for a mismatch of the model and nonlinear behaviour observed in RC structures.

Table 5.5 Identification errors of stiffness degradation of Model I under SHW2 using the HLA and adaptive LMS method

DOF	Simulated true stiffness degradation	HLA		Adaptive LMS	
		Identified	Error	Identified	Error
1	35.3%	37.4%	2.1%	59.6%	24.3%
2	50.5%	52.9%	2.4%	78.4%	27.9%
3	52.7%	54.0%	1.3%	80.0%	27.3%
4	51.4%	53.6%	2.2%	79.3%	27.9%
5	35.5%	37.8%	2.3%	63.7%	28.2%
6	24.9%	23.4%	1.5%	59.5%	24.6%

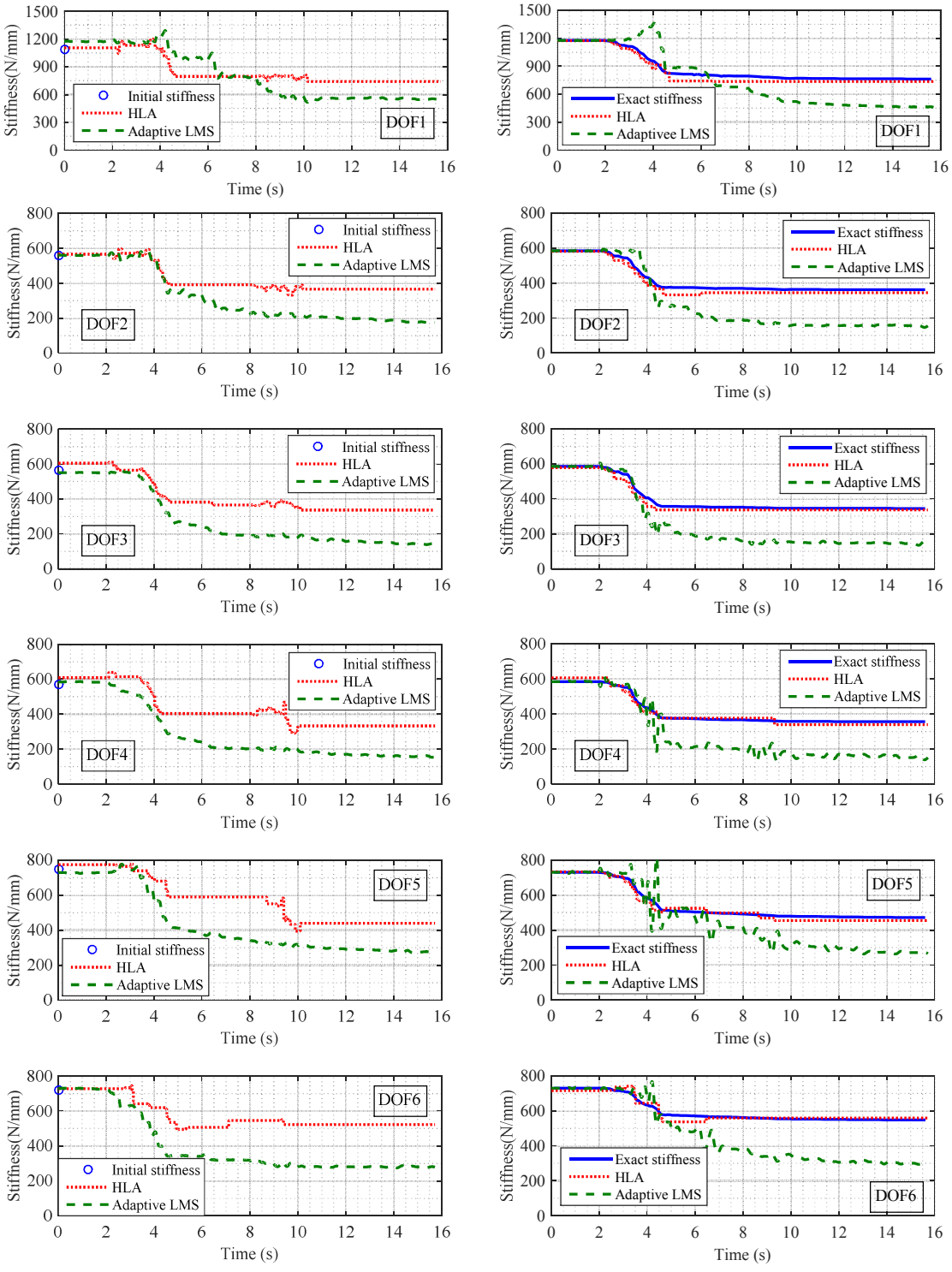

Figure 5.4: Comparison of SHM results under SHW2 for (a) the experimental structure data and (b) the numerical simulated structure (Model I).

SHM results of both the experimental structure and Model I for SHW2 indicate the model-free HLA method is more accurate in identifying highly nonlinear RC structures that exhibit pinching and rocking behaviours. The performance of adaptive LMS filer is limited to the baseline linear, time-varying stiffness model for the identification of nonlinear hysteretic behaviour. However, it was till adequate for capturing the general trends in dynamic stiffness changes or identifying model errors for highly nonlinear RC structure, which indicates a more complex baseline mode for this adaptive LMS method could achieve more accurate estimation, as might be expected, as long as it included similar nonlinear behaviour, such as in (Nayyerloo et al., 2011).

5.4 Case Study 2: Performance Evaluation of SHM Methods for SMRF Structures

Seismic damage for RC structures, such as the experimental structure in Case Study 1, is most commonly caused by pinching and yielding hysteretic behaviours that may not match common, simpler models used in many model-based SHM methods (Park, 1986; Toussi and Yao, 1983). However, damage of a steel moment resistance frame (SMRF) structure is primarily due to the excessive yielding behaviour (Mahin, 1998; Malley, 1998; Tremblay et al., 1996) and is a better match to such models. Therefore, a six DOF numerical model (Model II) with only yielding deformation considered for stiffness degradation was simulated using the classical Bouc-Wen hysteretic model (Bouc, 1967; Wen, 1976) that is representative of the hysteretic behaviour of a SMRF structure.

The simulation of the 6-DOF system Model II is also generalized using Equations (5.11)-(5.13). Because pinching behaviour is not considered in the Bouc-Wen model, the hysteretic displacement z_i at the i-th storey is rewritten:

$$\dot{z}_i = [A\dot{x}_i - \nu(\beta|\dot{x}_i||z_i|^{n-1} z_i + \gamma\dot{x}_i|z_i|^n)]/\eta \tag{5.22}$$

where ν and η are defined by Equations (5.15) and (5.16), respectively. The model parameters for Model II are listed in Table 5.

Table 5.6 Bouc-Wen model parameters for Model II

Parameters	DOF1	DOF2	DOF3	DOF4	DOF5	DOF6
A	1.0	1.0	1.0	1.0	1.0	1.0
β	0.5	0.5	0.5	0.5	0.5	0.5
γ	0.5	0.5	0.5	0.5	0.5	0.5
n	2	2	2	2	2	2
δ_ν	0.01	0.01	0.01	0.01	0.01	0.01
δ_η	0~0.04	0.016~0.15	0.009~0.144	0.034~0.144	0~0.144	0~0.134

The mass and initial stiffness of Model II were chosen to be the same as the experimental structure, as well as Model I. The stiffness degradation of Model II is also simulated to be similar to the experimental structure and Model I. Structural responses for Model II subjected to the SHW1 and SHW2 event are generated at a sample rate of 250Hz using the Runge-Kutta integration method. Structural accelerations of each DOF of Model II are assumed to be measured with a 10% RMS sensor noise added. The hysteresis loops of each DOF of Model II subjected to the SHW1 and SHW2 event are plotted in Figure 5.5. SHM results of the two algorithm for Model II under SHW1 and SHW2 are shown in Figures 5.6 and 5.7, respectively.

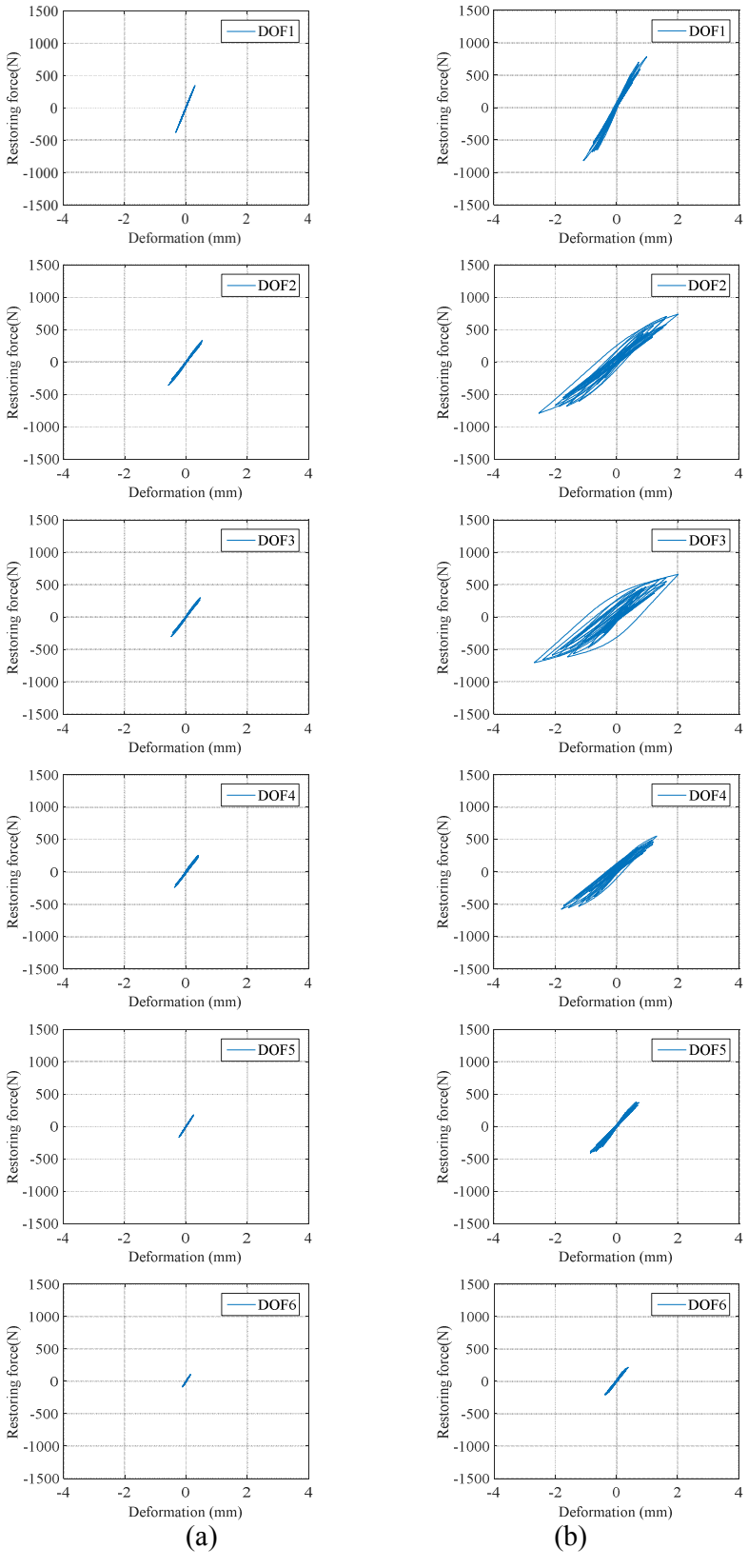

Figure 5.5: Hysteresis loop for each DOF of Model II subjected to (a) the SHW1 event and (b) the SHW2 event.

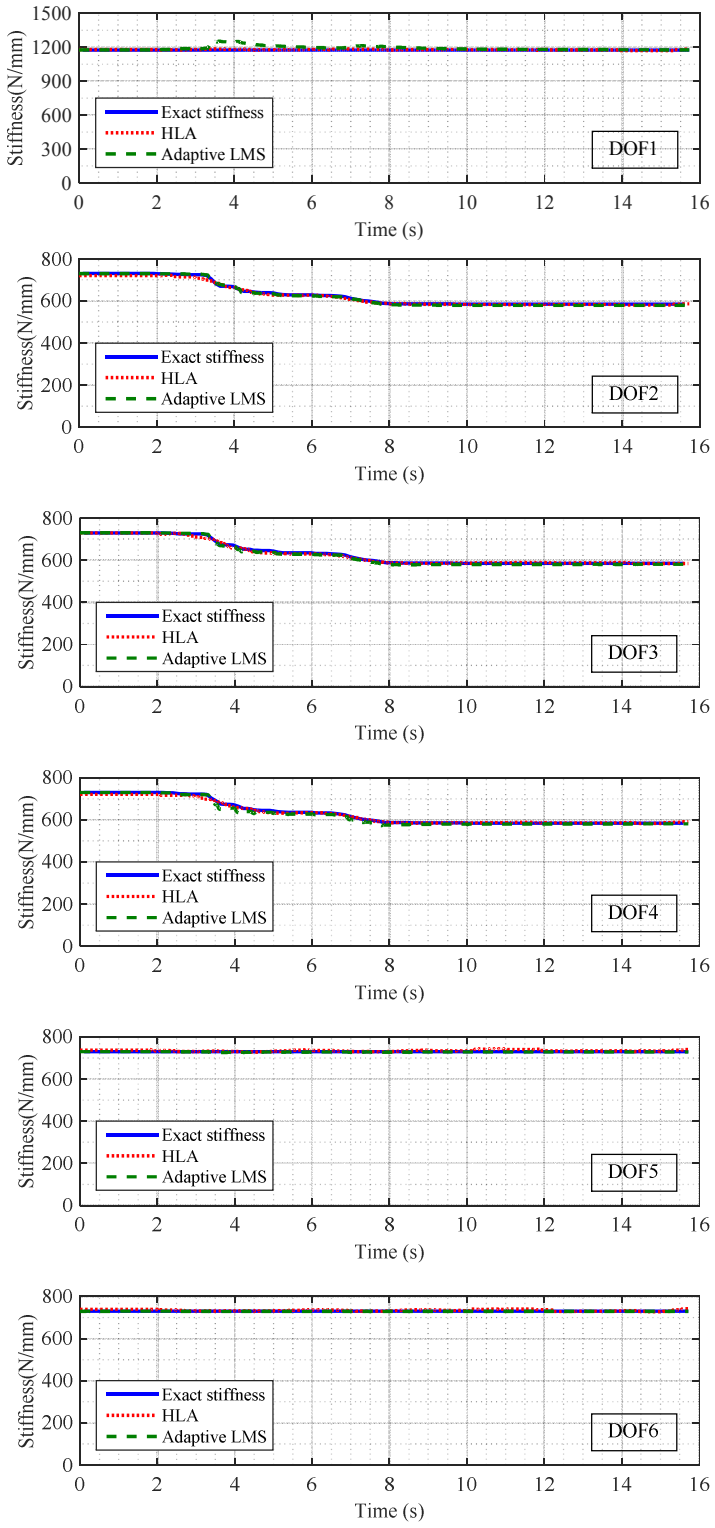

Figure 5.6: SHM results of Model II using the adaptive LMS and the HLA method under the SHW1 event.

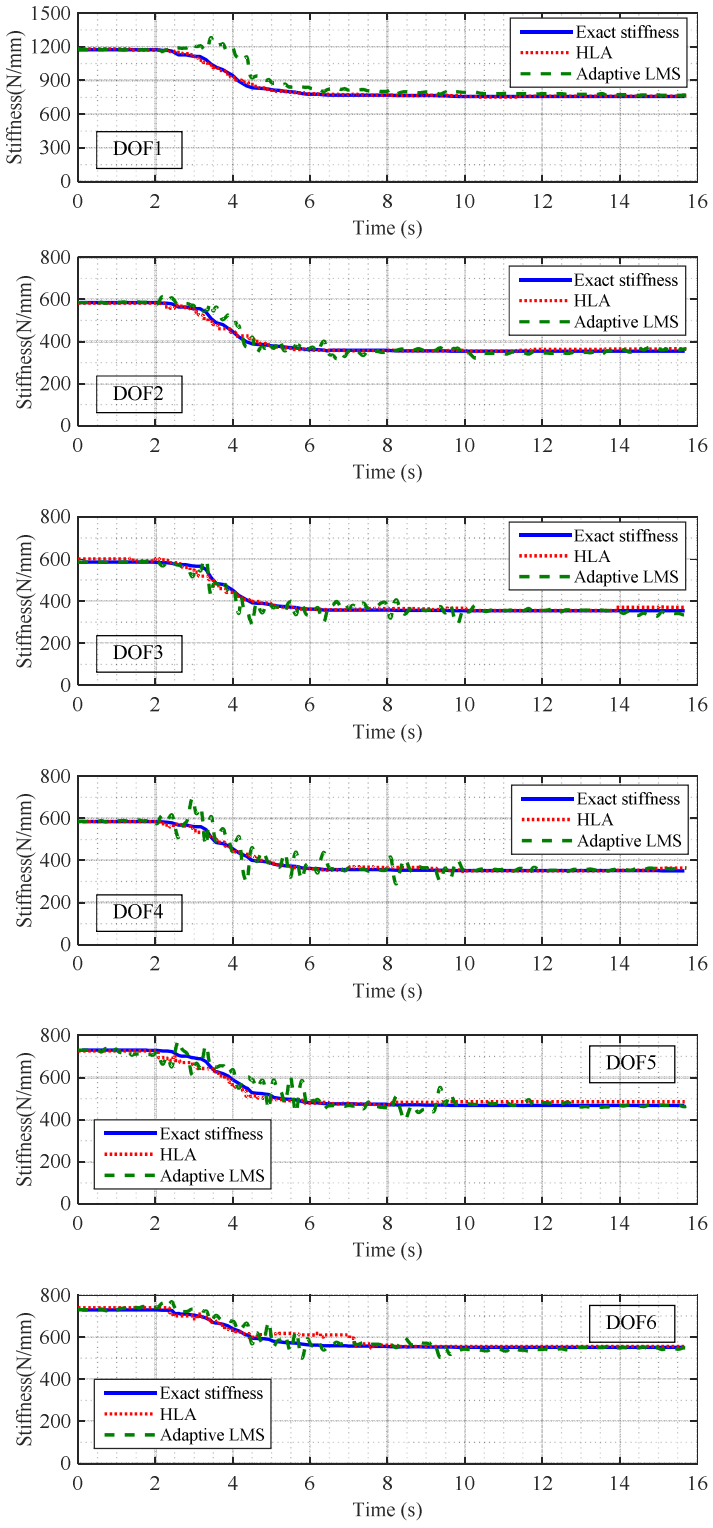

Figure 5.7: SHM results of Model II using the adaptive LMS and the HLA method under the SHW2 event.

The SHM results clearly show that the HLA algorithm still accurately captures, modelled and thus known, the proper changes and trends in stiffness evolution of each DOF of Model II, and the largest identification error for the final stiffness degradation is only 2.5%, as listed in Table 5.7. However, unlike the identification of RC structures in Case Study 1, the adaptive LMS algorithm also yields very accurate estimation of the stiffness evolution for Model II with only simpler bilinear yielding hysteretic behaviour considered. The largest identification error for the final stiffness degradation is also very small and only 1.9%, as shown in Table 5.7. This outcome is attributed to the adaptive LMS filter and time varying parameters being a better match to such a bilinear hysteresis loop compared to the RC structure's pinching and rocking. Thus, the identified stiffness using the adaptive LMS filter fluctuates between two values for linear and yielding stiffness, and the adaptive LMS algorithm and baseline model are capable of capturing those changes.

Table 5.7 Identification errors of final stiffness degradation of Model II

DOF	SHW1		SHW2	
	HLA	Adaptive LMS	HLA	Adaptive LMS
1	0.5%	0.0%	0.3%	0.9%
2	0.3%	0.4%	1.5%	1.2%
3	0.1%	0.7%	2.2%	1.8%
4	0.7%	0.4%	1.8%	1.9%
5	1.2%	0.3%	2.5%	0.7%
6	1.1%	0.1%	0.5%	0.5%

In addition the first, fifth and six DOF were identified as remaining linear without stiffness degradation during the SHW1 event, matching the strictly linear behaviour simulated for this event. These results indicate these two algorithms are robust to both linear and nonlinear response when only yielding hysteretic behaviour occurs in the structural response, and for the adaptive LMS method, the model matches the observed response well.

The SHM results are equally good for the SHW2 event where all six DOFs experience yielding and degradation. Both algorithms track the changes well in the presence of significant sensor noise. Hence, the choice of the baseline model must accurately capture the damage observed to obtain accurate SHM identification results. Thus, model-based methods are less robust to variation in the type of damage from an expected behaviour than the model-free HLA method.

5.5 Summary

In this chapter, the effectiveness of the model-free HLA method was compared to a known model-based adaptive LMS method for damage identification of structures with different hysteretic behaviours and damage.

SHM results of the experimental structure and matching numerical Model I show that the HLA algorithm is more accurate in identifying the highly nonlinear RC structures that exhibit hysteretic pinching and rocking behaviours due to damage that the baseline time-varying stiffness model of the adaptive LMS filter could not capture well. Thus, the performance of the adaptive LMS algorithm is limited when identifying time varying linear stiffness changes for the identification of RC structure. In particular, the stiffness degradation was overestimated for the damaged DOFs with hysteretic pinching behaviour as a result of a

mismatch between the baseline model and the observed data leading to the stiffness of undamaged DOFs identified as significantly different values to compensate. However, the adaptive LMS method still captures the general trends in stiffness changes. Future work on incorporating a more complex baseline model for this adaptive LMS method would broaden the application of this algorithm to hysteretic pinching systems with more accurate estimation.

Finally, a simulated Model II with only hysteretic yielding behaviour typical of a SMRF structure is considered. Both algorithms were robust to both linear and nonlinear response for Model II. Undamaged floors were identified as remaining linear without stiffness degradation if no damage occurred at those floors during the earthquake, as desired, by both algorithms. In addition, the two algorithms were capable of capturing the proper changes in stiffness and identifying the final stiffness accurately for the simulated Model II.

Hence, it is clear that the model-based SHM methods are less robust to damage behaviours that their underlying assumed models cannot capture well. The baseline model for such methods must therefore be chosen with care in experimental studies where ground truth may not fully known.

Chapter 6: HLA and MRA-based SHM of Reinforced Concrete Structures with Damage Occurred Prior to a Sequence of Earthquake Events

6.1 Introduction

Reinforced concrete structures are very common in seismic zones. However, structural health monitoring for RC structures can be problematic and subjective due to their highly nonlinear and time-varying behaviour, particularly when structures were damaged with stiffness changing across elastic, pinched and hybrid regimes that are not known *a priori* and difficult to include in model-based SHM. As discussed in Chapter 5, the model-based SHM techniques require a suitable baseline model for the real system to yield accurate SHM results, which is not always the case where ground truth is not fully known. In addition, the accuracy of estimation also depends on *a priori* knowledge and the initial guesses of unknown parameters during the identification process. Thus, there are still significant limitations in the model-based methods that, in turn, limit realistic monitoring of nonlinear structural response.

The results in Chapters 4 and 5 show the proposed HLA method is capable of identifying changes of nonlinear stiffness for damage detection and localization, as well as damage assessment. In addition, the HLA method avoids the constraint of an assumed baseline model as the model-based methods require for damage identification. Although, the overall results in Chapters 4 and 5 provide an excellent numerical and experimental validation of the effectiveness of the HLA method, it would be useful to extend the investigation to equally or more complex hysteretic behaviours.

In Chapters 4-5, the experimental structure is a single-bay 12-storey RC building. In this chapter, the HLA method is applied to a two-bay 12-storey RC building with cracks visually observed in the beam-column joints prior to a sequence of four shaking table tests that lead to different hysteretic behaviours.

Hysteresis loops are reconstructed using the corrected accelerations and displacement measurements based on a multi-rate Kalman filter. Nonlinear stiffness of the experimental building is calculated for every half cycle using the HLA method to examine the evolution of structural behaviour during the four input ground motions. Structural degradation is evaluated by tracking changes of the stiffness of significant half cycles with full dynamic response. Finally, a wavelet multiresolution analysis (MRA) is proposed to extract an effective linear stiffness from the nonlinear stiffness identified using HLA. Both the presence and extent of the structural damage, as well as resulting natural frequency are determined using the identified effective linear stiffness. The accuracy and continuity of the proposed method are illustrated on modal analysis before and after the test.

6.2 Testing Structure and Test

The test structure is a twelve-storey 1:10 scaled RC frame building, denoted RCF12 in Figure 6.1. The RCF 12 was designed with two bays in the *x*-direction of shaking and one bay in the *y*-direction. The dimensions in the two and one bay directions are 360mm×2 and 600mm, respectively. Each storey consists of a 12mm thick floor slab and the storey height is 300mm. Thus, the total height of RCF12 is 3600mm excluding a 110mm high rigid base. All the columns have a constant cross section of 50×50 mm, and the beams also have the same cross section of 30×60 mm. Considering the weight of non-structural elements and 50% live load,

the artificial mass is adopted as 113.3kg for the top (12th) floor and 122.3kg for the other floors, respectively.

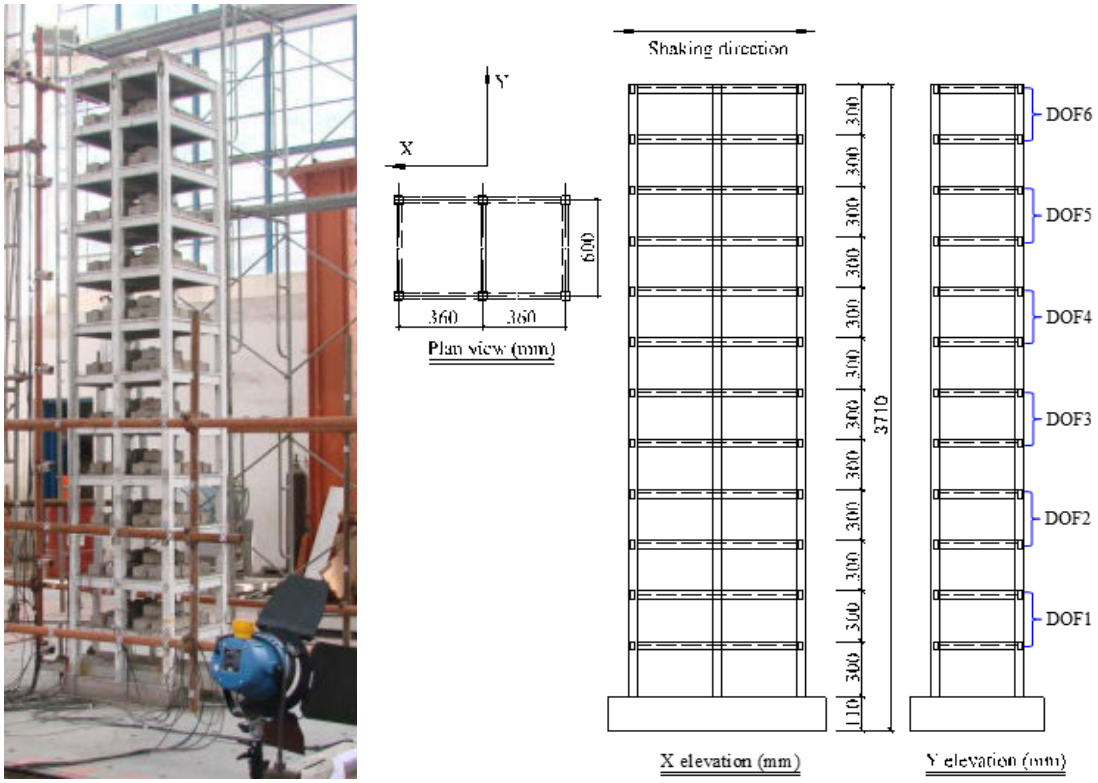

Figure 6.1: Photo and configuration of the tested RCF12.

Four input ground motions were applied to the RCF12 in the uniaxial *x*-direction. The four input motions include the El Centro wave (El) from the Imperial Valley earthquake in Southern California (PEER, 2005), Shanghai artificial wave (SHW) based on the Shanghai Code for Seismic Design of Building (SGCMC, 2013), as well as the Wolong wave (WL) and Shifang wave (SF) from the 2008 Wenchuan earthquake (Li et al., 2008). Figure 5.2 shows the peak ground accelerations (PGA) and time histories of these four earthquake records. Accelerations and displacements were recorded at the base, 2nd, 4th, 6th, 8th, 10th, and 12th (top) floors, at a sampling rate of 62Hz.

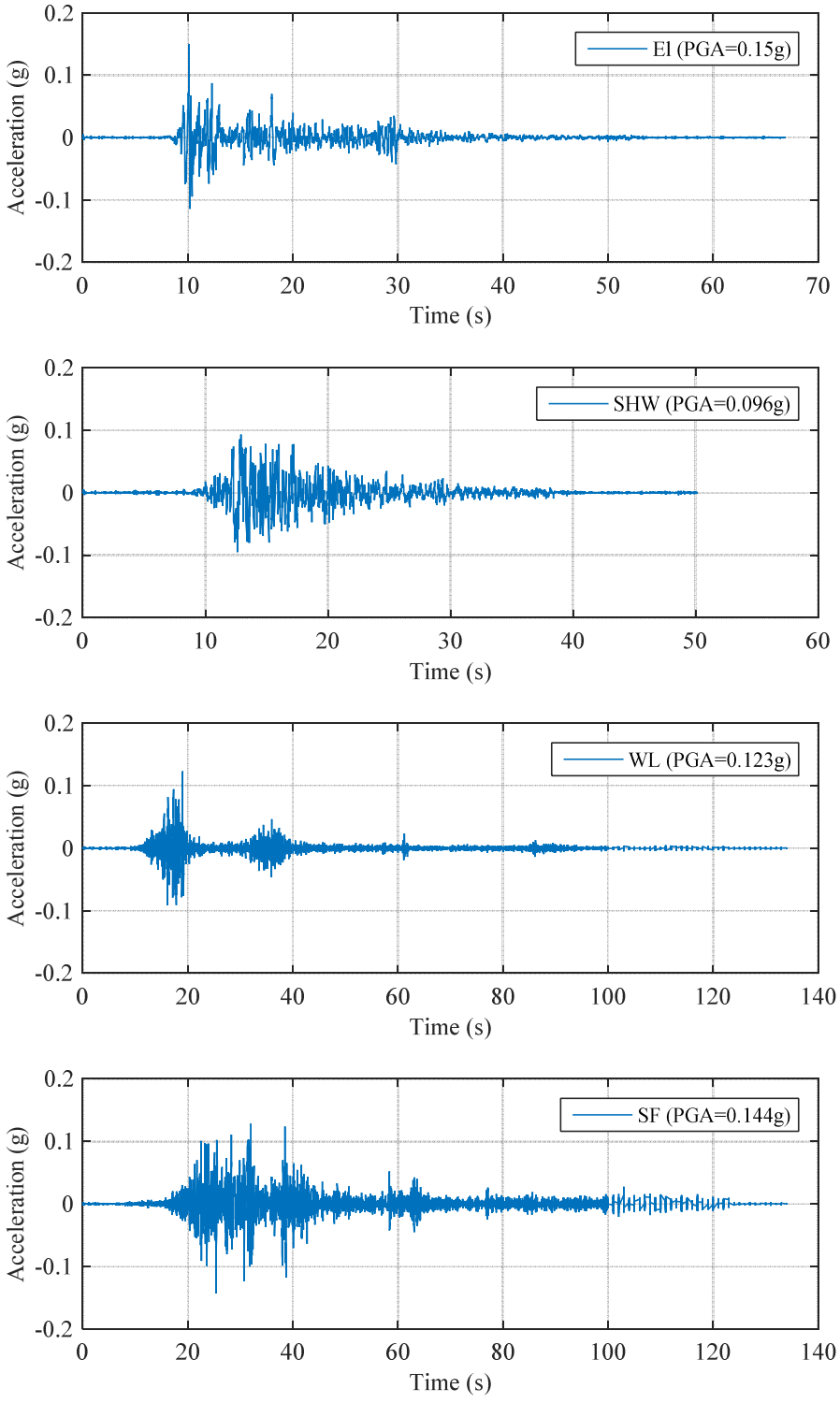

Figure 6.2: Time histories of input ground motions in the sequence order: El, SHW, WL and SF (top to bottom).

It must be noted that the tested RCF12 was already a damaged structure before the shaking table tests (El, SHW, WL and SF) in this study. Vertical cracks were visually observed at the beam-column joint connections in the lower floors before the El event, as shown in Figure 6.3. More vertical cracks were observed at these storeys after the test. In addition, diagonal cracks were also observed at the third, fourth and fifth floors, as shown in Figures 6.4(a)-(d), which indicate hinges had developed in these regions. Finally, vertical cracks were also found at the sixth and seventh storeys after the test, as shown in Figures 6.4(e)-(f).

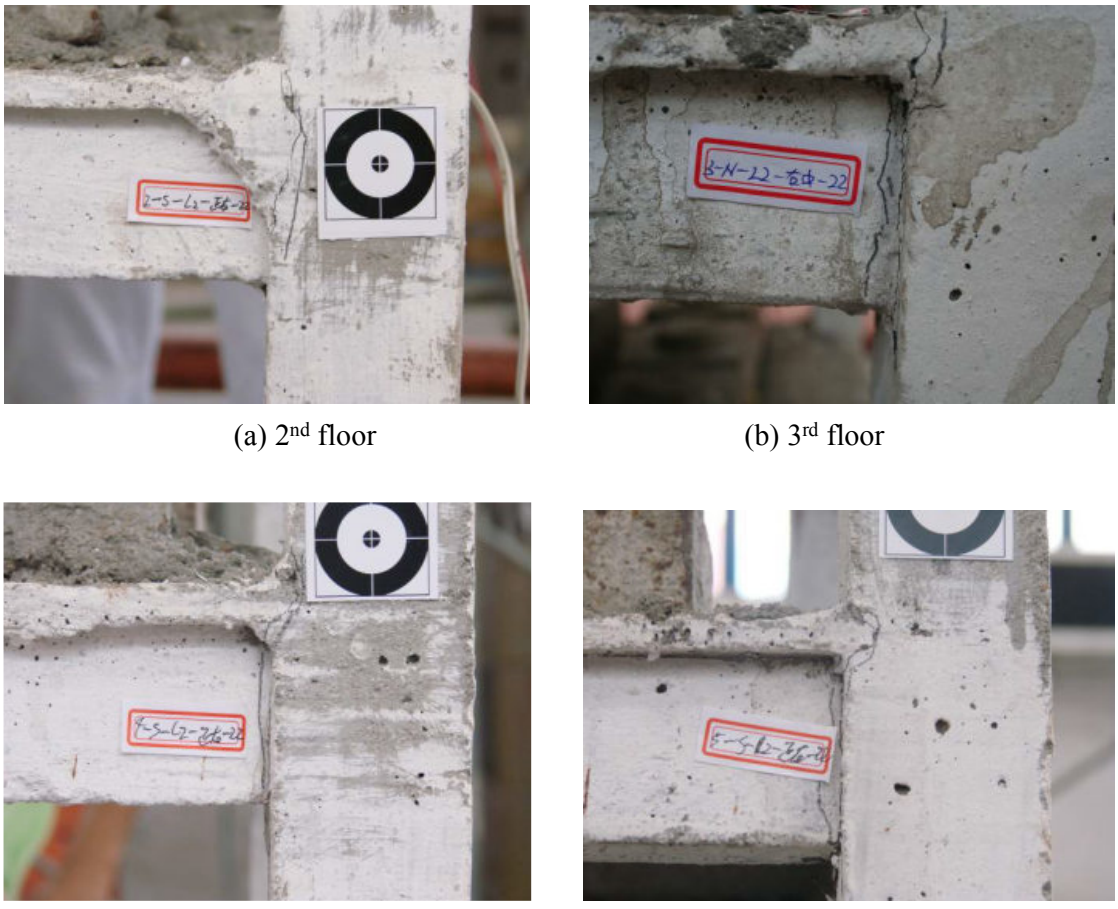

(a) 2nd floor (b) 3rd floor

(c) 4th floor (d) 5th floor

Figure 6.3: Photo of vertical cracks at the beam-column joints of RCF12 before El event.

(a) 3nd floor

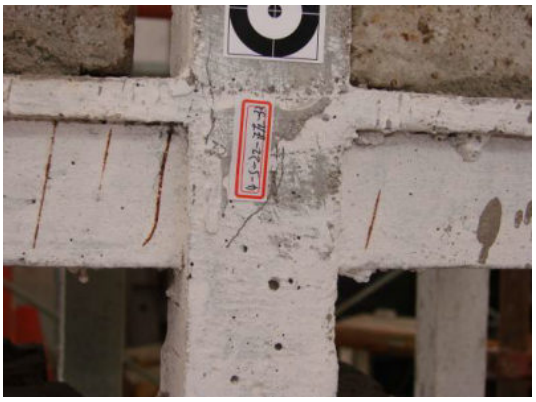

(b) 4th floor

(c) 4th floor

(d) 5th floor

(e) 6th floor

(f) 7th floor

Figure 6.4: Photos of diagonal and vertical cracks at the beam-column joints after the test.

6.3 Reconstruction of Hysteresis Loops

While accelerations and displacements were measured at the same sampling rate during the test, high-rate acceleration and low-rate displacement measurements are commonly applied for field monitoring (Li et al., 2006). In addition, direct integration of measured accelerations to obtain velocity is sensitive to noise (Worden, 1990; Xu et al., 2015). Hence, reconstruction of hysteresis loops can be distorted using the noisy measured accelerations and displacements directly, even with the same sampling rate.

As a result, an online multi-rate Kalman filter method is used to estimate corrected displacement, velocity and acceleration based dual measurements of accelerations and displacements with either the same in this case or different sampling rate (Smyth and Wu, 2007). In particular, the state space equations for a discrete system can be given:

$$x_{k+1} = Ax_k + Bu_k + w_k \tag{6.1}$$

$$y_k = Cx_k + v_k \tag{6.2}$$

where x_k is the state variable vector of displacement and velocity, u_k is the input of measured acceleration, and y_k is the measured output of displacement, w and v are white noise Guassion processes with distribution $(0,Q)$ and $(0,R)$, respectively.

The covariance matrices Q and R for discrete system can be obtained (Smyth and Wu, 2007):

$$Q = \begin{bmatrix} q\Delta t^3/3 & q\Delta t^2/3 \\ q\Delta t^2/3 & q\Delta t \end{bmatrix} \qquad R = \frac{r}{\Delta t} \tag{6.3}$$

where Δt is the displacement measurement sampling interval. The system matrices A, B and C are defined (Smyth and Wu, 2007):

$$A = \begin{bmatrix} 0 & \Delta t \\ 0 & 0 \end{bmatrix} \qquad B = \begin{bmatrix} \Delta t^2 / 2 \\ \Delta t \end{bmatrix} \qquad C = \begin{bmatrix} 1 & 0 \end{bmatrix} \tag{6.4}$$

Hence, the discrete time Kalman filter can be processed using the steps:

$$\hat{x}_{k+1,k} = A\hat{x}_{k,k} + Bu_k \tag{6.5}$$

$$P_{k+1,k} = AP_{k,k}A^{\mathrm{T}} + Q \tag{6.6}$$

$$K_{k+1} = P_{k+1,k}C^{\mathrm{T}}[CP_{k+1,k}C^{\mathrm{T}} + R]^{-1} \tag{6.7}$$

$$\hat{x}_{k+1,k+1} = \hat{x}_{k+1,k} + K_{k+1}[y_{k+1} - C\hat{x}_{k+1,k}] \tag{6.8}$$

$$P_{k+1,k+1} = [\mathbf{I} - K_{k+1}C]P_{k+1,k} \tag{6.9}$$

Therefore, the displacements and velocities can be estimated in real time using Equations (6.5)-(6.9) at time $k\Delta t$ when displacement and acceleration are both measured, and using Equations (6.5)-(6.9) between the times $k\Delta t$ when only acceleration measurements are available. Finally, a better estimation can then be obtained by smoothing a set of fixed interval data using a Rauch-Tung-Striebel (RTS) algorithm (Brown and Hwang, 1997). All of these well-known techniques can be readily applied in real-time.

Hence, the hysteresis loops can be reconstructed for every two floors based on the corrected estimations of displacement, velocity and acceleration. Figure 6.5 shows the reconstructed hysteresis loops for each DOF sequentially subjected to the El, SHW, WL and SF earthquake event from the top to bottom. It can be seen that significant nonlinear behaviours occur at the first, second, third and fourth DOF (floors 1-8) during the earthquake excitations, which correspond to the observed cracking damage at the beam-column joint connections before and after the tests, some of which are shown in Figures 6.3-6.4.

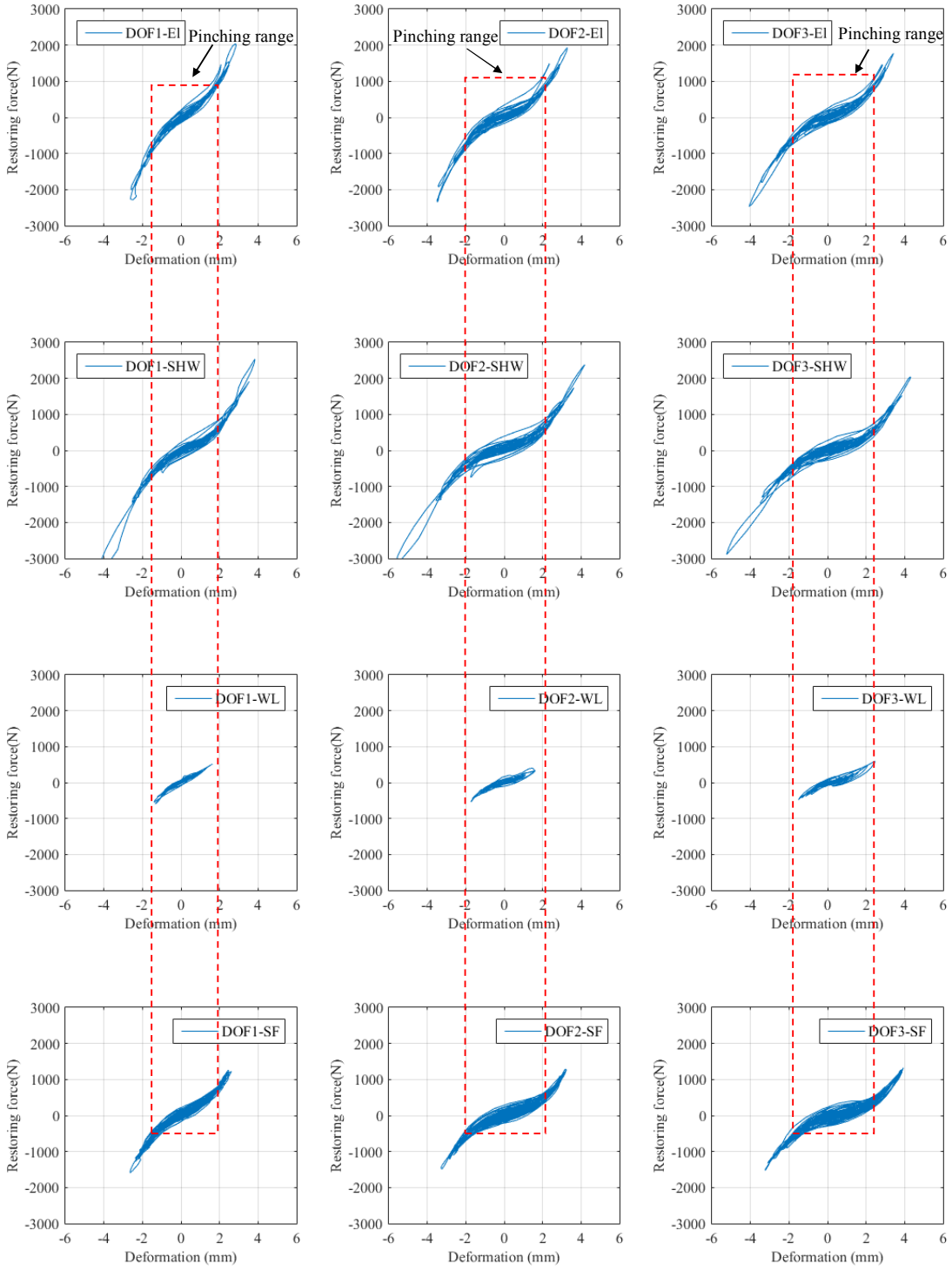

(a) First DOF (b) Second DOF (c) Third DOF

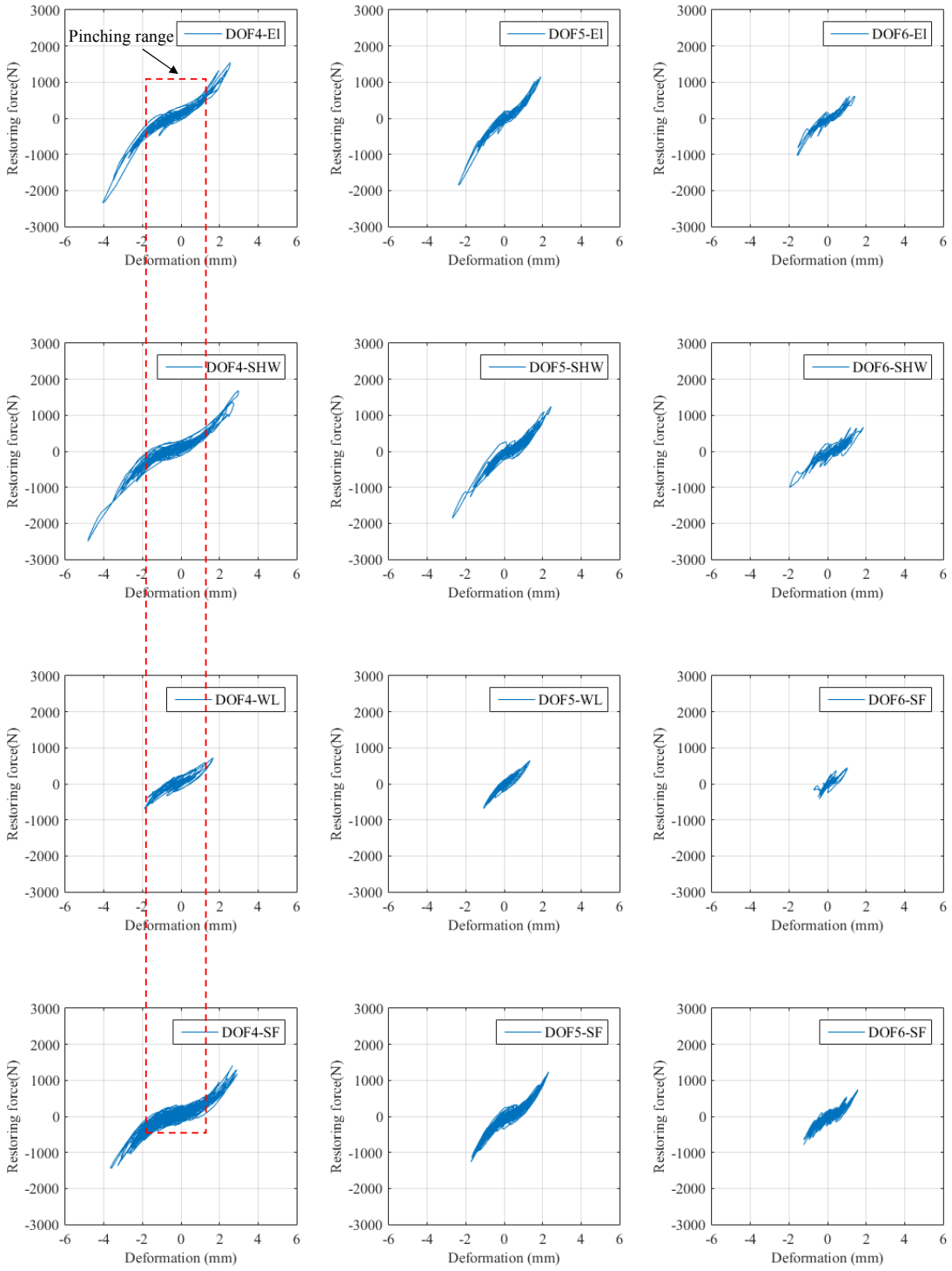

(d) Fourth DOF (e) Fifth DOF (f) Sixth DOF

Figure 6.5: Reconstructed hysteresis loops for (a) first DOF, (b) second DOF, (c) third DOF, (d) fourth DOF, (e) fifth DOF and (f) sixth DOF sequentially (top to bottom) subjected to the El, SHW, WL and SF events from the top to bottom.

In addition, it also can be seen from Figure 6.5 that the structural behaviour for a seriously damaged floor is in a pinching response regime when the magnitude of the dynamic response is small, and then moves to an elastic range as the response increases to significant magnitude. In particular, the hysteresis loops for DOF1-4, in which cracks were observed prior to the test, clearly shows that the slopes of the loop curves for the small WL event are similar to the slopes of the pinching range for the other large events, as shown in Figures 6.5(a)-(d). However, the slopes for the WL event are much smaller than the slopes outside the pinching range for the other events, which indicates the structural behaviour of the WL event is only vibrating within the pinching and/or hybrid range outside of pinching motion, but not fully in an elastic range.

6.4 SHM Results Using HLA Method

6.4.1 Identified Evolution of Nonlinear Stiffness and Elastic Stiffness

Figure 6.6 shows the identified evolution of nonlinear stiffness for the first DOF (DOF1) using all half cycles during the El, SHW, WL and SF event sequentially. It can be seen that the identified stiffness changes between the elastic stiffness, hybrid stiffness and pinching stiffness regimes during the El, SHW, WL and SF event. In particular, the changes of hybrid stiffness are very variable and determined by the relative size of the elastic segment during the half cycles where the ground motion is not strong. However, the changes of elastic stiffness are mainly due to structural degradation and can thus be identified using significant (large) half cycles of response, such as S1, S2 and S3 shown in Figure 6.6.

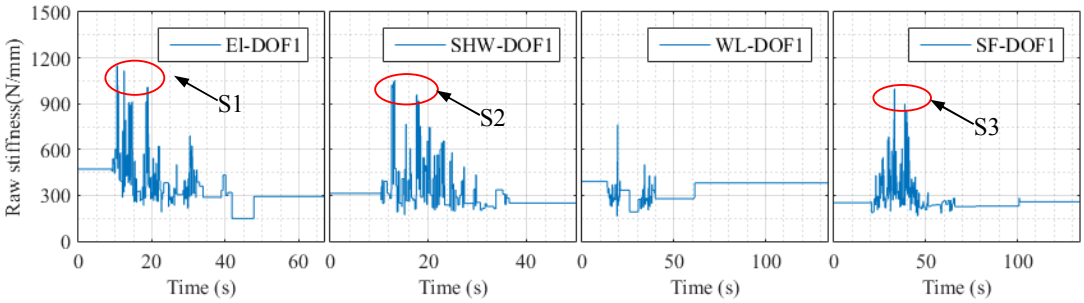

Figure 6.6: Identified evolution of stiffness for the first DOF (DOF1) using all half cycles.

Figures 6.7-6.9 shows the details of the selected half cycles S1, S2 and S3 during the EI, SHW and SF events. It can be seen that the measurement data of all these half cycles fitted well using the identified HLA regression models, and significant elastic segments are obtained in these half cycles for the evaluation of structural degradation. In addition, the integrations of these half cycles in Figures 6.7(b)-6.9(b) include a full nonlinear dynamic response compared to the measured hysteresis loops in Figures 6.7(c)-6.9(c), which clearly show that all the critical nonlinear characteristics of the hysteresis loops can be well represented by these significant half cycles. Therefore, the elastic stiffness of significant half cycles can be used for damage identification when the ground motion is strong, as also seen in Chapter 4.

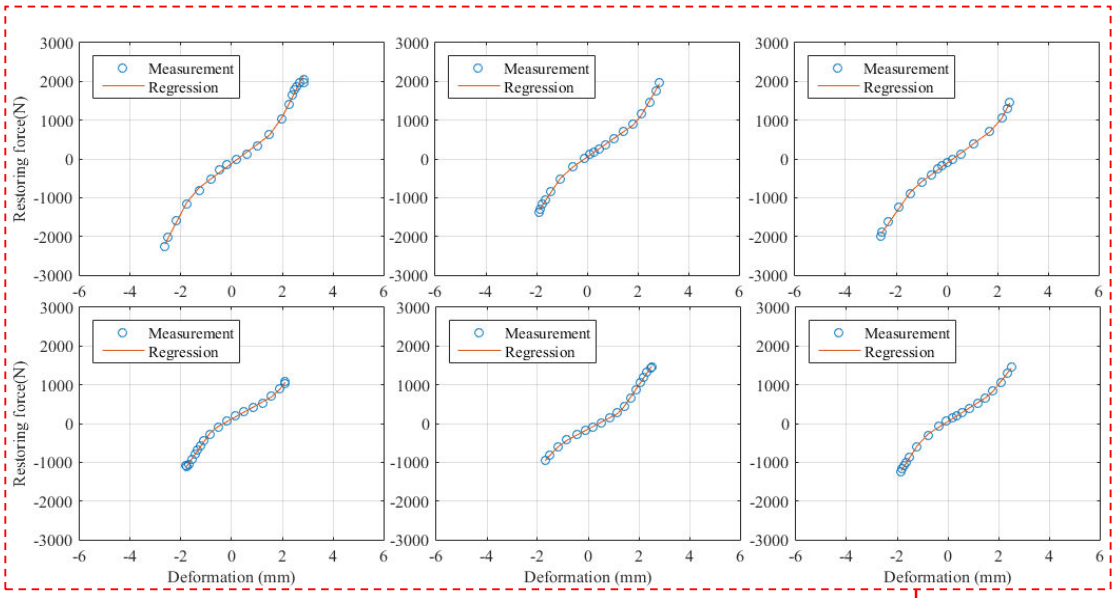

(a) Selected significant half cycles of S1

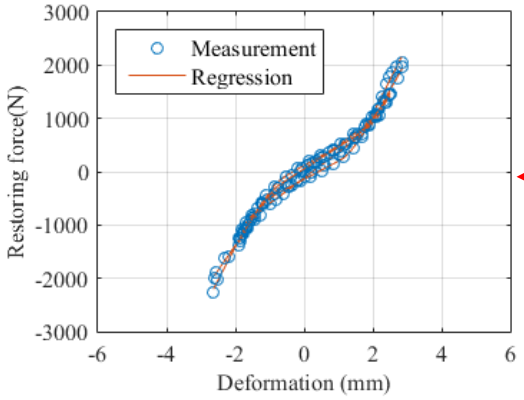

(b) Half cycle integration of S1

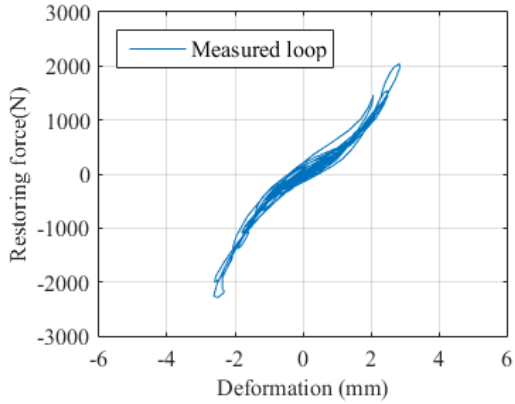

(c) Measured hysteresis loop of El (all half cycles)

Figure 6.7: Significant half cycles of S1 during El event.

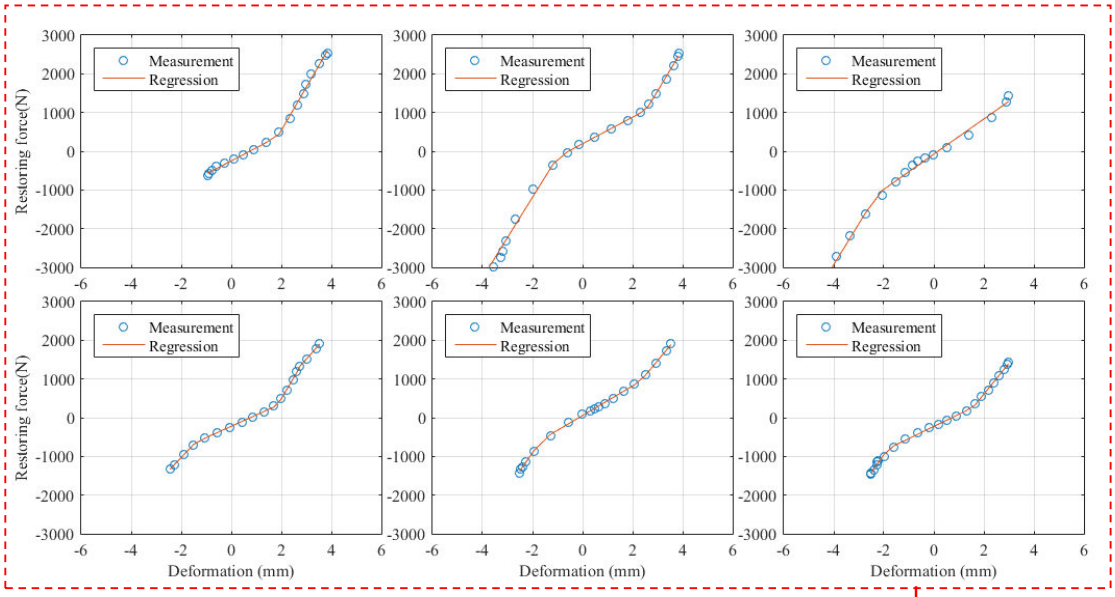

(a) Selected significant half cycles of S2

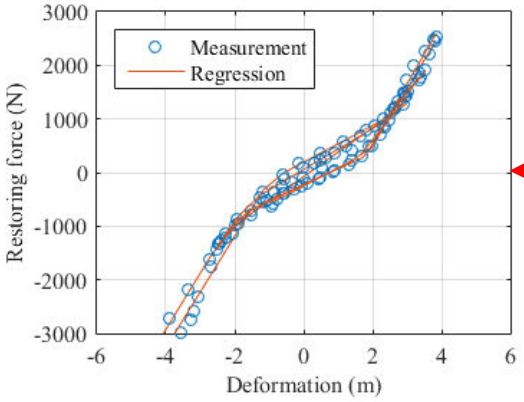

(b) Half cycle integration of S2

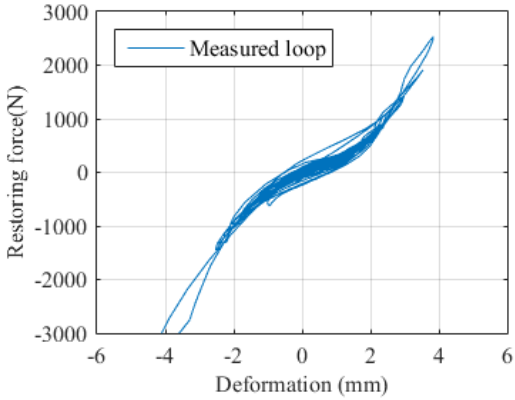

(c) Measured hysteresis loop of SHW (all half cycles)

Figure 6.8: Significant half cycles of S2 during SHW event.

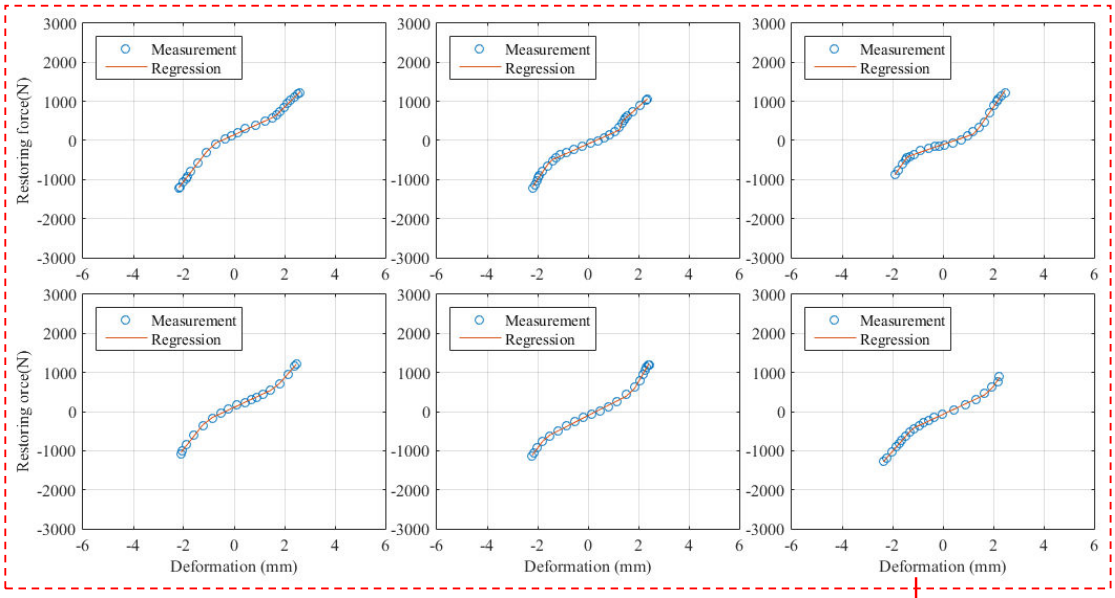

(a) Selected significant half cycles of S3

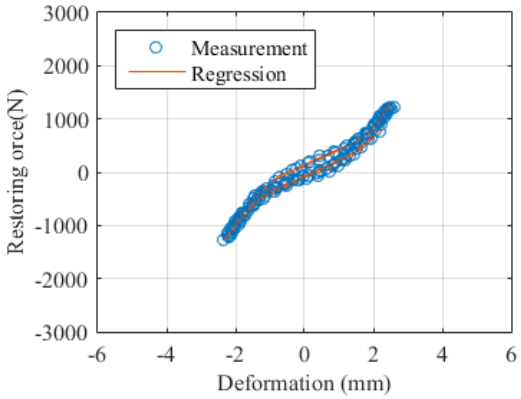

(b) Half cycle integration of S3

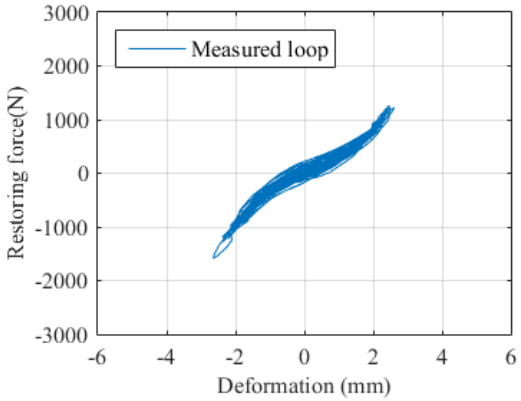

(c) Measured hysteresis loop of SF (all half cycles)

Figure 6.9: Significant half cycles of S3 during SF event.

Figure 6.10 shows the identified elastic stiffness for the first DOF (DOF1) using the significant half cycles S1, S2 and S3. Figures 6.11-6.15 show the identified nonlinear and elastic stiffness for the other DOFs (DOF2-DOF6). It is noted that the ground motion during the WL event is very small and the seismic response is only within the pinching and/or a slightly hybrid range, as shown in Figure 6.5. Thus, no significant half cycles were generated during the WL event and the elastic stiffness for WL can be considered to be the same as the previous event.

Importantly, it can be seen that the identified initial stiffness of the SHW event matched well with the identified final stiffness of the El event. These results should be expected, and thus help validate the method and its continuity over different sequential events. In addition, the identified initial stiffness of the SF event also matched well with the identified final stiffness of the SHW event, which also shows that no stiffness degradation occurred during the WL event.

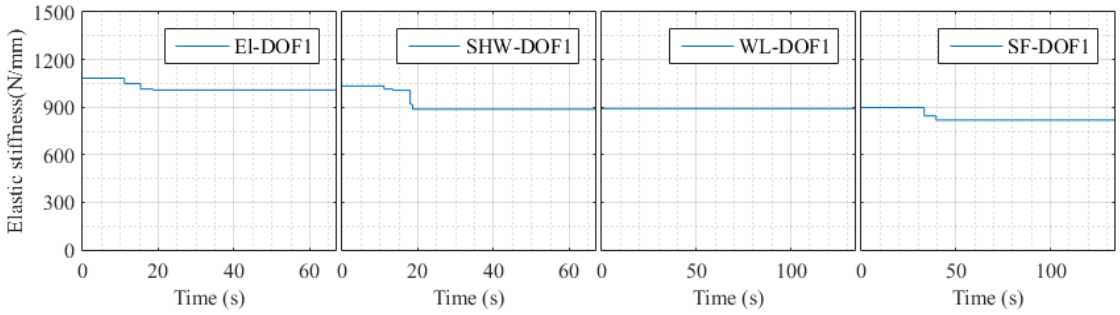

Figure 6.10: Identified elastic stiffness for the first DOF using significant half cycles.

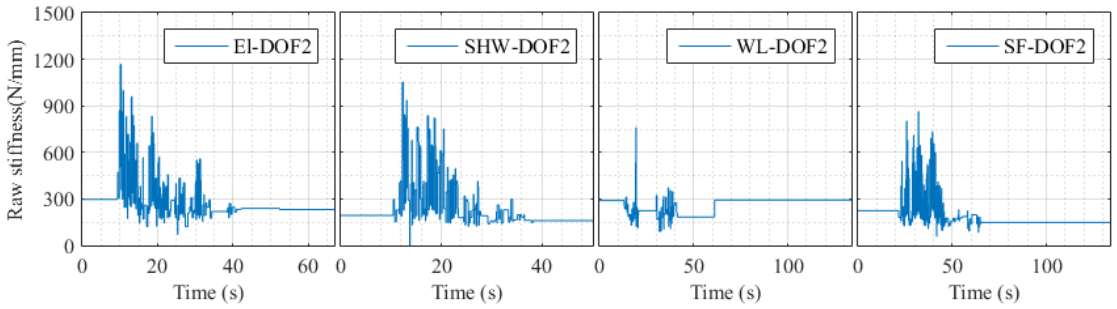

(a)

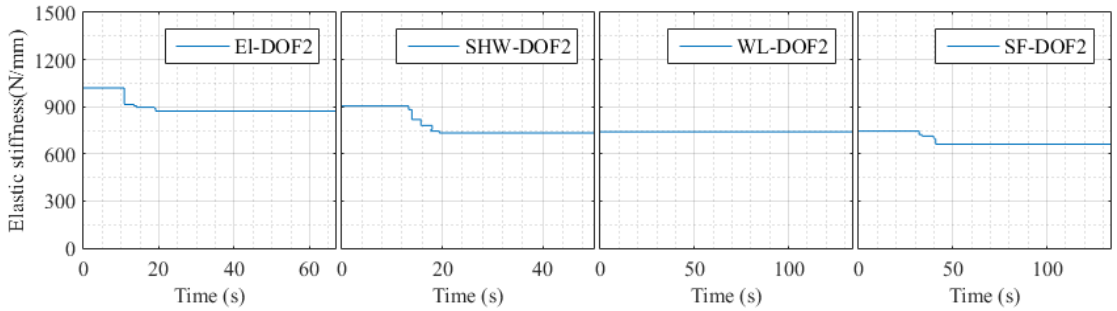

(b)

Figure 6.11: Identified evolution of stiffness for the second DOF using (a) all half cycles and (b) significant half cycles.

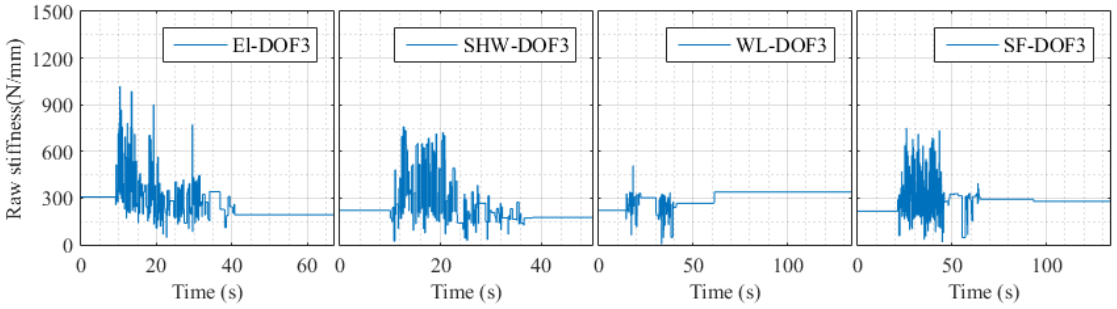

(a)

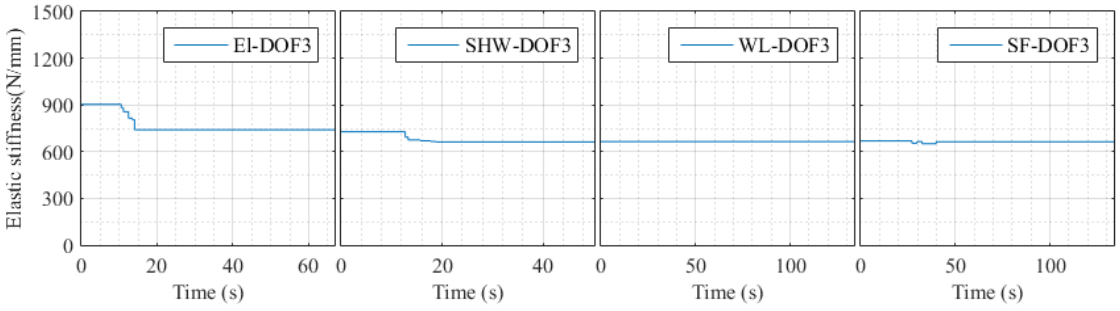

(b)

Figure 6.12: Identified evolution of stiffness for the third DOF using (a) all half cycles and (b) significant half cycles.

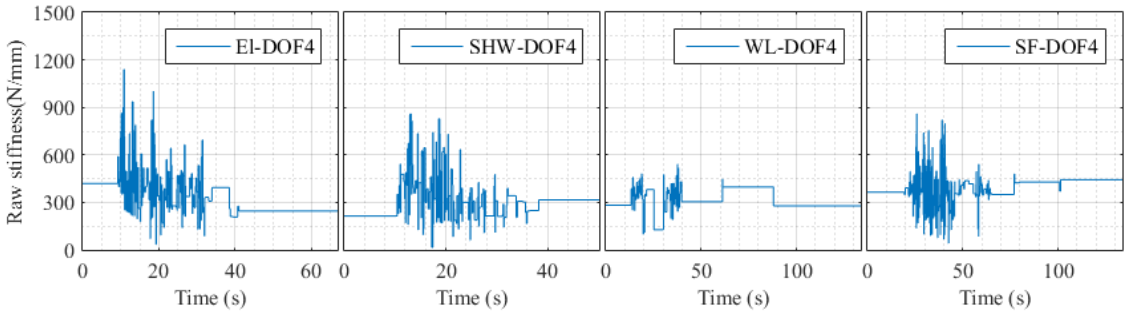

(a)

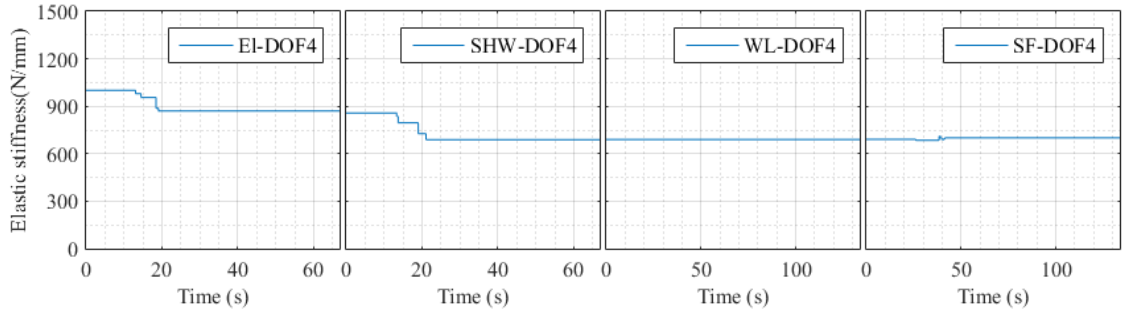

(b)

Figure 6.13: Identified evolution of stiffness for the fourth DOF using (a) all half cycles and (b) significant half cycles.

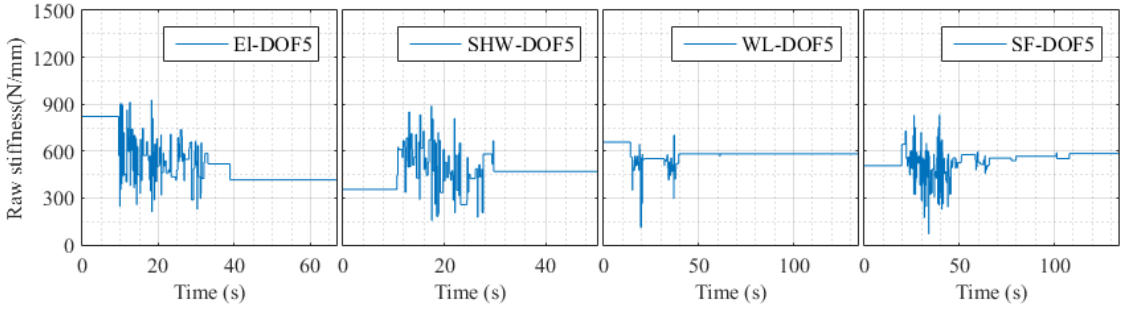

(a)

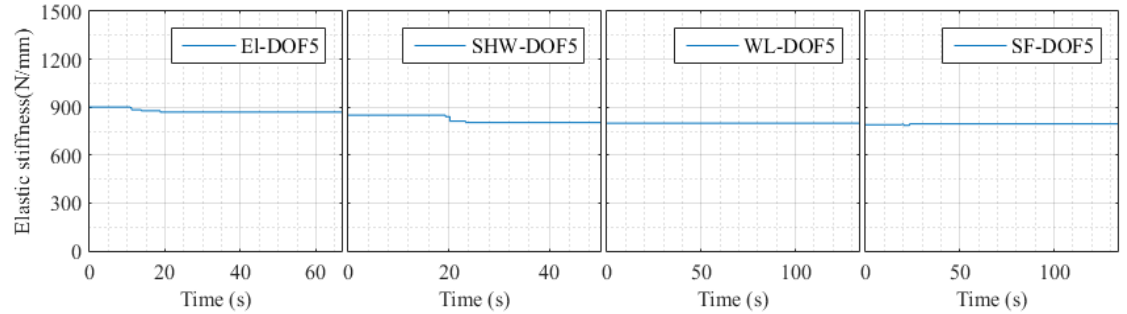

(b)

Figure 6.14: Identified evolution of stiffness for the fifth DOF using (a) all half cycles and (b) significant half cycles.

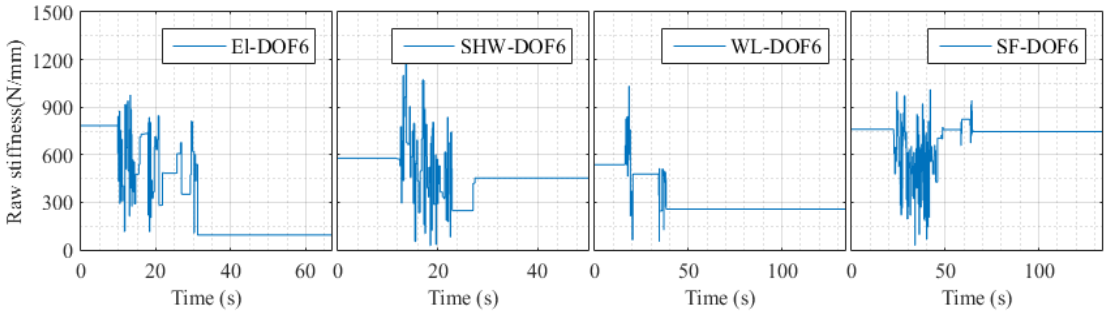

(a)

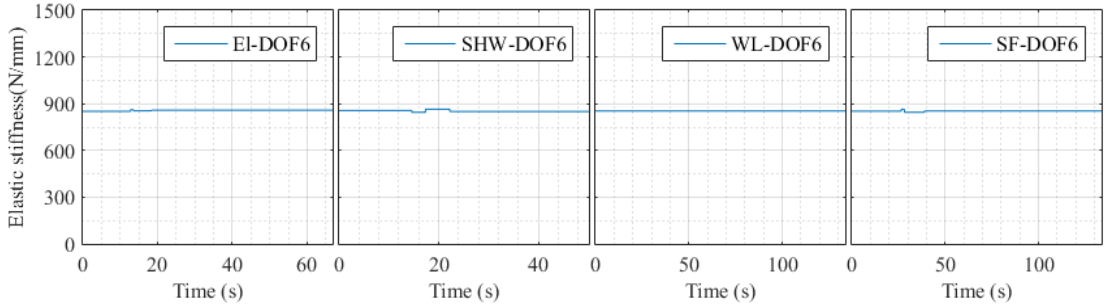

(b)

Figure 6.15: Identified evolution of stiffness for the sixth DOF using (a) all half cycles and (b) significant half cycles.

6.4.2 Summary of Damage of RCF12

Table 6.1 lists the identified degradation of elastic stiffness for each DOF of RCF12. It can be seen that the stiffness degradation for DOF2-DOF4 are much larger than for DOF5 and DOF6 due to the larger shear force in the lower floor. These results are validated by the fact that more severe damage including cross cracks and diagonal cracks were observed at the beam-column joints for the third, fourth and fifth storey, as shown in Figure 6.4. However, only a few vertical cracks were observed at the higher sixth and seventh storey, and no cracks were visually observed for the 8^{th}-12^{th} storey.

Table 6.1 Identified degradation of elastic stiffness of RCF12

DOF	Degradation of elastic stiffness				Total degradation	Identified final stiffness (N/mm)
	El	SHW	WL	SF		
1	4.5%	13.6%	0%	8.8%	18.1%	818
2	11.2%	16.9%	0%	5.9%	34.0%	685
3	18.0%	8.7%	0%	0%	26.7%	660
4	13.1%	16.6%	0%	0%	29.7%	695
5	3.5%	5.1%	0%	0%	8.6%	791
6	0%	0%	0%	0%	0%	853

In addition, the stiffness degradation for the first DOF (DOF1) is smaller than the upper storeys and no cracks were observed at the first floor, which is similar to the experimental and SHM results of the single-bay experimental RC building in Chapter 4. Because the damage or failure of RC buildings has been mainly attributed to soft-storey mechanisms during earthquakes (Goel, 2003; Naeim et al., 2000; Park, 1986; Sezen et al., 2003), many buildings have a soft storey at the first-floor level.

The first storey of such structures is often used for stores and open commercial area without structural walls (Doğangün, 2004). An abrupt change of lateral stiffness between frames of the first storey to the structural walls of the upper storeys can thus lead to a dangerous concentration of ductility demand in the soft first storey and further cause severe damage or collapse of the building during earthquakes (Park, 1986). Therefore, adequate structural walls should be considered and arranged in the first soft storey provided with poor structural features to prevent building collapse. A few examples that cracks were observed at the interior beam-column joints of the second storey rather than the first storey of RC frame building due to the construction of infill walls in the first storey, were presented during the field investigation after 2008 Wenchuan earthquake in China (Zhao et al., 2009).

The soft storeys for both the single-bay and two-bay RC frame experimental buildings are also upper storeys rather the first storey, because the experimental buildings were built without structural walls at any storey and the first storey had a much larger lateral stiffness than the upper storeys due to the strong connection between the columns of the first storey and the base. Therefore, damage primarily occurred at the upper storeys due to the greater deformation demand required during the earthquakes.

6.5 Determination of Effective Stiffness Using MRA

The application of the HLA method enables rapid identification of nonlinear structural stiffnesses for damaged structures. The extraction of the elastic stiffness based on the selection of significant half cycles can be used to examine structural degradation readily under strong earthquake excitations, such as the El, SHW and SF events used here. However, the elastic range became negligible when the structural response was small, as during the WL event, and only stiffnesses of pinching and/or hybrid range were identified to characterize structural deterioration. Therefore, a wavelet multiresolution analysis (MRA) is proposed to decompose an effective linear stiffness from the identified nonlinear half cycles using the HLA method for identifying the structural deterioration under both large and small event.

In particular, the equation of motion for a MDOF nonlinear system can be defined:

$$M\ddot{X}(t) + C\dot{X}(t) + K_e X(t) + F_k(X(t)) = F(t) \tag{6.10}$$

where M, C and K_e are the mass, damping and linear stiffness matrices, respectively. F is the force excitation vector. The nonlinear stiffness force F_k represents a deviation from the linear stiffness force $K_e X$ and can be approximated (Muravyov and Rizzi, 2003; Rizzi and Muravyov, 2000):

$$F_k(X(t)) \approx K_n X(t) \tag{6.11}$$

where K_n is the nonlinear contribution to the total stiffness and depends on the amplitude of vibration. Thus, the total nonlinear stiffness force F_T can be defined:

$$F_T = K_T X(t) = (K_e + K_n) X(t) \tag{6.12}$$

When the displacement is small, the nonlinear stiffness becomes negligible and the total stiffness K_T is reduced to the regular linear term K_e. Note that the natural frequency, w_0, which is typically used for damage detection, is also measured from the linear response and can be calculated in terms of structural mass M and the effective linear stiffness K_e (Londoño et al., 2015; Rao and Gupta, 1999). However, the amplitude-dependent stiffness K_T is attributed to the changes of nonlinear resonance frequency, w, which also depends on the amplitude of vibration and is shifted from its linear elastic natural frequency, w_0, (Landau and Lifshi͡ts, 1976; Papadrakakis et al., 2011; Papadrakakis et al., 1996; Wang and Zheng, 2016).

Therefore, the degradation of the effective linear stiffness K_e can be tracked to identify the damage that usually leads to a decrease of natural frequency, w_0. In addition, the effective stiffness K_e is determined at each storey and can thus localize the damage, which is not the case for frequency-based SHM methods because damage in different storeys may cause similar changes in overall natural frequency (Pandey and Biswas, 1994; Vafaei et al., 2013). Finally, the effective stiffness K_e is present under both linear and nonlinear dynamic behaviour and can be identified at different event levels.

To extract the effective linear stiffness K_e from the total stiffness K_T, a multiresolution analysis (MRA) is applied to the total stiffness K_T at each segment of the half cycles identified using the HLA in the previous section. In particular, any given signal $f(x) \in L^2(R)$ in

MRA can be decomposed to a sequence of closed subspace V_j of $L^2(R)$, $j \in Z$, which have the following properties (Mallat, 1989):

$$\cdots V_{-2} \subset V_{-1} \subset V_0 \subset V_1 \subset V_2 \cdots \tag{6.13}$$

$$f(x) \in V_j \Leftrightarrow f(2x) \in V_{j+1}, \qquad j \in Z \tag{6.14}$$

$$f(x) \in V_j \Leftrightarrow f(x-k) \in V_j, \qquad j,k \in Z \tag{6.15}$$

$$\overline{\bigcup_{j \in Z} V_j} = L_2(R), \ \bigcap_{j \in Z} V_j = \{0\} \tag{6.16}$$

Consider j and k to be a dilation and translation index, respectively. An orthonormal basis, ϕ, for the scaling function is constructed for the approximation space V_j:

$$\phi(x) = \sqrt{2} \sum_{k \in Z} h_k \phi(2x-k) \tag{6.17}$$

where h_k is the discrete low-pass filter. Hence, any function $f(x) \in L^2(R)$ can be approximated with resolution of 2^j using its projection $P_j f$ on V_j. In addition, an approximation at a space V_{j+1} with the resolution of 2^{j+1} also contains all the information to compute the same function at a smaller space V_j because $V_j \subset V_{j+1}$. The difference details between the approximation space V_{j+1} and V_j can represented using a wavelet detailed space W_j that is the orthogonal complement space of V_j in V_{j+1}, such that:

$$V_{j+1} = V_j \oplus W_j \tag{6.18}$$

Using the decomposition of Equation (6.18) recursively, V_{j+1} can be written:

$$V_{j+1} = V_l \oplus W_l \oplus \cdots \oplus W_{j-1} \oplus W_j \qquad l \in Z \tag{6.19}$$

where all the subspaces are orthogonal. An orthonormal basis, ψ, that is related to the scaling function, ϕ, is also formed for the wavelet space W:

$$\psi(x) = \sqrt{2} \sum_{k \in Z} g_k \phi(2x-k) \tag{6.20}$$

where g_k is the symmetric filter with $g_k=(-1)^{1-k}h_{1-k}$. Therefore, the original signal $f(x)$ can be expressed using the scaling (approximation) function ϕ and the wavelet (detail) function ψ at all decomposition levels:

$$f(x)=\sum_k c_{l,k}\phi_{l,k}(x)+\sum_{j=l+1}^{\infty}\sum_k d_{j,k}\psi_{j,k}(x) \tag{6.21}$$

where $c_{j,k}$ and $d_{j,k}$ are the scaling and wavelet coefficients, respectively, and can be computed:

$$c_{j,k}=<f,\phi>=\int f(x)\tilde{\phi}_{j,x}(x)dx \tag{6.22}$$

$$d_{j,k}=<f,\psi>=\int f(x)\tilde{\psi}_{j,x}(x)dx \tag{6.23}$$

where $\tilde{\phi}$ and $\tilde{\psi}$ are the complex conjugates of ϕ and ψ, respectively. Note $\phi=\tilde{\phi}$ and $\psi=\tilde{\psi}$ if ϕ and ψ are orthogonal bases.

Thus, the time-varying vector of the identified raw stiffness K_T can be transferred into a series of time-invariant scale and wavelet coefficients using multiresolution expansion:

$$K_T(t)=K_e(t)+K_n(t)+e(t)=\sum_{k=-\infty}^{\infty}c_{J,k}\phi_{l,k}(t)+\sum_{j=1}^{J}\sum_{k=-\infty}^{\infty}d_{J,k}\psi_{j,k}(t) \tag{6.24}$$

The approximation terms interpret the inherent linear stiffness K_e that is amplitude-independent in the total stiffness K_T at a coarse scale J. However, the detail terms characterize the discontinuity and uncertainty information, whose evolution is based on the magnitude of vibration and noise level, in the raw stiffness at a finer scale $j=1,\ldots,J$.

Because the resolution scale can determine the occurrence or absence of a certain phenomenon, selecting an appropriate scale J is important for identifying the particular interest of K_e. Statistical laws of the loglog type offer a rough indication for selecting a resolution scale, J (Coca and Billings, 2001; Sjöberg et al., 1995; Wei and Billings, 2002):

$$\frac{N}{\ln N} \leq 2^J \leq \frac{2N}{\ln N} \tag{6.25}$$

where N is the number of observations. In addition, the scale will be also such that at least one observation is within the support of the corresponding wavelet.

Note that the application of MRA is not unique and depends on the choice of wavelet. Thus, no class of wavelets can yield good results for all applications (Chang and Shi, 2010). The selection of wavelet in this study is mainly based on the properties of good regularity and symmetry of the wavelet, which ensures smoothness and linearity in the frequency response phase as it is a very desirable property in many applications (Ovanesova and Suarez, 2004). Hence, the biorthogonal wavelet *bior6.8*, which is compactly supported spline wavelet for symmetry and exact reconstruction, is chosen for MRA from the Matlab Toolbox, and is shown in Figure 6.16.

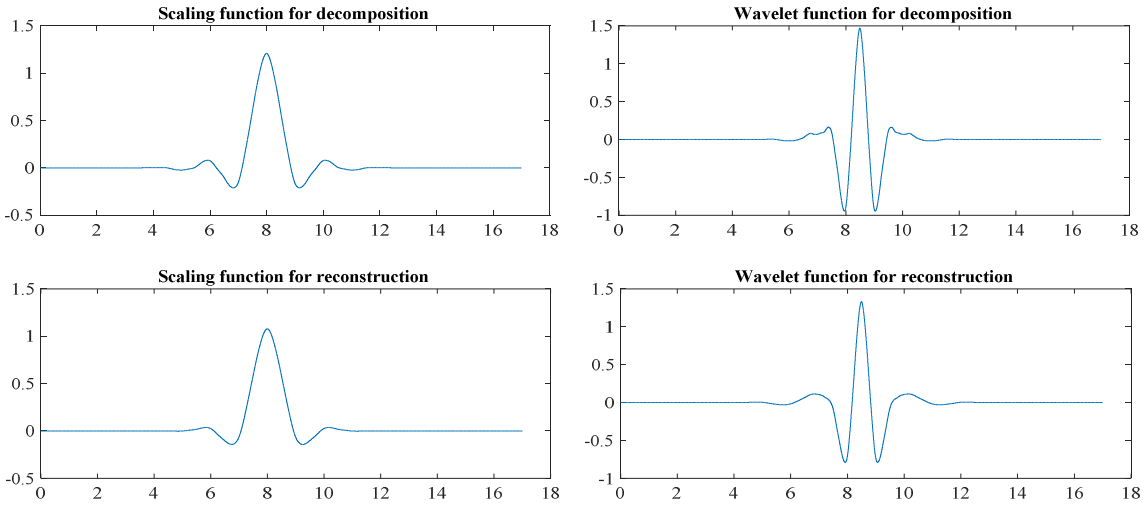

Figure 6.16: *bior6.8* wavelet and scaling functions

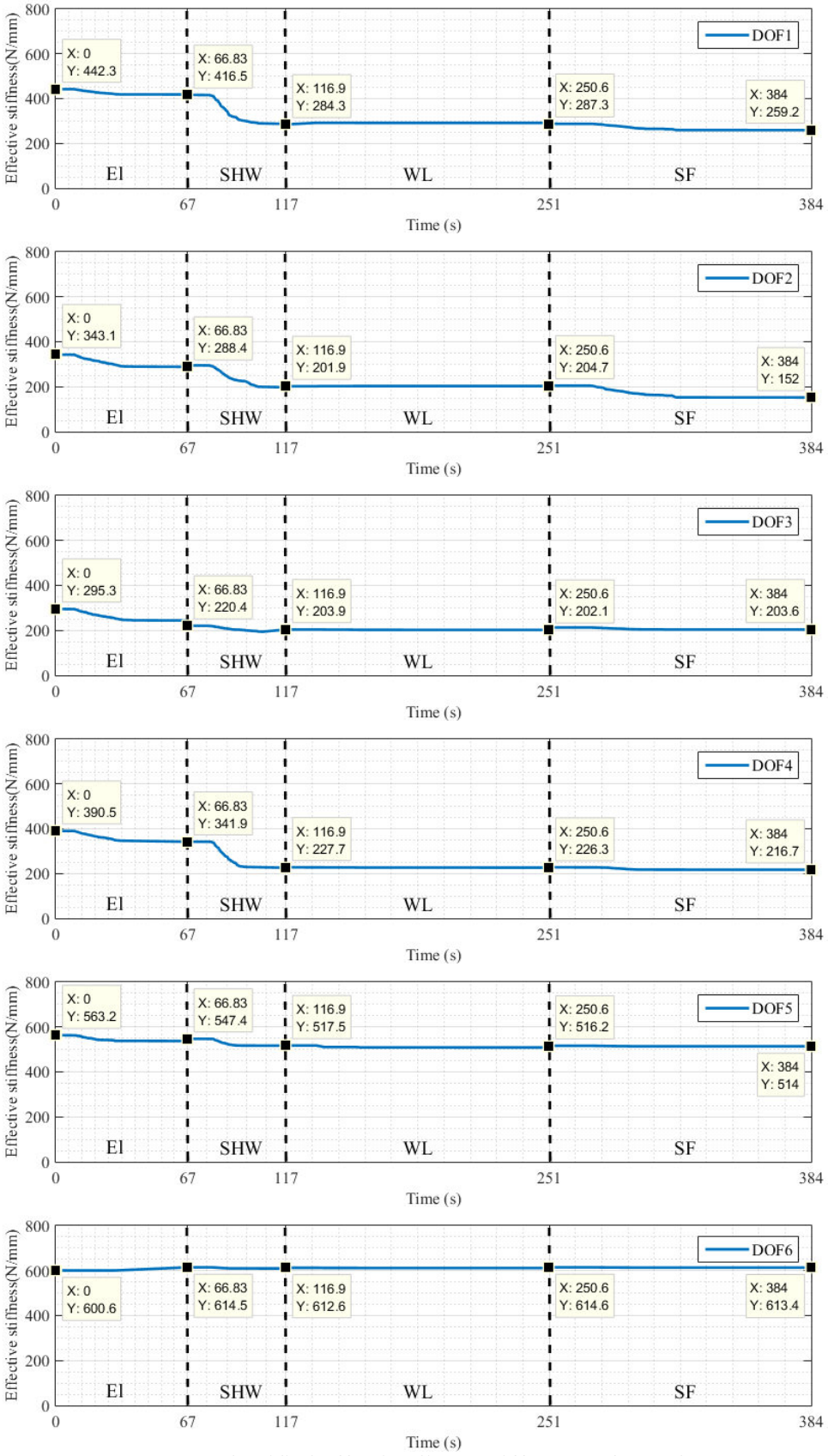

Figure 6.17: Identified effective linear stiffness K_e for each DOF.

Figure 6.17 shows the identified effective linear stiffness K_e for each DOF subjected to El, SHW, WL and SF event, sequentially. It can be seen that the effective stiffnesses were identified consistently between each event. The identified final stiffness of the nonlinear SHW event matched well with the identified initial stiffness of the linear WL event, and also the identified final stiffness of the WL event matched well with the initial stiffness of the following nonlinear SF event, which indicates the effective linear stiffness can be tracked for and over both linear and nonlinear events.

To assess the accuracy of the identified results, the fundamental natural frequency is calculated using the identified initial stiffness of the El event, and then compared to the measured frequency from the transfer function of the white noise test WN1 before the El event. In addition, the fundamental frequency after the SHW event can also be obtained from the transfer function of the WL event for comparison to the calculated frequency using the identified final stiffness of the SHW event, because the amplitude of vibration for the WL event is mainly within the linear range and the natural frequency can thus be considered to be amplitude-independent.

Figure 6.18 shows the measured transfer functions of the white noise test WN1 and the linear WL event. Table 6.2 lists the identified and measured frequency during these events. It can be seen that the identified fundamental frequency before the El event matched very well with the measured frequency of WN1 with only 1.4% estimation error. In addition, the identified frequency for the linear WL event also matched well with the measured frequency with 5.7% estimation error. These results imply that the effective linear stiffnesses that are related to the changes of natural frequency, were accurately identified for each DOF using MRA and can thus be used as an index for damage assessment and localization for both linear and nonlinear

earthquake events.

Table 6.2 Comparison of the identified and measured frequency

Event	Measured (Hz)	Identified (Hz)	Difference
Before the El event (WN1)	1.44	1.42	1.4%
WL event	1.21	1.14	5.7%

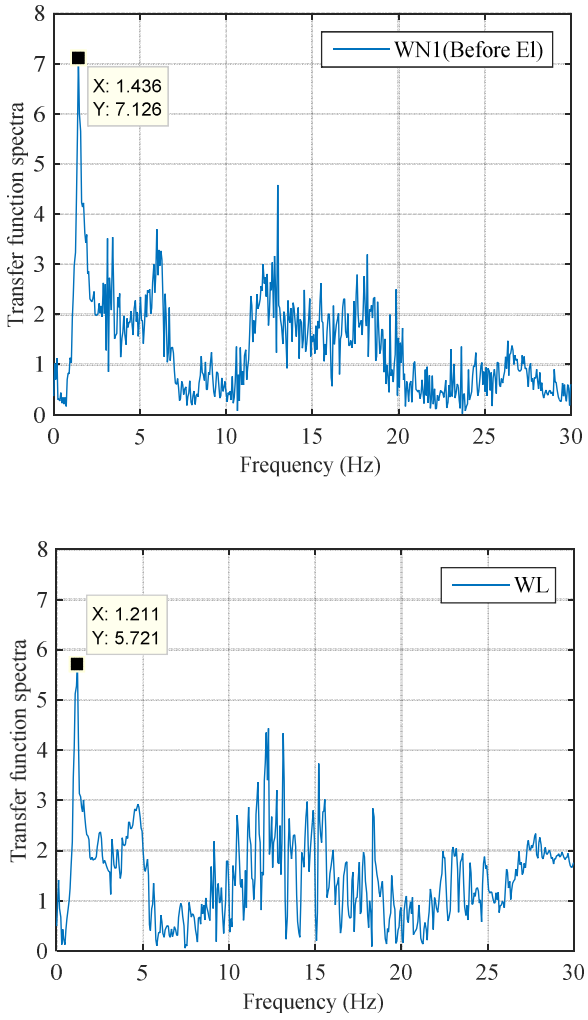

Figure 6.18: Measured transfer functions of WN1 and WL event.

6.6 Summary

In this chapter, the HLA method is further validated using a similar experimental two-bay RC building to the single-bay building in Chapter 4. Severe damage cracks were observed prior to the shaking table test El, SHW, WL and SF event, and thus lead to more complex hysteretic behaviours.

The identification of the evolution of the nonlinear stiffness for each DOF show that the stiffness is changing among the pinching, hybrid and elastic stiffness based on the magnitude of the structural dynamic response. The elastic stiffness was obtained by selecting the significant half cycles and then used for identifying the stiffness degradation under strong earthquake events El, SHW and SF. The results show that the application of the HLA method enables an accurate and consistent identification of stiffness degradation over different strong events. In addition, the elastic range was negligible and no significant half cycles were generated during the small WL event, which indicated no further degradation occurred for this event.

The proposed MRA method extracted an effective linear stiffness from the identified nonlinear stiffness by the HLA method. The results show that the effective linear stiffnesses were identified consistently between each event, and can thus be tracked for both large and small ground motions. In addition, the calculated fundamental natural frequency using the identified effective linear stiffness matched very well with the measured frequency. The estimation errors are only 1.4% and 5.7% for the WN1 and WL event, respectively. This results implies the effective linear stiffness was accurately identified for each story using the MRA method and can be an efficient index for damage for damage assessment and localization during earthquakes.

Chapter 7: Performance Evaluation of the Base-isolated Christchurch Women's Hospital (CWH) Building during Two Major Earthquakes in Christchurch

7.1 Introduction

Isolating of structures from ground motion is an effective way to protect the structure from damage in a strong earthquake. The basic concept of base isolation is to provide a low lateral stiffness between the structure and the foundation to lengthen the natural period of the building form its fixed base value and the dominant periods (1/frequencies) of the seismic ground motion. Thus, the transmission of earthquake motion and force to the superstructure of the isolated building can be significantly reduced (Skinner, 1993).

Successful field performance of a base-isolated building was first recorded and validated in the University of South California (USC) Hospital building during the 1994 Northridge earthquake, USA. Due to the lead rubber bearings (LRB) isolation system, peak roof accelerations were reduced to 50% of the foundation acceleration, and the peak drift of the superstructure was less than 30% of the code specification (Nagarajaiah and Sun, 2000).

The measured response of two high damping rubber bearing isolated buildings in Miyagi and Chiba, Japan were investigated during the 2011 Tohoku earthquake (Miwada et al., 2012). The study confirmed acceleration reductions in both buildings, and the maximum accelerations at the floor above the isolated layer were 41%-83% of those at the basement. The strong motion seismic records of Fukushima Dai-Ichi Nuclear Power Plant were also reported during the Great East Japan Earthquake in 2011 (Hijikata et al., 2011). This base isolated structure performed well in horizontal motion with the response reduced by 30%

from the basement pit.

The Christchurch Women's Hospital (CWH) building was opened in 2005 and is the only base-isolated structure in the South Island of New Zealand. The city of Christchurch was shocked by a series of major earthquakes between September 2010 and December 2011. A magnitude 7.1 earthquake (Mw7.1) on September 4th, 2010 caused widespread damage to the structures of the city, and a magnitude 6.3 earthquake (Mw6.3) on February 22nd, 2011 caused more severe damage to the city business district and resulted in the losses of 185 lives. Because of the repeated occurrence of earthquakes in this region, a seismic monitoring system was installed at the CHW in September 2011 to collect the seismic response data for performance evaluation of a modern base-isolated structure in service during subsequent aftershocks (Gavin et al., 2012; Sridhar et al., 2014). In particular, seismic response of the CWH building during two major events (Mw5.8 at 1:58pm and Mw6.0 at 3:18pm local time) were recorded on December 23rd, 2011 and are the largest magnitude events among over a hundred recorded seismic events (Kuang et al., 2015). These measurements thus provide a unique opportunity to identify a structure for two, similarly sized large events occurring within a few hours on an essentially unchanged structure.

In this chapter, the seismic measurements of the CWH building are used to investigate its structural behaviour, which is largely linear, during the two major Mw5.8 and Mw6.0 earthquakes in December 2011. The hysteresis loops for the base isolation system and superstructure system are constructed using the recorded accelerations and/or displacements. The HLA method is then applied to the reconstructed hysteresis loops to identify the structural stiffness of each system for performance evaluation of the CWH building during the two events.

7.2 Building and Instrumentation

The CWH building is a nine-storey reinforced concrete frame structure with cast-in-place columns and pre-cast beam elements. The building is regular in plan and elevation. The main dimensions are 76m long, 32m wide and 33m high. The four lower storeys were built with steel V-bracing to support transverse lateral loading, and the three higher storeys were built without V-bracing. The top two levels contain building service equipment and water tanks (Gavin and Wilkinson, 2010). In addition, the corridor of the CWH building is linked to adjacent Parkside West building at the fourth above-ground floor with sliding cover plates to provide seismic separation. The base isolation system of the CWH building consists of 41 LRBs and four pot bearings founded on a concrete raft foundation slab. The design specifications of the LRBs and pot bearings are listed in Tables 7.1 and 7.2, respectively (Sridhar et al., 2014).

Accelerometers and/or string potentiometer are located across the isolation layer, below and above the isolator, and the sixth storey (Kuang et al., 2015). In particular, a tri-axial accelerometer were installed at each location below the isolator and the sixth storey in both Northeast (NE) and Southwest (SW) corners. In addition, uni-axial accelerometers were installed above the isolator in both the NE and SW corners. The relative displacement between the foundation and the ground floor was also measured by uni-axial displacement sensors, providing a second, direct measure of this important motion. The installation of sensors in both NE and SW corner ensure both the translational and torsional responses of the superstructure are measured. Figure 7.1 shows the configurations and sensor locations of the CWH building. The detailed design and structural drawings of the CWH building were received from Holmes Consulting (Sridhar et al., 2014).

Table 7.1 Design parameters for LRB bearings

Designation	LRB
Total design displacement (mm)	265
Total maximum displacement (mm)	420
Compression stiffness (kN/mm)	1794
Design shear force at total design displacement (kN)	740
Design area of hysteresis loop at total design displacement (kN.mm)	366600
Average (dead load(DL)+serviceability live load (SLL)) (kN)	3495
Average (DL+ SLL+$E_{(DBE)}$) (kN)	4466
Average (DL-$E_{(DBE)}$) (kN)	2166
Maximum (DL+live load (LL)) (kN)	4417
Maximum (DL+SLL+$E_{(MCE)}$) (kN)	6570
Minimum (DL-$E_{(MCE)}$) (kN)	357

Note:
1. Total design displacement is DBE (design basis earthquake)
2. Total maximum displacement is MCE (maximum considered event).
3. Design shear force is calculated as $F=Q_d+K_r\Delta$ where Q_d is the isolator characteristic strength, K_r is the stiffness and Δ is the DBE displacement.
4. Area of hysteresis loop is calculated as $4Q_d(\Delta-\Delta_y)$ where Δ_y is the yield displacement of the isolator.

Table 7.2 Design parameters for pot bearings

Designation	LRB
Average (DL+ SLL) (kN)	4986
Maximum (DL+ SLL) (kN)	5768
Maximum motion (mm)	+/-420
Maximum rotation (rad)	0.006
Maximum dynamic friction coefficient (dry)	0.12

(a)

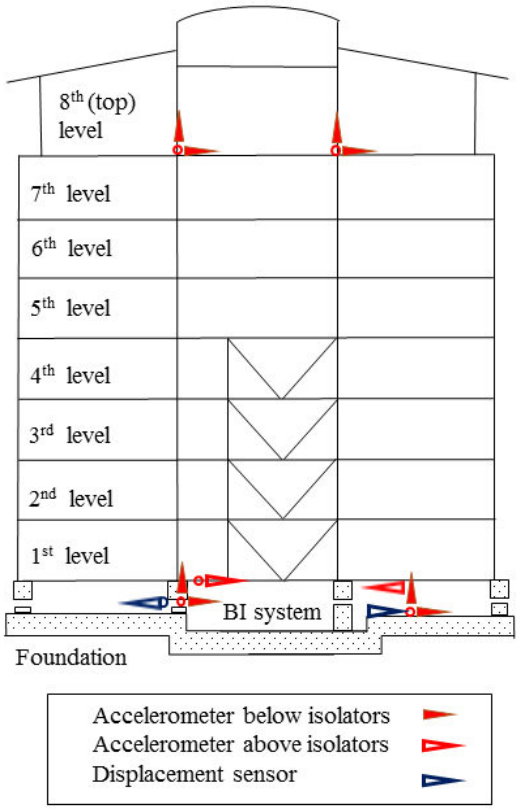

(b)

Figure 7.1: (a) Photo of CWH building (Holmes Consulting Group) and (b) elevation of CWH building.

7.3 Recorded Response

Figures 7.2 and 7.3 shows the recorded accelerations of both the NE and SW corners in the *y*-direction for the Mw5.8 and Mw6.0 events, respectively. It can be seen that there is almost no difference in recorded accelerations between the NE and SW corners for the foundation and first level, and the recordings for the top level are also largely identical between both corners. This result indicates no significant torsional component was present in the building response, and thus only the recordings in the NE corner are used for the reconstruction of hysteresis loop and system identification.

The superstructure of a base-isolated building is frequently assumed to be a lumped mass, since the isolated building should be quite rigid in comparison to the isolation system (Kulkarni and Jangid, 2002). However, the magnitude and phase of the recorded accelerations are different between the first and sixth levels during both the Mw5.8 and Mw6.0 events, as shown in Figures 7.2-7.3. Therefore, the superstructure of the CWH building does not approximate a rigid body as might be expected for a base-isolated structure.

It also can be seen from Figures 7.2-7.3 that the peak accelerations of the top level were significantly increased compared to the isolator level and foundation, rather than reduced, as in successful performance cases of base isolation (Hijikata et al., 2011; Miwada et al., 2012; Nagarajaiah and Sun, 2000) from Introduction. In addition, the acceleration above the isolator was consistent with the acceleration below the isolator, which indicates the base isolation system was still within the stiffer linear range and did not significantly deform or lead to the period separation of the ground shaking and the building during the two events. These results imply both the BI and superstructure were behaving within a linear range during the two major events and further support a consideration of a multi-degree of freedosm of linear shear

model for the modelling of the superstructure (Kuang et al., 2015; Sridhar et al., 2014; Zhou et al., 2015; Zhou et al., 2015).

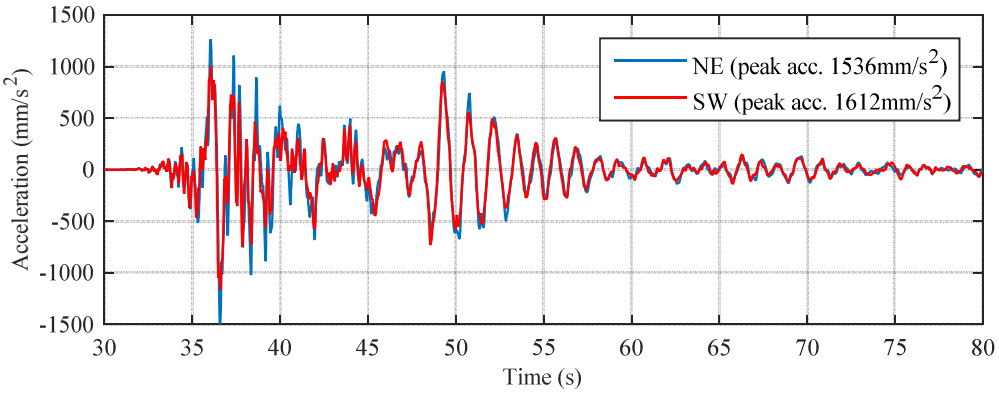

(a)

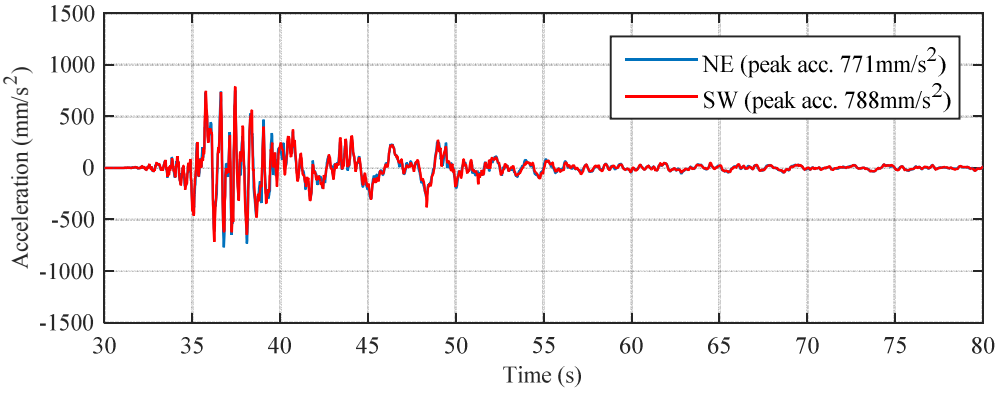

(b)

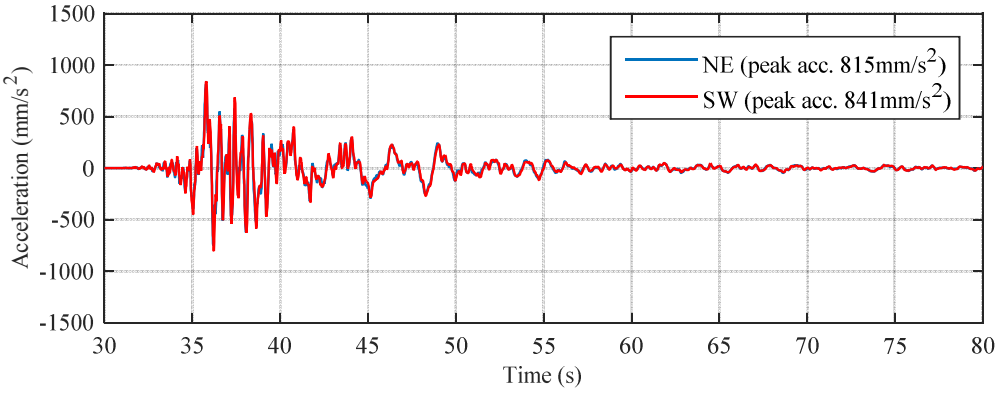

(c)

Figure 7.2: Recorded accelerations of Mw 5.8 event for (a) the top level, (b) above the isolator (first level), and (c) below the isolator (foundation).

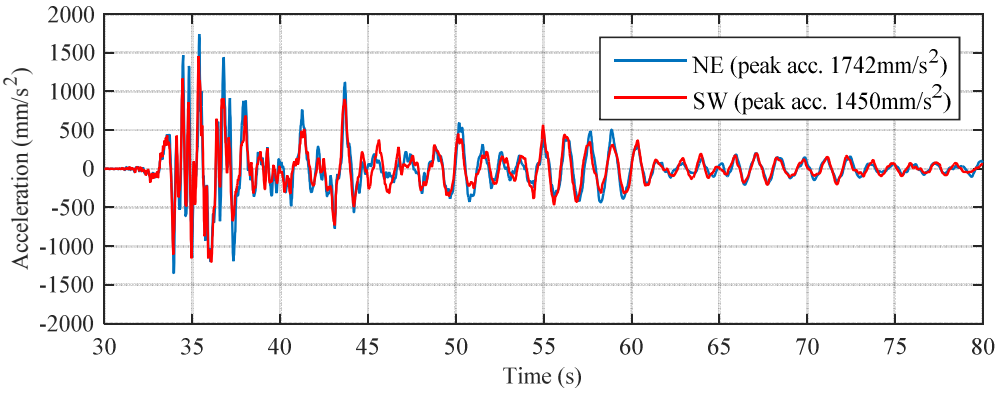

(a)

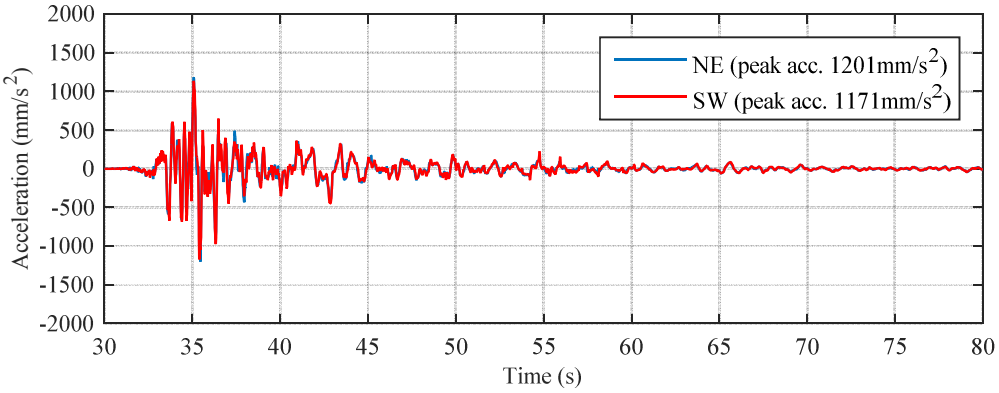

(b)

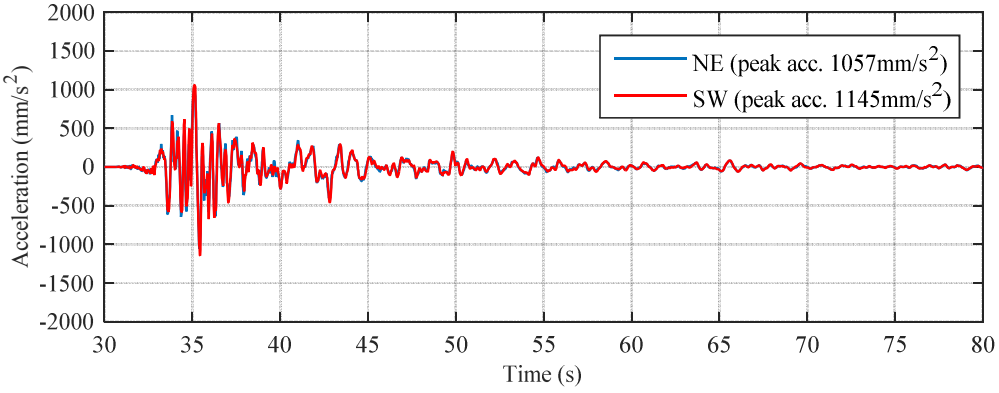

(c)

Figure 7.3: Recorded accelerations of Mw 6.0 event for (a) the top level, (b) above the isolator (first level), and (c) below the isolator (foundation).

7.4 Reconstruction of Hysteresis Loop

With the recorded response of the top floor, the ground floor (above the isolator) and the foundation (below the isolator), the CWH building is modelled as a two degrees of freedom system, as shown in Figure 7.4. Thus, two hysteresis loops can be reconstructed for the CWH building using just the measured data. In particular, the restoring force for each DOF (F_1, F_2) can be written:

$$F_1(t) = -m_1(\ddot{x}_1 + \ddot{x}_g) - c_1\dot{x}_1 - F_2(t) \tag{7.1}$$

$$F_2(t) = -m_2(\ddot{x}_2 + \ddot{x}_g) - c_2(\dot{x}_2 - \dot{x}_1) \tag{7.2}$$

where $\ddot{x}_g$, $\ddot{x}_1$ and $\ddot{x}_2$ are measured accelerations for the foundation, ground floor and top floor, $\dot{x}_1$ and $\dot{x}_2$ are the velocities of the ground floor and top floor, respectively, and m_1 and m_2 are the mass of the BI system and the top level. The damping coefficients c_1 and c_2 can be obtained using the half-power bandwidth approach, as stated in Chapter 4.

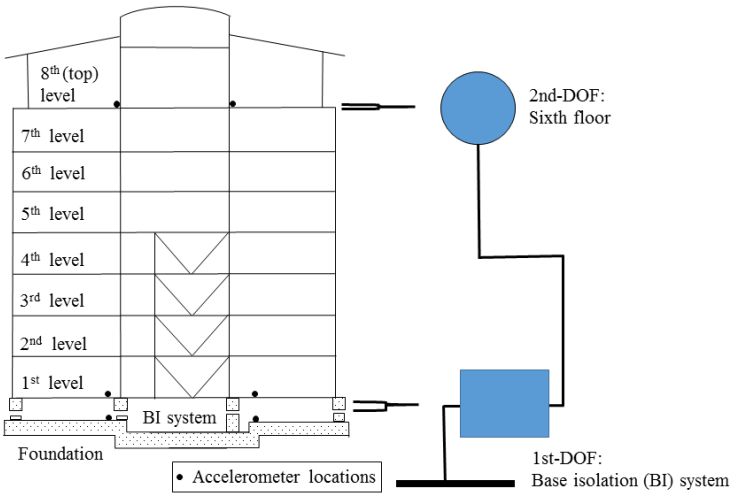

Figure 7.4: Two-DOF model for the CWH building.

Because only the displacement between the foundation and ground floor (isolator displacement) was measured and no measurement was available for the top floor, the relative displacements between each DOF for the construction of hysteresis loop are obtained by double integration of measured accelerations of each DOF after band-pass filtering with a cut-off frequency of 0.5-15Hz to eliminate high frequency noise and low frequency drift. Figure 7.5 compares the integrated isolator displacement to the directly measured displacement, as well as the filtered displacement using the Multi-rate Kalman filter in Chapter 6. It can be seen that the integrated isolator displacement matched very well with the measured and filtered displacement, which indicates the application of band-pass filtering integration was capable of yielding accurate estimations of the relative displacements for the hysteresis loop of the first and second DOF using only acceleration measurements during these two major events. In addition, the corrected velocities $\dot{x}_1$ and $\dot{x}_2$ for the first and second DOF in Equations (7.1)-(7.2) can thus also be obtained using the numerical differentiation of the integrated displacements, or the single, first integration.

Hence, the hysteresis loop for the first and second DOF can be reconstructed using the calculated restoring force (F_1,F_2) and relative displacement (x_1,x_2-x_1) during the Mw5.8 and Mw6.0 event, as shown in Figures 7.6 and 7.7, respectively. It can be seen from Figures 7.6(a) and 7.7(a) that the BI system (DOF1) behaved linearly in both events. In addition, the slope of the hysteresis loop for the superstructure (DOF2) is much smaller than the slope for the BI system (DOF1), and also shows almost entirely linear elastic behaviour during the two events. However, higher mode response was present in the loop due to the assumption of one DOF for the entire superstructure, the actual response of which occurred in a flexible and likely multi-DOF manner during the strong shock of the earthquake.

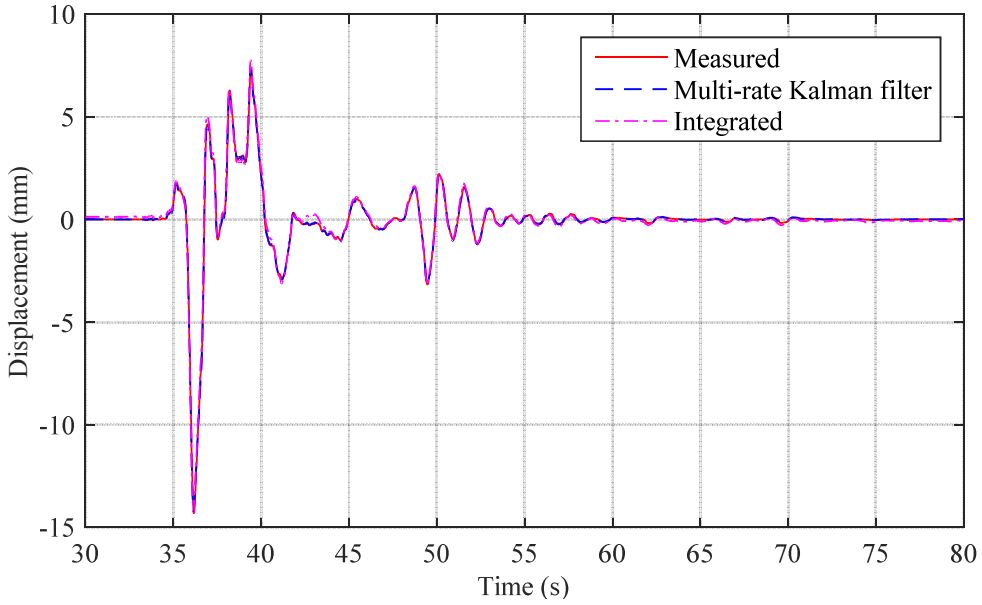

(a)

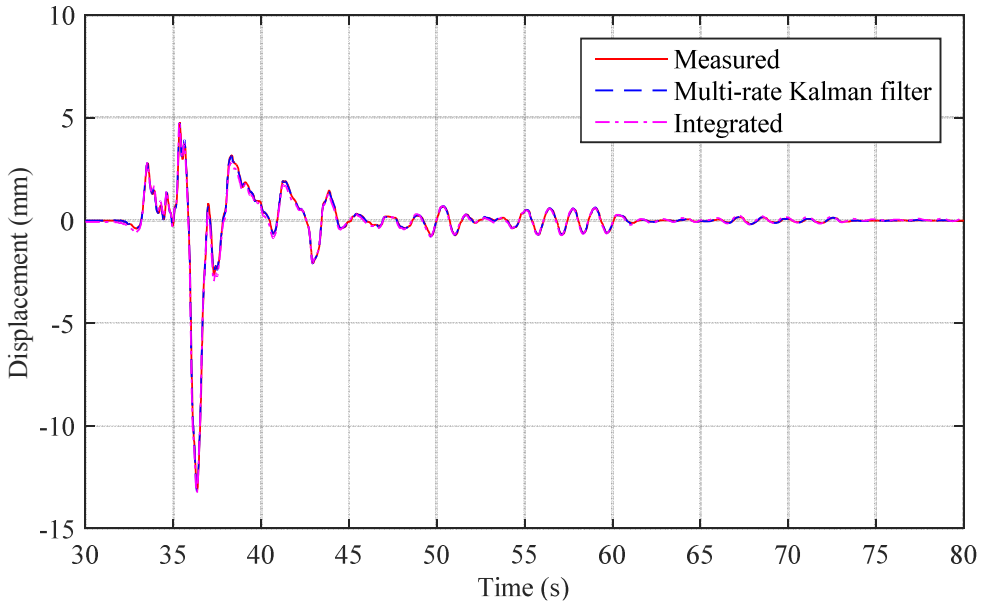

(b)

Figure 7.5: Comparing the integrated isolator displacement to the measured displacement, as well as the Kalman filtered displacement for (a) the Mw5.8 event and (b) the Mw6.0 event.

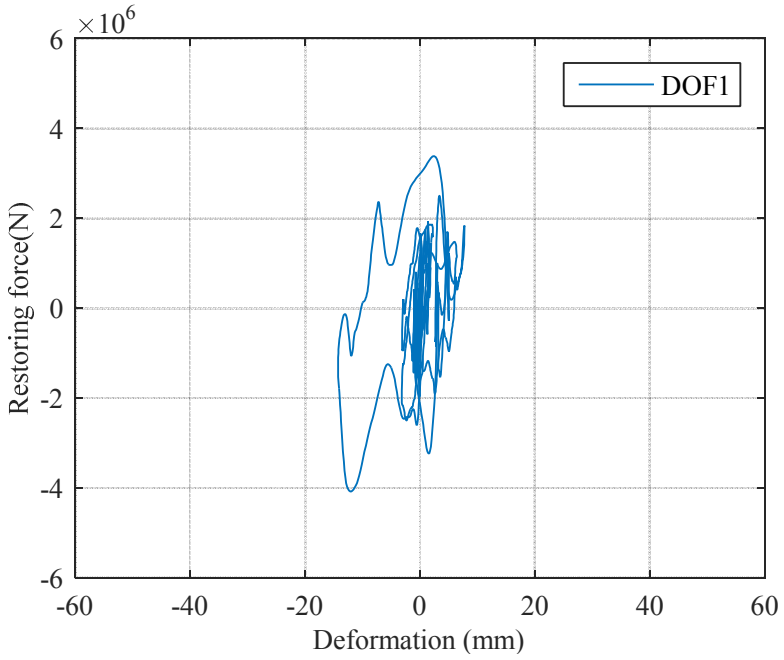

(a)

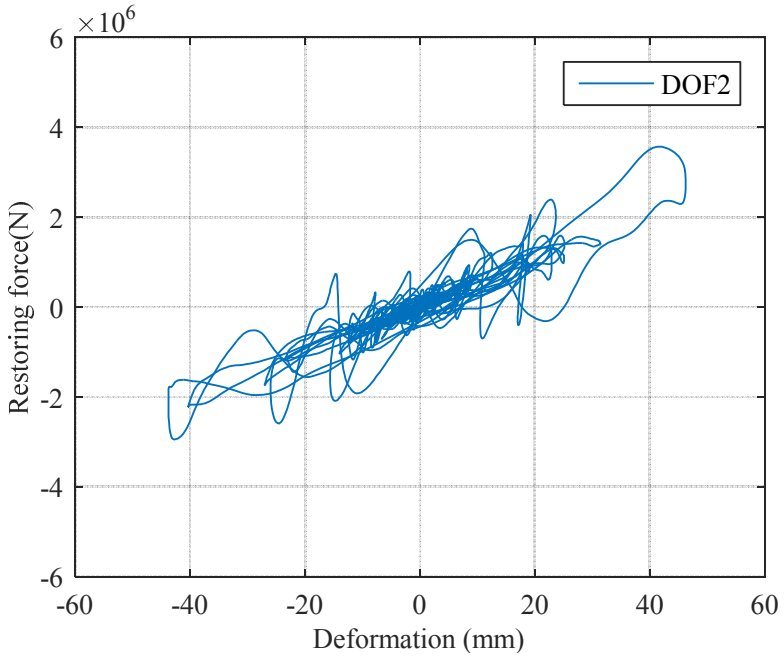

(b)

Figure 7.6: Hysteresis loop for (a) the first DOF and (b) the second DOF during the Mw5.8 event.

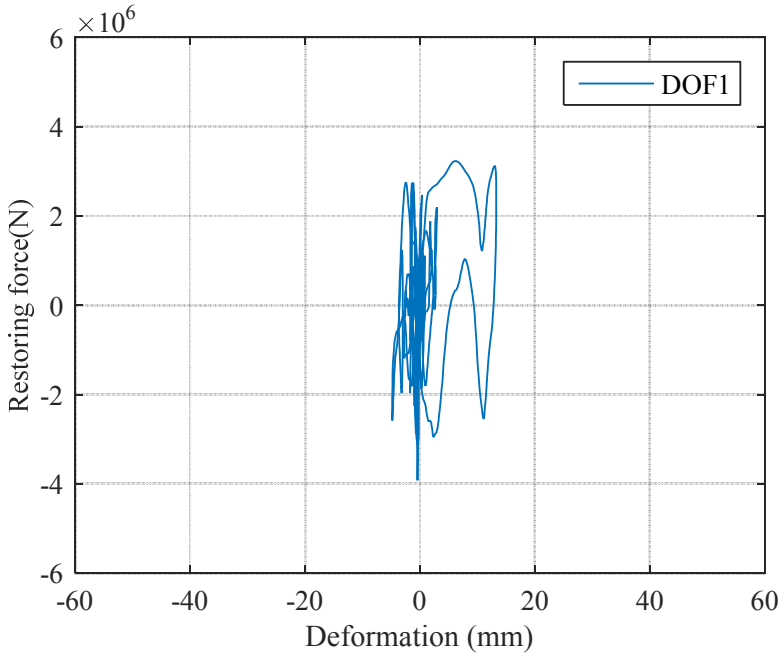

(a)

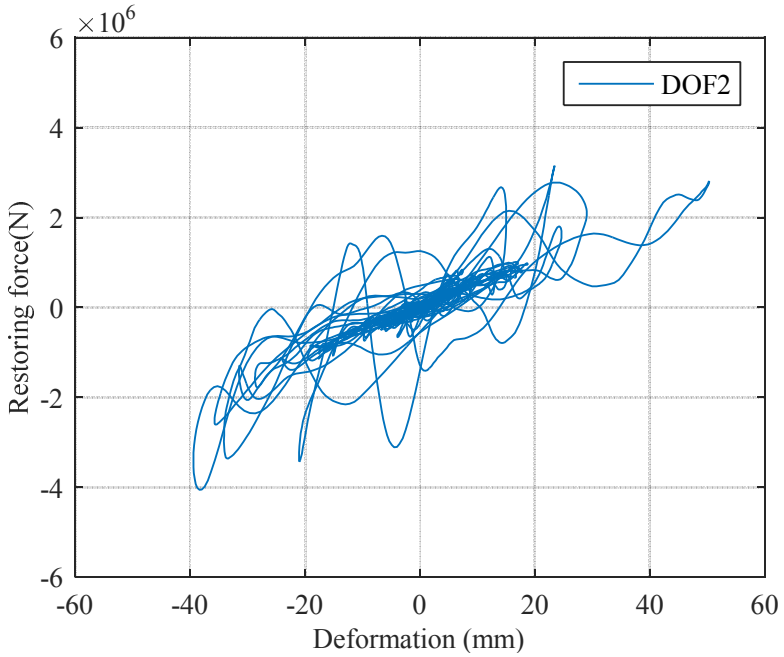

(b)

Figure 7.7: Hysteresis loop for (a) the first DOF and (b) the second DOF during the Mw6.0 event.

7.4 SHM results of the CWH building using HLA

7.4.1 Identification for the BI system (DOF1)

The reconstructed hysteresis loops for the base isolation (BI) system (DOF1) is first identified for both events. From Equation (7.1), it can be seen that the restoring force F_1 for the BI system is affected by the restoring force F_2 derived from the superstructure. However, the load-deformation relationship for the BI system can be still well represented using one DOF model (DOF1) because both the measurements below and above the isolator were recorded during the earthquakes, which directly yields the hysteresis loops with good linear behaviour compared to the superstructure (DOF2), which is less accurately approximated using only a single degree of freedom (DOF2) from the ground to measured top level.

Hence, the hysteresis loops for the BI system are divided into half cycles using the loading-unloading turning points. Because the hysteresis loops show highly linear behaviour during both events, as shown in Figures 7.6(a)-7.7(a). The separated half cycles are identified with one-segment and two-segment piecewise linear models, and the slope of the identified linear segments for the selected half cycles are then used to calculate the elastic stiffness for the BI system during both events.

Figure 7.8 shows the identified evolution of elastic stiffness for the BI system during both events. It can be seen that no significant stiffness degradation or post-yielding stiffness of the base isolator is identified for the BI system during both events, which indicates the base isolator did not provide an effective yielding performance for energy absorption during the earthquake. .These results also match the observed behaviour of the hysteresis loops in Figures 7.6(a)-7.7(a) that only enclose a minimal energy absorbing area.

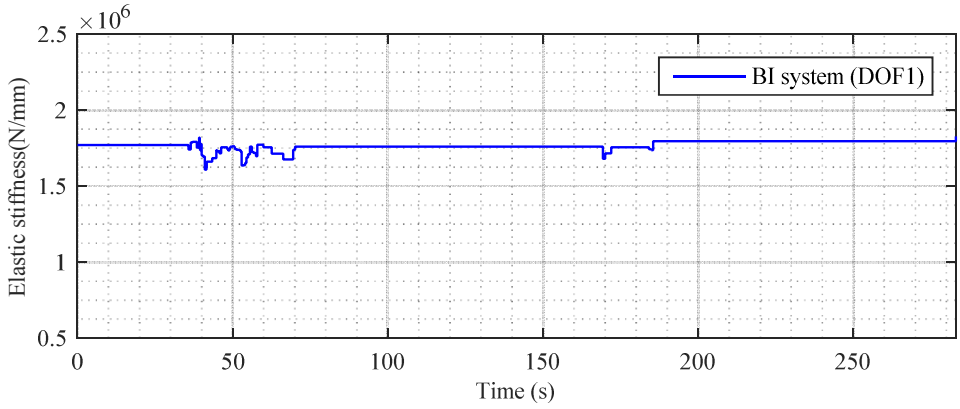

(a)

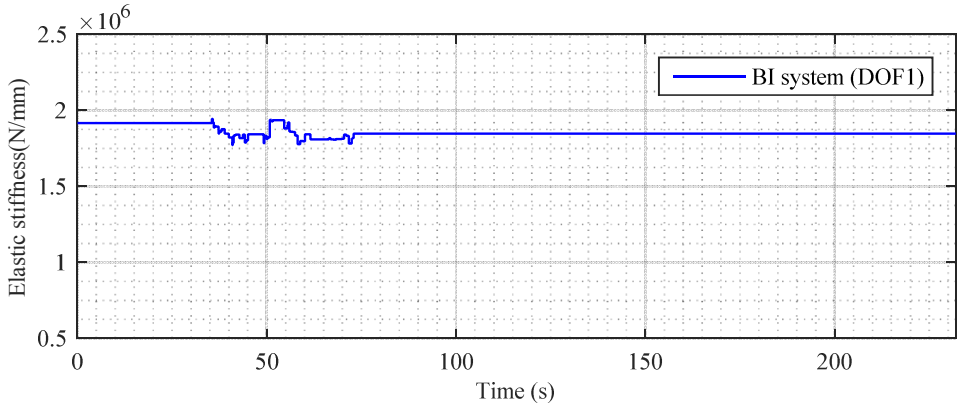

(b)

Figure 7.8: Identified elastic stiffness for the BI system of the CWH building subjected to (a) the Mw5.8 event and (b) the Mw6.0 event.

In addition, the proposed MRA method in Chapter 6 is also applied to the identified half cycles using the HLA method to obtain the effective linear stiffness of the BI system during these two major earthquakes. Figure 7.9 shows the identified effective linear stiffness for the BI system (DOF1). It can be seen the effective stiffness remains linear during the two events and also matches the identification results of Figure 7.8, which indicate no damage or change in stiffness occurred to the BI system. However, the identified effective stiffness is much smaller than the elastic stiffness for the experimental RC structure in Chapter 6, because the hysteretic pinching occurred in the experimental RC structure and caused a more significant degradation in the effective stiffness for pinching regime than the elastic stiffness for elastic regime under strong earthquake excitations.

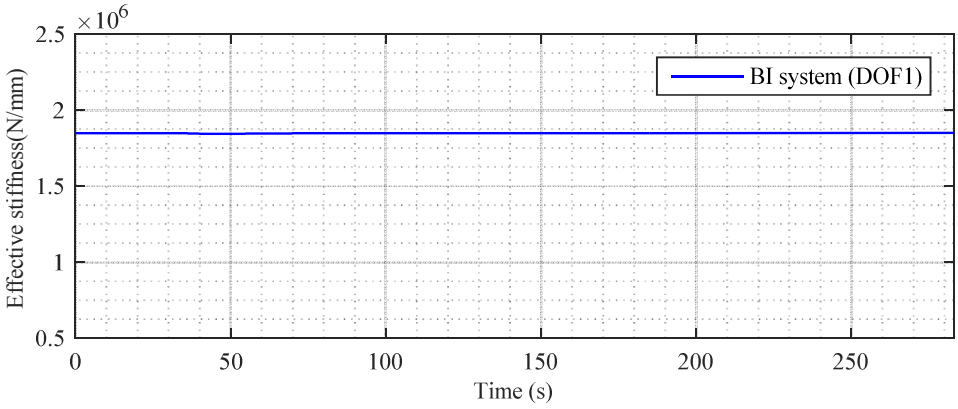

(a)

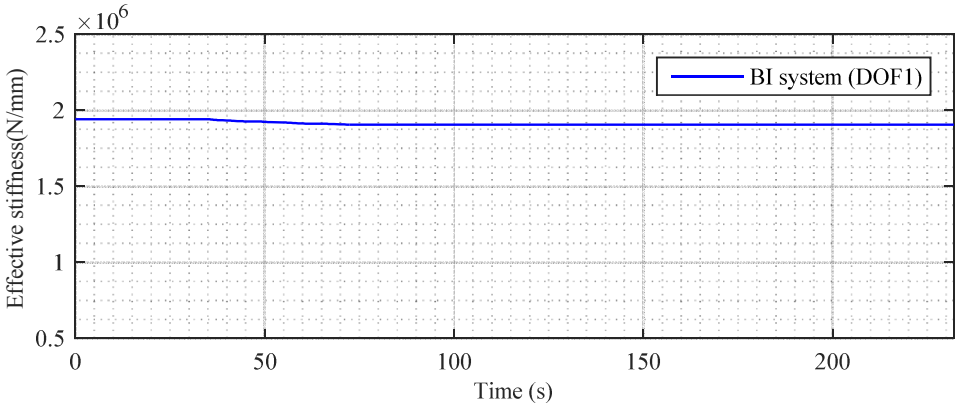

(b)

Figure 7.9: Identified effective linear stiffness for the BI system of the CWH building subjected to (a) the Mw5.8 event and (b) the Mw6.0 event.

Finally, both the identified elastic and effective stiffness are compared to the "corrected design stiffness" from the preliminary report that also assumed the CWH building as a similar two-DOF system (Kuang et al., 2015), is shown in Table 7.3. It can be seen that the identified stiffnesses match well with the corrected design stiffness with a maximum difference of 6.5%. In addition, identified stiffnesses between the two events also matched each other indicating that the results are as consistent as they should be across two events in very close succession. These results validate the accuracy of the identification results, and also clearly indicate the isolator behaved linearly, not performing as designed, in both events.

Table 7.3 Comparison of the identified and corrected design BI stiffness

Event	"Design" stiffness (kN/mm)	Elastic stiffness (kN/mm)		Effective stiffness (kN/mm)	
		Identified	Difference	Identified	Difference
Mw5.8	1920	1795	6.5%	1849	3.7%
Mw6.0	1920	1850	3.6%	1910	0.5%

7.4.2 Identification for the superstructure (DOF2)

In Chapter 4 and Chapter 6, the two 12-storey RC experimental buildings with every two floors recorded during the shaking table tests are accurately reduced to 6-DOF systems, because the response of the test structures are dominated by the fundamental mode and an equivalent single DOF model with an equivalent mass and lateral stiffness can be calculated to represent each two storeys. However, only the top floor of the superstructure for the base isolated CWH building was measured during the earthquakes. Thus, the nine-storey superstructure can only be reduced to a single degree of freedom for the reconstruction of hysteresis loop, and the lateral stiffness manifested in the hysteresis loop did not show a good linear behaviour when higher modes were involved in the structural response during the strong shocks, as shown in Figures 7.6 (b)-7.7(b). This issue is due to the fact that stiffness varies significantly over these stories, by design, due to the lower levels being braced, while the upper levels were not.

Hence, the identification is applied to the half cycles that occurred during these main shocks when the fundamental mode dominates the structure response, and the equivalent linear stiffness is then identified for the equivalent single DOF of the superstructure during the two events. Figures 7.10-7.11 show the identified evolution of the elastic stiffness and effective stiffness for DOF2 during both events. It can be seen that the identified stiffnesses remain

linear during both events, which indicates no stiffness degradation or damage occurred for the CWH building during the two major earthquakes, although the BI system did not perform as designed. In addition, the identified average stiffnesses values also matched well between the two events, as listed in Table 7.4, which also suggests the superstructure behaved in a similar linear manner without damage during the two events.

Table 7.4 Comparison of the identified stiffness for DOF2 between the two events

Event	Elastic stiffness (kN/mm)	Effective stiffness (kN/mm)
Mw5.8	992	973
Mw6.0	975	938

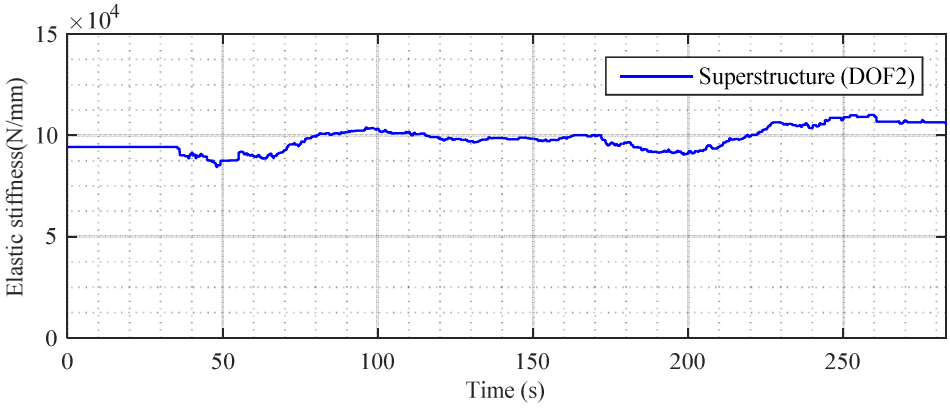

(a)

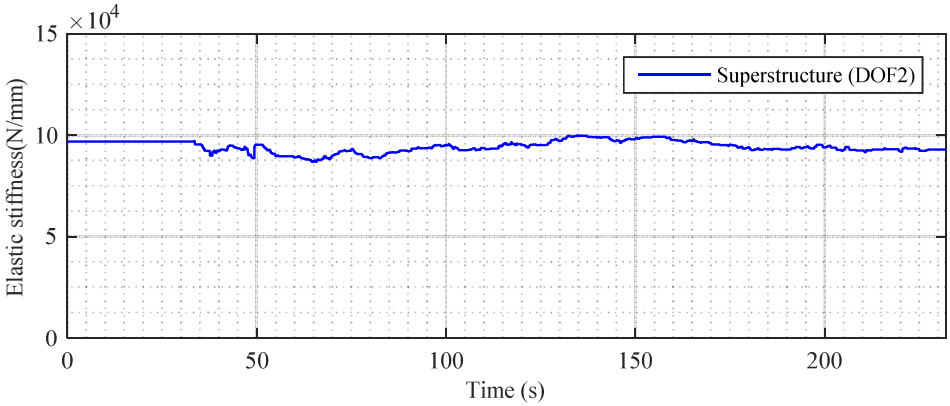

(b)

Figure 7.10: Identified elastic stiffness for the superstructure of the CWH building subjected to (a) the Mw5.8 event and (b) the Mw6.0 event.

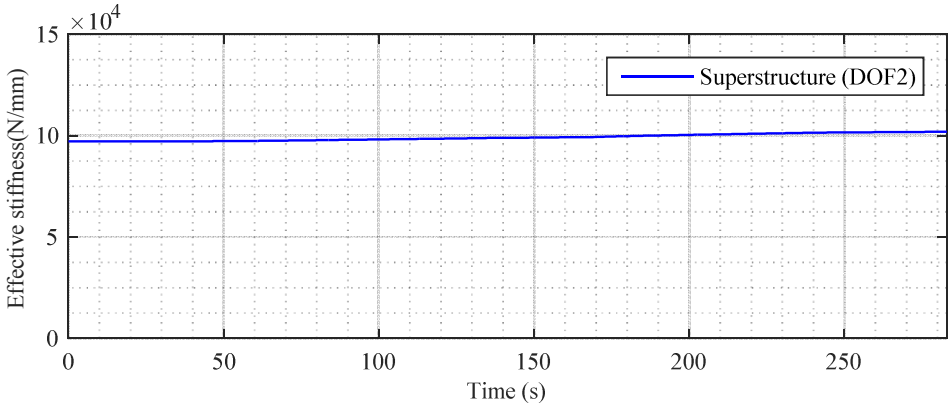

(a)

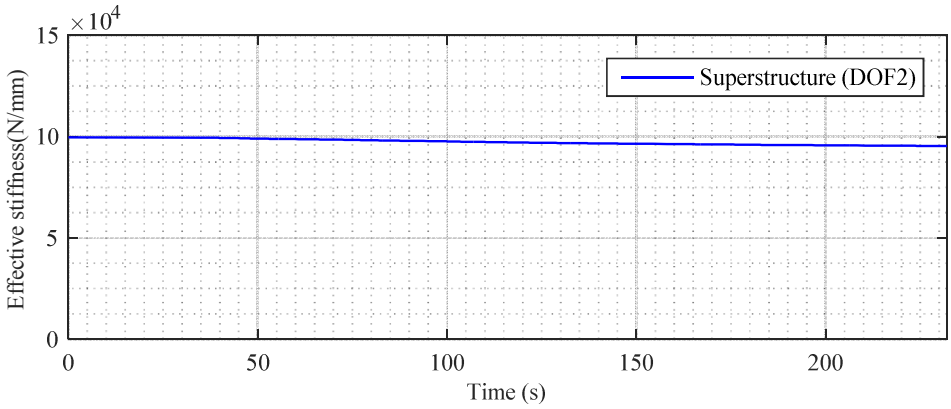

(b)

Figure 7.11: Identified effective linear stiffness for the superstructure of the CWH building subjected to (a) the Mw5.8 event and (b) the Mw6.0 event.

7.5 Summary

In this chapter, the base-isolated CHW hospital building is identified for two major earthquakes Mw5.8 and Mw6.0 in December 2011 using the HLA method. The CWH building is reduced to a two-DOF system based on the recorded response below the isolator, above the isolator and the top floor of the superstructure.

The identification results show that the base isolation system behaved entirely linearly during both events, and no yielding or nonlinear response was observed or identified for the isolator,

which shows a distinct, significant difference from the design intent and prediction. In addition, the comparison between the identified stiffnesses values and the "corrected design stiffness" calculated from the preliminary report also indicates the good accuracy of the HLA method.

The superstructure of the CWH building was approximated as a single-degree of freedom due to the single measured floor in the top level. The lateral stiffness manifested in the hysteresis loop for the superstructure is determined by the contribution of higher modes during the strong shocks. However, the identification results of the half cycles occurred in the aftershocks indicate the superstructure also behaved in a linear manner without damage or structural degradation when the structural response is dominated by the fundamental mode. The identification for the response with higher modes could also be implemented if more storeys are measured that allows for more natural modes included in the response analysis during the earthquakes.

Chapter 8: Parameter Identification of the CWH Building Based on a Four-DOF Shear Force Model during the Two Major Earthquakes.

8.1 Introduction

As discussed in Chapter 7, the base isolation (BI) system of the CWH building behaved in a linear manner during the two Mw5.8 and Mw6.0 Christchurch earthquakes in December, 2011. In addition, the dynamic behaviour of the superstructure of the CWH building was also found to be within linear range, and no damage or structural degradation were identified for the CWH building over these two events. However, the hysteresis loop of the superstructure did not show a good linear behaviour during the strong shocks of the two events because the superstructure did not behave as a rigid body, as successfully base isolated typical performs (Hijikata et al., 2011; Miwada et al., 2012; Nagarajaiah and Sun, 2000). Therefore, a more suitable model than a SDOF system is required to identify the parameters and characterize the dynamic behaviour of the nine-storey superstructure when higher modes were involved in the structural response during the two events.

A number of researchers have investigated parameter identification methods for base-isolated buildings using different system models. Stewart et al. (1999) identified the structural model parameters of four base-isolated buildings using an equivalent time-varying linear model, based on the assumption of the superstructure as a SODF system and the isolation system with time-varying effective stiffness, to characterize the isolation performance during an earthquake. Furukawa et al. (2005) proposed a least-squares output-error minimization method to identify a base-isolated building affected by the 1995 Hyogoken-Nambu earthquake in Japan. The superstructure was modelled as a rigid body and the isolation

system was identified based on three different models, including a linear equivalent model, a bilinear mode and a tri-linear model. Results showed that the model parameters can be reasonably estimated and the trilinear model best fit the recorded response time histories. Huang et al. (2009) developed an iterative trial-and-error optimization procedure, based on a simplified bilinear model for the base isolation system and a multi-storey linear model for the superstructure. They identified the structural parameters of a base-isolated building using a Masing criterion to transform a multi-valued hysteretic restoring force function into a single-valued function so that ordinary optimization methods can be applied. Xu et al. (2014) recently proposed a two-step regression analysis procedure to identify the physical parameters of a base-isolated structure. A bilinear model was chosen for modelling the base isolator, and the superstructure was assumed as a single-degree of freedom system. The hysteresis loops were divided into a number of half cycles and multiple linear regression analysis was applied to all half cycles to yield equivalent linear structural stiffness and damping.

For all these system identification methods, a key element is the choice of proper models for the base isolation system and superstructure. The choice is primarily based on the actual or expected response of the building and isolators, and is thus extremely critical for accurate identification. Since, in a properly designed and implemented structure, the isolated building should be quite rigid in comparison to the isolation system, a superstructure is frequently assumed to be a lumped mass that significantly reduces computational effort (Kulkarni and Jangid, 2002). Otherwise, a multi-story linear model is considered for the superstructure (Kulkarni and Jangid, 2003). For the base isolation system, a nonlinear hysteretic model (Park et al., 1986) is widely used to characterize the nonlinear force-deformation behaviour of the LRB experiencing the inelastic seismic response expected by design (Gavin and

Wilkinson, 2010; Matsagar and Jangid, 2008; Nagarajaiah and Sun, 2000). However, the properties of a LRB can be modelled using a spring equivalent linear horizontal stiffness in the case that the ground motion is not very large or the base isolation system has no yielding under the ground shaking (Chen et al., 2007). Hence, the isolation layer response may vary significantly from the expected performance or have a range of behaviours, and thus have a significant, negative impact on the identified model's accuracy.

In this chapter, a four degree of freedom linear shear force model is proposed for the CWH building based on the identified eventually linear characteristics of the dynamic behaviour of the BI system and the superstructure, as well as the limited sensor measurements for the isolator and the sixth-story. They also account for the design evident change in superstructure stiffness. A modified Gauss-Newton method is then employed to identify the equivalent stiffness and damping coefficients of the proposed model and further validated using a simulated structure. The real seismic data are finally used for parameter identification to validate the seismic performance of the CWH building during the two earthquakes in Christchurch.

8.2 Four-DOF Shear Force Model for the CWH Building

The response analyses and identification results in Chapter 7 show that the dynamic behaviour of both the BI system and superstructure of the CWH building were essentially linear during the Mw5.8 and Mw6.0 earthquakes. Thus, the BI system is also modelled as a linear single degree of freedom system, the first DOF (DOF1), as in Chapter 7. However, the superstructure is modelled with a three DOF system, including the second DOF (DOF2), the third DOF (DOF3) and the fourth DOF (DOF4).

In particular, the second DOF (DOF2) represents the lower four levels with V-bracing, and the third DOF (DOF3) represents the higher three levels without V-bracing. The fourth DOF (DOF4) contains the top levels with service equipment and water tanks. This model is shown in Figure 8.1. Therefore, the accelerations for the first DOF (DOF1) and fourth DOF (DOF4), as well as the ground motion in the foundation, were recorded for the 4-DOF linear shear force model. To identify the equivalent stiffness and damping coefficients for the CWH building, the response for the second and third DOFs must be estimated using the recorded response and the assumed model, from which a modified Gauss-Newton method is employed to identify the parameters of the system.

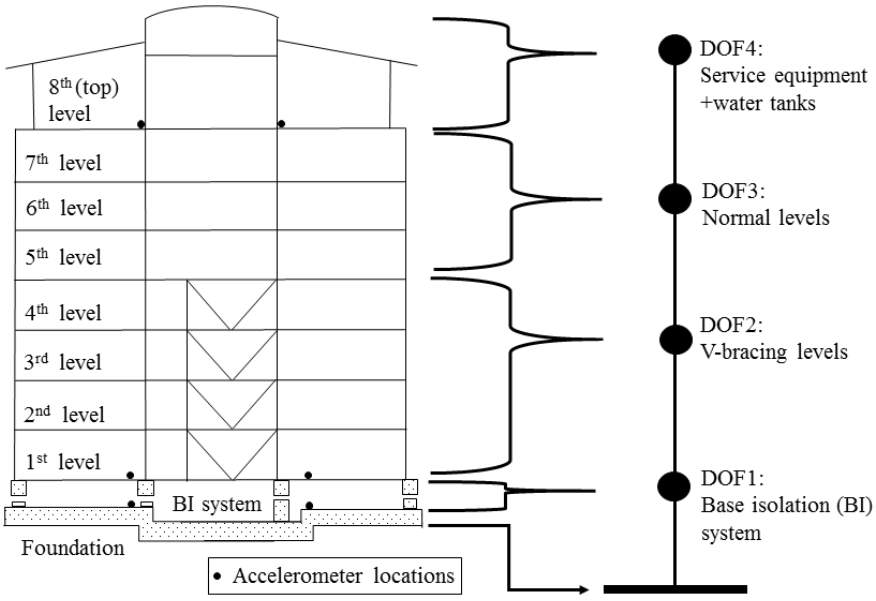

Figure 8.1: The four-DOF linear shear force model for the base isolated CWH building.

8.3 Identification Method

The equation of motion for the base-isolated building subjected to seismic excitation is defined:

$$\mathbf{M}\ddot{x} + \mathbf{C}\dot{x} + \mathbf{K_T}x = -\mathbf{M}\mathbf{I}\ddot{x}_g \tag{8.1}$$

where x=[x_1 x_2 x_3 x_4]^T, and the mass, stiffness and estimated Rayleigh damping matrices are defined:

$$\mathbf{M} = \begin{bmatrix} m_1 & 0 & 0 & 0 \\ 0 & m_2 & 0 & 0 \\ 0 & 0 & m_3 & 0 \\ 0 & 0 & 0 & m_4 \end{bmatrix} \tag{8.2}$$

$$\mathbf{K_T} = \begin{bmatrix} K_1 + K_2 & -K_2 & 0 & 0 \\ -K_2 & K_2 + K_3 & K_3 & 0 \\ 0 & -K_3 & K_3 + K_4 & -K_4 \\ 0 & 0 & -K_4 & K_4 \end{bmatrix} \tag{8.3}$$

$$\mathbf{C} = a_0\mathbf{M} + a_1\mathbf{K_T} = \begin{bmatrix} C_{11} & -C_{12} & 0 & 0 \\ -C_{21} & C_{22} & -C_{23} & 0 \\ 0 & -C_{32} & C_{33} & -C_{34} \\ 0 & 0 & -C_{43} & C_{44} \end{bmatrix} \tag{8.4}$$

where the elements in the Rayleigh damping matrix C_{ij} are defined:

$$\begin{aligned} C_{11} &= a_0 m_1 + a_1(K_1 + K_2) \\ C_{22} &= a_0 m_2 + a_1(K_2 + K_3) \\ C_{33} &= a_0 m_3 + a_1(K_3 + K_4) \\ C_{44} &= a_0 m_4 + a_1 K_4 \\ C_{12} &= C_{21} = a_1 K_2 \\ C_{23} &= C_{32} = a_1 K_3 \\ C_{34} &= C_{43} = a_1 K_4 \end{aligned} \tag{8.5}$$

Using Equations (8.1)-(8.4), the equation of motion for the directly measured first and fourth DOF are defined:

$$m_1\ddot{x}_1 + C_{11}\dot{x}_1 - C_{12}\dot{x}_2 + (K_1 + K_2)x_1 - K_2 x_2 = -m_1\ddot{x}_g \tag{8.6}$$

$$m_4\ddot{x}_4 - C_{43}\dot{x}_3 + C_{44}\dot{x}_4 - K_4 x_3 + K_4 x_4 = -m_4\ddot{x}_g \tag{8.7}$$

where the accelerations were measured, the velocity and displacement of x_1 and x_4 can be

obtained by direct integration after band pass filtering, and K_{ij} and C_{ij} are to be identified.

Equations (8.6) and (8.7) can thus be rewritten in terms of unknown and unmeasured x_2 and x_3:

$$\dot{x}_2 + P_1(K_2, C_{12})x_2 = Q_1(K_1, K_2, C_{11}, C_{12}, t) \tag{8.8}$$

$$\dot{x}_3 + P_2(K_4, C_{43})x_3 = Q_2(K_4, C_{43}, C_{44}, t) \tag{8.9}$$

where:

$$P_1 = \frac{K_2}{C_{12}} \tag{8.10}$$

$$Q_1 = \frac{m_1\ddot{x}_1 + C_{11}\dot{x}_1 + (K_1 + K_2)x_1 + m_1\ddot{x}_g}{C_{12}} \tag{8.11}$$

$$P_2(K_2, C_{12}) = \frac{K_4}{C_{43}} \tag{8.12}$$

$$Q_2 = \frac{m_4\ddot{x}_4 + C_{44}\dot{x}_4 + K_4 x_4 + m_4\ddot{x}_g}{C_{43}} \tag{8.13}$$

The general solutions for Equations (8.8) and (8.9) are obtained:

$$x_2(t) = A_i e^{-\int P_1(K_2,C_{12})dt} + e^{-\int P_1(K_2,C_{12})dt} \int Q_1(K_1, K_2, C_{11}, C_{12}, t) e^{\int P_1(K_2,C_{12})dt} dt \tag{8.14}$$

$$x_3(t) = B_i e^{-\int P_2(K_4,C_{43})dt} + e^{-\int P_2(K_4,C_{43})dt} \int Q_2(K_4, C_{43}, C_{44}, t) e^{\int P_2(K_4,C_{43})dt} dt \tag{8.15}$$

For each time step $h=t_i-t_{i-1}$, the free terms Q_1 and Q_2 in Equations (8.11) and (8.13) can be written as a moving average for $t_{i-1} \le t \le t_i$:

$$Q_{1i} = \frac{Q_1(K_1, K_2, C_{11}, C_{12}, t_{i-1}) + Q_1(K_1, K_2, C_{11}, C_{12}, t_i)}{2} \tag{8.16}$$

$$Q_{2i} = \frac{Q_2(K_4, C_{43}, C_{44}, t_{i-1}) + Q_2(K_4, C_{43}, C_{44}, t_i)}{2} \tag{8.17}$$

Substituting Equations (8.16)-(8.17) into Equations (8.14)-(8.15), respectively, yields:

$$x_2(t) = e^{-(t-t_{i-1})/a_1}(A_i + a_1 Q_{1i} e^{(t-t_{i-1})/a_1}) \tag{8.18}$$

$$x_3(t) = e^{-(t-t_{i-1})/a_1}(B_i + a_1 Q_{2i} e^{(t-t_{i-1})/a_1}) \tag{8.19}$$

where A_i and B_i are constants determined by initial condition at $t=t_{i-1}$. If $x_2(t_{i-1})$ and $x_3(t_{i-1})$ are known from the prior time-step $t=t_{i-1}$, or initial condition at $t=t_{i-1}=t_0$, then the constants A_i and B_i can be determined using Equations (8.18) and (8.19):

$$A_i = x_2(t_{i-1}) - a_1 Q_{1i} \tag{8.20}$$

$$B_i = x_3(t_{i-1}) - a_1 Q_{2i} \tag{8.21}$$

Then from Equations (8.18)-(8.21), the complete estimates for $x_2(t_i)$ and $x_3(t_i)$ with sampling time interval $h=t_i-t_{i-1}$ are obtained iteratively given $x_2(0)$ and $x_3(0)$ to start:

$$x_2(t_i) = x_2(t_{i-1})e^{-h/a_1} + a_1(1-e^{-h/a_1})Q_{1i} \tag{8.22}$$

$$x_3(t_i) = x_3(t_{i-1})e^{-h/a_1} + a_1(1-e^{-h/a_1})Q_{2i} \tag{8.23}$$

Using Equations (8.1)-(8.4), the equations for the full system at $t=t_i$ can be expressed:

$$\begin{aligned} f_{1i}(\boldsymbol{\theta}) &= m_1(\ddot{x}_1(t_i) + \ddot{x}_g(t_i)) + C_{11}\dot{x}_1(t_i) - C_{12}\dot{x}_2(t_i) + (K_1+K_2)x_1(t_i) \\ &- K_2 x_2(t_i) = 0 \end{aligned} \tag{8.24}$$

$$\begin{aligned} f_{2i}(\boldsymbol{\theta}) &= m_2(\ddot{x}_2(t_i) + \ddot{x}_g(t_i)) - C_{21}\dot{x}_1(t_i) + C_{22}\dot{x}_2(t_i) - C_{23}\dot{x}_3(t_i) \\ &- K_2 x_1(t_i) + (K_2+K_3)x_2(t_i) - K_3 x_3(t_i) = 0 \end{aligned} \tag{8.25}$$

$$\begin{aligned} f_{3i}(\boldsymbol{\theta}) &= m_3(\ddot{x}_3(t_i) + \ddot{x}_g(t_i)) - C_{32}\dot{x}_2(t_i) + C_{33}\dot{x}_3(t_i) - C_{34}\dot{x}_4(t_i) \\ &- K_3 x_2(t_i) + (K_3+K_4)x_3(t_i) - K_4 x_4(t_i) = 0 \end{aligned} \tag{8.26}$$

$$\begin{aligned} f_{4i}(\boldsymbol{\theta}) &= m_4(\ddot{x}_4(t_i) + \ddot{x}_g(t_i)) - C_{43}\dot{x}_3(t_i) + C_{44}\dot{x}_4(t_i) - K_4 x_3(t_i) \\ &+ K_4 x_4(t_i) = 0 \end{aligned} \tag{8.27}$$

where $\boldsymbol{\theta}=[K_1, K_2, K_3, K_4, a_0, a_1]$ is the parameter vector to be identified and it is iteratively updated using a Gauss-Newton formula:

$$\hat{\boldsymbol{\theta}}^{(s+1)} = \hat{\boldsymbol{\theta}}^{(s)} - \alpha(\mathbf{J}^{\mathbf{T}}\mathbf{J})^{-1}\mathbf{J}^{\mathbf{T}}\mathbf{R}^{(s)} \tag{8.28}$$

where s is the iteration step, α is the step length and $\mathbf{J}$ is the Jacobian matrix of of $f_i(\hat{\boldsymbol{\theta}}^{(s)})$:

$$\mathbf{J} = \left[\mathbf{J}_1 \ \cdots \ \mathbf{J}_i \ \cdots \ \mathbf{J}_n\right]^{\mathbf{T}} \tag{8.29}$$

where $\mathbf{J}_i$ is determined:

$$\mathbf{J}_i = \begin{bmatrix} \frac{\partial f_{1i}(\hat{\boldsymbol{\theta}}^{(s)})}{\partial K_1} & \frac{\partial f_{2i}(\hat{\boldsymbol{\theta}}^{(s)})}{\partial K_1} & \frac{\partial f_{3i}(\hat{\boldsymbol{\theta}}^{(s)})}{\partial K_1} & \frac{\partial f_{4i}(\hat{\boldsymbol{\theta}}^{(s)})}{\partial K_1} \\ \frac{\partial f_{1i}(\hat{\boldsymbol{\theta}}^{(s)})}{\partial K_2} & \frac{\partial f_{2i}(\hat{\boldsymbol{\theta}}^{(s)})}{\partial K_2} & \frac{\partial f_{3i}(\hat{\boldsymbol{\theta}}^{(s)})}{\partial K_2} & \frac{\partial f_{4i}(\hat{\boldsymbol{\theta}}^{(s)})}{\partial K_2} \\ \frac{\partial f_{1i}(\hat{\boldsymbol{\theta}}^{(s)})}{\partial K_3} & \frac{\partial f_{2i}(\hat{\boldsymbol{\theta}}^{(s)})}{\partial K_3} & \frac{\partial f_{3i}(\hat{\boldsymbol{\theta}}^{(s)})}{\partial K_3} & \frac{\partial f_{4i}(\hat{\boldsymbol{\theta}}^{(s)})}{\partial K_3} \\ \frac{\partial f_{1i}(\hat{\boldsymbol{\theta}}^{(s)})}{\partial K_4} & \frac{\partial f_{2i}(\hat{\boldsymbol{\theta}}^{(s)})}{\partial K_4} & \frac{\partial f_{3i}(\hat{\boldsymbol{\theta}}^{(s)})}{\partial K_4} & \frac{\partial f_{4i}(\hat{\boldsymbol{\theta}}^{(s)})}{\partial K_4} \\ \frac{\partial f_{1i}(\hat{\boldsymbol{\theta}}^{(s)})}{\partial a_0} & \frac{\partial f_{2i}(\hat{\boldsymbol{\theta}}^{(s)})}{\partial a_0} & \frac{\partial f_{3i}(\hat{\boldsymbol{\theta}}^{(s)})}{\partial a_0} & \frac{\partial f_{4i}(\hat{\boldsymbol{\theta}}^{(s)})}{\partial a_0} \\ \frac{\partial f_{1i}(\hat{\boldsymbol{\theta}}^{(s)})}{\partial a_1} & \frac{\partial f_{2i}(\hat{\boldsymbol{\theta}}^{(s)})}{\partial a_1} & \frac{\partial f_{3i}(\hat{\boldsymbol{\theta}}^{(s)})}{\partial a_1} & \frac{\partial f_{4i}(\hat{\boldsymbol{\theta}}^{(s)})}{\partial a_1} \end{bmatrix}^{\mathbf{T}} \tag{8.30}$$

where n is the number of time step samples. The error matrix $\mathbf{R}^{(s)}$ at iteration is defined:

$$\mathbf{R}^{(s)} = [f_{11}(\hat{\boldsymbol{\theta}}^{(s)}) \cdots \ f_{41}(\hat{\boldsymbol{\theta}}^{(s)}) \cdots \ f_{1i}(\hat{\boldsymbol{\theta}}^{(s)}) \cdots \ f_{4i}(\hat{\boldsymbol{\theta}}^{(s)}) \cdots f_{1n}(\hat{\boldsymbol{\theta}}^{(s)}) \ \cdots \ f_{4n}(\hat{\boldsymbol{\theta}}^{(s)})]^{\mathbf{T}} \tag{8.31}$$

The estimated $\hat{\boldsymbol{\theta}}$ seeks to minimize the error function:

$$\varepsilon(\hat{\boldsymbol{\theta}}) = \sum_{i=1}^{n} f_1(\hat{\boldsymbol{\theta}}) + \sum_{i=1}^{n} f_2(\hat{\boldsymbol{\theta}}) + \sum_{i=1}^{n} f_3(\hat{\boldsymbol{\theta}}) + \sum_{i=1}^{n} f_4(\hat{\boldsymbol{\theta}}) \tag{8.32}$$

8.4 Simulation and Validation Case Study

A numerical study is first carried out to validate the performance of the proposed model, model-estimated DOF and final identification procedure in a controlled example where everything is known. The example structure is a four degree of freedom system with a set of parameters, including: m_1=3892e+3kg, m_2=12974e+3kg, m_3=2595e+3kg, m_4=3892e+3kg, and stiffness: K_1=728kN/mm, K_2=1120kN/mm, K_3=280kN/mm, K_4=300kN/mm. The

Rayleigh damping coefficients are a_0=0.261 and a_1=0.0087, yielding damping ratios of 5% for the first and second modes.

The simulated structure was subjected to the El Centro earthquake of 1940. The system response was simulated using a Runge-Kutta method with a time step of Δt=0.005s. The calculated response data was first utilised without added noise first, for proof of concept of the identification procedure.

Figure 8.2 shows the estimates and convergence for the proposed parameters with different initial value guesses for $K_{1\text{-}4}$ and $a_{0\text{-}1}$. It can be seen that the final values of estimated parameters $K_{1\text{-}4}$ and a_1 rapidly converge to the exact values with different guesses. However, the convergence rate of a_0 is shown to be slower than a_1 because the proportion of the mass damping a_0 is very small and sometimes almost negligible for the construction of the classical damping matrix (Chopra, 1995). Thus, the weight of a_0 is much smaller than the weight of a_1 in the iteration process, which requires more iterations to obtain the exact value of a_0. However, they all converge to the exact values with sufficiently small step size and large number of iterations. Thus, the identification method can yield accurate estimates of equivalent stiffness and damping coefficients of the system, including the use of unmeasured degrees of freedom x_2 and x_3, with clean measurements.

Figure 8.3 compares the estimated and true simulated responses for x_2 and x_3 using an initial guess of 200% of the exact structural parameter values. The estimated response fits well with the simulated response, indicating the method can yield good estimates of the unrecorded response for x_2 and x_3 with clean (noise-free) measurements of for $\ddot{x}_1$ and $\ddot{x}_4$ .Hence, the model-based estimate yields true values.

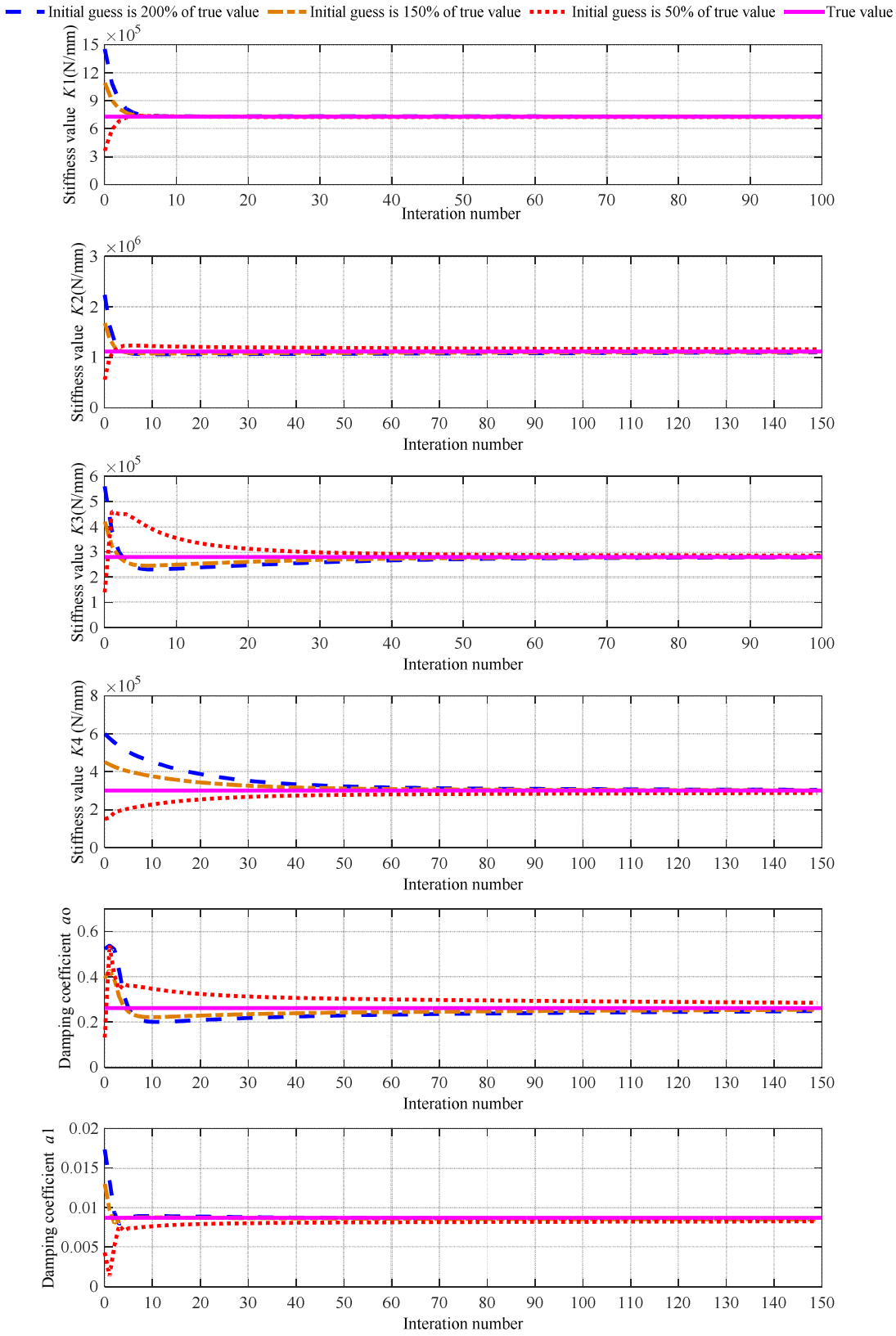

Figure 8.2: Parameter estimation performance with different initial guess values.

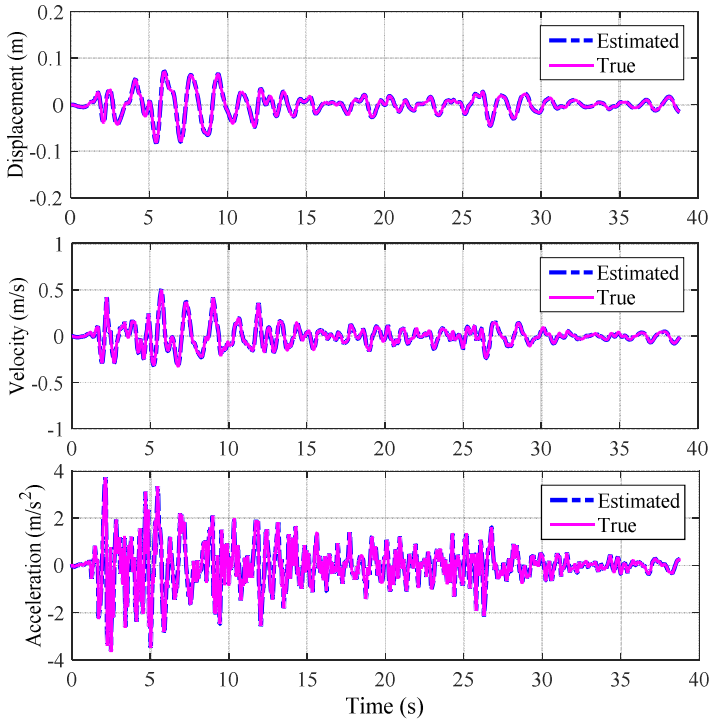

(a)

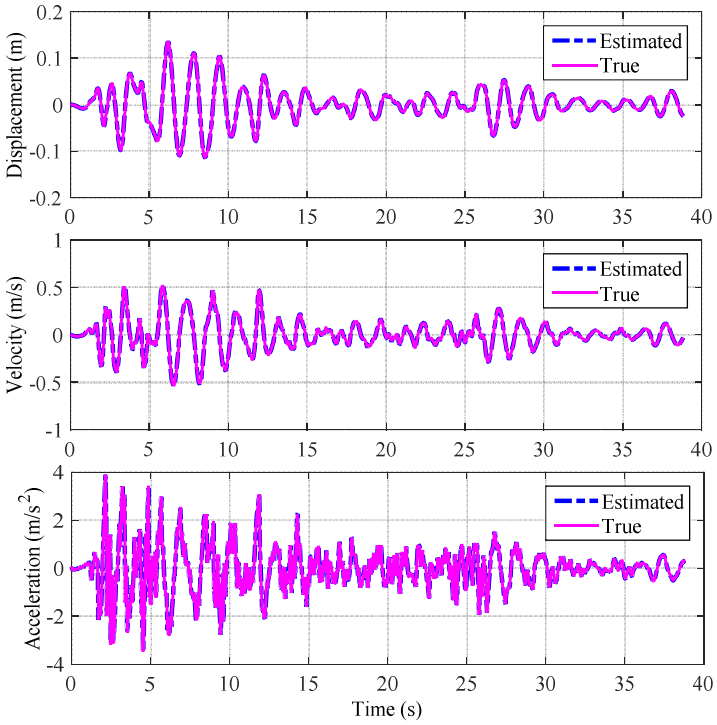

(b)

Figure 8.3: Comparison of the estimated response and the true response for the unmeasured DOF using the initial guesses of 200% of exact parameter values: (a) DOF2 and (b) DOF3.

To assess this approach's robustness to noise, 10% random RMS noise was added to the measured ground and structural accelerations ($\ddot{x}_g, \ddot{x}_1, \ddot{x}_4$). The mean values of the estimated parameters for 100 Monte-Carlo runs with random added noise and different initial guesses, are listed in Table 8.1. It can be seen that the average error of the estimated stiffness values is 16.6% with the largest Monte-Carlo mean error of 31.7% using an initial guess of 200% of the exact parameter values. However, the average error of the estimated stiffness values is 8.7% with the largest Monte-Carlo mean error 13.9% using an initial guess of only 150% of the exact parameter values and 11.5% with the largest Monte-Carlo mean error 19.3% using an initial guess of 50% exact parameter values. Most initial guesses, based on the knowledge of the design and structural dimensions would be well within ±50% for an undamaged structure. Hence, the robustness appears to be good for relatively large added noise.

In addition, the robustness to noise was also evaluated using different levels of noise with different initial guesses, as shown in Figure 8.4. It can be seen that the average errors show a small increase with increasing noise. Good estimates with average errors less than 10% were obtained using an initial guesses of 150% of the exact parameter values for variable noise levels. Thus, the initial guess affects the identification accuracy with measurement noise. However, the estimated response using the estimated parameters shows good agreement with the true response for the unrecorded DOF2 and DOF3, even with 10% added noise using an initial guess of 200% of exact parameter values, as shown in Figure 8.5.

Table 8.1 Mean estimated results with 10% RMS noise for different initial guesses.

Parameters	K_1 (kN/mm)	K_2 (kN/mm)	K_3 (kN/mm)	K_4 (kN/mm)	a_0	a_1
Initial guess (200% of true value)	1456	2240	560	600	0.522	0.0174
Estimated	738	1053	231	395	0.336	0.0093
True	728	1120	280	300	0.261	0.0087
Monte-Carlo mean absolute error	1.4%	6.0%	17.5%	31.7%	28.7%	6.9%
Average error of parameters	16.6%					
Initial guess (150% of true value)	1092	1680	420	450	0.392	0.0131
Estimated	734	1074	241	340	0.296	0.0091
True	728	1120	280	300	0.261	0.0087
Monte-Carlo mean absolute error	0.8%	4.1%	13.9%	13.3%	13.4%	4.7%
Average error of parameters	8.7%					
Initial guess (50% of true value)	364	560	140	150	0.131	0.0044
Estimated	670	1132	301	242	0.212	0.0093
True	728	1120	280	300	0.261	0.0087
Monte-Carlo mean absolute error	8.0%	1.1%	7.5%	19.3%	18.8%	6.9%
Average error of parameters	11.5%					

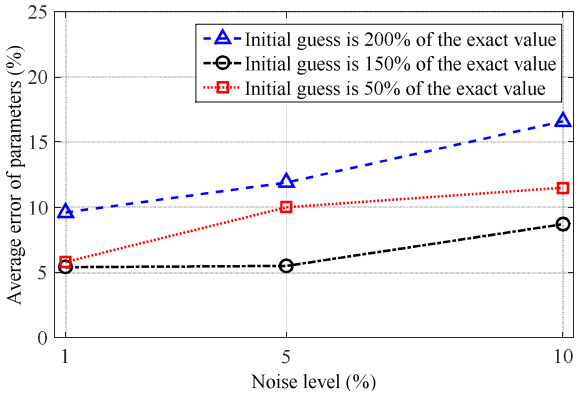

Figure 8.4: Average errors of the estimated parameters with variable noise level.

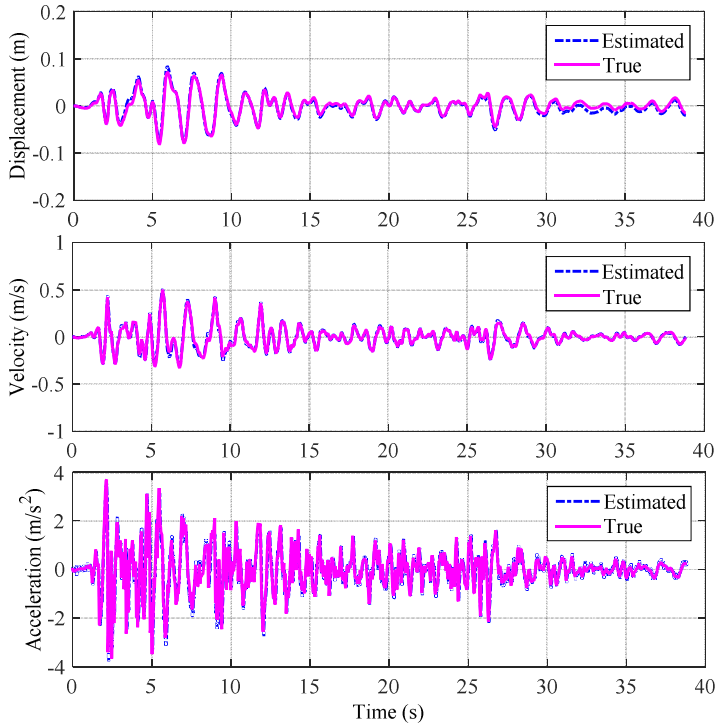

(a)

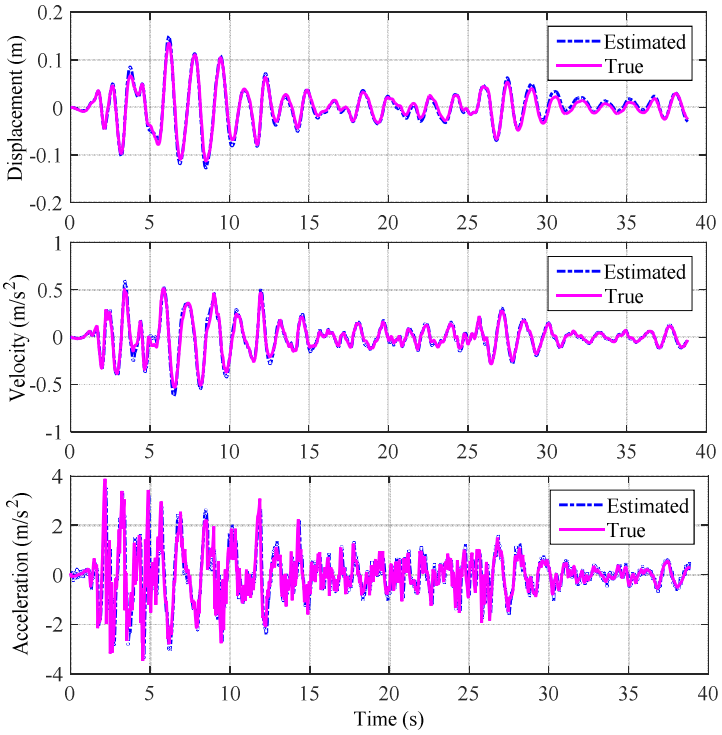

(b)

Figure 8.5: Comparison of the estimated response and the true response for the unmeasured DOF with 10% RMS added noise using the initial guesses of 200% of exact parameter values: (a) DOF2 and (b) DOF3.

8.5 Identification of the CWH Building

The initial choice of the stiffness parameters for the superstructure is based on the assumption that the floors are rigid, the columns are axially inextensible and no additional stiffness is taken into account due to the non-structural walls and panels (Chopra, 1995). Torsion was neglected because recorded acceleration data from the northeast corner are very similar to the southwest corner, as discussed in Chapter 7, despite a slightly irregular cross section. Therefore, stiffness, k_s, for each level without V-bracing is approximated using the sum of the lateral stiffness of all columns. Considering approximately 80%-90% of the original elastic stiffness to be provided by bracing (Sabelli et al., 2013), the stiffness for the lower floors with V-bracing was assumed to be $2k_s$ in the initial guess. These estimates should be well within ±50% of the exact value.

The total seismic weight of the CWH building is approximately 170,000kN (17.3×10^6kg), including the dead loads and the live loads. In particular, the dead loads are calculated from the dimensions of the structural elements and a normal concrete density of 23kN/m^3(CCANZ, 2010). The basic live loads are taken as 2kN/m^{3}for the lower seven levels with wards, and 3kN/m^{3}for the top two levels with heavy equipment and utility (Standards New Zealand, 1992). In addition, the inner foundation and the base isolation system is considered 15% to comprise the seismic weight (Kuang et al., 2015). Thus, the estimated mass for each DOF is m_1=2.6×10^6kg, m_2=7.8×10^6kg, m_3=3.9×10^6kg and m_4=4.7×10^6kg.

The preliminary report and the identification results in Chapter 7 both show that the post-yielding stiffness is not observed to be as prevalent as that of the pre-yielding stiffness from the measured load-deformation relationship, which indicate the isolation deformation is occurred in the linear region of the isolators. Thus, the initial estimation of stiffness for the

base isolation system is estimated to be 1921kN/mm from the corrected design linear stiffness. The classic Rayleigh damping ratio is assumed to be 5% for the first mode, and higher damping is assumed for higher modes (Clough and Penzien, 1993).

8.5.1 First Cross Validation

The method was first applied to identify the CWH building using the recorded accelerations of Mw6.0 earthquake. Although the overall duration of the earthquake excitation was ~ 232s, the parameter identification was carried out using only the main excitation measurements from 30s to 60s, as shown in Figure 8.6. The identified results were then used to simulate the response of the Mw 5.8 earthquake for cross validation of the identified parameters against data not used to identify the structural parameters. This approach should provide a robust, independent means of validation.

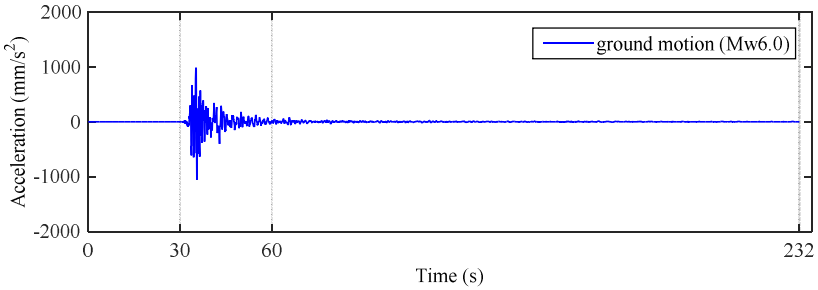

Figure 8.6: Recorded time history of ground acceleration for Mw6.0 event.

Table 8.2 lists the assumed initial guesses and final identified parameter values for the 4-DOF shear force model of the CWH building using the recorded data of Mw6.0. The parameters T_1 and ζ_1 represent the fundamental natural period and damping factor. The identified parameters are then used to predict the response of the CWH building, while subjected to the Mw5.8 event. Comparison of the estimated model and recorded accelerations at the first DOF (DOF1) and the fourth DOF (DOF4), for both earthquakes are shown in Figure 8.7.

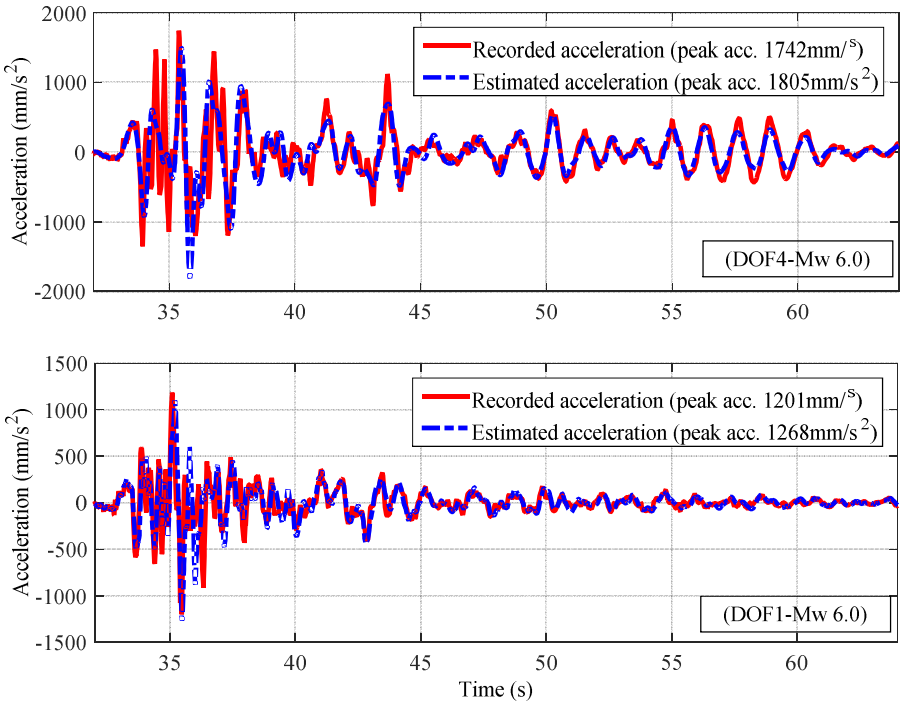

(a)

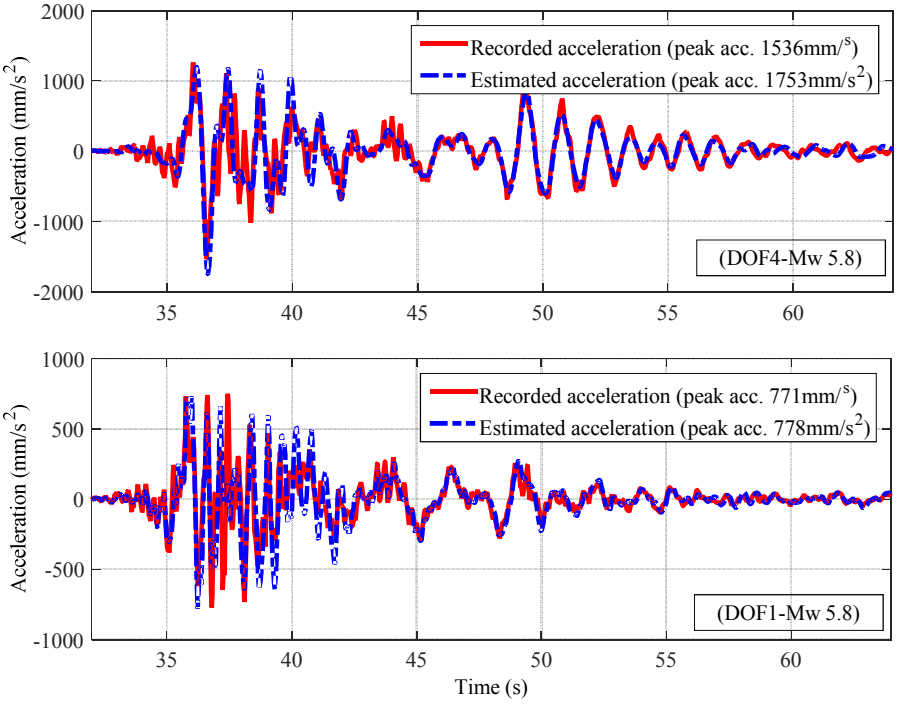

(b)

Figure 8.7: Comparison of the estimated model and recorded accelerations for (a) the Mw6.0 event and (b) the Mw5.8 event.

Table 8.2 Identified results for the 4-DOF shear force model using the data of Mw6.0.

Parameters	K_1 (kN/mm)	K_2 (kN/mm)	K_3 (kN/mm)	K_4 (kN/mm)	a_0	a_1	T_1 (s)	ζ_1
Initial guess	1921	1120	300	400	0.269	0.0088	1.42	5%
Estimated (E6.0)	1594	1261	336	458	0.661	0.0090	1.37	9%

It can be seen that the assumed 4-DOF shear model was able to yield a very replication of the recorded accelerations from 42s to 60s for both events. However, the assumption of the superstructure as a three-DOF system only allows for three natural modes to be included in the response analysis, which leads to a less consistent match between the estimated and recorded accelerations from 32s to 42s when higher modes and greater deformation of the superstructure occurred during the strong shocks of the earthquakes. Thus, the flexibility of the CWH building was not exactly modelled using the 4-DOF linear shear model and a model with increased DOFs might produce a better replication of the actual response if more stories were instrumented for the CWH building during the earthquakes.

However, it can be seen from Table 8.3 that the difference between the recorded and estimated peak accelerations are a maximum of 5.6% and 14.1% for the first and fourth DOF, respectively. In addition, Table 8.3 also lists the results of the cross correlation coefficients ($R_{corrcoef}$) and the mean absolute percentage errors between the estimated model and recorded acceleration response to evaluate the point-to-point accuracy of the trajectory of identified model time histories (Swanson et al., 2011). $R_{corrcoef}$ and MAPE were calculated:

$$\overline{X}_{actual} = \sqrt{\left(\sum_{i=1}^{N} X_{i,actual}^{2} - \frac{\left(\sum_{i=1}^{N} X_{i,actual} \right)^{2}}{N} \right)} \tag{8.33}$$

$$\overline{X}_{estimated} = \sqrt{\left(\sum_{i=1}^{N} X_{i,estimated}^{2} - \frac{\left(\sum_{i=1}^{N} X_{i,estimated} \right)^{2}}{N} \right)} \tag{8.34}$$

$$R_{corrcoef} = \frac{\sum_{i=1}^{N} X_{i,actual} X_{i,estimated} - \frac{\sum_{i=1}^{N} X_{i,actual} \sum_{i=1}^{N} X_{i,estimated}}{N}}{\overline{X}_{actual} \cdot \overline{X}_{estimated}} \tag{8.35}$$

$$MAPE = \frac{\sum_{i=1}^{N} \left| X_{i,actual} - X_{i,estimated} \right|}{\sum_{i=1}^{N} \left| X_{i,actual} \right|} \times 100\% \tag{8.36}$$

where X_{actual} is the recorded accelerations, $X_{\text{estimated}}$ is the estimated model accelerations, and N is the number of estimated data points.

It can be seen from Table 8.3 that the values of MAPE for the Mw6.0 earthquake are small with the largest value of 5.1% and the values of MAPE for the Mw5.8 event are relatively larger with the largest value of 13.7%. However, the values of $R_{corrcoef}$ are more than 0.74 for both events, which indicates a strong positive correlation between the estimated and recorded measurements trajectories over 30 seconds of strong motion response.

Table 8.3 Difference between the recorded and estimated peak acceleration, $R_{corrcoef}$ and *MAPE* using parameters of E6.0.

Identified parameters	Earthquake		Peak acceleration (kN/mm)			$R_{corrcoef}$	MAPE
			Recorded	Estimated	Error		
E6.0	M_w 6.0	DOF1	1201	1268	5.6%	0.80	5.1%
		DOF4	1742	1805	3.6%	0.76	3.9%
	M_w 5.8	DOF1	771	778	1.0%	0.74	13.7%
		DOF4	1536	1753	14.1%	0.78	5.3%

In addition, the recorded velocities and displacements computed by single and double integration of measured accelerations are compared to the model estimated results, as shown in Figures 8.8 and 8.9. It can be seen that the peak values of the estimated displacements and velocities are slightly larger than the recorded values. However, the phase of the time histories matched well between the estimated and recorded response.

These results indicate that the identified linear shear force model can be considered to be sufficient for the prediction of the structural response during these two earthquake events. The CWH building performed elastically with no significant stiffness loss, as identified in Chapter 7, during these two events because the seismic response for both events can be predicted well using the identified parameters form the Mw6.0 event (E6.0). Hence, this cross validation provides significant, independent validation against data not used in the original model identification.

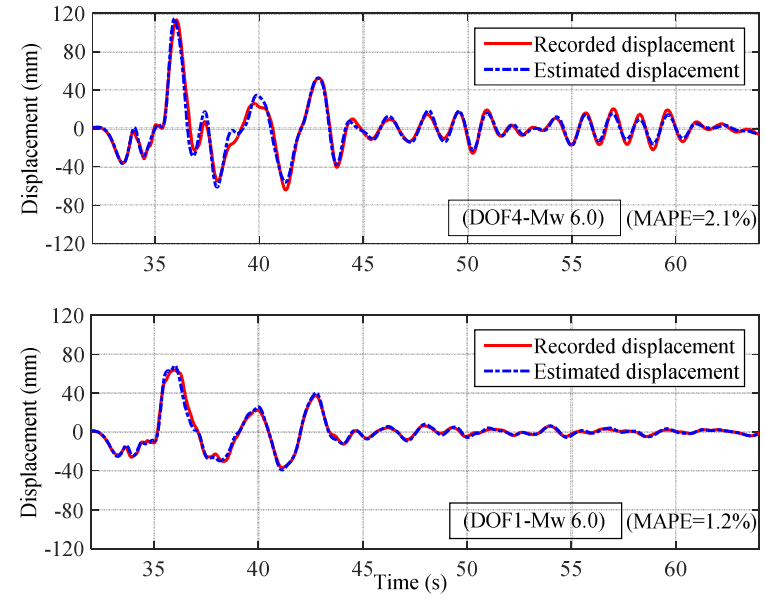

(a)

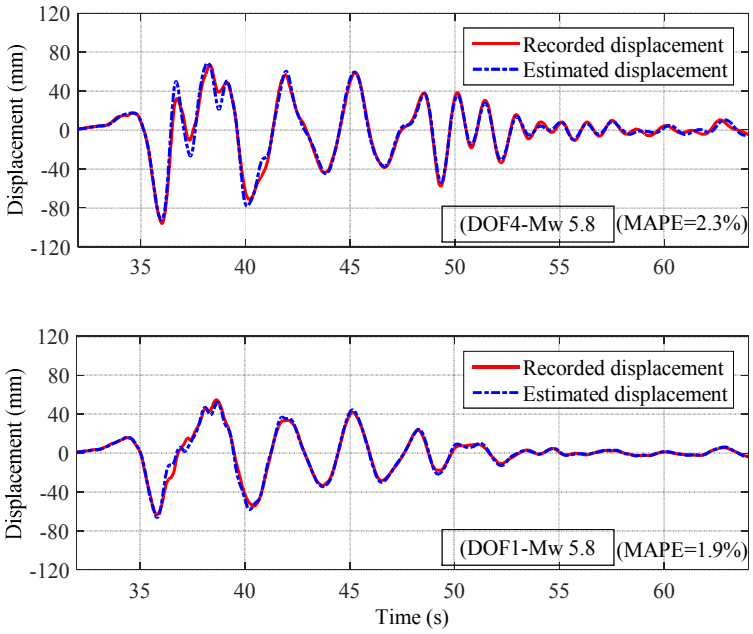

(b)

Figure 8.8: Comparison of the estimated and recorded displacements for (a) the Mw6.0 event and (b) the Mw5.8 event.

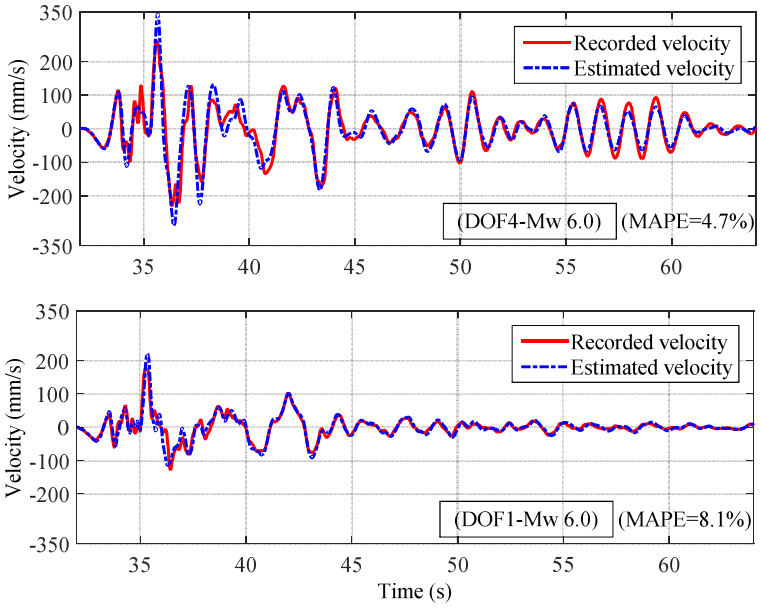

(a)

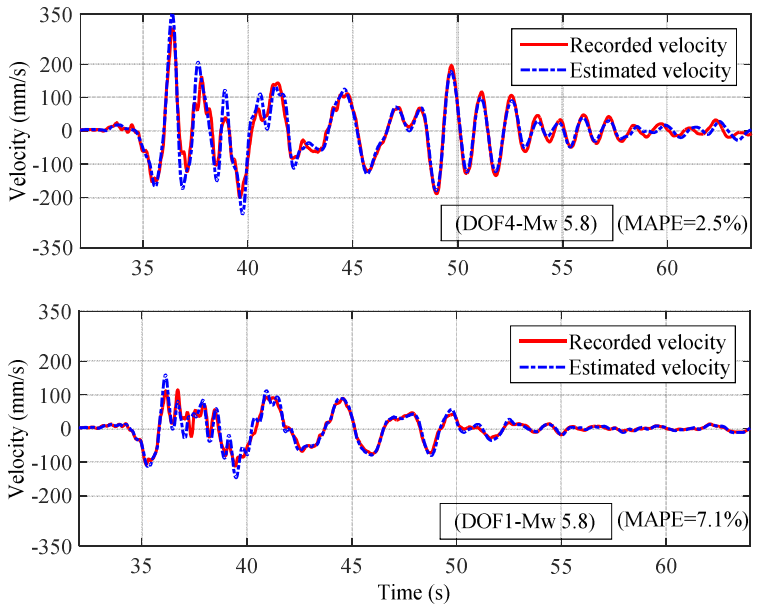

(b)

Figure 8.9: Comparison of the estimated and recorded velocities for (a) the Mw6.0 event and (b) the Mw5.8 event.

8.5.2 Second Cross Validation

The recorded data of the Mw5.8 event was also used to identify the model parameters as listed in Table 8.4, and the identified parameters were then used to simulate the response of the 4-DOF model subjected to the Mw6.0 event. This approach reverses the analysis of Mw6.0 to further assess the seismic performance of the CWH building, as well as the robustness of the identification method. Table 8.5 lists the results of comparison of peak accelerations between the recorded and estimated response, and the calculated $R_{corrcoef}$ and MAPE.

Table 8.4 Identified results for the 4-DOF shear force model using the data of Mw5.8.

Parameters	K_1 (kN/mm)	K_2 (kN/mm)	K_3 (kN/mm)	K_4 (kN/mm)	a_0	a_1	T_1 (s)	ζ_1
Initial guess	1921	1120	300	400	0.269	0.0088	1.42	5%
Estimated (E5.8)	1633	1043	305	395	0.607	0.0171	1.45	10%

Table 8.5 Difference between the recorded and estimated peak acceleration, $R_{corrcoef}$ and *MAPE* using parameters of E5.8.

Identified parameters	Earthquake		Peak acceleration (kN/mm)			$R_{corrcoef}$	MAPE
			Recorded	Estimated	Error		
E5.8	M_w 6.0	DOF1	1201	1050	12.5%	0.82	4.0%
		DOF4	1742	1528	12.2%	0.73	8.1%
	M_w 5.8	DOF1	771	735	4.7%	0.84	4.2%
		DOF4	1536	1505	2.0%	0.76	10.9%

It can be seen from Table 8.4 that the identified parameters, E5.8, using the data from the Mw5.8 event are slightly different from the identified parameters of E6.0 in Table 8.3 using

the data from the Mw6.0 event. This discrepancy could be caused by the effect of the adjacent Christchurch Hospital building with interconnecting walkways at the bottom four floors and soil-structure interaction (Gavin and Wilkinson, 2010; Kuang et al., 2015). However, the difference of peak accelerations between the recorded and estimated response are less than 4.7% for the Mw5.8 event and 12.5% for the Mw6.0 event, respectively. The MAPE values are less than 10.9% for both events. In addition, the values of $R_{corrcoef}$ are more than 0.76 for the Mw5.8 event and 0.73 for the Mw6.0 event, respectively. Thus, given very similar results with good, albeit not perfect matches to the prior, reversed analysis, the identified parameters E5.8 also well predict the seismic response for both events and yield slightly better estimated model response.

8.6 Summary

This chapter identifies the equivalent stiffness and damping coefficients of the base isolated CWH building based on a 4-DOF linear shear force model during the two major earthquakes in Christchurch that occurred within a few hours in December 2011. Numerical validation of the proposed identification method showed that the estimated structural parameters converge from a range of initial guesses and are generally robust to added noise, which validates the method is capable of identifying the stiffness and damping coefficients accurately with the lack of the response data from the second and third DOF.

The timing of these two large events permitted a unique cross validation identification analyses of the CWH building, which showed that using identified parameters from one event provided a very good match of the model and measured response for the other large event. These independent validation tests provide a strong validation for the chosen model and method. Comparison of the measured and identified model response also show that the

structure behaved essentially linearly in both events, regardless of the event used to identify the model, and that the base isolation system acted in the stiff linear range in both events. All of these results match the identification results in Chapter 7 and other preliminary published reports. Thus, this method and approach provide good estimates of the structural properties for any subsequent modelling of the structure from which to propose and design any needed retrofit.

Chapter 9: Conclusions

This thesis examines structure health monitoring from a unique perspective. Its main goal is to create practical, efficient SHM methods that clearly delineate changes in stiffness and plastic deformation with accuracy and location. To date computationally efficient methods to accomplish these goals for nonlinear structures have been lacking, preventing greater uptake of SHM.

This research develops and validates a model-free hysteresis loop analysis (HLA) method for damage identification and structural health monitoring of civil engineering structures subjected to earthquake excitations. Overall, the reconstructed hysteresis loops capture crucial linear and nonlinear structural characteristics associated with seismic damage during earthquakes. The HLA method developed provides a novel and relatively very simple means application to accurately detect, localize and quantify structural damage for different types of hysteretic structures during or immediately after an earthquake.

Importantly, structural degradation and damage that may not be visible were identified by tracking elastic stiffness, effective linear stiffness and/or plastic stiffness over time for both experimental RC structures and calibrated numerical models. Real data from a base-isolated building was also used to validate the method and demonstrate its utility. Finally, the model-free HLA method was able to clearly demonstrate its advantages over any of the vibration-based and/or model-based methods for the identification of highly nonlinear hysteretic behaviours.

The HLA methods were developed in Chapters 2 and 3 for SODF structural system with different type of hysteretic behaviours, including flag-shaped and more complex hysteretic pinching behaviour. The LLTR method based on least squares liner regression and the log likelihood hypothesis test is capable of identifying the underlying physical parameters from the reconstructed hysteresis loop of a SDOF flag-shaped hysteretic structural system. A threshold for ignoring narrow nonlinear half cycles enables accurate estimation of the post-yielding stiffness, and good estimates of the pre-yielding stiffness, yield displacement and hysteretic energy dissipation can be obtained without using the threshold. A sensitivity analysis showed that the LLTR method is robust to a wide range of linear and nonlinear earthquake events, as well as different levels of measurement noise that are close to, or higher than, practical environmental and sensor noise in today's state of the art.

Further, a modified HLA method based on the *F* type test allows for an independent statistic test at each regression function, which thus enables the identification of more complex hysteretic pinching behaviours and also improves the computational efficiency. Proof-of-concept validation using various SDOF hysteretic pinching models indicates the method is robust to evolution in response model parameters or degradation in the presence of different noise levels and damping ratios. Hence, it is able to handle nonlinearity, as well as evolving nonlinearity, in response and structural properties.

The extension of the HLA-based SHM method for MDOF structural systems was readily implemented with measurements data available or reliably estimated at each DOF of the two RC experimental buildings in Chapters 4-6. The two 12-storey RC buildings can be accurately represented using equivalent 6-DOF systems, the dynamic responses of which are dominated by the fundamental mode of vibration. Hysteresis loops were reconstructed for

each DOF using the corrected estimations of displacements, velocities and accelerations based on a Multi-rate Kalman filter, low-frequency GPS measured displacement method and/or by simply using a band-passing filter if only acceleration is measured. Hence, the ability to obtain measurements from existing, low-cost sensors ensures this approach is possible with minimum added investment in cost, computation or complexity.

Severity assessment and localization of structural degradation for damaged floors in these MDOF cases is achieved by tracking the changes in structural stiffness over time, if damage occurs in those layers. The SHM results for the single-bay experimental RC building subjected to the SHW1 event clearly shows that the method is capable of identifying damage that was not evident by external visual appearance, and also offers significant advantages and insights in detection location and severity of damage over any typical frequency analysis. Hence, it can detect damage accurately and robustly, as well as, critically, damage that may not be found by traditional methods.

The identified elastic stiffness in this MDOF case, found by selecting the significant half cycles, matched well over different earthquake events for both MDOF RC experimental buildings, which thus validated the continuity and accuracy of the method, and also indicated no significant degradation occurred during small half cycles. To date, no prior experimental on nonlinear SHM method has demonstrated the ability to detect damage this accurately or the continuity of that detection. It thus provides significant validation well beyond other published SHM methods.

The application of wavelet multiresolution analysis enables extraction of the effective linear stiffness from the identified nonlinear structural stiffness using the HLA method. The

effective linear stiffnesses were identified consistently between the large and small events, thus providing a further useful tool to characterize structural deterioration when the elastic range is negligible during small responses or after the more common small events. Changes in natural frequency due to structural deterioration were also estimated accurately using the identified effective linear stiffness at each storey, which thus furthers validate the accuracy of the SHM results and the ability to localize damage occurrence. This approach thus extends the capability and potential of this overall approach to much smaller and more common events.

Seismic damage for the experimental RC buildings was mainly caused by the cracking of concrete at the beam-column joint connections, rather than excessive plastic or yielding deformations as observed in SMRF structures. Stiffness degradation could also occur for the floors without visual damage, while no yielding behaviour was observed in the response. Thus, the elastic stiffness and efficient linear stiffness were found to be more efficient damage indices for the SHM of the RC structures with hysteretic pinching behaviours than plastic deformation along.

The model-free HLA method has shown a more effective performance in identifying the highly nonlinear RC structures compared to the model-based method. It avoids constraints to a single or fixed baseline model, and is thus fully generalizable to different types of structural behaviours that the underlying assumed model of a mode-based method cannot always capture. It is also not a completely black box approach as it is implicitly based on fundamental underlying structural mechanics and uses a far simpler computational method, thus enabling a higher computational efficiency than GA's and many other nonparametric algorithms.

As a further validation example, the base-isolated CWH building behaved entirely linearly during two similarly sized large earthquakes Mw5.8 and Mw6.0 occurring within a few hours in Christchurch. For the base isolator, the hysteresis loop can be directly reconstructed using measurements below and above the isolator. The identification of the hysteresis loop for the isolator using the HLA method indicated the base isolator did not provide any effective yielding performance for energy absorption from the design intent and prediction, and acted as a linear stiffness value matching "the corrected design stiffness", thus identifying a key isolation failure.

In addition, higher modes of vibration were involved in the dynamic structural response of the superstructure of the base-isolated CWH building during the strong shocks, thus leading to the lateral stiffness manifested in the hysteresis loop behaving in a flexible manner rather than a linear manner as identified in the aftershocks. A three DOF model was used for the superstructure to allow for three natural modes to be included in the response analysis in Chapter 8, resulting in a better replication between the model response and recorded response.

The structural parameters of the 4-DOF linear shear model identified based on the Gauss-Newton method from one event provided a very good match of the model response and measured response for the other large event. These unique cross validations thus permitted significant, independent validation for the sufficiency of the chosen linear model and method for the base isolated CWH building. Therefore, this outcome provides good estimates of the structural properties for any subsequent modelling of the structure from which to propose and design any needed retrofit.

Overall, this thesis developed an efficient HLA-based SHM method to ensure a rapid assessment of the structural damage and safety during or immediately after an earthquake. The method has been experimentally validated using two similar RC buildings with different types of linear and nonlinear hysteretic behaviours, and further proven using the real data of a based-isolated building. Finally, the method has shown its advantages by comparing to other types of SHM methods, including model-based methods and vibration-based methods.

Chapter 10: Future Work

This thesis has developed an efficient SHM method based on the identification of the reconstructed hysteresis loop of structural system. Successful performance of the HLA method has been validated against both experimental and real data. Several areas of further interest have also been identified as a result of this work. The areas of particular interest for future work are detailed within this chapter.

10.1 P-delta Effect

The P-delta effect is essential in structural analysis for tall and heavy buildings, particularly when the structure is subjected to significant lateral deformation. The secondary P-delta effect may lead to a negative post-yield stiffness and the displacement responses tend to be amplified in one direction, which may cause the dynamic instability at a rapid rate and highly increase the potential risk of building collapse during strong earthquakes. In this thesis, the P-delta effect was not simulated in the numerical models, and the negative stiffness commonly caused by this P-delta effect is not observed from the experimental buildings either. Thus, the ability of this method to identify the P-delta effect remains to be validated in the future work. However, the proposed method in this thesis avoids the consideration of any pre-defined form of structural behaviour. Thus, the P-delta effect should be observed with an additional segment after the post-yielding segment in the reconstructed hysteresis loop, if there is any. Therefore, the main focus in the future work is how to assess this P-delta effect on structural degradation using the identified regression coefficients.

10.2 Effect of Damping Force on the Identified Paramters

In this thesis, the estimated stiffness value is more real and close to the true stiffness of the structure, because the damping force is separated from the restoring force with the assumption of a 5% viscous damping coefficient that is regular used in spectral design analysis. More importantly, the effect of variable damping ratio on the estimated parameters of the SDOF system was also investigated in Chapter 3, which indicate the damping force is a relatively small part of the total restoring force during both elastic and plastic responses. However, the damping force is changing over time and different types of structures. Thus, the effect of the damping force on the identified parameters for both the MDOF numerical models and real structures still needs to be investigated in the future work.

10.3 Defining Acceptable Damage Levels or Safety Limits

The developed method has shown its ability to accurately track the evolution of structural stiffness and/or the accumulation of yielding deformation if occurred. If these identified damage indices exceed pre-defined damage levels or safety limits, an alarm or other notice can be provided immediately to emergence response and/or the owner and managers of the structure without detailed engineering analysis. Although the experimental investigations of the two typical RC frame buildings in Chapters 4-6 have provided significant insights into the effect of stiffness degradation on damage severity and cracking patterns, as well as the changes in hysteretic behaviours, delimiting such detailed damage levels and acceptable values for allowing reoccupation should be incorporated with a range of different structures. Indeed, every structure is unique and the idea of having structure specific or even storey specific damage is still relatively a novel idea. Therefore, further research remains to be undertaken before the field as a whole can assess or define what level of damage is

acceptable or what pre-defined value is appropriate for the alarm outside of the more obvious and extreme cases.

10.4 Considerations of Non-structural Components

The proposed HLA method has been successfully validated against two experimental RC buildings subjected to different levels of earthquake events that lead to both linear and highly nonlinear hysteretic behaviours in the structural response. However, these two buildings were built without any structural shear walls and non-structural elements, such as partitions, stairways and masonry walls. Investigations of building performance during earthquakes has shown that numerous building failures result from the neglecting of the structural modification induced by the addition of non-structural elements (NISEE) that affect the dynamic response the structural system. Thus, it will be important to validate the performance of the method on more typical structures, in which non-structural elements are built to consider the interaction effects of the non-structural components on structural response.

In addition, occurrence of stiffness degradation in the two experimental RC buildings in this research clearly indicated structural damage or visible cracking at the beam-column joints. However, non-structural damage could also occur and cause stiffness degradation during an earthquake, particular in very flexible structures, in which case only non-structural components need to be removed for the retrofit of the building without any structural damage. Therefore, it would be useful if damage category can also be determined to enable an optimum repair plan after an earthquake.

10.5 Optimum Sensor Deployment

The two 12-storey experimental RC buildings in Chapters 4 and 6 were reduced to 6-DOF systems justified based on the fact that the structural responses were dominated by the fundamental mode during the earthquakes. However, higher modes could be involved in the dynamic response of some complex structures designed with evident changes in stiffness, such as the CWH building in Chapter 7, in which case an equivalent system cannot be obtained using the approximation method in Chapter 4. It may be possible to measure the accelerations and/or displacements at each floor during the earthquakes. In that case, the hysteresis loops could simply be reconstructed accurately at each floor for the implementation of the HLA method, but it would also highly increase the cost of the monitoring system. In addition, the installation of sensors could also affect the operation of equipped electronic devices and utilities in some functional stories of important infrastructures, such as hospitals. Therefore, using limited sensors for damage identification is important in the real application of SHM. Optimum sensor deployment will capture the dominated modes in the structural response, which ensure the reduction of DOF account for the involvement of higher modes. Thus, an accurate input force can be obtained for the reconstruction of hysteresis loop of the equivalent system required by the HLA method. Another interesting work will be the response prediction of the unmeasured floors based on the modal analysis and system identification method.

Only one direction of earthquake input is considered in both the numerical models and the experimental buildings within this thesis. However, the earthquake excitations are three directions in reality, which could cause significant torsional components in the dynamic response with irregular hysteresis loops. In addition, the method is based on the analysis of the hysteresis loop. Thus, it is critical to build the hysteresis loop that can accurately capture

the desired dynamic behaviours using the installed sensors. In the numerical examples in Chapters 2, 3 and 5, the numerical models are assumed to be rigid and the reconstructed hysteresis loop can thus accurately represent the true response of the model. However, the slab or beam where the sensors are installed for real structures could be very flexible, and the responses of different location at the same story might be very different due to the torsional and bending effect, in which case the shape of hysteresis loop depends on the location of the measured response at the same floor. Therefore, the reconstruction of a suitable hysteresis loop for real structures by eliminating the slab torsion and beam bending effect will be studied in the future work.

10.6 Reconstruction of Hysteresis Loops Automatically

If both noisy accelerations and displacements are measured, the hysteresis loop can be reconstructed automatically using the corrected displacement, velocity and acceleration based on the multi-rate Kalman filter in Chapter 6. The identification algorithm can then be implemented automatically without requiring human input. However, the displacements and velocities were obtained by direct integration of measured accelerations after a band pass filtering with a cut-off frequency of 0.5-20Hz to eliminate low and high frequency noise in Chapter 4. Thus, a user selected cut-off frequency is needed to reconstruct the hysteresis loop when only acceleration is available for the structure. To perform the whole algorithm automatically, a signal processing method that can automatically filter the noise-contaminated acceleration to obtain the unmeasured displacement and velocity, will be considered in the future work. Equally important, the effect of different cut-off frequency on the identification results should be assessed, although, the HLA method has shown its robustness to different levels of noise.

10.7 Application in the Field Monitoring

Although the method has been tested against the real data from the base-isolated CWH building, the dynamic behaviours of the superstructure are largely linear and thus do not stretch the algorithm. The implementation of the algorithm still requires engineering analysis operated by the profession before the final validation against dynamic and plastic real data. However, the research within this thesis has provided all the basic tools and proof-of-concept for this SHM method to be incorporated into a realistic real-time monitoring system.

References

Adeli H. (2001), Neural networks in civil engineering: 1989 – 2000, *Computer - Aided Civil and Infrastructure Engineering*, **16**(2), 126-142.

Adeli H. and Jiang X. (2006), Dynamic fuzzy wavelet neural network model for structural system identification, *Journal of Structural Engineering*, **132**(1), 102-111.

Aktan A., Lee K., Chuntavan C. and Aksel T. (1994), *Modal testing for structural identification and condition assessment of constructed facilities*, Proceedings of the 12th International Modal Analysis, Honolulu, Hawaii, January 31-February 3, 462-468.

Alam M. S., Nehdi M. and Youssef M. A. (2009), Seismic performance of concrete frame structures reinforced with superelastic shape memory alloys, *Smart Struct Syst*, **5**(5), 565-585.

Astaneh A., Nader M. N. and Malik L. (1989), Cyclic behavior of double angle connections, *Journal of Structural Engineering*, **115**(5), 1101-1118.

Atkinson G. M. and Pierre J.-R. (2004), Ground-motion response spectra in eastern North America for different critical damping values, *Seismological Research Letters*, **75**(4), 541-545.

Attanasi G., Auricchio F. and Fenves G. L. (2009), Feasibility assessment of an innovative isolation bearing system with shape memory alloys, *Journal of Earthquake Engineering*, **13**(S1), 18-39.

Baber T. T. and Noori M. N. (1985), Random vibration of degrading, pinching systems, *Journal of Engineering Mechanics*, **111**(8), 1010-1026.

Bai J. and Perron P. (1998), Estimating and testing linear models with multiple structural changes, *Econometrica*, **66**(1), 47-78.

Balafas K. and Kiremidjian A. S. (2015), Development and validation of a novel earthquake damage estimation scheme based on the continuous wavelet transform of input and output acceleration measurements, *Earthquake Engineering & Structural Dynamics*, **44**(4), 501-522.

Baptista F. G., Vieira Filho J. and Inman D. J. (2012), Real-time multi-sensors measurement system with temperature effects compensation for impedance-based structural health monitoring, *Structural Health Monitoring*, **11**(2), 173-186.

Bartera F. and Giacchetti R. (2004), Steel dissipating braces for upgrading existing building frames, *Journal of Constructional Steel Research*, **60**(3), 751-769.

Basu B. (2005), Identification of stiffness degradation in structures using wavelet analysis, *Construction and Building Materials*, **19**(9), 713-721.

Bazant Z. P., Pan J. and Pijaudier-Cabot G. (1987), Softening in reinforced concrete beams and frames, *Journal of Structural Engineering*, **113**(12), 2333-2347.

Berman A. and Nagy E. (1983), Improvement of a large analytical model using test data, *AIAA journal*, **21**(8), 1168-1173.

Bernal D. (2002), Load vectors for damage localization, *Journal of Engineering Mechanics*, **128**(1), 7-14.

Bernal D. and Gunes B. (2000), *Observer/Kalman and subspace identification of the UBC benchmark structural model*, Proceedings of the 14th ASCE Engineering Mechanics Conference, Austin, Texas, May 23-26, 21-24.

Bernal D. and Levy A. (2001), *Damage localization in plates using DLVs*, Proceedings of the 19th International Modal Analysis Conference, Orlando, Florida, February 5-8, 1205-11.

Blome C. F. (2004), *LMS-based health monitoring of a non-linear rocking structure*, University of Canterbury, Christchurch.

Boroschek R. L., Moroni M. O. and Sarrazin M. (2003), Dynamic characteristics of a long span seismic isolated bridge, *Engineering Structures*, **25**(12), 1479-1490.

Bouc R. (1967), *Forced vibration of mechanical systems with hysteresis*, Proceedings of the fourth conference on non-linear oscillation, Prague, Czechoslovakia.

Brincker R., Zhang L. and Andersen P. (2000), *Modal identification from ambient responses using frequency domain decomposition*, Proceeding of the 18th International Modal Analysis Conference (IMAC), San Antonio, Texas, February 7-10, 1-6.

Brown R. G. and Hwang P. Y. (1997), *Introduction to random signals and applied Kalman filtering: with MATLAB exercises and solutions*, Wiley, New York.

Brownjohn J. M., Xia P.-Q., Hao H. and Xia Y. (2001), Civil structure condition assessment by FE model updating:: methodology and case studies, *Finite Elements in Analysis and Design*, **37**(10), 761-775.

Brownjohn J. M. W., Moyo P., Omenzetter P. and Lu Y. (2003), Assessment of highway bridge upgrading by dynamic testing and finite-element model updating, *Journal of Bridge Engineering*, **8**(3), 162-172.

Caicedo J. M., Dyke S. J. and Johnson E. A. (2003), Natural excitation technique and eigensystem realization algorithm for phase I of the IASC-ASCE benchmark problem: Simulated data, *Journal of Engineering Mechanics*, **130**(1), 49-60.

Cao X., Sugiyama Y. and Mitsui Y. (1998), Application of artificial neural networks to load identification, *Computers & structures*, **69**(1), 63-78.

Casciati S. and Hamdaoui K. (2008), Experimental and numerical studies toward the implementation of shape memory alloy ties in masonry structures, *Smart Structures and Systems*, **4**(2), 153-169.

Catbas F. N., Brown D. L. and Aktan A. E. (2006), Use of modal flexibility for damage detection and condition assessment: case studies and demonstrations on large structures, *Journal of Structural Engineering*, **132**(11), 1699-1712.

Cawley P. and Adams R. (1979), The location of defects in structures from measurements of natural frequencies, *The Journal of Strain Analysis for Engineering Design*, **14**(2), 49-57.

Cement & Concrete Association of New Zealand (2010) *New Zealand Guide to Concrete Construction* Wellington, Cement & Concrete Association of New Zealand

Chan T. H., Tam H.-Y., Ni Y.-Q., Chung S., Guan B.-O. and Chan T. (2004), *Using optical fibre sensors for structural health monitoring of Tsing Ma Bridge*, 1st Workshop on Smart Materials and Structures Technology, Hawaii, USA., January 12-14, 539-546.

Chan W.-S., Xu Y.-L., Ding X.-L., Xiong Y.-L. and Dai W.-J. (2006), Assessment of dynamic measurement accuracy of GPS in three directions, *Journal of surveying engineering*, **132**(3), 108-117.

Chang C.-C. and Shi Y. (2010), Identification of time-varying hysteretic structures using wavelet multiresolution analysis, *International Journal of Non-Linear Mechanics*, **45**(1), 21-34.

Chang P. C. and Liu S. C. (2003), Recent research in nondestructive evaluation of civil infrastructures, *Journal of materials in civil engineering*, **15**(3), 298-304.

Chase J. G., Leo Hwang K., Barroso L. and Mander J. (2005a), A simple LMS‐based approach to the structural health monitoring benchmark problem, *Earthquake engineering & structural dynamics*, **34**(6), 575-594.

Chase J. G., Spieth H. A., Blome C. F. and Mander J. (2005b), LMS‐based structural health monitoring of a non‐linear rocking structure, *Earthquake engineering & structural dynamics*, **34**(8), 909-930.

Chaudhary M. T. A., Abe M., Fujino Y. and Yoshida J. (2000), System identification of two base-isolated bridges using seismic records, *Journal of Structural Engineering*, **126**(10), 1187-1195.

Chen J., Liu W., Peng Y. and Li J. (2007), Stochastic seismic response and reliability analysis of base-isolated structures, *Journal of Earthquake Engineering*, **11**(6), 903-924.

Chopra A. K. (1995), *Dynamics of structures*, Prentice Hall, New Jersey.

Chopra A. K. (2001), *Dynamics of structures: Theory and applications to earthquake engineering*, Prentice Hall Saddle River, New York.

Chou J.-H. and Ghaboussi J. (2001), Genetic algorithm in structural damage detection, *Computers & Structures*, **79**(14), 1335-1353.

Christopoulos C., Filiatrault A. and Folz B. (2002), Seismic response of self‐centring hysteretic SDOF systems, *Earthquake engineering & structural dynamics*, **31**(5), 1131-1150.

Christopoulos C., Tremblay R., Kim H.-J. and Lacerte M. (2008), Self-centering energy dissipative bracing system for the seismic resistance of structures: development and validation, *Journal of Structural Engineering*, **134**(1), 96-107.

Cifuentes A. O. and Iwan W. D. (1989), Nonlinear system identification based on modelling of restoring force behaviour, *Soil Dynamics and Earthquake Engineering*, **8**(1), 2-8.

Clinton J. F., Bradford S. C., Heaton T. H. and Favela J. (2006), The observed wander of the natural frequencies in a structure, *Bulletin of the Seismological Society of America*, **96**(1), 237-257.

Clough R. W. and Penzien J. (1993), *Dynamics of structures*, McGraw-Hill, New York.

Coburm A., Spence R. and Pomonis A. (1992), *Factors determining human casualty levels in earthquakes: mortality prediction in building collapse*, Proceedings of the tenth world conference on earthquake engineering, Madrid, Spain, July 19-24, 5989-5994.

Coca D. and Billings S. (2001), Non-linear system identification using wavelet multiresolution models, *International Journal of Control*, **74**(18), 1718-1736.

Creed S. (1987), *Assessment of large engineering structures using data collected during in-service loading*, Proceedings of structural assessment based on full and large scale testing, Butterworks, UK, 55-62.

Cunha A. and Caetano E. (2006), Experimental modal analysis of civil engineering structures, *Sound and Vibration*, **40**(6), 12-20.

Davey F. (2011), Natural hazards—the Christchurch earthquakes, *New Zealand Journal of Geology and Geophysics*, **54**(2), 149-150.

Diniz P. S. R. (2013), *Adaptive Filtering: Algorithms and Practical Implementation*, Springer, US.

Docherty P. D., Chase J. G., Lotz T. F. and Desaive T. (2011), A graphical method for practical and informative identifiability analyses of physiological models: A case study of insulin kinetics and sensitivity, *Biomed Eng Online*, **10**(1), 39.

Doebling S. W., Farrar C. R., Prime M. B. and Shevitz D. W. (1996), *Damage identification and health monitoring of structural and mechanical systems from changes in their vibration characteristics: a literature review*, Los Alamos National Lab., NM (United States), Los Alamos National Lab., NM (United States).

Doğangün A. (2004), Performance of reinforced concrete buildings during the May 1, 2003 Bingöl Earthquake in Turkey, *Engineering Structures*, **26**(6), 841-856.

Elkordy M., Chang K. and Lee G. (1993), Neural networks trained by analytically simulated damage states, *Journal of Computing in Civil Engineering*, **7**(2), 130-145.

Fan W. and Qiao P. (2011), Vibration-based damage identification methods: a review and comparative study, *Structural Health Monitoring*, **10**(1), 83-111.

Feder P. I. (1975a), The log likelihood ratio in segmented regression, *The Annals of Statistics*, **3**(1), 84-97.

Feder P. I. (1975b), On asymptotic distribution theory in segmented regression problems--identified case, *The Annals of Statistics*, **3**(1), 49-83.

Flood I. and Kartam N. (1994), Neural networks in civil engineering. I: Principles and understanding, *Journal of computing in civil engineering*, **8**(2), 131-148.

Foliente G. C. (1995), Hysteresis modeling of wood joints and structural systems, *Journal of Structural Engineering*, **121**(6), 1013-1022.

Foliente G. C. and Noori M. N. (1996), Equivalent Linearization of Generally Pinching Hysteretic, Degrading Systems, *Earthquake Engineering and Structural Dynamics*, **25**(1), 611-629.

Fritzen C.-P., Jennewein D. and Kiefer T. (1998), Damage detection based on model updating methods, *Mechanical Systems and Signal Processing*, **12**(1), 163-186.

Fu G. and Moosa A. G. (2002), An optical approach to structural displacement measurement and its application, *Journal of Engineering Mechanics*, **128**(5), 511-520.

Funahashi K.-I. (1989), On the approximate realization of continuous mappings by neural networks, *Neural networks*, **2**(3), 183-192.

Furukawa T., Ito M., Izawa K. and Noori M. N. (2005), System identification of base-isolated building using seismic response data, *Journal of engineering mechanics*, **131**(3), 268-275.

Garlock M. M., Ricles J. M. and Sause R. (2005), Experimental studies of full-scale posttensioned steel connections, *Journal of Structural Engineering*, **131**(3), 438-448.

Gavin H. P., Nigbor R., Lawson W., Macrae G., Rodgers G. W., Chase J. G. and Gutschmidt

S. (2012), *Seismic response monitoring of the base-isolated Christchurch Women's Hospital*, NSF-EERI Japan-New Zealand RAPID Awardee Worshop, Virginia.

Gavin H. P. and Wilkinson G. (2010), Preliminary Observations of the Effects of the 2010 Darfield Earthquake on the Base-Isolated Christchurch Women's Hospital, *Bulletin of the New Zealand Society for Earthquake Engineering*, **43**(4), 360-367.

GeoNet https://www.geonet.org.nz/quakes.

Ghobarah A., Aziz T. and Abou-Elfath H. (1999), Softening effects on the seismic response of non-ductile concrete frames, *Journal of earthquake engineering*, **3**(1), 59-81.

Goel R. K. (2003), *Performance of buildings during the January 26, 2001 Bhuj earthquake*, Earthquake Engineering Research Institute, Oakland, CA.

Graf W., Freitag S., Sickert J. U. and Kaliske M. (2012), Structural analysis with fuzzy data and neural network based material description, *Computer‐Aided Civil and Infrastructure Engineering*, **27**(9), 640-654.

Hann C. E., Singh-Levett I., Deam B. L., Mander J. B. and Chase J. G. (2009), Real-time system identification of a nonlinear four-story steel frame structure—application to structural health monitoring, *Sensors Journal, IEEE*, **9**(11), 1339-1346.

Hao H. and Xia Y. (2002), Vibration-based damage detection of structures by genetic algorithm, *Journal of Computing in Civil Engineering*, **16**(3), 222-229.

Hera A. and Hou Z. (2004), Application of wavelet approach for ASCE structural health monitoring benchmark studies, *Journal of Engineering Mechanics*, **130**(1), 96-104.

Hijikata K., Takahashi M., Aoyagi T. and Mashimo M. (2011), *Behavior of a base isolated building at Fukushima Dai-Ichi Nuclear Power Plant during the Great East Japan Earthquake*, Proceedings of the International Symposium on Engineering Lessons Learned from the 2011 Great East Japan Earthquake, Tokyo, Japan, March 1-4, 1542-1551.

Holmes Consulting Group, http://www.holmesgroup.com/services.

Hoshiya M. and Saito E. (1984), Structural identification by extended Kalman filter, *Journal of Engineering Mechanics*, **110**(12), 1757-1770.

Hou Z., Noori M. and Amand R. S. (2000), Wavelet-based approach for structural damage detection, *Journal of Engineering mechanics*, **126**(7), 677-683.

Housner G. W., Bergman L. A., Caughey T., Chassiakos A., Claus R., Masri S., Skelton R., Soong T., Spencer B. and Yao J. T. (1997), Structural control: past, present, and future, *Journal of engineering mechanics*, **123**(9), 897-971.

Hsieh K. H., Halling M. W. and Barr P. J. (2006), Overview of vibrational structural health monitoring with representative case studies, *Journal of Bridge Engineering*, **11**(6), 707-715.

Huang M.-C., Wang Y.-P., Chang J.-R. and Chen Y.-H. (2009), Physical-Parameter Identification of Base-Isolated Buildings Using Backbone Curves, *Journal of structural engineering*, **135**(9), 1107-1114.

Hudson D. J. (1966), Fitting segmented curves whose join points have to be estimated, *Journal of the American Statistical Association*, **61**(316), 1097-1129.

Hung S. L., Huang C., Wen C. and Hsu Y. (2003), Nonparametric identification of a building structure from experimental data using wavelet neural network, *Computer‐Aided Civil and Infrastructure Engineering*, **18**(5), 356-368.

Hwang J., Yun H., Park S.-K., Lee D. and Hong S. (2012), Optimal methods of RTK-GPS/Accelerometer integration to monitor the displacement of structures, *Sensors*, **12**(1), 1014-1034.

Iannone F., Latour M., Piluso V. and Rizzano G. (2011), Experimental analysis of bolted steel beam-to-column connections: component identification, *Journal of Earthquake Engineering*, **15**(2), 214-244.

Ifeachor E. C. and Jervis B. W. (2002), *Digital signal processing: a practical approach*, Addison-Wesley, UK.

Iwan W. D. (2002), *R-SHAPE: a real-time structural health and performance evaluation system*, Proceedings of the US Europe Workshop on Sensors and Smart Structures Technology, Como and Somma Lombardo, Italy, April 12-13 33-38.

Iwan W. D., Radulescu D. C. and Radulescu C. (2013), *Extreme event performance evaluation using real-time hysteresis monitoring*, US Patent 8,538,734.

Jaishi B. and Ren W.-X. (2005), Structural finite element model updating using ambient vibration test results, *Journal of Structural Engineering*, **131**(4), 617-628.

Jeen-Shang L. and Yigong Z. (1994), Nonlinear structural identification using extended Kalman filter, *Computers & Structures*, **52**(4), 757-764.

Ji X., Fenves G. L., Kajiwara K. and Nakashima M. (2010), Seismic damage detection of a full-scale shaking table test structure, *Journal of Structural Engineering*, **137**(1), 14-21.

Jiang X. and Adeli H. (2005), Dynamic wavelet neural network for nonlinear identification of highrise buildings, *Computer‐Aided Civil and Infrastructure Engineering*, **20**(5), 316-330.

Juang J.-N. and Pappa R. S. (1985), An eigensystem realization algorithm for modal parameter identification and model reduction, *Journal of guidance, control, and dynamics*,

8(5), 620-627.

Juang J.-N. and Suzuki H. (1988), An eigensystem realization algorithm in frequency domain for modal parameter identification, *Journal of Vibration and Acoustics*, **110**(1), 24-29.

Kam W. Y., Pampanin S., Dhakal R., Gavin H. and Roeder C. (2010), Seismic performance of reinforced concrete buildings in the September 2010 Darfield (Canterbury) earthquakes, *Bulletin of New Zealand Society of Earthquake Engineering*, **43**(4), 340-350.

Khoo L. M., Mantena P. R. and Jadhav P. (2004), Structural damage assessment using vibration modal analysis, *Structural Health Monitoring*, **3**(2), 177-194.

Kijewski T. and Kareem A. (2003), Wavelet transforms for system identification in civil engineering, *Computer‐Aided Civil and Infrastructure Engineering*, **18**(5), 339-355.

Kim J.-T., Ryu Y.-S., Cho H.-M. and Stubbs N. (2003), Damage identification in beam-type structures: frequency-based method vs mode-shape-based method, *Engineering structures*, **25**(1), 57-67.

Ko J. and Ni Y. (2005), Technology developments in structural health monitoring of large-scale bridges, *Engineering structures*, **27**(12), 1715-1725.

Krawinkler H. and Zohrei M. (1983), Cumulative damage in steel structures subjected to earthquake ground motions, *Computers & Structures*, **16**(1), 531-541.

Kroggel O. (1993), *Nondestructive testing of the integrity of bridges: an EC project in Bridge Management 2: Inspection, Maintence Assessment and Repair*, the Second International Conference on Bridge Management University of Surrey, Guildford.

Kuang A., Sridhar A., Garven J., Gutschmidt S., Rodgers G. W., Chase J. G., Gavin H. P., Nigbor R. and Macrae G. (2015), Christchurch Women's Hospital: Performance Analysis of the Base-Isolation System during the Series of Canterbury Earthquakes 2011–2012, *Journal of Performance of Constructed Facilities*, **04015**(096), 1-10.

Kulkarni J. A. and Jangid R. (2002), Rigid body response of base‐isolated structures, *Journal of structural control*, **9**(3), 171-188.

Kulkarni J. A. and Jangid R. (2003), Effects of superstructure flexibility on the response of base-isolated structures, *Shock and Vibration*, **10**(1), 1-13.

Kunnath S. K., Mander J. B. and Fang L. (1997), Parameter identification for degrading and pinched hysteretic structural concrete systems, *Engineering Structures*, **19**(3), 224-232.

Landau L. D. and Lifshi͡ts E. M. (1976), *Mechanics: by L.D. Landau and E.M.Lifshitz*, Pergamon Press, Oxford.

Lee J. and Fenves G. L. (1998), A plastic‐damage concrete model for earthquake analysis of dams, *Earthquake engineering & structural dynamics*, **27**(9), 937-956.

Li S., Suzuki Y. and Noori M. (2004), Identification of hysteretic systems with slip using bootstrap filter, *Mechanical systems and signal processing*, **18**(4), 781-795.

Li X., Ge L., Ambikairajah E., Rizos C., Tamura Y. and Yoshida A. (2006), Full-scale structural monitoring using an integrated GPS and accelerometer system, *GPS solutions*, **10**(4), 233-247.

Li X., Zhou Z., Yu H., Wen R., Lu D., Huang M., Zhou Y. and Cu J. (2008), Strong motion observations and recordings from the great Wenchuan Earthquake, *Earthquake Engineering and Engineering Vibration*, **7**(3), 235-246.

Lin C., Soong T. and Natke H. (1990), Real-time system identification of degrading structures, *Journal of engineering mechanics*, **116**(10), 2258-2274.

Londoño J. M., Neild S. A. and Cooper J. E. (2015), Identification of backbone curves of nonlinear systems from resonance decay responses, *Journal of Sound and Vibration*, **348**(1), 224-238.

Lozano‐Galant J. A., Nogal M., Castillo E. and Turmo J. (2013), Application of observability techniques to structural system identification, *Computer‐Aided Civil and Infrastructure Engineering*, **28**(6), 434-450.

Lu X. and Li P. (2004), *Benchmark test of a 12-story reinforced concrete frame model on shaking table*, State Key Laboratory of Disaster Reduction of Civil Engineering, Tongji University.

Lus H., Betti R., Yu J. and De Angelis M. (2003), Investigation of a system identification methodology in the context of the ASCE benchmark problem, *Journal of engineering mechanics*, **130**(1), 71-84.

Lynch J. P., Law K. H., Kiremidjian A. S., Carryer E., Farrar C. R., Sohn H., Allen D. W., Nadler B. and Wait J. R. (2004), Design and performance validation of a wireless sensing unit for structural monitoring applications, *Structural Engineering and Mechanics*, **17**(3-4), 393-408.

Lynch J. P., Partridge A., Law K. H., Kenny T. W., Kiremidjian A. S. and Carryer E. (2003), Design of piezoresistive MEMS-based accelerometer for integration with wireless sensing unit for structural monitoring, *Journal of Aerospace Engineering*, **16**(3), 108-114.

Maeck J., Wahab M. A., Peeters B., De Roeck G., De Visscher J., De Wilde W., Ndambi J.-M. and Vantomme J. (2000), Damage identification in reinforced concrete structures by dynamic stiffness determination, *Engineering structures*, **22**(10), 1339-1349.

Mahin S. A. (1998), Lessons from damage to steel buildings during the Northridge earthquake, *Engineering structures*, **20**(4), 261-270.

Maia N., Silva J., Almas E. and Sampaio R. (2003), Damage detection in structures: from mode shape to frequency response function methods, *Mechanical systems and signal processing*, **17**(3), 489-498.

Mallat S. G. (1989), A theory for multiresolution signal decomposition: the wavelet representation, *Pattern Analysis and Machine Intelligence, IEEE Transactions on*, **11**(7), 674-693.

Malley J. O. (1998), SAC Steel Project: Summary of Phase 1 testing investigation results, *Engineering structures*, **20**(4), 300-309.

Mander J., Panthaki F. and Kasalanati A. (1994), Low-cycle fatigue behavior of reinforcing steel, *Journal of Materials in Civil Engineering*, **6**(4), 453-468.

Maruyama O., Yun C., Hoshiya M. and Shinozuka M. (1990), *Program EXKAL2 for identification of structural dynamical systems*, National Center for Earthquake Engineering Research, Buffalo.

Masri S., Sheng L., Caffrey J., Nigbor R., Wahbeh M. and Abdel-Ghaffar A. (2004), Application of a web-enabled real-time structural health monitoring system for civil infrastructure systems, *Smart Materials and Structures*, **13**(6), 1269-1283.

Matsagar V. A. and Jangid R. (2008), Base isolation for seismic retrofitting of structures, *Practice Periodical on Structural Design and Construction*, **13**(4), 175-185.

Melhem H. and Kim H. (2003), Damage detection in concrete by fourier and wavelet analyses, *Journal of Engineering Mechanics*, **129**(5), 571-577.

Miwada G., Yoshida O., Ishikawa R. and Nakamura M. (2012), *Observation records of base-isolated buildings in strong motion area during the 2011 Off the Pacific Coast of Tohuku earthquake*, Proceedings of the International Symposium on Engineering Lessons Learned from the 2011 Great East Japan Earthquake, Tokyo, Japan, March 1-4, 1017-1024.

Mufti A. A., Tadros G. and Jones P. R. (1997), Field assessment of fibre-optic Bragg grating strain sensors in the Confederation Bridge, *Canadian Journal of Civil Engineering*, **24**(6), 963-966.

Muravyov A. A. and Rizzi S. A. (2003), Determination of nonlinear stiffness with application to random vibration of geometrically nonlinear structures, *Computers & Structures*, **81**(15), 1513-1523.

Nader M. and Astaneh A. (1991), Dynamic behavior of flexible, semirigid and rigid steel frames, *Journal of Constructional Steel Research*, **18**(3), 179-192.

Naeim F., Lew M., Huang S. C., Lam H. K. and Carpenter L. D. (2000), The performance of tall buildings during the 21 September 1999 Chi-Chi earthquake, Taiwan, *The Structural Design of Tall Buildings*, **9**(2), 137-160.

Nagarajaiah S. and Sun X. (2000), Response of base-isolated USC hospital building in Northridge earthquake, *Journal of Structural Engineering*, **126**(10), 1177-1186.

Nayyerloo M., Chase J., MacRae G. and Chen X. (2011), LMS-based approach to structural health monitoring of nonlinear hysteretic structures, *Structural Health Monitoring*, **10**(4), 429-444.

Olmos B. A. and Roesset J. M. (2010), Evaluation of the half‐power bandwidth method to estimate damping in systems without real modes, *Earthquake Engineering & Structural Dynamics*, **39**(14), 1671-1686.

Ovanesova A. and Suarez L. (2004), Applications of wavelet transforms to damage detection in frame structures, *Engineering structures*, **26**(1), 39-49.

Ozbulut O. E. and Hurlebaus S. (2011), Seismic assessment of bridge structures isolated by a shape memory alloy/rubber-based isolation system, *Smart Materials and Structures*, **20**(1), 015003.

Ozcebe G. and Saatcioglu M. (1989), Hysteretic shear model for reinforced concrete members, *Journal of Structural Engineering*, **115**(1), 132-148.

Pacific Earthquake Engineering Reseach Center (2005), *strong motion database,* http://peer.berkeley.edu/smcat

Pandey A. and Biswas M. (1994), Damage detection in structures using changes in flexibility, *Journal of sound and vibration*, **169**(1), 3-17.

Pandey A., Biswas M. and Samman M. (1991), Damage detection from changes in curvature mode shapes, *Journal of sound and vibration*, **145**(2), 321-332.

Papadrakakis M., Fragiadakis M., Lagaros N. D. and Plevris V. (2011), *Computational methods in earthquake engineering*, Springer, Netherlands.

Papadrakakis M., Papadopoulos V. and Lagaros N. D. (1996), Structural reliability analyis of elastic-plastic structures using neural networks and Monte Carlo simulation, *Computer methods in applied mechanics and engineering*, **136**(1), 145-163.

Park H., Lee H., Adeli H. and Lee I. (2007), A new approach for health monitoring of structures: terrestrial laser scanning, *Computer‐Aided Civil and Infrastructure Engineering*, **22**(1), 19-30.

Park R. (1986), Ductile design approach for reinforced concrete frames, *Earthquake spectra*,

2(3), 565-619.

Park Y., Wen Y. and Ang A. (1986), Random vibration of hysteretic systems under bi‐directional ground motions, *Earthquake engineering & structural dynamics*, **14**(4), 543-557.

Park Y. J., Ang A. H. S. and Wen Y. K. (1985), Seismic damage analysis of reinforced concrete buildings, *Journal of Structural Engineering*, **111**(4), 740-757.

Pekcan G., Mander J. B. and Chen S. S. (1999), Fundamental considerations for the design of non‐linear viscous dampers, *Earthquake engineering & structural dynamics*, **28**(11), 1405-1425.

Perera R. and Torres R. (2006), Structural damage detection via modal data with genetic algorithms, *Journal of Structural Engineering*, **132**(9), 1491-1501.

Powell G. H. and Allahabadi R. (1988), Seismic damage prediction by deterministic methods: concepts and procedures, *Earthquake engineering & structural dynamics*, **16**(5), 719-734.

Psimoulis P. A. and Stiros S. C. (2008), Experimental assessment of the accuracy of GPS and RTS for the determination of the parameters of oscillation of major structures, *Computer‐Aided Civil and Infrastructure Engineering*, **23**(5), 389-403.

Qiao L., Esmaeily A. and Melhem H. G. (2012), Signal pattern recognition for damage diagnosis in structures, *Computer‐Aided Civil and Infrastructure Engineering*, **27**(9), 699-710.

Quandt R. E. (1958), The estimation of the parameters of a linear regression system obeying two separate regimes, *Journal of the american statistical association*, **53**(284), 873-880.

Rajasekaran S., Febin M. and Ramasamy J. (1996), Artificial fuzzy neural networks in civil engineering, *Computers & Structures*, **61**(2), 291-302.

Rajeev S. and Krishnamoorthy C. (1992), Discrete optimization of structures using genetic algorithms, *Journal of structural engineering*, **118**(5), 1233-1250.

Rao J. and Gupta K. (1999), *Introductory course on theory and practice of mechanical vibrations*, New Age International, New Delhi.

Ren W.-X. and Chen H.-B. (2010), Finite element model updating in structural dynamics by using the response surface method, *Engineering Structures*, **32**(8), 2455-2465.

Ricles J. M., Sause R., Garlock M. M. and Zhao C. (2001), Posttensioned seismic-resistant connections for steel frames, *Journal of Structural Engineering*, **127**(2), 113-121.

Rizzi S. A. and Muravyov A. A. (2000), *Comparison of nonlinear random response using*

equivalent linearization and numerical simulation, Structural dynamics: recent advances, proceedings of the 7th international conference, Southampton, UK, July 24-27, 833-846.

Rodgers G. W., Solberg K. M., Chase J. G., Mander J. B., Bradley B. A., Dhakal R. P. and Li L. (2008), Performance of a damage‐protected beam–column subassembly utilizing external HF2V energy dissipation devices, *Earthquake engineering & structural dynamics*, **37**(13), 1549-1564.

Saatcioglu M. and Ozcebe G. (1989), Response of reinforced concrete columns to simulated seismic loading, *ACI Structural Journal*, **86**(1),

Sabelli R., Mahin S. and Chang C. (2003), Seismic demands on steel braced frame buildings with buckling-restrained braces, *Engineering Structures*, **25**(5), 655-666.

Sabelli R., Roeder C. W. and Hajjar J. F. (2013), *Seismic Design of Steel Special Concentrically Braced Frame Systems*, National Institute of Standards and Technology, California.

Safak E. and Hudnut K. (2006), *Real-time structural monitoring and damage detection by acceleration and GPS sensors*, 8th US National Conference on Earthquake Engineering, San Francisco, California, April 18-22, 1-10.

Salawu O. (1997), Detection of structural damage through changes in frequency: a review, *Engineering structures*, **19**(9), 718-723.

Sato T. and Qi K. (1998), Adaptive H∞ filter: its application to structural identification, *Journal of Engineering Mechanics*, **124**(11), 1233-1240.

Schwarz B. J. and Richardson M. H. (1999), Experimental modal analysis, *CSI Reliability week*, **35**(1), 1-12.

Sezen H., Whittaker A., Elwood K. and Mosalam K. (2003), Performance of reinforced concrete buildings during the August 17, 1999 Kocaeli, Turkey earthquake, and seismic design and construction practise in Turkey, *Engineering Structures*, **25**(1), 103-114.

Shanghai Government Construction and Management Commission (2013), *Code for Seismic Design of Buildings (DGJ08-9-2013)*, Shanghai Standardization Office, Shanghai, China.

Sirca Jr G. and Adeli H. (2012), System identification in structural engineering, *Scientia Iranica*, **19**(6), 1355-1364.

Sjöberg J., Zhang Q., Ljung L., Benveniste A., Delyon B., Glorennec P.-Y., Hjalmarsson H. and Juditsky A. (1995), Nonlinear black-box modeling in system identification: a unified overview, *Automatica*, **31**(12), 1691-1724.

Skinner R. I., William H. Robinson, and Graeme H. McVerry. (1993), *An introduction to*

seismic isolation with additional material on added damping, Robinson Seismic Ltd, New Zealand.

Skolnik D. A. and Wallace J. W. (2010), Critical assessment of interstory drift measurements, *Journal of Structural Engineering*, **136**(12), 1574-1584.

Smith H. A. and Chase J. G. (1994), Identification of structural system parameters using the cascade-correlation neural network, *Journal of dynamic systems, measurement, and control*, **116**(4), 790-792.

Smyth A. and Wu M. (2007), Multi-rate Kalman filtering for the data fusion of displacement and acceleration response measurements in dynamic system monitoring, *Mechanical Systems and Signal Processing*, **21**(2), 706-723.

Spencer B. F., Ruiz‐Sandoval M. E. and Kurata N. (2004), Smart sensing technology: opportunities and challenges, *Structural Control and Health Monitoring*, **11**(4), 349-368.

Sridhar A., Kuang A., Garven J., Gutschmidt S., Chase J. G., Gavin H. P., Nigbor R. L., Rodgers G. W. and MacRae G. A. (2014), Christchurch Women's Hospital: Analysis of Measured Earthquake Data during the 2011-2012 Christchurch Earthquakes, *Earthquake spectra*, **30**(1), 383-400.

Standards New Zealand (1992), *Code of Practice for General Structural Design and Design Loadings for Buildings*, Wellington, Standards New Zealand.

Stelmack T. W., Marley M. J. and Gerstle K. H. (1986), Analysis and tests of flexibly connected steel frames, *Journal of Structural Engineering*, **112**(7), 1573-1588.

Stephens J. E. and Yao J. T. (1987), Damage assessment using response measurements, *Journal of Structural Engineering*, **113**(4), 787-801.

Stewart J. P., Conte J. P. and Aiken I. D. (1999), Observed behavior of seismically isolated buildings, *Journal of Structural Engineering*, **125**(9), 955-964.

Stoimenova E., Datcheva M. and Schanz T. (2004), Application of two-phase regression to geotechnical data, *Pliska Studia Mathematica Bulgarica*, **16**(1), 245p-257p.

Story B. A. and Fry G. T. (2014), A Structural Impairment Detection System Using Competitive Arrays of Artificial Neural Networks, *Computer‐Aided Civil and Infrastructure Engineering*, **29**(3), 180-190.

Stubbs N. and Kim J.-T. (1996), Damage localization in structures without baseline modal parameters, *Aiaa Journal*, **34**(8), 1644-1649.

Swanson D. A., Tayman J. and Bryan T. (2011), MAPE-R: a rescaled measure of accuracy for cross-sectional subnational population forecasts, *Journal of Population Research*, **28**(2-3),

225-243.

Taha M. R., Noureldin A., Lucero J. and Baca T. (2006), Wavelet transform for structural health monitoring: a compendium of uses and features, *Structural Health Monitoring*, **5**(3), 267-295.

Teran-Gilmore A., Avila E. and Rangel G. (2003), On the use of plastic energy to establish strength requirements in ductile structures, *Engineering structures*, **25**(7), 965-980.

Teran-Gilmore A. and Jirsa J. O. (2005), A damage model for practical seismic design that accounts for low cycle fatigue, *Earthquake Spectra*, **21**(3), 803-832.

Tierney K. J. and Goltz J. D. (1997), *Emergency response: lessons learned from the Kobe earthquake*, Disaster Research Center, University of Delaware.

Toussi S. and Yao J. T. (1983), Hysteresis identification of existing structures, *Journal of Engineering Mechanics*, **109**(5), 1189-1202.

Tremblay R., Filiatrault A., Bruneau M., Nakashima M., Prion H. G. and DeVall R. (1996), Seismic design of steel buildings: lessons from the 1995 Hyogo-ken Nanbu earthquake, *Canadian Journal of Civil Engineering*, **23**(3), 727-756.

Tremblay R., Lacerte M. and Christopoulos C. (2008), Seismic response of multistory buildings with self-centering energy dissipative steel braces, *Journal of Structural Engineering*, **134**(1), 108-120.

United States Geological Survery (USGS) 2012, http://earthquake.usgs.gov/earthquakes/eqarchives/year/eqstats.php.

Vafaei M., Adnan A. b. and Abd. Rahman A. B. (2013), Real-time seismic damage detection of concrete shear walls using artificial neural networks, *Journal of Earthquake Engineering*, **17**(1), 137-154.

Walpole R. E., Myers R. H. and Myers S. L. (2011), *Probability and statistics for engineers and scientists*, Prentice Hall, New Jersey.

Wang X. and Zheng G. (2016), Equivalent Dynamic Stiffness Mapping technique for identifying nonlinear structural elements from frequency response functions, *Mechanical Systems and Signal Processing*, **68**(394-415.

Wei H.-L. and Billings S. (2002), Identification of time-varying systems using multiresolution wavelet models, *International Journal of Systems Science*, **33**(15), 1217-1228.

Wen Y.-K. (1976), Method for random vibration of hysteretic systems, *Journal of the engineering mechanics division*, **102**(2), 249-263.

Whitley D., Starkweather T. and Bogart C. (1990), Genetic algorithms and neural networks: Optimizing connections and connectivity, *Parallel computing*, **14**(3), 347-361.

Worden K. (1990), Data processing and experiment design for the restoring force surface method, part I: integration and differentiation of measured time data, *Mechanical Systems and Signal Processing*, **4**(4), 295-319.

Wu M. and Smyth A. W. (2007), Application of the unscented Kalman filter for real‐time nonlinear structural system identification, *Structural Control and Health Monitoring*, **14**(7), 971-990.

Wu M. and Smyth A. W. (2008), Real-time parameter estimation for degrading and pinching hysteretic models, *International Journal of Non-Linear Mechanics*, **43**(9), 822-833.

Wu X., Ghaboussi J. and Garrett J. H. (1992), Use of neural networks in detection of structural damage, *Computers & structures*, **42**(4), 649-659.

Xu C., Chase J. G. and Rodgers G. W. (2014), Physical parameter identification of nonlinear base-isolated buildings using seismic response data, *Computers & Structures*, **145**(1), 47-57.

Xu C., Chase J. G. and Rodgers G. W. (2015), Nonlinear Regression Based Health Monitoring of Hysteretic Structures under Seismic Excitation, *Shock and Vibration*, **2015**(2015), 1-12.

Yamanouchi H., Midorikawa M., Nishiyama I. and Watabe M. (1989), Seismic behavior of full-scale concentrically braced steel building structure, *Journal of Structural Engineering*, **115**(8), 1917-1929.

Yan Y., Cheng L., Wu Z. and Yam L. (2007), Development in vibration-based structural damage detection technique, *Mechanical Systems and Signal Processing*, **21**(5), 2198-2211.

Yang J. N. and Lin S. (2004), On-line identification of non-linear hysteretic structures using an adaptive tracking technique, *International Journal of Non-Linear Mechanics*, **39**(9), 1481-1491.

Yang J. N., Lin S., Huang H. and Zhou L. (2006), An adaptive extended Kalman filter for structural damage identification, *Structural Control and Health Monitoring*, **13**(4), 849-867.

Yang J. N., Pan S. and Lin S. (2007), Least-squares estimation with unknown excitations for damage identification of structures, *Journal of Engineering Mechanics*, **133**(1), 12-21.

Yao R. and Pakzad S. N. (2014), Time and frequency domain regression‐based stiffness estimation and damage identification, *Structural Control and Health Monitoring*, **21**(3), 356-380.

Yi T. H., Li H. N. and Gu M. (2013), Recent research and applications of GPS‐based

monitoring technology for high‐rise structures, *Structural Control and Health Monitoring*, **20**(5), 649-670.

Yoshimoto R., Mita A. and Okada K. (2005), Damage detection of base-isolated buildings using multi-input multi-output subspace identification, *Earthquake engineering & structural dynamics*, **34**(3), 307-324.

Zhang H., Foliente G. C., Yang Y. and Ma F. (2002), Parameter identification of inelastic structures under dynamic loads, *Earthquake engineering & structural dynamics*, **31**(5), 1113-1130.

Zhao B., Taucer F. and Rossetto T. (2009), Field investigation on the performance of building structures during the 12 May 2008 Wenchuan earthquake in China, *Engineering Structures*, **31**(8), 1707-1723.

Zhong J., Gardoni P. and Rosowsky D. (2009), Stiffness degradation and time to cracking of cover concrete in reinforced concrete structures subject to corrosion, *Journal of engineering mechanics*, **136**(2), 209-219.

Zhou C., Chase J., Rodgers G., Kuang A. and Xu C. (2015), *Response prediction and parameter identification for base-isolated buildings with limited sensors*, 2015 New Zealand Society for Earthquake Engineering (NZSEE) Annual Technical Conference, Rotorua,New Zealand.

Zhou C., Chase J., Rodgers G. and Xu C. (2014), *Damage identification of a flag-shaped hysteresis structure subject to seismic excitation*, 2014 New Zealand Society for Earthquake Engineering (NZSEE) Annual Technical Conference, Aucland,New Zealand.

Zhou C., Chase J. G., Rodgers G. W., Kuang A., Gutschmidt S. and Xu C. (2015), Performance Evaluation of CWH Base Isolated Building During Two Major Earthquakes in Christchurch., *Bulletin of the New Zealand Society for Earthquake Engineering* **48**(4), 264-273.

Zhou C., Chase J. G., Rodgers G. W., Tomlinson H. and Xu C. (2015), Physical Parameter Identification of Structural Systems with Hysteretic Pinching, *Computer-Aided Civil and Infrastructure Engineering*, **30**(4), 247-262.

Zhou C., Chase J. G., Rodgers G. W. and Xu C. (2015), *Real-time structural health monitoring of reinforced concrete frame structure using a hysteresis loop method*, 2015 New Zealand Society for Earthquake Engineering (NZSEE) Annual Technical Conference, Rotorua,New Zealand.

Zhou C., Chase J. G., Rodgers G. W., Xu C. and Tomlinson H. (2015), Overall damage identification of flag-shaped hysteresis systems under seismic excitation, *Smart Structures and Systems*, **16**(1), 163-181.

Zou Y., Tong L. and Steven G. (2000), Vibration-based model-dependent damage

(delamination) identification and health monitoring for composite structures—a review, *Journal of Sound and vibration*, **230**(2), 357-378.